Study of the stabilization mechanisms of tetragonal ZrO2 nanocrystals in supercritical fluids

Aimery Auxemery

université de BORDEAUX

THÈSE PRÉSENTÉE

POUR OBTENIR LE GRADE DE

DOCTEUR DE

L'UNIVERSITÉ DE BORDEAUX

ÉCOLE DOCTORALE DES SCIENCES CHIMIQUES

SPÉCIALITÉ Physico-chimie de la matière condensée

Par Aimery AUXÉMÉRY

Study of the stabilization mechanisms of tetragonal ZrO_2 nanocrystals in supercritical fluids

Sous la direction de : Cyril AYMONIER et Gilles PHILIPPOT

Soutenue le 18 décembre 2019

Membres du jury :

M. MASSON, Olivier	Professeur, Université de Limoges	Rapporteur
Mme ROGER, Anne Cécile	Professeure, Université de Strasbourg	Rapporteuse
M. AYMONIER, Cyril	Directeur de Recherche CNRS	Examinateur
M. HEINTZ, Jean Marc	Professeur, Bordeaux INP	Président
M. PHILIPPOT, Gilles	Maître de conférences, Université de Bordeaux	Examinateur
Mme SASSOYE, Capucine	Maître de conférences, Sorbonne Université	Examinatrice

Acknowledgments

The work presented throughout this thesis has been realized at the ICMCB in Bordeaux, therefore I would like to express my foremost gratitude towards Mario Maglione, director of the ICMCB.

I would also like to express my gratitude to the board of examiners that allowed me to defend my thesis on that very special day: Olivier Masson (IRCer), Anne-Cécile Roger (ICPEES), Cyril Aymonier (ICMCB), Jean-Marc Heintz (ICMCB), Gilles Philippot (ICMCB) and Capucine Sassoye (LCMCP). Thank you for having taken the time to assess the work presented in this manuscript and given me such feedback on my work.

However, my deepest gratitude is expressed to both Cyril Aymonier and Gilles Philippot, my thesis supervisors, who have chosen me for this work, provided me guidance, support and trusted in me in every moment during these years. Thank you for choosing me for this job, which I particularly loved performing.

I would also like to thank those that have helped me in my work: Eric Lebraud, Nicolas Penin, Véronique Jubéra, Alexandre Fargues, Fabien Palencia, Cyril Dufour, Stéphane Toulin, Sonia Buffière, Marion Gayot, Laetitia Etienne, though for some of you, the works were not presented in this thesis I would nevertheless like to thank you for your help and patience. Special thanks to you Guillaume Aubert for his patience and never-ending supply in pump elements! Sandrine for your everyday smile, thank you.

I could never forget you guys from the CMC group at the university of Aarhus for your help with pair distribution analysis of WAXS measurements: Professor Bo B. Iversen, Sanna Sommer, Martin Roelsgaard and Nils Lau Broge for introducing me the technique and its subtleties. To you guys and many more from the CMC group for all these days and endless nights spent together at the PETRA III synchrotron. How could I ever forget, Jonas Beyer and Martin Roelsgaard, these last ten hours in Beamline P02.1 with “epic sax guy” (you reader should check it out, it keeps your nerves real tight to keep going during the last night. I hope I’ll see you again someday.

Also, you are quite a few to thank from the Bachelor years through the Master years till the end of my PhD go first of all to Julien and Nicolas the crazy machine guys. Xavier, your presence at my defense really touched me. Thibault, now you’re a married man, I can understand. The members of the team “Les gros cèpes” Romain, Pierre, Arthur and Armand, you guys rock!

Marie (I’ll never forget you), Sandy, Samantha, Cédric, Cyril, Baptiste, Thomas, Thomas and Thomas, Mathias, Fan, Maria, Louisiane, Guillaume, Luc, Katarzyna, Christopher, Hélène, Quentin and probably more I haven’t forgotten in my heart. How could I not mention you Céline and Romain Discolab for the fun (in the night) all these years.

My deepest feelings are dedicated to my family, for their ever-lasting mental support, I could never have done this without you.

And finally, last but not least, to the most precious woman in my life, Maroussia for your patience (and mine also) throughout all these fantastic years following the same path together.

And to all those I did not mention for diplomatic reasons, you are sincerely in my deepest thoughts.

Étude des mécanismes de stabilisation de nanocristaux de zircone quadratique en milieux fluides supercritiques

Dans son effort à maîtriser les techniques d'élaboration de matériaux, l'Homme a, depuis plusieurs millénaires, parcouru un très long chemin pavé de difficultés. Ces dernières décennies, la maîtrise en synthèse de nanomatériaux a permis de franchir de nouvelles limites dans la capacité à créer de nouveaux matériaux menant à des propriétés physico-chimiques inconnues jusqu'à lors. Ceci est notamment possible, grâce à la présence de défauts structurels, notion faisant grandement partie de la réflexion menée lors de ces travaux de thèse.

La zircone étant un matériau polymorphique, la stabilisation de chacune des structures cristallines dépend des domaines de pression et de température choisis lors de la synthèse tel que le montre la Figure 1.

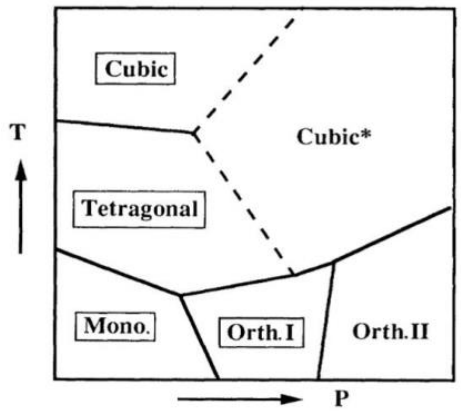

Figure 1 : diagramme de phase de la zircone en fonction de la pression et de la température.

Néanmoins, de nombreuses études ont démontré qu'il était possible de stabiliser de très petites nanoparticules de structure quadratique dans des domaines de pression et de température où la phase monoclinique est normalement stabilisée. La notion de taille critique a ainsi longtemps été mise en avant afin de permettre d'expliquer cette stabilisation pour des nanoparticules présentant une taille comprise entre 3 et 30 nanomètres.

Les études menées au cours de cette thèse auront pour but d'explorer les mécanismes de stabilisation de nanocristaux de zircone quadratique dont la taille est comprise entre 2 et 7 nanomètres non pas à travers le prisme de la notion de taille critique, mais en se basant sur les concepts déjà démontrés pour la zircone dont la taille de grain est supérieure au nanomètre, à savoir : la présence de lacunes d'oxygène au sein de la structure cristalline et le phénomène de cristallisation topotactique induit par la présence de similitudes structurelles entre

l'arrangement interatomique de la phase amorphe et de celui de la structure cristallisée. Nous verrons néanmoins que la taille est essentielle afin de générer les défauts structurels nécessaires à la stabilisation de la phase quadratique métastable. Les conclusions finales apportées à cette étude seront fondées sur des observations effectuées par analyse PDF (« Pair Distribution Function ») effectuées sur des mesures *in situ* en diffusion totale des rayons X lors de la cristallisation des nanocristaux de zircone dont la taille est comprise entre 2 et 7 nanomètres.
Les objectifs de ces travaux de thèse étaient donc dans un premier temps de définir la voie de synthèse appropriée afin de stabiliser des nanocristaux de zircone quadratique métastables dans une gamme de taille inférieure à 10 nanomètres. Puis, d'observer *in situ* la formation de ces nanocristaux lors de mesures de diffusion totale des rayons X. Finalement, ces mesures *in situ* nous ont permis de comprendre et déterminer les mécanismes permettant la stabilisation de ces nanocristaux de zircone quadratique, en se basant sur les concepts de lacunes en oxygène et la cristallisation topotactique. Dans le premier chapitre, nous nous sommes intéressés aux types de solvants et de précurseurs métalliques appropriés pour synthétiser des particules de zircone quadratique au travers d'une étude bibliographique. Ainsi, la voie de synthèse sol-gel non-hydrolytique a attiré notre attention. Et tentant de tirer parti de la déshydratation de l'éthanol supercritique, nous avons développé la voie de synthèse sol-gel non-hydrolytique « borderline » (S.G.N.H.B.) comme nous le verrons au cours du premier chapitre. On observe sur la Figure 2 que l'augmentation de la concentration en eau générée à partir d'éthanol absolu est linéaire au-delà de la température critique à 25 MPa.

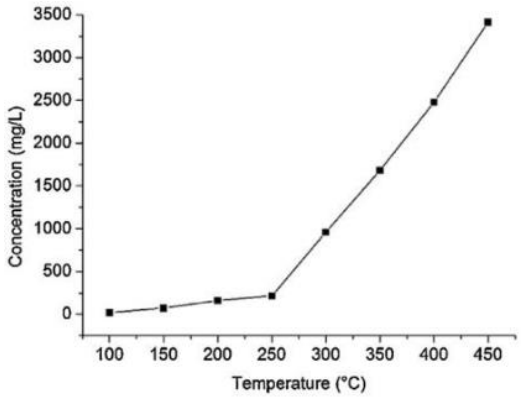

Figure 2 : Concentration en eau (mg d'eau/litre d'éthanol), à 25 MPa et pendant 36 s, en fonction de la température.

Ainsi, la voie de synthèse S.G.N.H.B. sera étudiée à 25 MPa et 400°C dans l'éthanol supercritique. Ensuite, les différences de cinétiques de déshydratation de l'éthanol

supercritique, ainsi que de la déshydratation d'autres alcools primaires supercritiques seront exploitées lors d'une étude *in situ* sur la formation de nanocristaux de zircone, développée au cours du Chapitre IV.

Au fil du second chapitre, le réacteur employé lors de cette thèse pour effectuer les synthèses de nanomatériaux (Figure 3), présentés dans le Chapitre III, en continu et en conditions supercritiques, ainsi que le dispositif expérimental employé lors des mesures *in situ* (Figure 4) détaillées du Chapitre IV seront présentés.

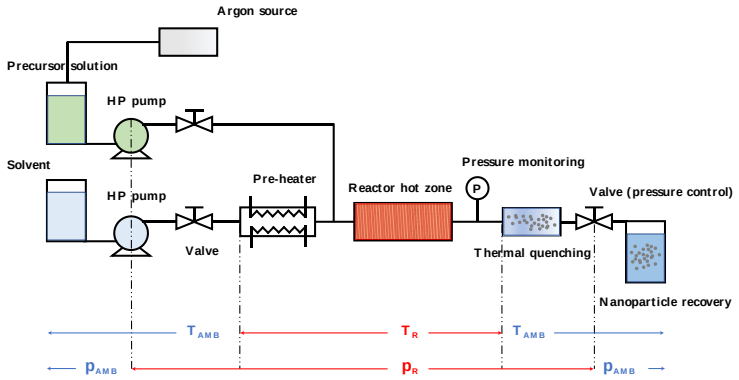

Figure 3 : Schéma du réacteur solvothermal supercritique utilisé lors des synthèses en continu au cours de cette thèse.

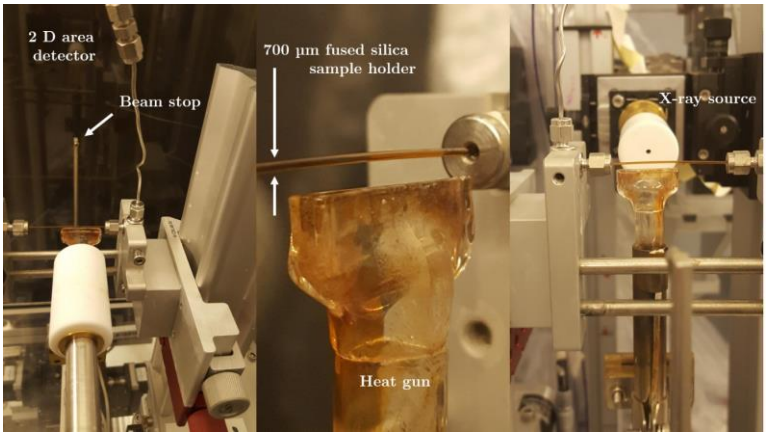

Figure 4 : Dispositif expérimental utilisé pour les mesures *in situ* en diffusion des rayons X.

Les différentes techniques de caractérisation structurelles *ex situ* et *in situ* seront également développées dans le Chapitre II. Afin de déterminer avec précision les variations de zircone quadratique et monoclinique présentes au sein des matériaux synthétisés, les études conventionnelles en diffraction des rayon X seront couplées à des étude en spectroscopie Raman, cette dernière étant extrêmement sensible à la structure à une échelle très locale,

contrairement à la première donnant des informations moyennes. La microscopie électronique en transmission haute résolution a été employée afin de confirmer que les matériaux synthétisés étaient bien des nanocristaux de zircone, mais également afin de démontrer que la stabilisation de la zircone quadratique était bien le résultat de la présence de défauts structurels. La spectroscopie infra-rouge par transformation de Fourier a été employée afin de confirmer l'efficacité de la fonctionnalisation par greffage de groupes carboxylates à la surface des nanoparticules, permettant ainsi de réduire la taille des nanocristaux. Ce second chapitre permettra finalement de présenter les principes de l'analyse PDF nécessaires à l'étude effectuée lors de mesures *in situ* faites en diffusion totale des rayons X présentées au cours du Chapitre IV.

Le chapitre III présentera ainsi les principaux résultats structurels obtenus et les observations effectuées par les techniques de caractérisation *ex situ* sur les matériaux produits avec notre réacteur continu. Seront ainsi étudiés au cours de ce chapitre l'influence de la nature du solvant et du précurseur, puis l'effet de la concentration en précurseur ainsi que le rapport molaire précurseur/agent de greffage sur les fractions molaires en zircone quadratique et monoclinique. Nous verrons dans cette partie que le choix du type de synthèse déterminé en Chapitre I a permis d'obtenir de la zircone quadratique quasiment pure, mais qu'une limite persiste malgré la très petite taille des nanoparticules obtenues (2-3 nm). La Figure 5 montre, sur différents diffractogrammes, l'efficacité du greffage de groupes carboxylates sur la réduction de la taille des nanocristaux de zircone, permettant la stabilisation de nanocristaux de zircone quadratique de 2 nanomètres.

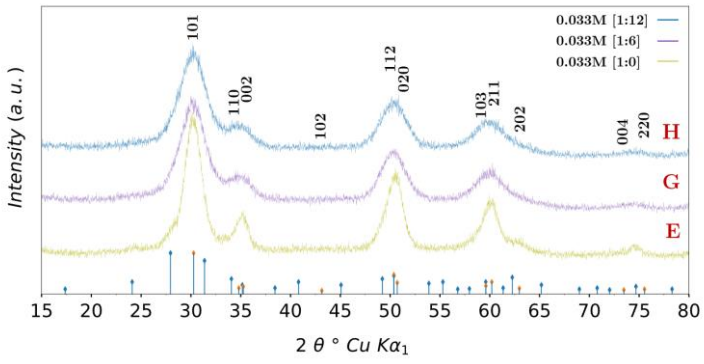

Figure 5 : Diffractogrammes des RX de nanopoudres de zircone en fonction des rapports molaires précurseur/surfactant ([Zr^{4+}:HA] = [1:0] ; [1:6] ; [1:12]), avec l'acide hexanoïque utilisé comme surfactant.

Nous verrons au cours de ce chapitre de quelle façon nos recherches ont été orientées par la suite vers une étude cinétique afin de stabiliser la phase quadratique pure plutôt que par effet de taille après avoir atteint une limite dans la possibilité de stabiliser des nanocristaux de zircone quadratique pure, tel que présenté dans la Figure 6. Dans cette figure, la poudre A a été synthétisée à partir d'oxynitrate de zirconium (IV) hydraté dans de l'eau, la B avec de l'isopropoxide de zirconium dans un mélange eau/éthanol 50/50 % massique et les poudres C à F avec de l'isopropoxide de zirconium uniquement dans l'éthanol an en augmentant ma concentration de précurseur, les poudres G et H, également avec de l'isopropoxide de zirconium dans l'éthanol mais en ajoutant progressivement de l'acide hexanoïque (1 mole de Zr pour 6 moles d'acide hexanoïque puis 1 pour 12).

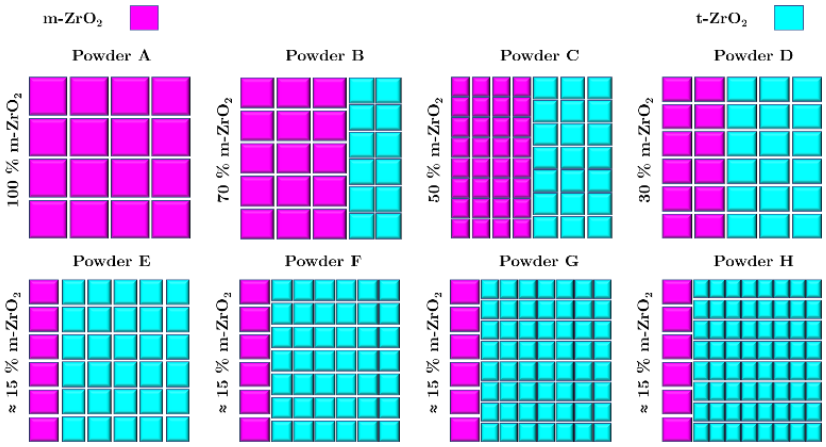

Figure 6 : Représentation de la limite à stabiliser des nanocristaux de zircone quadratique pure, malgré la diminution en taille.

Au cours du Chapitre IV, l'effet cinétique de déshydratation de l'éthanol sera étudié lors de réactions S.G.N.H.B. en fonction de la température de synthèse (Figure 7).

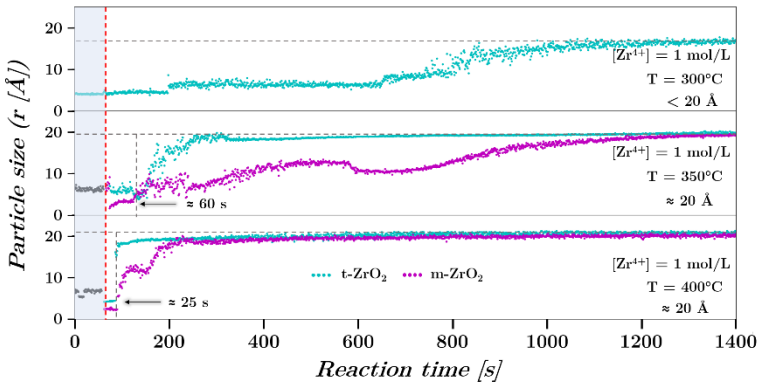

Figure 7 : Mesures *in situ* réalisées dans l'éthanol supercritique à 300, 350 et 400°C.

L’effet cinétique sera également étudié en subtilisant l’éthanol pur par des alcools primaires purs présentant des chaines carbonées plus longues (Figure 8), suivant les observations faites lors du Chapitre I.

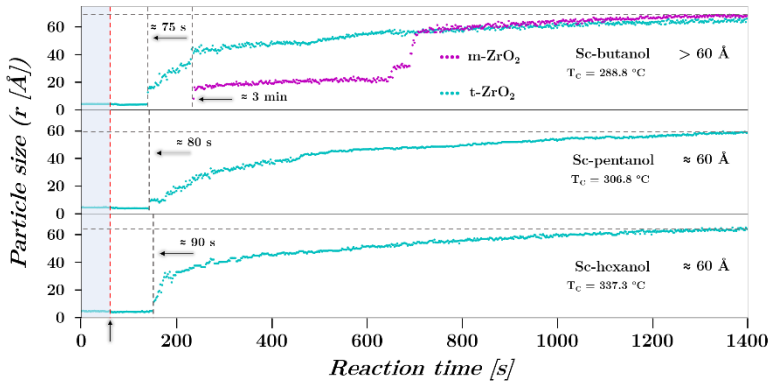

Figure 8 : Mesures *in situ* réalisées dans le butanol, le pentanol et l’hexanol supercritiques à 400°C.

Nous verrons au cours du Chapitre IV, qu’il est possible de stabiliser la phase quadratique pure pour des nanocristaux dont la taille peut être comprise entre 2 et 7 nanomètres (Figures 7 et 8). Cette stabilisation semble possible lorsque les cinétiques de déshydratation, donc de condensation, sont ralenties alors que lorsque les cinétiques de déshydratation sont trop importantes, il y a émergence de la phase monoclinique, induisant *in fine* un mélange des deux structures.

Il sera démontré grâce à l’analyse PDF que les nanoparticules de zircone quadratique pures présentent néanmoins en leur sein les distances interatomiques des structures monoclinique et quadratique (Figure 9)

Également, l’existence d’un décalage, visible lorsque la résolution le permettra, des distances interatomiques dès la première sphère de coordinence des atomes de zirconium révèlera que cette stabilisation est bien due à une expansion de la maille cristalline, résultant de la présence de lacunes en oxygène.

Ainsi, l’observation de la variation du nombre de coordinence des atomes de zirconium montre l’influence des lacunes en oxygène et l’importance des cinétiques relativement lentes dans la stabilisation de nanocristaux de zircon quadratique pure (Figure 10).

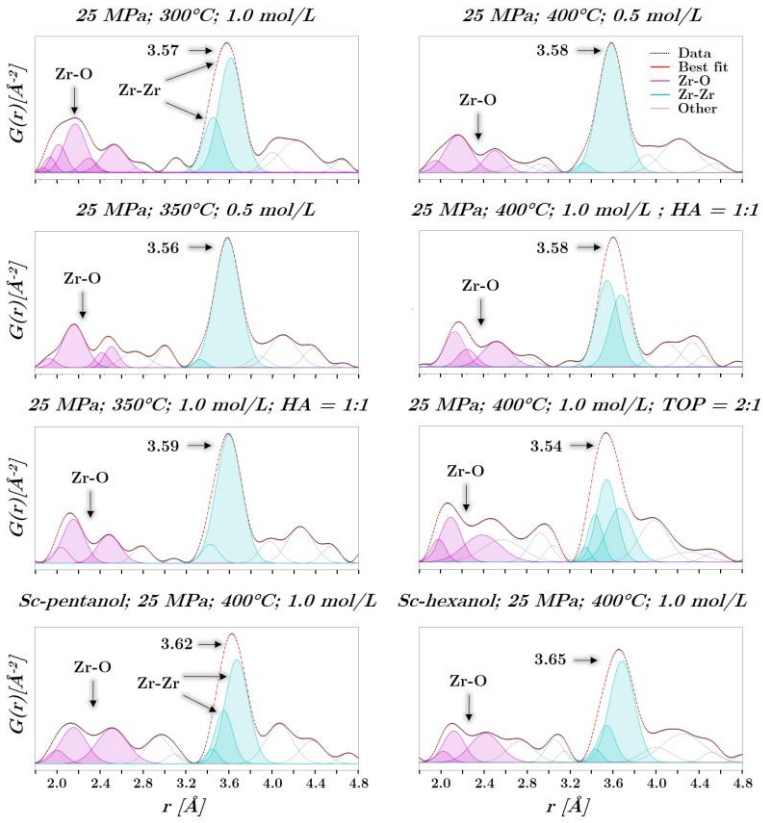

Figure 9 : Fonctions de distribution radiales de nanocristaux de zircone quadratiques, obtenues par analyse PDF de mesures en diffusion totale des rayons X.

Nous verrons ainsi que plus les cinétiques de déshydratation sont ralenties, plus la première sphère de coordinence autour des atomes de zirconium se réarrange lentement, permettant ainsi

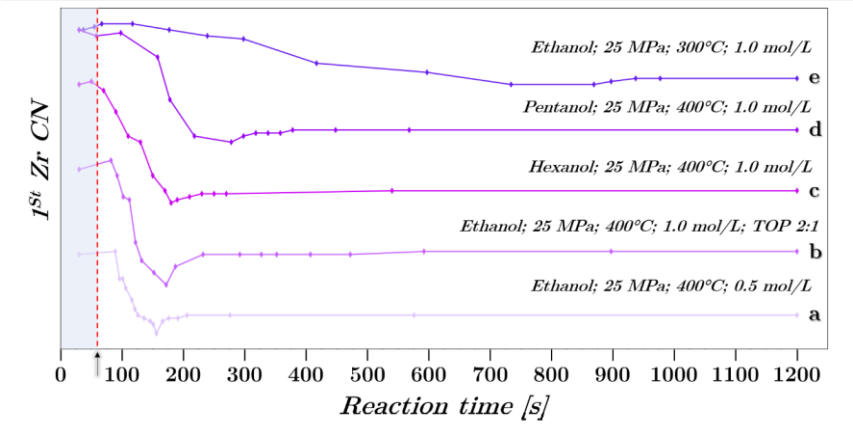

la stabilisation de la phase quadratique en maintenant un niveau bas d'atomes d'oxygène dans la première sphère de coordination des atomes de zirconium (Figure 10).

Figure 10 : Évolution du nombre d'atomes d'oxygène dans la première sphère de coordinence d'atomes de zirconium, observée lors des mesures en diffusion totale des rayons X.

L'étude des fonctions de distribution de paires faite au Chapitre IV, a permis également de mettre en avant que les relativement lentes cinétiques entraînent la condensation lente de molécules de précurseurs à la surface des nanoclusters, formant ainsi de petits nanocristaux de zircone quadratique (Figure 11).

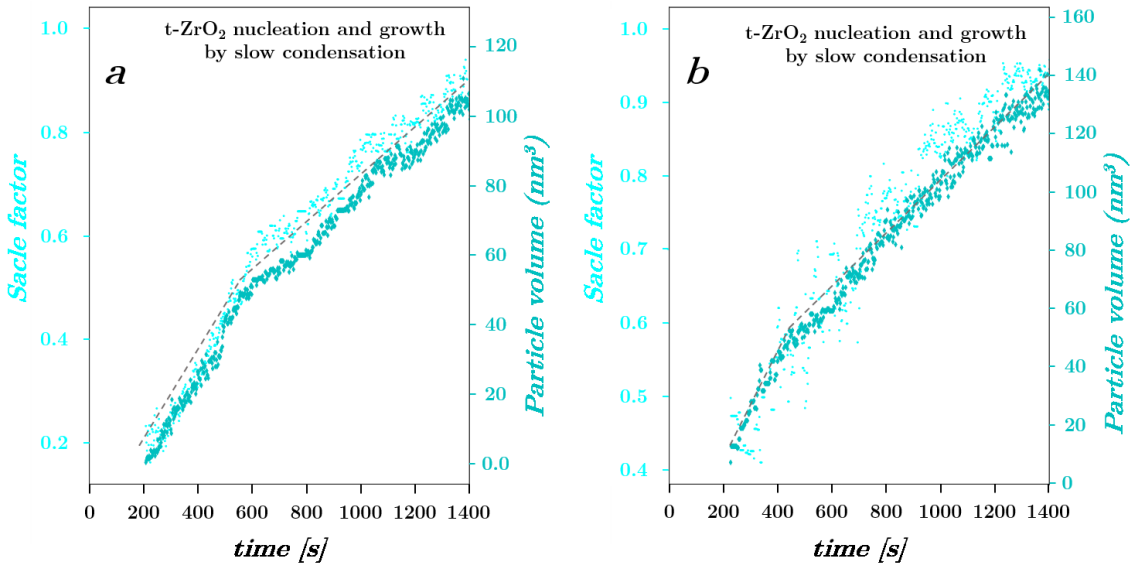

Figure 11 : Variation de l'intensité de diffusion totale des rayons X et du volume des nanocristaux de zircone quadratique au cours du temps lors de mesures *in situ* réalisées dans le pentanol et l'hexanol supercritiques.

Finalement, les similitudes structurelles induisant une cristallisation topotactique sont mises en évidence lors des mesures en diffusion totale des rayons X en synchrotron, par observation des similitudes entres les distances interatomiques (arrangement atomique) présentes aussi bien au sein des molécules de précurseur qu'au sein des nanocristaux en fin de synthèse jusque dans la deuxième sphère de coordinence (Figure 12).

Après étude de l'arrangement interatomique au sein des clusters en pression et à température ambiante, on observe des corrélations dans les distances interatomiques propres aux structures monoclinique et quadratique de la zircone.

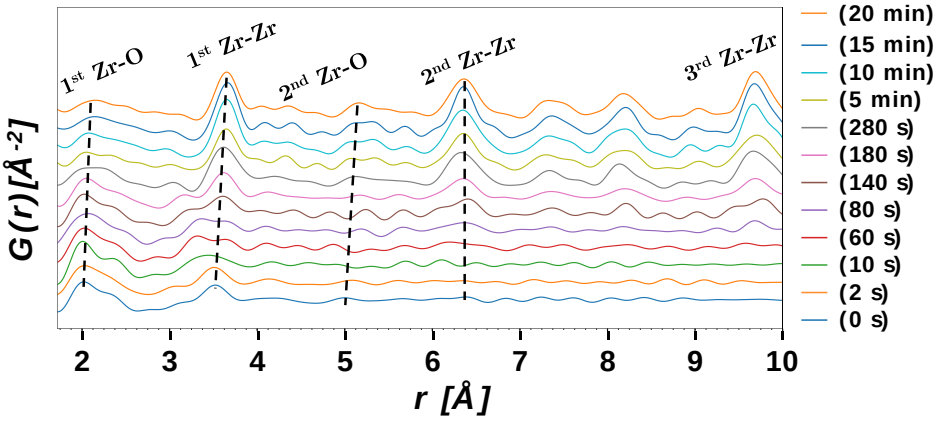

Figure 12 : Observation des similitudes entre l'arrangement interatomique des précurseurs (t = 0s), et lors de la cristallisation de zircone quadratique (1 min < t < 20 min)

En conclusion, les synthèses S.G.N.H.B. permettent de générer, en conditions supercritiques, des molécules d'eau par déshydratation d'alcools primaires purs. Le contrôle des cinétiques de déshydratation, essentiellement par variation de la température de synthèse ou la longueur de la chaîne carbonée d'un alcool considéré permet de modifier les cinétiques de réaction. Il a alors été observé lors de mesures *in situ* en diffusion totale des rayons X, que les réactions les plus lentes permettaient de produire des nanocristaux de zircone quadratique pure par condensation progressive des molécules de précurseur à la surface des nanoclusters formés. Ainsi, il a été possible à l'aide de l'outil PDF d'observer lors des mesures *in situ* que les variations de cinétiques de réaction permettent de stabiliser soit des nanocristaux de zircone à la fois monocliniques et quadratiques ou bien purement quadratiques, et ce quel que soit la taille des nanocristaux, dont les tailles sont comprises entre 2 et 7 nanomètres. Ainsi, ce sont les effets cinétiques plutôt que l'effet de taille qui permettent la stabilisation de nanocristaux de structure quadratique, à partir de nanoclusters présentant des arrangements interatomiques similaires aux structures monoclinique et quadratique.

Table of content

Introduction

A step back in time to present days

In 1907, Henry Bergson, in his book *Creative Evolution* [1], refers to the antique term *Homo faber* rather than *Homo sapiens* to define our genre and its intelligence, considering what seems to be its original feature is "the faculty of manufacturing artificial objects, especially tools to make tools, and of indefinitely varying the manufacture".

During the Neolithic period (10.000 to 2.000 B. C.), Humanity has first learned to engineer native metals such as gold, silver and copper in Mesopotamia and ever since, knowledge in metal manufacturing and shaping spread worldwide to all known civilizations. From the early Bronze Age (2000 to 800 B. C.) until the late Iron Age (800 to 50 B. C.), technological progress deeply influenced many societies by means of greater weaponry, improvement in agricultural equipment and yields, resulting in an exponential demographic growth, and in the early 21st a revolution in communications.

However, only a handful of chemical elements, rarely isolated as pure, were yet known before the end of the Renaissance due to the limitations in chemical reduction techniques. But with the advent, in the 19th century, of electrolysis and spectrographs, not only were a colossal number of elements discovered, but their purification had also become possible as exemplified in Figure 0-1. Though steel had been known and widely crafted ever since antic times, it was only then and owing to increasingly efficient production methods that large-scale industrial use of quality steel led to the Industrial Revolution, major technological innovations and breakthroughs in element discoveries. Hafnium, in 1922, was the last natural element to be discovered after almost three centuries of fertile chemistry and great scientific adventure.

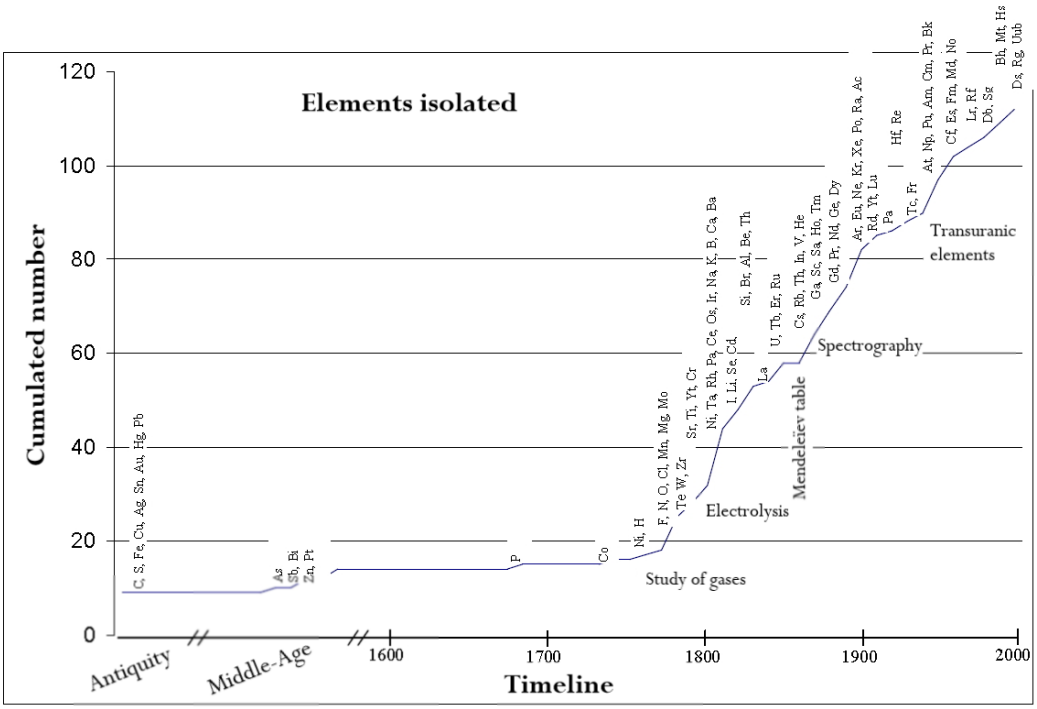

Figure 0-1. Illustration of the evolution in chemical elements discoveries throughout history [2].

At that precise moment in time, theory for X-ray scattering was only at its early stage but rapidly became essential in fabricating new materials with, until then, inconceivable physical properties and thus opening new fields in industrial applications and synthesis techniques. The potential of crystallography exploded, shortly after the theory had been accepted, owing its powerful regularity to describe and characterize crystalline materials. But with statistical mechanics and the advent of fast calculating computers, total X-ray scattering observations on local structural ordering at the atomic scale became possible with the introduction of pair distribution function (PDF) analysis and is nowadays performed on a daily basis on gases, liquids and solids, allowing fundamental understanding in the randomly distributed defects in materials, and on various chemical processes by monitoring *in situ* chemical reactions.

Nowadays, the unique physical, chemical and structural properties of metal oxides are widely employed in numerous applications that range from the simplest ceramics to the most complex engineered materials such as superconductors [3] and nano-scaled ferroelectrics [4, 5] and their high surface reactivity is crucial in heterogeneous catalysis as solid phases or supports [6, 7, 8, 9, 10, 11, 12, 13]. Such diversity in applications originates not only from their complex electronic and crystal structures, but also our incapacity to generate flawless structures, which we have learned to use at our advantage.

While the solid-state synthesis route has been the most widely used to produce metal oxide materials, the demand in high added value functional materials as given rise to the "bottom-up" approach, where atoms are sequentially added to one another with relatively fine control over the final properties and size achieved, and has been extended over the twentieth century to a large variety of synthesis procedures. The supercritical fluid technology is, in terms of size downscaling, probably one of the most promising scalable approaches developed in the late 20th to produce very fine and uniform metal oxide nanoparticles in a single step procedure and mild synthesis conditions [5, 14, 15, 16, 17, 18, 19, 20, 21, 22, 23, 24, 25]. Therefore, the supercritical solvothermal process will be used to synthesize ultrafine ZrO_2 nanoparticles in the bottom-up approach in order to obtain the smallest possible particles and investigate the possibility to stabilize metastable tetragonal ZrO_2 (t-ZrO_2).

The main objectives of this PhD are to study and unravel the mechanisms governing the stabilization of t-ZrO_2 nanocrystals. The elaboration of a synthesis method, from the information on solvent stability gathered in Chapter I, to produce t-ZrO_2 nanoparticles in supercritical fluids is critical. Secondly, confirming the possibility to stabilize metastable t-ZrO_2 nanocrystals during borderline non-hydrolytic sol-gel (B.N.H.S.G.) syntheses in supercritical fluids. Finally, understanding of nanoparticle formation mechanisms in supercritical fluids from the dissolved cationic metal precursor organization to very fine crystallized nanoparticles *via* pair distribution function (PDF) analysis. As many theories have been exposed to explain the stabilization mechanisms [26], in this work, mainly three concepts will be discussed, based either on (i) the effect of the crystallite size, (ii) the influence of lattice oxygen vacancies (L.O.V.), and (ii) the role of structural similarities, all with the purpose of determining a relevant ZrO_2 nanocrystallite formation mechanism in supercritical fluids.

The context of this work, and its direction will be expressed in the first chapter, where the major parameters influencing, to our knowledge, the stabilization of t-ZrO_2 will be presented along with the various synthesis routes and techniques used to form this specific structure. The supercritical fluid technology will then be briefly introduced along with its advantages over other techniques and the reasons we chose to produce ultra-fine ZrO_2 nanoparticles with the sol-gel like approach in supercritical fluids. An important section of the chapter will be dedicated to the behavior of alcoholic solvents and their specific tendency to be dehydrated as it will be a key parameter in the syntheses presented in this work.

A brief description of the experimental and characterizations techniques used in this work to synthesize and characterize ZrO_2 nanoparticles will be introduced in the second chapter. The continuous flow reactors used for nanoparticle synthesis will be described, along with *ex situ*

X-ray diffraction, Raman spectroscopy and electronic microscopy techniques used to characterize the synthesized powders in terms of structure, purity, crystallinity and polydispersity. Finally, the experimental apparatus used to observe *in situ* ZrO_2 nanoparticle formation during total X-ray scattering measurements will be introduced at the end of the second chapter along with the theoretical background on PDF analysis necessary for this work. The third chapter will focus on demonstrating the feasibility of B.N.H.S.G. syntheses of ZrO_2 nanoparticles in supercritical fluids and optimizing the synthesis conditions to produce the finest nanoparticles to either confirm or infirm the effect of the crystallite size on stabilizing t-ZrO_2 at the nanoscale. X-ray diffraction, Raman spectroscopy and electronic microscopy techniques will be used to characterize the structure, purity and crystallinity of the synthesized powders.

Finally, in the fourth chapter, reactions performed in the third chapter will be reproduced during *in situ* X-ray total scattering measurements. Also, additional experiments that weren't performed *ex situ* will be introduced in this chapter. PDF analysis of total X-ray scattering measurements will be deeply realized to observe the influence the crystallite size, L.O.V. and structural similarities, but more specifically give a description of the observed nucleation and growth phenomena with the aim to finally unravel the formation mechanisms of ZrO_2 nanoparticles in supercritical fluids.

Knowledge in metallurgy has incredibly increased since the end of the Paleolithic period, when back then only native metals could be crafted. From Agricola [27], through Lavoisier [28], and to the atomic theory nowadays, *Homo faber* has come a long way in materials engineering. However, the path in full comprehension and mastering of material science is still a long road to experiment.

Chapter I
Zirconium dioxide, a state of the art

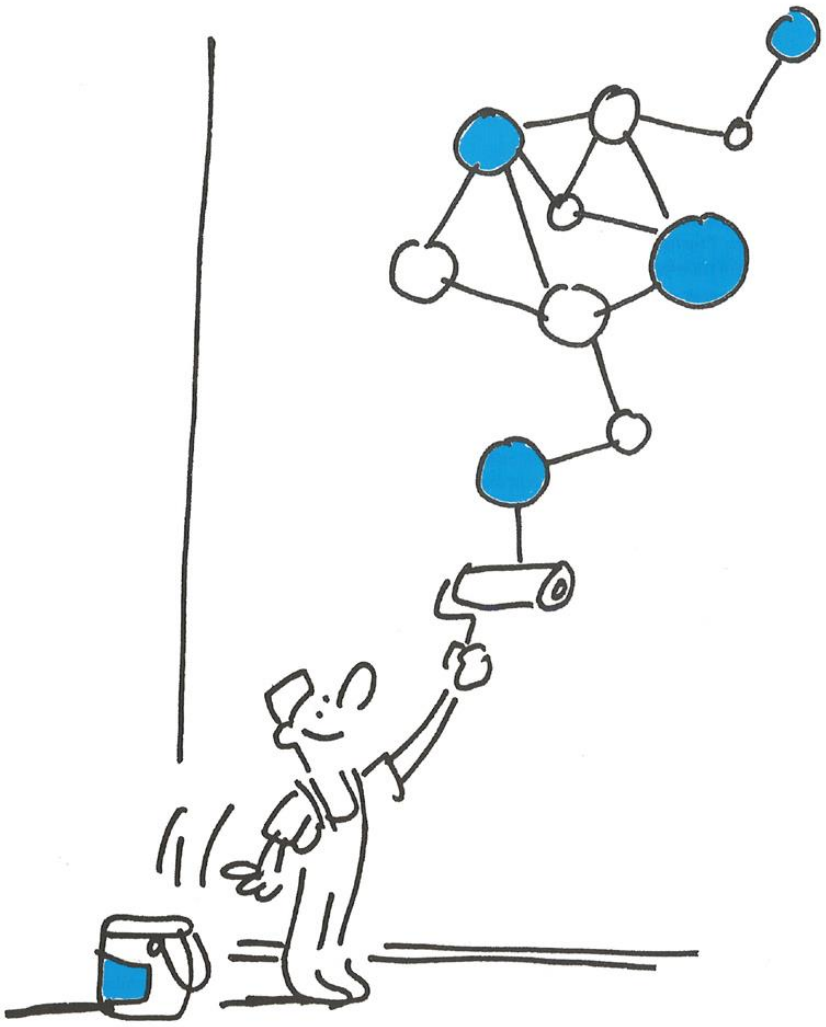

I.1 Zirconium dioxide

ZrO_2, or zirconia, is a metal oxide of the transition metal zirconium exhibiting $[Kr]4d^25s^2$ and $[Kr]4d^05s^0$ electronic configurations in the metallic and oxide forms, respectively. Though ZrO_2 occurs naturally as the mineral baddeleyite in many places worldwide (e.g., Brazil, South Africa, Sri Lanka or even Russia), pure zirconium metal (Zr) is usually extracted from zircon sands with the $Zr(Hf)SiO_4$ chemical formula. Zircon being an extremely refractory mineral, its decomposition requires elevated temperatures and the use of aggressive chemicals. Among many others, two of the main routes for zircon decomposition are caustic fusion and chlorination [29].

I.1.1 ZrO_2 crystalline structures

ZrO_2 is a polymorphic metal oxide that can exhibit up to five different crystal structures depending on the pressure and temperature conditions as schematized in Figure I-1 but is thermodynamically stable at standard temperature and pressure (STP) conditions in the monoclinic structure (m-ZrO_2, space group $P12_1/c$). The two general procedures used to induce structural changes to m-ZrO_2 are developed in Figure I-1 with the temperature versus pressure phase diagram for ZrO_2 [30].

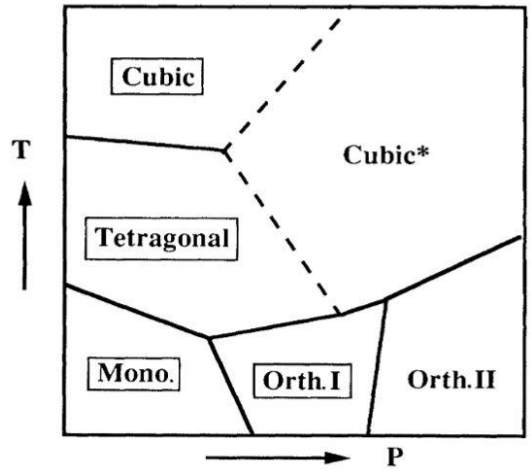

Figure I-1. P, T phase diagram for ZrO_2, where orthorhombic (I) is stable at room temperature between 3.5 and 13-16 GPa with zirconium in a sevenfold coordination, and orthorhombic (II) transition is expected at ≈ 19 GPa with zirconium coordinated to nine oxygen atoms.

Though it is thermally and mechanically stable from room temperature up to its melting point (≈ 2710°C), we can see in Figure I-1 that both thermal and mechanical energies applied to the material may induce changes in its crystalline structure. Thermally, ZrO_2 can undergo two phase transformations: from m-ZrO_2 to tetragonal (t-ZrO_2) at ≈ 1205°C which is generally accompanied by ≈ 4-5 % [31, 32] increase in the unit-cell volume; and at ≈ 2377°C cubic zirconia (c-ZrO_2) stabilizes and will be stable until the structure melts at ≈ 2710°C [33]. Mechanically, the monoclinic to orthorhombic I and II transitions were studied *in situ* for the first time at room temperature in 1986 and orthorhombic(I) was reported to exhibit a structure closely related to the monoclinic structure with Zr atoms coordinated to 7 oxygen atoms. However, orthorhombic(II) displayed a distorted cotunnite ($PbCl_2$) structure where Zr atoms were coordinated to 9 oxygen atoms [30, 34, 35].

Though this thesis will not focus on the two orthorhombic structures, it is nevertheless necessary to mention their existence and the difference in pathways to achieve either m-, t- and c- or o-ZrO_2 polymorphs.

Figure I-2 shows the main ZrO_2 crystal structures of interest in this thesis: m-ZrO_2; t-ZrO_2; and c-ZrO_2.

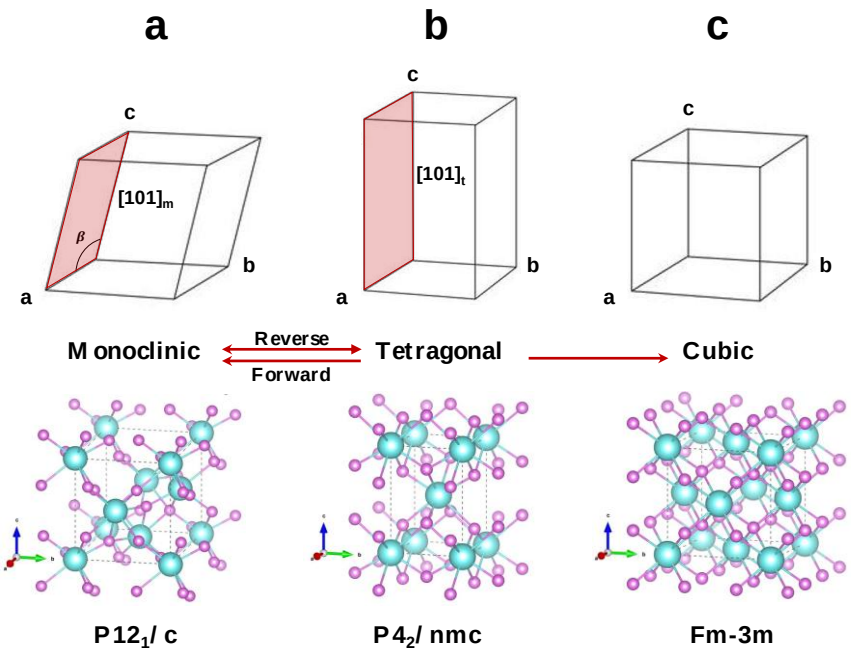

Figure I-2. Displaying: (a) m-ZrO_2; (b) t-ZrO_2 and (c) c-ZrO_2 crystal structures. Are emphasized the $(101)_m$ and $(101)_t$ habits planes generally reported between m- and t-ZrO_2.

m-ZrO_2 (Figure I-2 a) stabilizes in the $P12_1/c$ space group with the following lattice constants: a = 5.1514(4) Å; b = 5.2098(4) Å; c = 5.3204(4) Å; $\alpha = \beta = 90°$ and γ = 99.171(3)° [36]. The monoclinic zirconium ionic radius r_{Zr} is equal to 0.78 Å, too small to coordinate to eight oxygen ions at room temperature and is thus coordinated to 7 oxygen ions in the stable m-ZrO_2 structure.

t-ZrO_2 (Figure I-2 b) stabilizes in the $P4_2/nmc$ space group with the following lattice constants: a = b = 3.5960(1) Å; c = 5.1841(2) Å and $\alpha = \beta = \gamma = 90°$ [37]. Its zirconium ionic radius r_{Zr} = 0.84 Å in this crystal structure and thus may coordinate to 8 oxygen ions in the stable t-ZrO_2 structure. However, the stable t-ZrO_2 crystal structure is generally reported as slightly defective in terms of oxygen stoichiometry where lattice oxygen vacancies (L.O.V.) are responsible for the relieve in internal strain associated with the eightfold oxygen coordination [38].

c-ZrO_2 (Figure I-2 c) stabilizes in the Fm-3m space group. In this configuration, a = b = c = 5.135(9) Å and $\alpha = \beta = \gamma = 90°$ [39]. Its zirconium ionic radius r_{Zr} = 0.84 Å and Zr atoms are also coordinated to 8 O atoms as in t-ZrO_2, however its stabilization is favored by L.O.V. with concentrations even larger than in the case of t-ZrO_2 [38]. However, due to the similitudes between c-ZrO_2 and t-ZrO_2 X-ray diffraction patterns, and thus the difficulty generally encountered to distinguish both structures, careful attention was taken in this work to systematically carefully distinguish both structures, providing Raman spectra. Table I-1 lists the lattice constants for the 3 main ZrO_2 polymorphs.

Table I-1. List of the main lattice constants for the main ZrO_2 polymorphs

	ZrO_2 polymorphs		
Lattice constants	m-ZrO_2 (*$P12_1/c$*)	t-ZrO_2 (*$P4_2/nmc$*)	c-ZrO_2(*Fm-3m*)
a (Å)	5.1514(4)	3.5960(1)	5.135(9)
b (Å)	5.2098(4)	3.5960(1)	5.135(9)
c (Å)	5.3204(4)	5.1841(2)	5.135(9)
α (°)	90	90	90
β (°)	99.171(3)	90	90
γ (°)	90	90	90

I.2 Defects in metal oxides

Catalytic activity of metal oxide nanoparticles has been clearly linked, through numerous studies, to the presence of anionic vacancies and surface defects. Moreover, the presence of partially reduced surface cations is known to increase as the particle size decreases resulting in more reactive non-stoichiometric $MO_{2-\delta}$ simple dioxides, where δ is the amount of oxygen vacancies [40]. The following section will present, among the main types of defects in metal oxides (e.g., non-stoichiometry, Schottky and Frenkel point defects, etc.), the main type of interest in this thesis: lattice oxygen vacancies and their influence on lattice constants expansion and contraction.

I.2.1 Non-stoichiometry

Many categories of elements such as halides, hydrides, sulphides, but specifically oxides have found increasing number of industrial applications due to their mechanical, catalytic properties, etc., but also their non-stoichiometry [41, 42]. Precise control of stoichiometry is therefore of crucial importance to fulfil the desired applications and is generally accomplished either by controlling the nanoparticle size in simple metal oxides (MO, MO_2, MO_3, etc.) or by integrating dopants and impurities inside the crystal structure in the case of mixed oxides, thus generating point defects [43, 44, 45].

I.2.2 Point defects

The main types of defects at the atomic level in metal oxides are represented in Figure I-3.

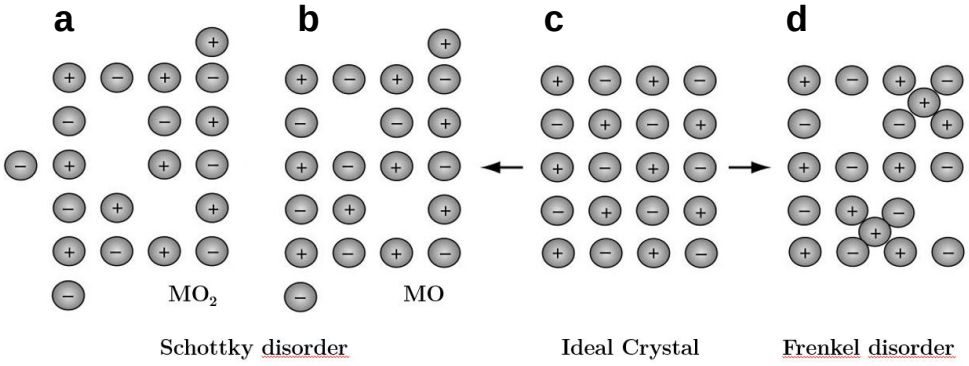

Figure I-3. Representation of (a) and (b) Schottky disorder in metal oxides for both MO_2 and MO simple oxides, respectively; (c) an ideal crystal structure and (d) Frenkel disorder. Adapted from [12].

In ideal crystal structures, all atomic sites are fully occupied with every atom in its regular lattice site as shown in Figure I-3 c. In a real thermodynamic system however, entropy generates lattice defects and therefore, all real crystals deviate from ideal structures. Lattice defects in metal oxides can be of many types: Schottky disorder (Figures I-3 a and b); Frenkel disorder (Figure I-3 d); oxygen vacancies; etc., and controlling their nature and concentration is of major importance in engineering science as they determine the material's properties. In the case of mixed oxides, interstitial or substitutional iso- or aliovalent impurities may lead to oxygen non-stoichiometry and influence either the final crystal structure [46], electronic properties, or both characteristics in the material [47, 48, 49, 50]. However, concerning simple oxides, it is generally the synthesis route that dictates the concentration in oxygen vacancies, thus the applicable properties of the material.

I.2.2.1 Extrinsic point defects: properties modification through cationic substitution

Extrinsic point defects can be of both the Schottky or Frenkel types depending on their substitutional or interstitial nature. These types of defects are generally spontaneously induced either through incorporation of dopants or of impurities inside the crystal structure, respectively but may also be generated by oxidation or reduction processes through creation or annihilation of oxygen vacancies [26, 51, 52, 53, 54].

I.2.2.2 Intrinsic point defects: deviations from perfect crystals

Interstitialcies and vacancies are the main intrinsic point defects occurring naturally during crystallization of metal oxides.

I.2.2.2.1 Interstitialcies in metal oxides

Neutral Frenkel defects are created when an ion, usually a cation due to the small size of interstitial sites, migrates from its regular lattice site to an interstitial site, thus generating a paired vacancy and interstitial site as shown in Figure I-3 d. When intrinsic defects involve both cation and anion sublattices, it results in neutral Schottky disorder (Figure I-3 a and b). However, as interstitialcies are usually high-energy defects compared to vacancies and exhibit unfavorable bonding configurations, their presence is relatively uncommon in ultrafine nanocrystallites.

I.2.2.2.2 Vacancies in metal oxides

Lattice oxygen vacancies (L.O.V.) are generated by missing atoms from their regular lattice sites and may lead to charge unbalance in the material. However, cation and anion sublattice vacancies can either occur equally, or cations may undergo partial reduction to maintain charge balance locally and stability of the nanomaterial [26]. We have seen previously that control in oxygen non-stoichiometry in simple metal oxides could influence the crystallization of nanoparticles, and specifically in the case of ZrO_2 [26]. A section dedicated to this phenomenon of crucial importance in the course of this thesis will be introduced later in this chapter.
The next section will be fully dedicated to the impact of the particle size on the crystal structure of ZrO_2 as it is believed that the polymorphism barriers can be crossed by size adjustment.

I.3 Metastable nanocrystallites stabilization mechanisms

I.3.1 Stabilization by size effect

While for bulk crystals the surface-to-volume atomic ratio is extremely small, surface effect may be neglected. However, in very fine nanoparticles the surface atomic fraction increases drastically, and internal atom electronic states are similar to the electronic states of surface atoms, resulting in sharp discontinuities in the electronic states for globally every atom in the nanoparticle and giving rise to highly reactive materials as schematized in Figure I-4.

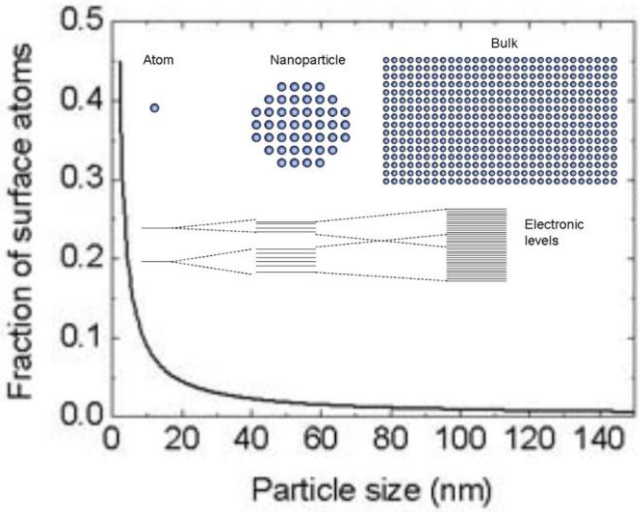

Figure I-4. Fraction of the total surface atoms as a function of the particle size and representation of the decreasing discontinuity in electronic energy levels from a lone atom, to a small nanoparticle and finally bulk solid where electronic energy levels are almost a continuum [55].

Therefore, when dimensions fall into the nanoscale realm, the solid's physical properties exhibit surface behavior that strongly differs from the bulk respective material properties.
In iono-covalent nanocrystals, the tendency for the lattice parameter to increase with decreasing nanoparticle size is generally observed. However, two theories are generally opposed. The first widely used theory, namely the space charge model, describes the volume changes associated with point defects (i.e. anionic vacancies) and the strain thus produced at the surface of ionic crystals [53]. Is opposed to this theory the effective negative Madelung pressure model which finds it source, in ionic nanocrystals, in the competition between the long-range Coulomb attractive and short-range repulsive interactions [56].

I.3.1.1 Lattice parameter expansion and contraction as a consequence of size reduction

Considering the first model for 3-30 nm quasi spherical nanoparticles, correlation between large variations in the particle size and the lattice parameters are attributed to the lattice strain generated by the introduction of oxygen vacancies. These are induced by the partial reduction of surface cations, thus discrepancies in cationic radii and the creation of L.O.V [57, 58]. This change in ionic radius combined with oxygen vacancies induces a distortion of the overall lattice parameter, hence of the local symmetry and a monotonous increase in the lattice strain.
This principle is applied to single as well as to mixed oxide materials with relatively reliable correspondence between observations and theoretical calculations [58, 59, 60]. In the case of single oxides, steric effects induced by the change in cationic radius can be relatively important [60] when the cation coordination number changes and polymorphism barriers can be overcome, thus stabilizing metastable structures if the crystallite size is small enough as we will see in the following section.

I.3.1.2 Metastable tetragonal ZrO_2 stabilization by size effect

Numerous works have identified the t- and c-ZrO_2 doping stabilizing mechanisms over the whole size domains: bulk ZrO_2 (> 1 µm), submicrometer ZrO_2 (100 nm to 1 µm) and nanocrystalline ZrO_2 (<100 nm), all concluding on three different possible mechanisms: creation of L.O.V., relieve of the internal strain associated with the eightfold coordination number and the combination of both mechanisms [26].
It is generally admitted that doping mechanisms have no size limitation in stabilizing t- and c-ZrO_2 at room temperature and stabilization mechanisms are well understood [48, 50, 61]. However,

the role of the crystallite size in modifying the crystalline structure of ZrO_2 has still not found any general consensus as the proposed mechanisms are generally valid only for a given synthetic approach [26, 51, 62, 63, 64, 65, 66].

Garvie first demonstrated in 1964 the concept of critical size by measuring the influence of calcination treatment on t-ZrO_2 stabilization, and from XRD and BET analysis postulated the first value ever for a t-ZrO_2 critical size of 30 nm [62].

Shukla and Seal [26] reviewed in 2005 various thermodynamic models for nanocrystalline t-ZrO_2 stabilization at room temperature and different values for the critical size. Most of these models were based on specific surface and excess energy considerations [26 67 68], hydrostatic pressure [26, 69, 70, 71], structural similarities in the topotactic crystallization of ZrO_2 [16, 20, 51, 67, 72, 73, 74, 75, 76, 77, 78, 79, 80] and the role of oxygen vacancies [29, 81, 82, 83, 84, 85, 86, 87]. However, depending on the considered model, this value could vary between 3 and 30 nm. Therefore, it was decided to consider for the following work in this thesis to focus mainly on the role of oxygen vacancies and on the principle of topotactic crystallization of ZrO_2.

I.3.2 On the role of structural similarities

I.3.2.1 The topotactic crystallization of tetragonal ZrO_2

It has been observed through many different studies that t- and m-ZrO_2 structures expand one after the other from an initial amorphous phase during calcination treatments of both hydrolyzed zirconium precursors and zirconium hydroxide gels [51, 67 72, 73, 74, 75, 76, 77] as can be seen in Figure I-5.

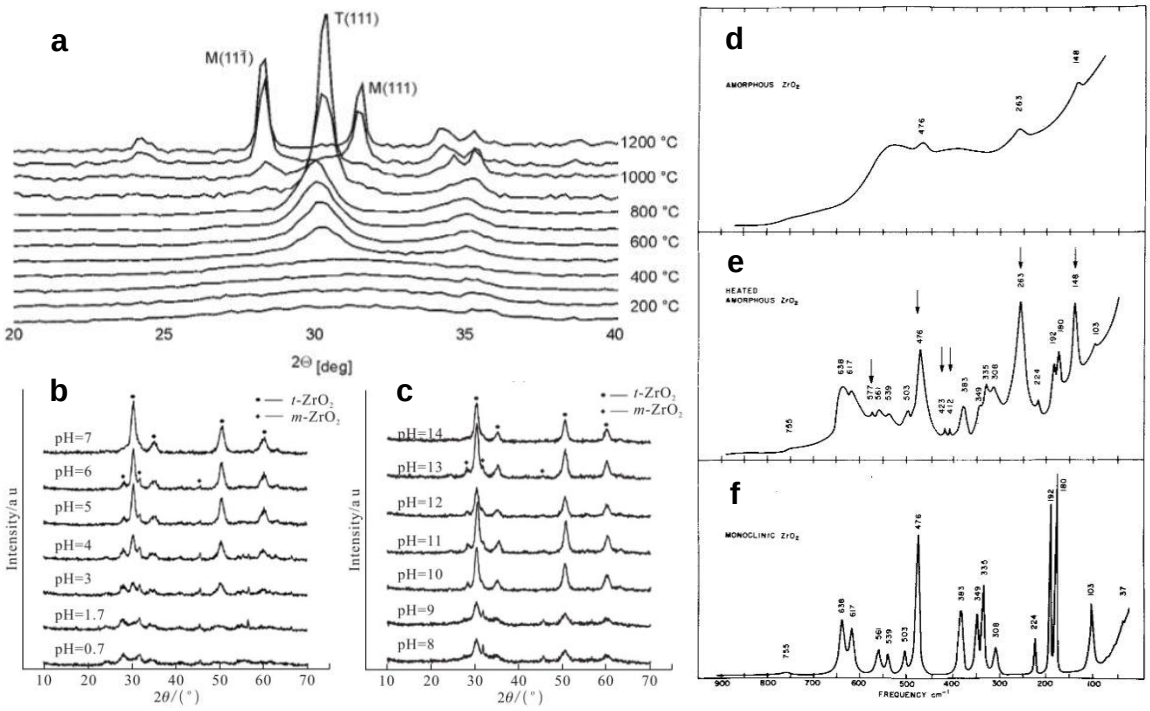

Figure I-5. a, Variable-temperature XRD patterns of dried hydrous zirconia, obtained by forced hydrolysis method, heated stepwise and measured every 100°C up to 1200°C [77]; b and c, variation in crystal structure of ZrO_2 samples prepared by microwave hydrothermal method at different pH. d, e and f, Raman spectra of pre-organized amorphous ZrO_2, t- and m-ZrO_2 mixture, and pure m-ZrO_2, respectively [88].

During the thermally driven crystallization process from an amorphous hydrous zirconia phase, a tetragonal-like structure or metastable tetragonal polymorph becomes visible, between 400 and 600°C, and ultra-fine t-ZrO_2 nanocrystallites are formed as can be seen in Figure I-5 a. Finally, monoclinic Bragg reflections appear clearly in the XRD pattern at ≈ 900°C.

Starting pH is also generally a reliable lever to choose a pathway in the topotactic crystallization of ZrO_2 [16, 20, 78, 79, 80] as can be seen in Figures I-5 b and c where pH controlled syntheses show the critical role of pH to favor either monoclinic or tetragonal nano-ZrO_2 crystallization. It is believed that at high pH values, trapped hydroxyl groups inside the structure greatly contribute to the stabilization mechanism of t-ZrO_2.

Figures I-5 d, e and f show the Raman spectra of a dehydrated zirconium oxychloride precipitate subject to thermal treatment. At 200°C the 3 major t-ZrO_2 Raman active modes are visible in the pre-organized amorphous ZrO_2 phase (Figure I-5 d). Then, at 500°C, Raman active modes for both t- and m-ZrO_2 are clearly visible, thus revealing a mixture of both structures (Figure I-5 e). Finally, at 1000°C, Raman active modes are visible only for m-ZrO_2 (Figure I-5 f).

These structural similarities between amorphous phase and tetragonal structure of ZrO_2 were also pointed out from electron density and neutron diffraction where the Zr-Zr interatomic distances in the amorphous dried ZrO_2 where found to be the same as the Zr-Zr distances in crystallized ZrO_2 $(111)_t$ plane [89].

Lately, pair distribution function (PDF) analysis on ZrO_2 crystallization clearly labeled the correspondence in Zr-Zr and Zr-O bond length correlations between amorphous and crystallized ZrO_2 for experiments carried out in deionized subcritical water and supercritical methyl alcohol [17] as shown in Figure I-6.

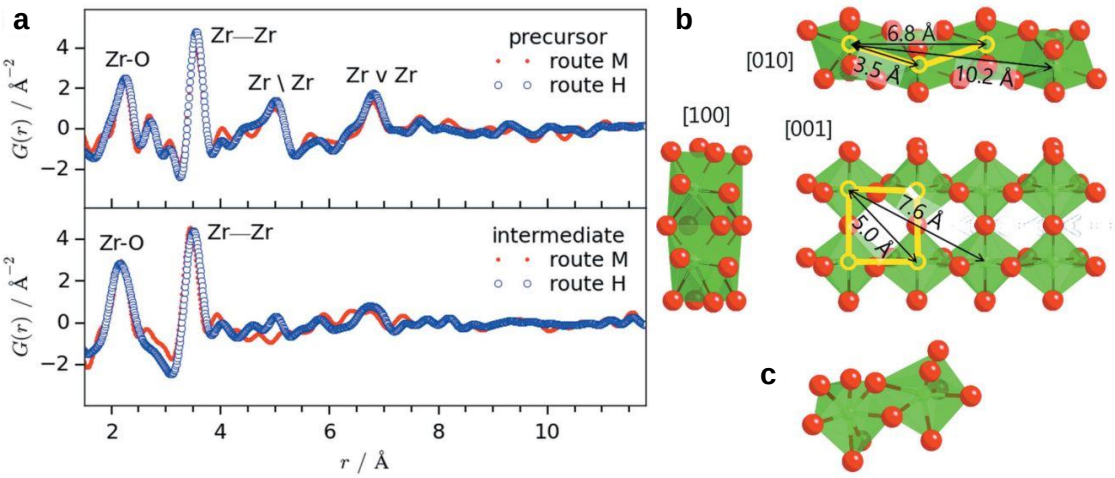

Figure I-6. Representation of: a, normalized PDF of precursor and intermediate bond length correlations in the r range (Å) for zirconium oxynitrate in methanol and zirconium acetate in water, labeled as routes M and H, respectively; b, structural models for the precursor oligomers in solution with oxygen atoms represented as red spheres and zirconium atoms inside the polyhedra in the [010], [100] and [001] directions; and c, the structural model proposed for the disordered intermediate phase.

The study revealed that though both precursor solutions were extremely similar with Zr-Zr and Zr-O bond lengths close to that of m-ZrO_2, polymorphism was linked to the fact that when the differences in atomic correlations between the precursor and the intermediate phase were not significant, the monoclinic structure ended up being the major phase after ≈ 10 minutes reaction time (route (H) with a 1:9 t- to m-ZrO_2 phase ratio), while when the first Zr-Zr distances expanded from the precursor to the intermediate phase, the end product was majorly tetragonal (route (M) with a 1:3 t- to m-ZrO_2 phase ratio).

This bond distance expansion was directly linked, according to the authors, to the formation of oxygen vacancies due to the fast transition from a long-range ordered tetrameric precursor solution to a short-range dimeric intermediate solution (Figure I-6 b).

All these different results seem to reveal that the creeping crystallization of ZrO_2 is a highly ordered process that *in situ* analyses have only started to unravel owing recently designed analysis techniques allowing observation at the atomic level and as a function of time to understand formation mechanisms during nanoparticle synthesis.

I.3.3 Influence of oxygen vacancies on the stability of ZrO_2

The key role of oxygen vacancies in stabilizing bulk t- and c-ZrO_2 polymorphs has found unanimous consensus in the research community and the mechanisms governing the structural transformations is believed to be greatly influenced by the increasing lattice oxygen vacancy concentration. This has been formally evidenced, at temperatures close to the reverse transformation temperature (≈ 1150-1200°C), under vacuum conditions ($p_{O_2} \approx 10^{-19}$ Pa) but also when the material was exposed to oxidizing conditions, where the reversibility of these transformations was observed [90].

Their importance in stabilizing metastable t-ZrO_2 has been highlighted in many research works either by Reitveld analysis of room temperature neutron diffraction measurements and electron spin resonance (ESR) spectroscopy [82, 83, 84, 85]. Figure I-7 a and b shows the evolution of lattice constants as a function of temperature in metastable t-ZrO_2 and of the oxygen shift parameter δ [87].

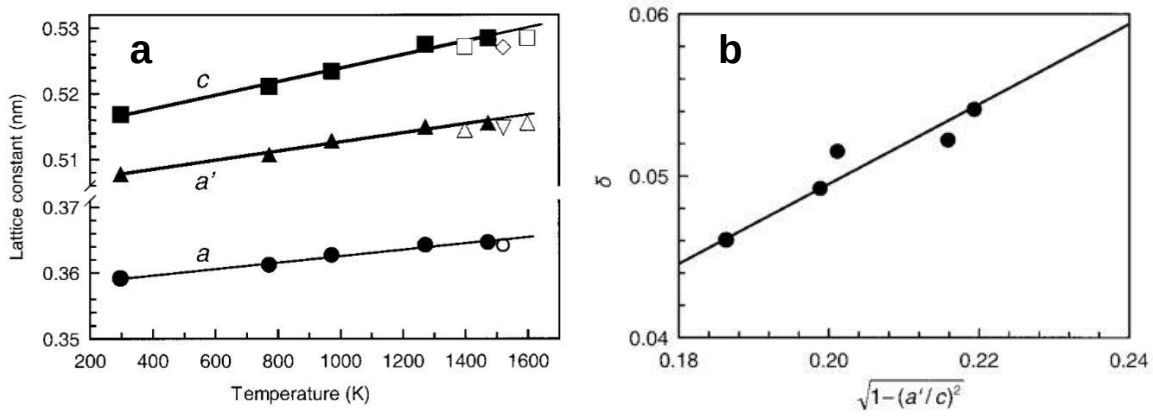

Figure I-7. Evolution of: a, the lattice constants in metastable t-ZrO_2 as a function of the temperature with a' = √(2) a corresponding to a face-centered tetragonal cell; and b, δ the oxygen shift parameter.

In Figure I-7 a, the evolution of lattice constants is plotted against the increase in temperature, while in Figure I-7 b the oxygen displacement parameter δ corresponding to the fractional

displacement of O^{2-} ions in the [001] direction in metastable t-ZrO_2 clearly shows the relaxation of oxygen vacancies in metastable t-ZrO_2 and the similitude between both metastable t-ZrO_2 and high temperature undoped t-ZrO_2 [87].

The formation of oxygen vacancies can be easily understood in the case of the sol-gel route as schematized in Figure I-8.

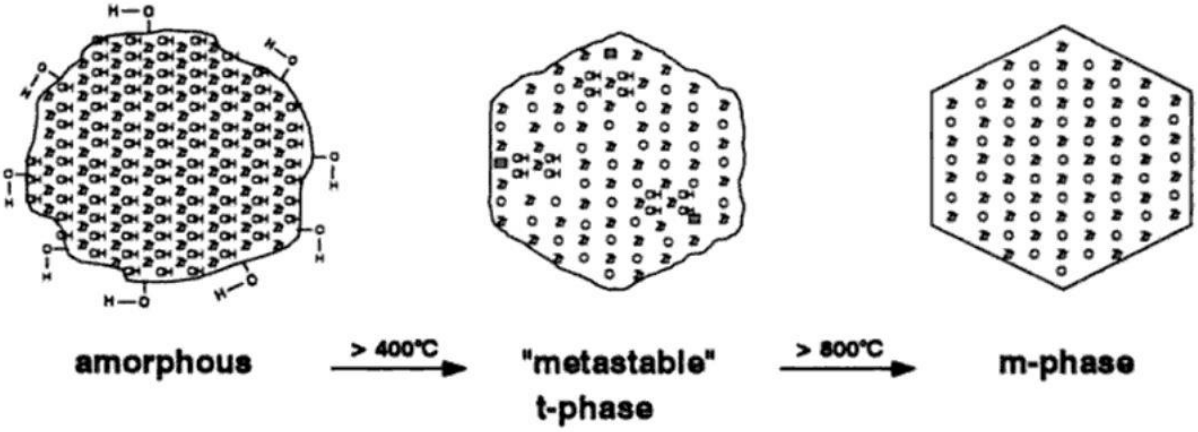

Figure I-8. Possible formation mechanism for metastable t-ZrO_2 through formation of oxygen vacancies from non-fully condensed zirconium hydroxides and subsequent filling of these vacancies to stabilize m-ZrO_2 in the sol-gel route [29].

In Figure I-8, the incomplete condensation of the precursors results in hydroxides trapped inside the metastable tetragonal-like structure. Upon heating of the metastable phase, further removal of these trapped hydroxides may occur via proton transfer between neighboring hydroxyl groups as depicted in Equation I-1,

$$OH^-_{lattice} + OH^-_{lattice} \rightarrow H_2O_{desorbed} + O^{2-}_{lattice} + V_O^{\bullet\bullet} \qquad \text{I-1.}$$

Further increase in temperature diffuses these newly formed water molecules to the surface of the newly formed amorphous quasi ZrO_2 particles, leaving in the process a lattice O^{2-} anion in its regular site and one lattice oxygen vacancy [29].

Considering these results, it appears that the most impactful mechanism responsible for metastable t-ZrO_2 stabilization at room temperature is the same as for bulk, doped and high-temperature undoped t-ZrO_2 where stabilization is governed by the generation of oxygen vacancies within the nano-ZrO_2 crystal structure due to lattice oxygen deficiency [15, 91], and

more specifically at the surface of very small nanoparticles where nucleation sites are most abundant.

Another commonly given explanation for structural transformations in ZrO_2 and based on the principle of lattice oxygen vacancy concentrations is the concept of habit planes (briefly introduced in Figure I-2). In this concept, the increasing and randomly diffused oxygen vacancies are believed to force lattice expansion at the reverse and forward transformation temperatures, thus generating a martensitic phase transformation occurring in two steps: (i), between ≈ 930 and 1100 °C a pre-transformation relieves the internal strain associated with the eightfold oxygen coordination, generating in a second step (ii) a hybrid structure between 1100 and 1220°C [38, 92]. This concept was evidenced on single and polycrystals where t-ZrO_2 built up inside m-ZrO_2 matrix while sharing common $(101)_m$ and $(101)_t$ crystallographic, or habit planes. However, this hypothesis will not be retained in this thesis as our interest lies in extremely small nanoparticles.

I.4 ZrO_2 main synthesis routes reported

The wide variety in synthesis methods to produce metal oxides is probably the main factor that contributed to its rise and the "bottom up" and "top down" approaches encompass, in nanoscience engineering, mainly dry processes [93, 94, 95, 96, 97, 98, 99, 100, 101, 102] and wet processes [14, 48, 63, 103, 104, 105, 106, 107, 108, 109, 110, 111, 112, 113, 114, 115, 116, 117].

I.4.1 Solid-state synthesis of ZrO_2

Solid-state synthesis is probably the oldest technique mankind has used to elaborate materials owing its large-scale production possibilities. The basic principle of metal oxide solid-state synthesis is the diffusion of one element inside the matrix of another: e. g., the thermal oxidation of a metallic source through diffusion of oxygen activated by oxygen partial pressure gradients [118]; cationic diffusion inside a metal oxide matrix through unoccupied interstitial host cationic sites; etc. In the case of full thermal oxidation of zirconium under atmospheric pressure, the presence of a $[ZrO_{2-\delta} + O_{2(g)}]$ two-phase field is inevitable for compositions immediately above 66.6 at.% of oxygen [119]. Also, a decrease in oxygen concentration with sample penetration depth usually occurs for metallic elements [120]. Unfortunately, both mechanisms propagate defects in the structure [121] and producing materials with the desired stoichiometry, composition and

morphology with this technique goes along with two major difficulties: the precursor source size and the high calcining temperatures.

These intrinsic problems linked to the solid-state approach makes this method inadequate for production of materials designed for applications such as catalysis, electronics, etc. where performances are greatly influenced by the grain size, as well as demands from industry for miniaturization of highly performant materials with precise composition has reduced its potential applicability in favor of alternative and more appropriate synthesis approaches.

Deposition techniques may also be used to coat thin ZrO_2 films on substrates [47, 122, 123]. These techniques, though allowing the elaboration of high added value materials (optical coatings, [47], thermal barrier applications [124], etc.), necessitate however precise control of many experimental parameters (pressure inside the chamber, oxygen percentage in the gases, substrate temperature, rf power and time [47], etc.).

I.4.2 Sol-gel synthesis of ZrO_2

Two main directions in sol-gel synthesis of metal oxides to be presented in the following sections, with their respective pros and cons, are the hydrolytic sol-gel (HSG) and the non-hydrolytic sol-gel (NHSG) processes.

I.4.2.1 Hydrolytic sol-gel approach

The hydrolytic sol-gel (H.S.G.) approach, where hydroxyl functions (-OH) from the aqueous media are active in the formation of OXO bridges, is almost uniquely dedicated to metal oxide synthesis in a two-step reaction consisting of (i) hydrolysis of metal alkoxide precursors, and (ii) condensation of the hydrolyzed media [108, 125, 126, 127, 128]. During the first step of the reaction, a colloidal suspension, namely “the sol”, is formed from the hydrolysis of the alkoxide precursors in aqueous solution to form fully or partially hydrolyzed $M(OH)_{4-n}$ ($0 < n < 3$) metal hydroxide monomers. Subsequent condensation of the $M(OH)_{4-n}$ monomers occurs during the second step by polymerization and formation of 1-, 2-, or 3-Dimensional networks containing the aqueous solution, namely “the gel”. Figure I-9 illustrates a typical sol-gel synthesis methodology.

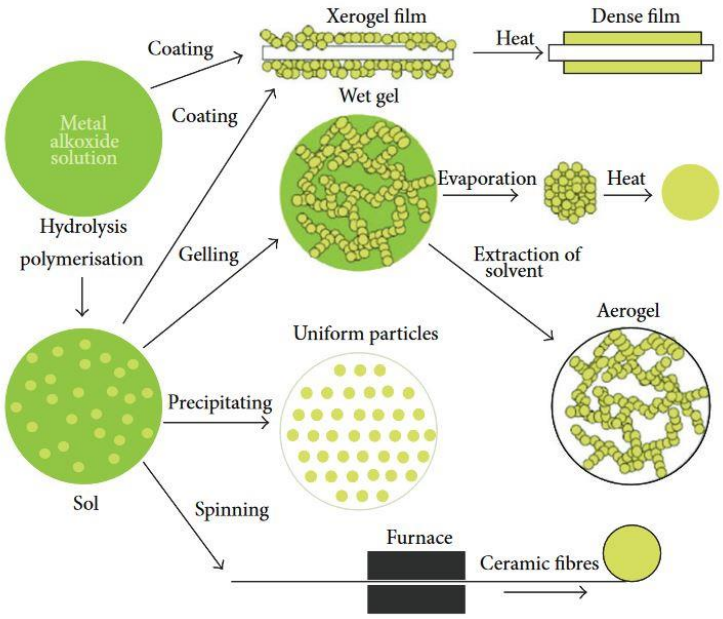

Figure I-9. Illustration of a conventional sol-gel reaction methodology starting from metal alkoxide precursors [129].

This technique is widely used to form ZrO_2 with relatively fine nanoparticle size (ranging from 4 to 500 nm), size distribution, but generally exhibiting a mixture of both m- and t-ZrO_2 phases [51, 66, 84, 103, 104, 128, 130, 131, 132, 133]. However, depending on the application, the precipitated gel can be directly deposited on films or substrates by spin- or deep-coating; subsequent evaporation of the aqueous media to form dense small amorphous micro- or nanoparticles or even complex multidimensional structures; solvent can also be extracted through various methods (e.g., supercritical CO_2 evaporation) to retrieve aero- or xerogels. Either ways, thermal treatment is a mandatory step to achieve crystallization for each chosen route and though this technique is best suited for nanoparticle engineering than the solid-state method, this annealing step still represents a limit in downsizing particle size due to grain growth during the thermal treatment. Though the sol-gel approach enables to largely decrease the particle size in regards of the solid state approach, the possibility to synthesize ZrO_2 nanoparticles displaying an average crystallite size (A.C.S.) of ≈ 4-5 nm is however greatly limited [51, 103].

I.4.2.2 Non-hydrolytic sol-gel approach

Non-hydrolytic sol-gel (N.H.S.G.) synthesis of metal oxides has gained increasing interest in the scientific community only over the previous three decades, as can be seen in Figure I-10, relatively to sol-gel synthesis.

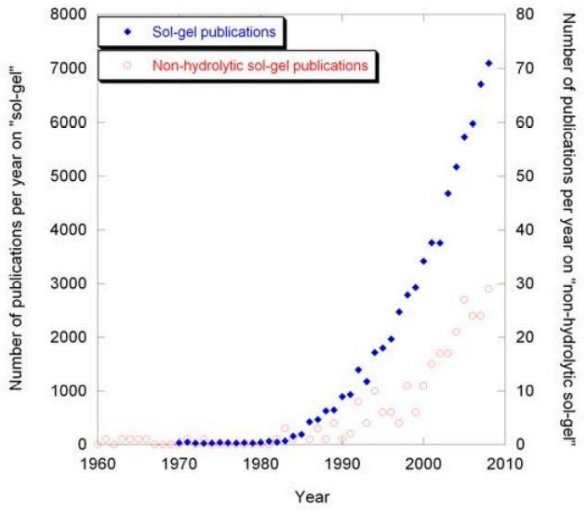

Figure I-10. Representation of the increase in interest in N.H.S.G. synthesis of metal oxides.

Figure I-10 illustrates the sudden interest in N.H.S.G. synthesis over the past decades [134]. In the non-hydrolytic sol-gel approach, it is organic oxygen donors from organic media (ethers, alcohols, carboxylates, carboxylic acids, etc.) that intervene in the formation of OXO bridges. Unlike the HSG approach, wide ranges of precursor sources (alkoxides, halides, acetates, acetylacetonates, etc.) and reaction media are available with this approach [63, 75, 135, 136, 137, 138, 139, 140, 141, 142, 143, 144, 145], and the lower activation energies required in N.H.S.G. syntheses open to more controllable routes for the synthesis of mixed metal oxides with strict homogeneity and stoichiometry achieved in binary, ternary and doped metal oxide nanoparticles with high yields [139, 144, 145].

The technique enables the formation of ultra-fine ZrO_2 nanoparticles with A.C.S. ranging between 2 to 4 nm [63, 75, 135, 138]. However N.H.S.G. reactions require the use of hazardous precursors and indispensable surfactants, such as oleyamine, trioctylphosphine oxide (TOPO), etc., as well as relatively longer reaction times for condensation to occur [63, 138, 143]. Also, few OH defects, which we believe are mandatory in the formation mechanism of metastable t-ZrO_2, are reported at the surface of nanoparticles due to the inherent absence of hydroxyl groups in the reaction process. Nevertheless, XRD patterns of ultrafine ZrO_2 nanoparticles generally seem

to exhibit purely the t-ZrO_2 metastable crystalline structure when synthesized with the N.H.S.G. synthesis procedure [63, 75, 138].

There is however another domain relatively unexplored in the sol-gel process known as the "borderline" non-hydrolytic sol-gel (B.N.H.S.G.) approach.

I.4.2.3 The "borderline" non-hydrolytic sol-gel approach

When water molecules are generated *in situ* from organic solvents and participate to the formation of OXO bridges, the reaction cannot then be considered strictly as N.H.S.G. and is generally mentioned as a "borderline" N.H.S.G. reaction [146, 142].

In situ generation of water from many organic pure solvents: ethanol, isopropanol, acetone and solvent mixtures: ethanol-acetone and ethanol-toluene, in sub- and supercritical conditions has been established lately, quantified by gas chromatography-mass spectrometry (GC-MS) in the 100 to 450°C temperature range and under a pressure of 25 MPa [146]. Given this information, any sol-gel synthesis driven in such solvents and under certain temperature and pressure conditions should not be considered as strictly non-hydrolytic condensation reactions, but rather as "borderline" non-hydrolytic condensation reactions.

Based on these facts, this synthesis approach has caught our attention considering the probability to stabilize very small and almost pure t-ZrO_2 nanoparticles and will therefore be transposed to the supercritical fluid technology, as it has to our knowledge not yet been reported for the formation of ultrafine ZrO_2 nanoparticles, to reduce reaction times and the use of hazardous organic solvents.

I.4.3 Solvothermal synthesis of ZrO_2

Solvothermal approaches refer to high temperature and pressure reactions occurring in aqueous and non-aqueous synthesis conditions. In such reactions, changes occurring in the solvent's characteristics such as density, dielectric constant and viscosity over the course of the reaction allow switching between both solvating and precipitating properties of the solvent with the aim to (i) dissolve, (ii) precipitate and (iii) crystallize materials in a fixed-volume system [147 148 149 150, 151]. Chemical additives called mineralizers are often used in such reactions to either promote solvation, or to act as surface modifiers by chemically bonding at the most reactive surface atoms of newly crystallized surface planes.

Solvothermal syntheses routes can be categorized into three major fields: (i) conventional; (ii) subcritical; and (iii) supercritical reactions, depending on the temperature and pressure conditions [152].

In a conventional solvothermal reaction the precursor solution is maintained at the equilibrium curve in the diphasic domain. In these synthesis conditions, diffusion of species is the main limiting step during the reaction. In such conditions, ZrO_2 usually forms with a size range of ≈ 8 to 60 nm and varying amounts of m- and t-ZrO_2 molar fractions mainly depending on pH and temperature conditions [16, 80, 151].

Temperature and pressure conditions in subcritical reactions are chosen in order to maintain the solvent below, but in the vicinity of its critical coordinates. Typically, the chosen pressure is higher than the value of the solvent's critical pressure (p_C), but temperature is always kept just below the solvent's critical temperature (T_C) and diffusion of species is usually accelerated compared to classical solvothermal reactions. ZrO_2 particles synthesized in this reaction media usually display smaller A.C.S. relatively to conventional hydrothermal reactions, though still fluctuate around ≈ 4 to 18 nm [15, 153] in faster synthesis procedures relatively to conventional hydrothermal reactions. However, variations in residence times are found to have a significant impact on the A.C.S. during subcritical synthesis of ZrO_2 with m- and t-ZrO_2 still in presence when either isopropanol or water are used as solvents [15].

With the supercritical fluid method, which will be introduced in the next section, both temperature and pressure are above the solvent's critical coordinates (p_C, T_C) to obtain a monophasic reaction media where reaction kinetics are extremely accelerated and supersaturation increased due to the decrease in density.

I.5 Supercritical fluids method, a perpetual attracting alternative to conventional synthesis techniques

I.5.1 A brief overview on the supercritical fluid technology

It is important to note that between the conventional and supercritical fluids approaches, reaction kinetics are greatly improved as supercritical fluids enable faster processes to synthesize smaller particles with better control over structure, morphology and chemical properties. This section on supercritical fluids will present how supercritical continuous syntheses allow the formation of ultrafine and uniform nanoparticles and nanocrystallites,

opening new horizons in the understanding of nanomaterials engineering, among which are the quantum confinement effect, and what is of most interest in this thesis, effects arising from the surface-to-volume inversed ratio as the crystallite size is drastically decreased. To achieve these performances, three key parameters need to be mastered: (i) ultrafast precursor transformation, (ii) controlled homogeneous nucleation conditions (iii) restraint of growth phenomenon in order to tune crystallite size and morphology at will.

I.5.1.1 Interest in supercritical solvent properties

A fluid may exist in three different states commonly known as the solid, liquid and vapor phases. Each phase is separated by phase boundaries (equilibrium curves) aside of which, when considering a p, T phase diagram as in Figure I-11, changes in either temperature or pressure modify the fluid's physical state and along which both phases coexist in either solid-liquid, liquid-vapor or vapor-solid coexistence domains. A common coordinate also exists for these three equilibrium curves, called the triple point (TP), which is also a function of temperature and pressure (p_T, T_T).

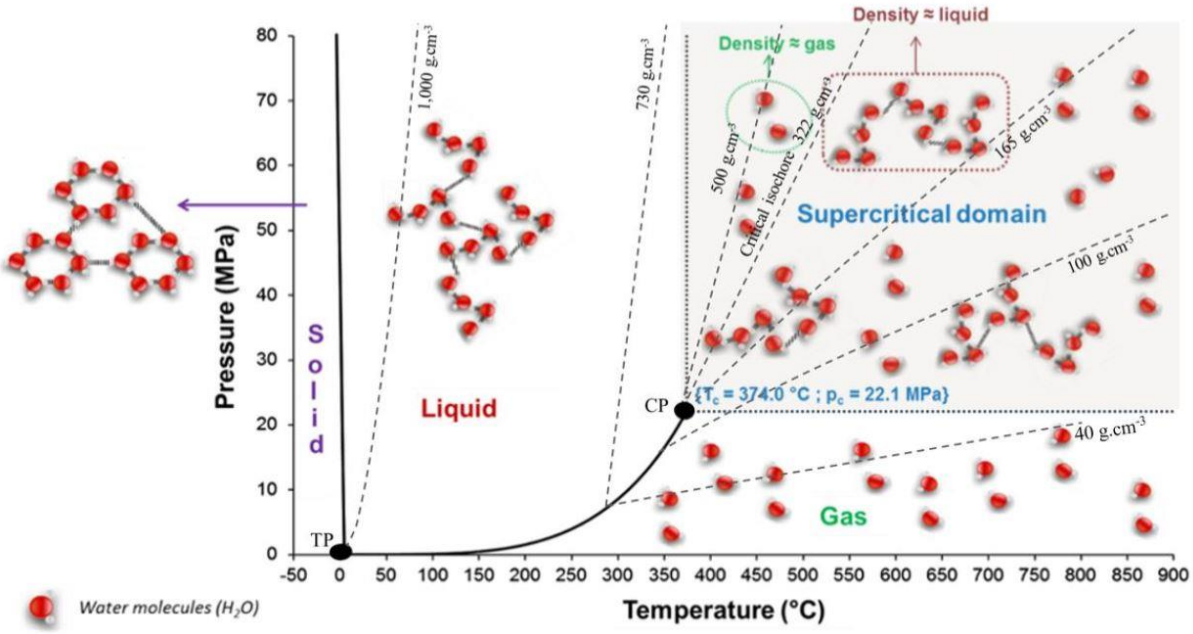

Figure I-11. P, T phase diagram for water representing: the phase equilibrium curves; the isochoric curves in the supercritical domain and emphasizing the wide range of solvent densities, thus viscosities and diffusivities applicable when in supercritical conditions. TP (p_T = 612 Pa, T_T = 0°C) and CP (p_C = 22.1 MPa, T_C = 374°C) are the triple and critical points of pure water, respectively [154].

At the end-point of the liquid-vapor equilibrium curve, the liquid-vapor phase boundary vanishes past the critical point (labeled as CP in Figure I-11) and thermophysical properties of the fluid change dramatically: e.g., the dielectric constants of water and alcohols undergo an abrupt drop near and past the critical point [155]; also, the decrease in viscosity enables higher molecular mobility, leading to higher species diffusivity in the solute, thus increased reaction kinetics. These solvent property changes, in terms of dielectric constant, density, viscosity and diffusivity, are directly related to the state of aggregation of the solvent molecules in the supercritical state, where the hydrogen bond network in supercritical water is subject to tremendous changes between low and high density supercritical conditions [156, 157]. At low densities, supercritical water consists mainly of monomers interacting through weak hydrogen bonds, whereas at high densities, the rearrangement of water molecules generates a majority of trimers coexisting with both dimers and monomers in the monophasic domain.

I.5.1.2 Supercritical fluid molecular configuration

FTIR and Raman spectroscopy observations on the state of aggregation of ethanol molecules in supercritical conditions revealed the same trend as in supercritical water. The variation in free OH as a function of pressure and temperature, used to probe the structure of ethanol, revealed that increasing pressures also led to increasing degrees of hydrogen bonding as emphasized in Figure I-12 [158].

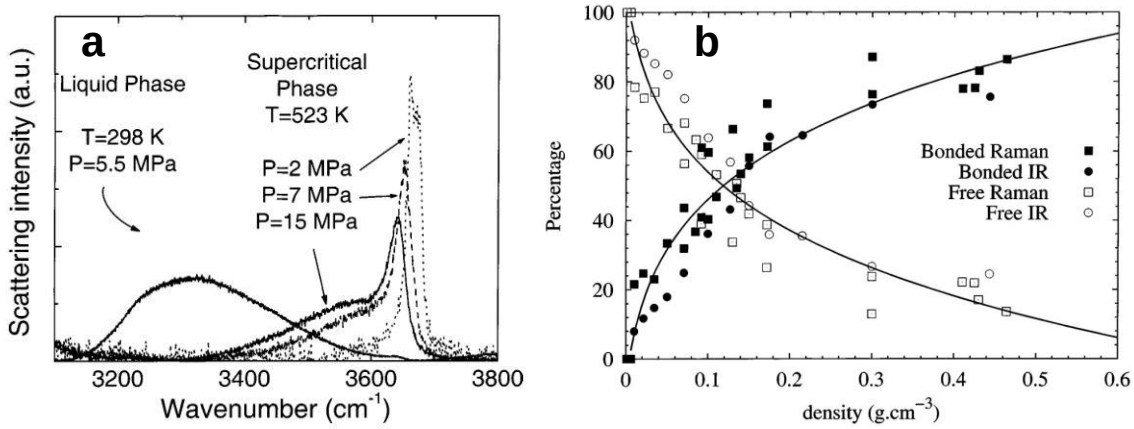

Figure I-12. Representing: a, the polarized I_{VV} ($\tilde{\nu}$) Raman spectra in the OH stretching domain for both liquid (p = 5.5 MPa, T = 25°C), and supercritical ethanol (p = 2, 7 and 15 MPa, T = 250°C); b, the percentage of free and bonded OH as a function of fluid density, obtained by ab initio calculations and fitted to both infra-red and Raman spectra used as experimental data.

In Figure I-12 a, the weak band (or intense peak) located at ≈ 3650cm^{-1} is associated with the free OH stretching mode of ethanol monomers. As the pressure is increased up to 7 MPa, a redistribution in the state of aggregation of ethanol occurs with a broad band at ≈ 3550 cm^{-1} and a narrow band at ≈ 3630 cm^{-1} which can be assigned to OH bonded groups of small ethanol oligomers and free OH stretching modes of monomeric ethanol molecules, respectively. Further increase in pressure up to 15 MPa slightly favors the oligomeric form of ethanol. It clearly appears that under supercritical conditions, the hydrogen bond network of ethanol, as that of water, can be seen as almost broken at high densities and shattered at lower densities.

Figure I-12 b shows the calculated infra-red and Raman spectroscopy intensities at 250°C for monomeric, dimeric as well as cyclic and linear trimeric ethanol clusters fitted against experimental data. The percentage of bonded OH was found to increase with increasing pressure, while the free OH conversely decreased, in good agreement with experimental data.

I.5.1.3 Supercritical fluid thermophysical properties

Table I-2 compares the thermophysical properties of supercritical fluids to those of the liquid and gas phases.

Table I-2. Variations in density, viscosity and diffusivity between liquid, supercritical and gaseous solvent phases [159].

Properties	***Liquid***	***Supercrtical fluid***	***gas***
Density (g/cm^3)	***1***	***0.1-0.5***	***10^{-3}***
Viscosity (µPa.s)	***10^{-3}***	***10^{-4}-10^{-5}***	***10^{-5}***
Diffusivity (cm^2/s)	***10^{-5}***	***10^{-3}***	***10^{-1}***

Due to its thermophysical properties, the supercritical fluid technology enables multiple types of chemical reactions such as hydrothermal; thermal decomposition; sol-gel; and red-ox reactions.

I.5.1.4 Supercritical fluid nanoparticle synthesis in continuous flow reactors

The supercritical fluids technology includes two processes in which highly crystalline large single crystals may be obtained in batch type reactors, while submicron to nanosized particles and crystallites may be obtained in short continuous flow reactions (e.g., typically a few

seconds). In this section we will only focus on supercritical continuous flow reactors designed for the supercritical solvothermal synthesis as depicted in Figure I-13.

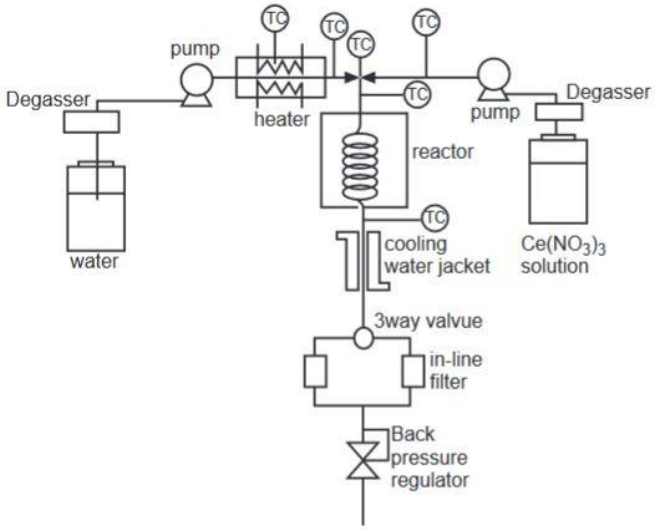

Figure I-13. Depicting a typical lab scale continuous flow reactor designed for the supercritical solvothermal synthesis of nanomaterials [160].

In a typical supercritical solvothermal continuous flow reactor as depicted in Figure I-13, solvents and precursor solutions are generally injected via high pressure pumps into a high temperature reactor at the end of which is generally placed a cooling device to quench particle growth. The pressure inside the whole system is maintained owing a back-pressure regulator, and manometers are placed, as well as thermocouples, at various locations of the system to monitor both pressure and temperature stability. Generally, three main parameters are monitored during a continuous flow synthesis that are the pressure and the temperature inside the reactor as well as the precursor solution flow rates. All three combined parameters define the final residence time (t_R) corresponding to the total time the reaction will occur inside the reactor as we will see in section II.2.1.2.1 and are the main parameters studied during crystallization of nanoparticles in supercritical solvothermal syntheses in supercritical continuous flow reactors other than those focusing on varying precursor type and concentration, solvent type, surfactant type and concentration, etc.

Also, the advantage of this synthesis method is that no annealing step is required to obtain crystallized materials as crystallization with accurate control over size, structure and morphology occurs directly inside continuous flow reactors [5, 16, 20, 23, 24, 25, 78, 160, 161, 162, 163, 164, 165].

I.5.1.5 Flexibility of continuous flow reactors

Continuous flow reactors, as depicted in Figure I-13, are used in supercritical solvothermal syntheses to optimize control over size, size distribution, structure and morphology of nanoparticles at relatively mild temperature and high-pressure working conditions as explained previously. In such reactors, residence times can be accurately controlled to maintain homogeneous nucleation conditions throughout the whole synthesis of nanoparticles. The advantage of continuous flow reactors over batch reactors is the flexibility allowed during syntheses as depicted in Figure I-14 [25].

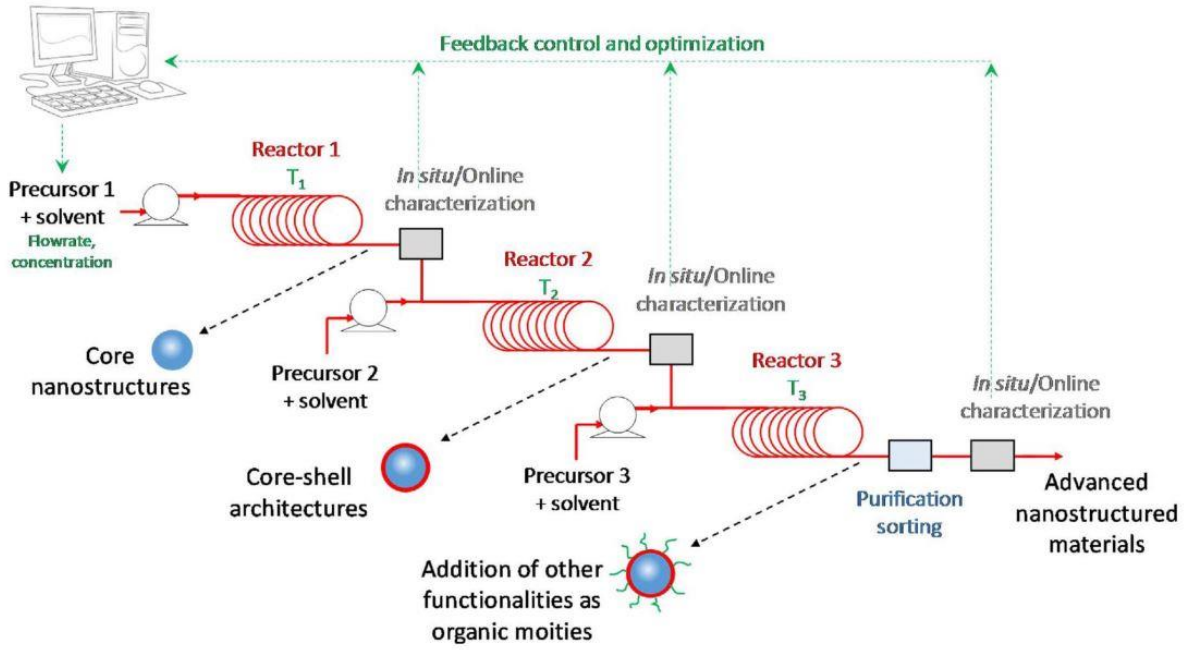

Figure I-14. Emphasizing the flexibility and possibility to fragment various reaction steps into a one-pot synthesis with continuous flow reactors.

Figure I-14 emphasizes the flexibility and tunability of continuous flow reactors where in the first step of the synthesis nanoparticles crystallize. Then, in a second step a coating may be applied at the surface of the nanoparticles, and finally, a third pumping system may allow surface functionalization before growth is abruptly quenched. In such a system, various temperatures are allowed as each of the three steps may be considered as a compartmented section inside one single reactor.

The next sections will briefly overview the stability of alcoholic solvents subject to relatively large variations in pressure and temperature conditions as they will be used in B.N.H.S.G. syntheses of ZrO_2 nanoparticles throughout this thesis.

I.5.1.6 Solvent stability under supercritical conditions

One important factor to keep in mind in solvothermal chemistry, and more specifically under supercritical conditions, is the solvent's stability as such temperature conditions are well above most solvent stability limits. For instance, the stability of ethanol has been investigated by gas chromatography coupled to mass spectrometry (GC-MS) at 20 MPa and between 100-450°C [146]. Figure I-15 shows the major decomposition reactions for supercritical ethanol and byproducts formed in continuous flow reactors.

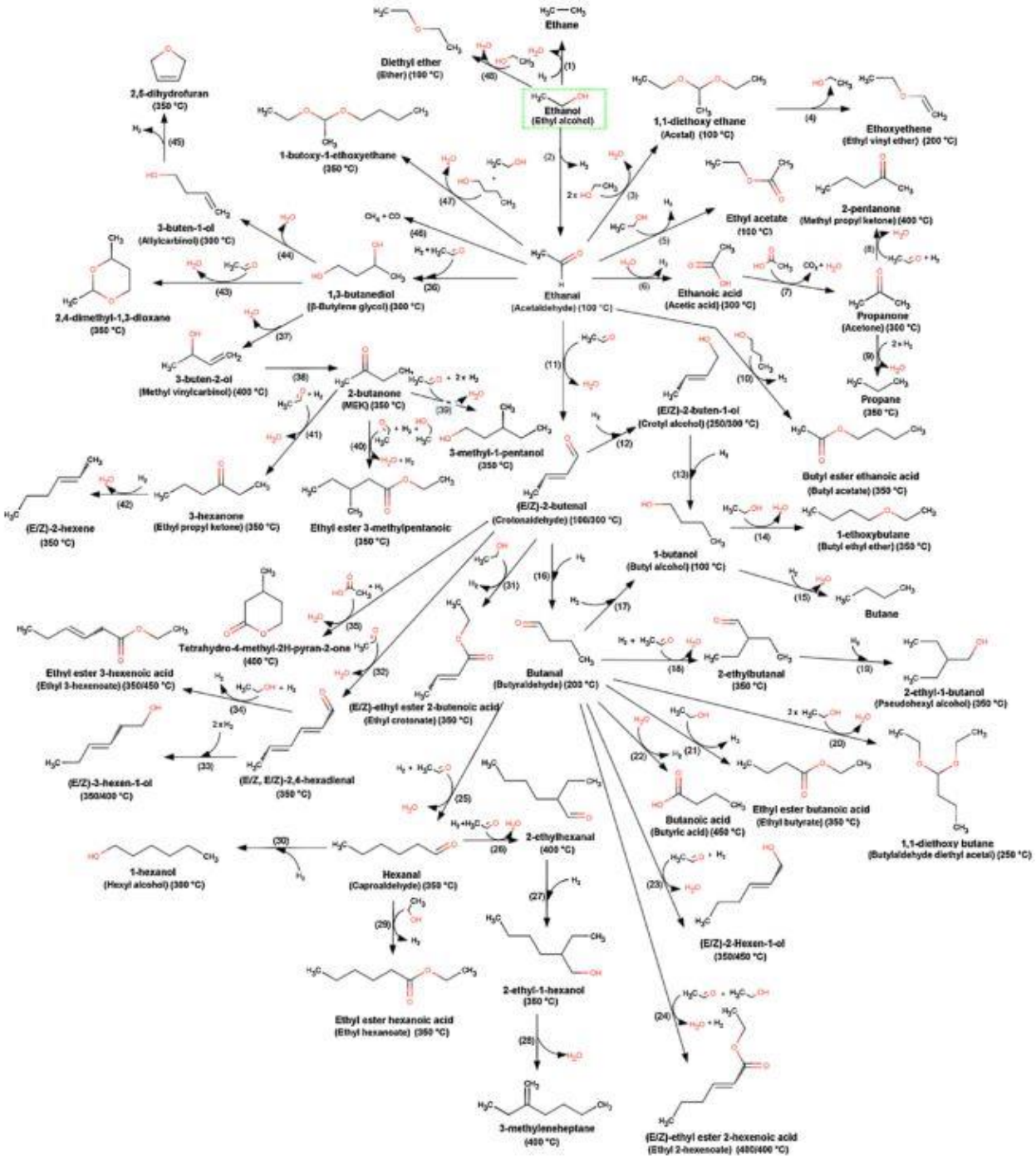

Figure I-15. Byproducts formed from decomposition of ethanol under supercritical conditions [146].

While ethanol was found to be relatively stable below its critical temperature with only a few byproducts formed, past the critical coordinates, in total an ensemble of not less than 71 byproducts issuing from decomposition reactions and byproduct recombination was identified at 20 MPa and 450°C and the evolution in their number is represented in Figure I-16 a.

Also, and of most interest in this thesis is the generation of water as a byproduct of ethanol decomposition and its quantification as shown in Figure I-16 b.

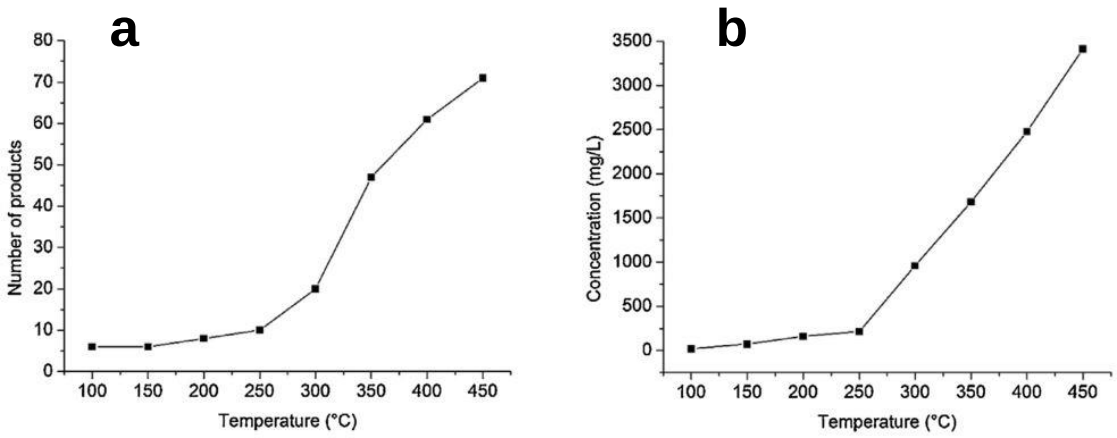

Figure I-16. Representing at 20 MPa and for a residence time of 36 seconds: a, the number of byproducts formed; b, the water concentration, in mg of water per liter of anhydrous ethanol, generated *in situ* from the decomposition of ethanol below and above its critical temperature [146].

Figure I-16 a shows how solvent stability is impacted by the drastic supercritical conditions in the case of ethanol where the number of byproducts formed increases with an increase in temperature at constant pressure and residence time. Figure I-16 b shows how the amount of water generated *in situ* from supercritical ethanol increases almost linearly with increasing temperature. This characteristic of supercritical ethanol, and other primary alcohols, will be used during this thesis in B.N.H.S.G. syntheses to initiate hydrolysis and condensation reactions for the synthesis of ZrO_2. Also, as the amount of water generated *in situ* increases as a function of the temperature it should thus be possible to control reaction kinetics for the production of ultrafine uniform ZrO_2 nanocrystallites and stabilization of metastable t-ZrO_2.

I.6 Alcohol dehydration mechanisms

B.N.H.S.G. reactions throughout this thesis will be performed in supercritical alcohols, thus an overview in their decomposition behavior, and specifically in terms of dehydration kinetic rates is mandatory as we expect to control the amount of water molecules generated *in situ* from the decomposition of primary alcohols to act as a kinetic lever in the bottom-up formation of ZrO_2 nanoparticles.

Among the various types of decomposition reaction classes reported in alcoholysis reactions [146, 166], the foremost and systematically observed are: unimolecular decomposition reactions; H-atom abstraction and transfer reactions; radical decomposition reactions; and radical isomerization reactions, and the mechanisms for these major reactions observed in pyrolysis and combustion experiments are usually supported by theoretical calculations. Lately, works realized on the decomposition and recombination of supercritical solvents showed that decomposition pathways, as well as dehydration kinetics for both ethanol and isopropanol, were very similar to those reported in pyrolysis and combustion experiments, paving the way to understanding decomposition processes occurring during supercritical fluids synthesis [146].

I.6.1 Alcohol chemical and physical properties

The differences in solvent molecular aggregation below and above the critical point lead to variations in decomposition channels characteristic of each domain. While below the critical point of alcoholic solvents acid/base catalyzed reactions involving elimination reactions generally dominate, at supercritical conditions however, the drop in ionic product of solvents allows more radical reactions to occur [167, 168, 169]. Also, quantifying the contribution of each process in both domains is still, to this day, a complicated task. However, from simple considerations on the properties of each alcohol, reasonable understanding on dehydration processes can easily be outlined. Table I-3 displays the major physical and chemical properties of C_1 to C_6 primary alcohols [166].

Table I-3. Physical and chemical properties of C_1-C_6 primary alcohols

Alcohol	Molar weight (g/mol)	Boiling point (°C)	Solubility in water at 25°C (wt%)	Density (25°C)	Critical coordinates {p (MPa), T (°C)}	Dielectric Constant (20°C)
methanol	32.04	64.7	miscible	0.792	{8.09, 239} [c]	32.35 [a]
ethanol	46.06	78	miscible	0.794	{6.29, 241.56} [d]	25.00 [a]
n-propanol	60.09	97	miscible	0.804	{5.2, 263.6} [d]	20.81 [a]
n-butanol	74.11	118	7.4	0.81	{4.5, 288.8} [d]	17.51 [b]
n-pentanol	88.14	138	2.2	0.816	{3,9, 306.8} [d]	15.13 [e]
n-hexanol	102.16	157	0.6	0.814	{3.4, 337.3} [d]	13.28 [e]

a [170], b [171], c [172], d , e [173] at 25°C

From Table I-2, one can see that both the boiling point and the critical temperature increase almost linearly with the alkyl chain length from ethanol to n-hexanol, and as we have seen in

the previous section, the amount of water generated *in situ* from supercritical ethanol increases linearly above the critical temperature up to 450°C.

The evolution of C_1 to C_4 primary alcohol dielectric constants versus temperature are represented in Figure I-17 where the temperature range for each alcohol investigated is encompassed between 25°C and 5-10 °C below its critical temperature, exception made for methanol.

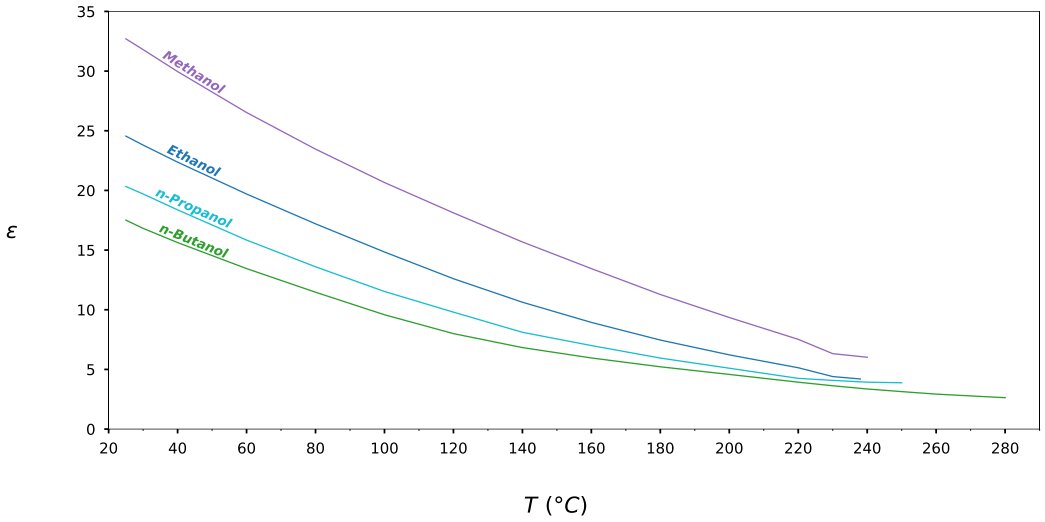

Figure I-17. Evolution of C_1 to C_4 primary alcohol dielectric constants (ε, real part of the relative permittivity) versus temperature. The ε values for each alcohol were obtained from [171].

Figure I-17 shows that the relatively polar character of primary alcohols used as solvents can be easily switched to become highly non-polar at the vicinity of and past the critical point and therefore homogeneous burst nucleation process is expected to occur.

I.6.1.1 Molecular structure of primary alcohols

The presence of the hydroxyl moiety attached to the hydrocarbon chain in alcohol molecules weakens the α-C-H bond, thus allowing interactions through hydrogen bonding [166]. However, beyond the β-site the hydrocarbon chemical properties are believed to resemble to those of typical alkanes [174]. These two major characteristics of alcohols lead to numerous decomposition channels depending on temperature, pressure, but also environmental conditions (e.g., combustion or pyrolysis), making it a difficult task to achieve characterization of alcoholysis reactions. To simplify however, low temperature decomposition reactions are reported to occur

principally by fragmentation of C-O and C-H bonds *via* multiple transition ring states involving α-, β-, γ-, δ- or ε-sites. At intermediate temperatures H-atom abstraction/transfer as well as radical decomposition reactions are favored while at higher temperatures, radical isomerization reactions are favored depending on the ability of the alcohol to produce radicals. Nevertheless, dehydration reactions compete systematically with all these reactions with however, different degrees of predominance. The understanding of decomposition mechanisms to obtain chemical kinetic models for decomposition pathways and dehydration reactions requires knowledge of the molecular structure of alcohols which are generally built on both theoretical bond dissociation energy (B.D.E.) and potential energy surface (P.E.S.) quantum chemistry calculations.

I.6.1.2 Bond dissociation energies for C_1 to C_5 primary alcohols

The bond dissociation energies for all alcohols vary in the order C-C < C-O < C-H < O-H with energies encompassed between 87-89 and 103-105 kcal/mol for the former (C-C) and the latter (O-H), respectively [168, 175]. Figure I-18 displays C-H and O-H BDEs for C_1 to C_5 primary alcohols obtained for the most stable conformers.

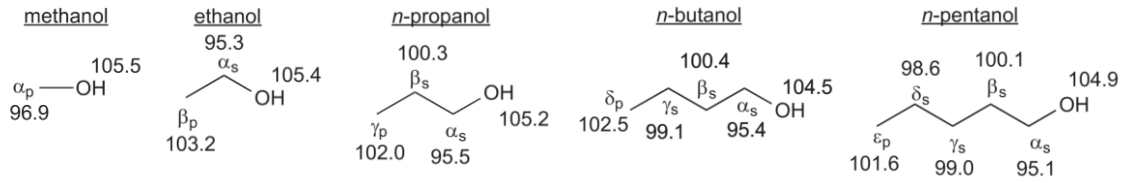

Figure I-18. Bond dissociation energies (kcal/mol at 25°C) for C_1 to C_5 primary alcohol stable conformers calculated at CBS-QB3 level of theory [166].

Due to the higher BDE of the hydroxyl moiety in primary alcohols (≈ 104.5-105.5 kcal/mol), thermal energy will generally lead to the dissociation of the C-O and β-H bonds during water elimination reactions. However, in the case of methanol the α-site is a primary C-H bond, thus of higher energy than secondary C-H bonds and as a consequence, dehydration of methanol is generally not expected.

I.6.1.3 Potential energy surface for C_1 to C_6 primary alcohols

The concept of potential energy surface, based on theoretical quantum chemistry calculations, consists in exploring theoretically molecular structures and their properties such as the energy minima of a stable conformer, transition state configurations along reaction coordinates, or computing chemical reaction kinetic rates. Figure I-19 shows typical results in decomposition reactions for ethanol and n-pentanol.

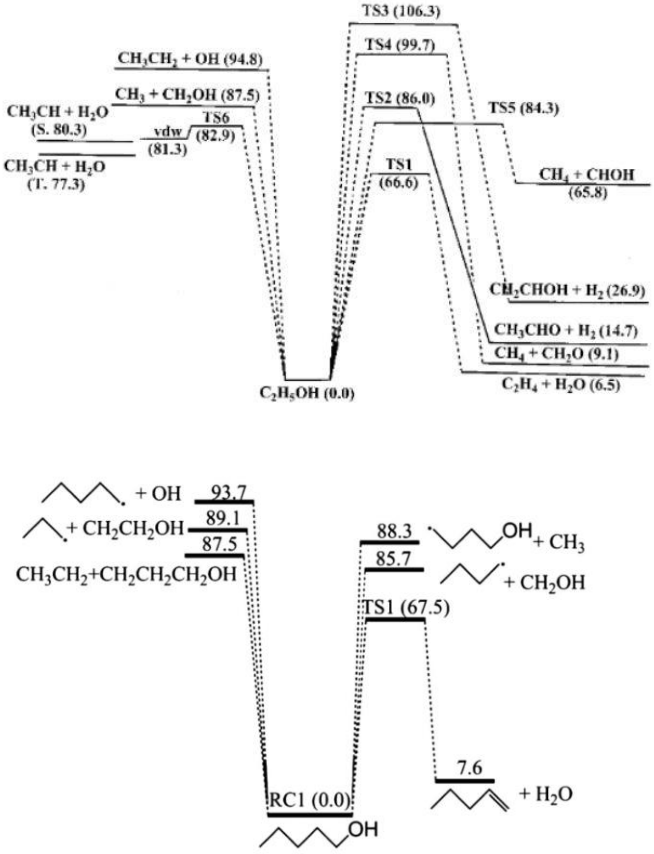

Figure I-19. Schema of the potential energy surfaces (PES) for the major unimolecular decomposition channels of both ethanol [176] and pentanol [175]. PES for ethanol and pentanol were obtained at the G2M(RCC2) and CBS-QB3 levels of theory, respectively.

According to PES calculations, primary thermal decomposition channels generally reported for C_1 to C_5 primary alcohols operate *via* both bond dissociation reactions and elimination reactions.

Table I-3 lists the bond dissociation and water elimination reaction energies where dehydration reactions, with 62-68 kcal/mol range [166, 175, 177, 178], appear to be 15-20 kcal/mol lower than the lowest bond dissociation energies (Figure I-18).

Table I-3 BDEs and elimination reactions energies for C_2 to C_5 primary alcohols.

Reaction	$E_{Elimination}$ (H_2O)	BDE (C-OH)	BDE (β-H)
$C_2H_5OH \rightarrow H_2C=CH_2+H_2O$	62.7 [a]	95.2 [a]	102.8 [a]
$C_3H_7OH \rightarrow H_4C_2=CH_2+H_2O$	63.1 [a]	95.5 [a]	99.9 [a]
$C_4H_9OH \rightarrow H_6C_3=CH_2+H_2O$	62.6 [a]	95.3 [a]	100.1 [a]
$C_5H_{11}OH \rightarrow H_8C_4=CH_2+H_2O$	67.5 [b]	95.3 [b]	100.1 [c]

a [174], b [175],c [166]

Energy values in Table I-3 were obtained with the CBS-QB3 level of theory and an estimated uncertainty of ± 1 kcal/mol. Unfortunately, to our knowledge no PES data has been reported on the unimolecular water elimination reaction for n-hexanol nor on decomposition channels as it has been for C_1 to C_5 primary alcohols.

I.6.2 Decomposition channels in primary alcohols

Two decomposition channels will be considered here, unimolecular elimination reactions and radical decomposition reactions, and their eventual predominance in our future synthesis conditions will be discussed in the following sections.

I.6.2.1 Elimination reactions

During a dehydration reaction, a primary alcohol molecule will undergo a single-step E_2 unimolecular elimination reaction, thus forming an alkene specie and a water molecule as shown in Figure I-20.

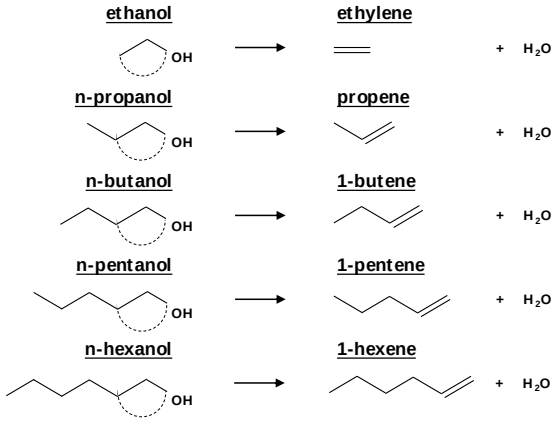

Figure I-20. Thermodynamically stable four-center transition rings in the process of water elimination reactions occurring during decomposition of alcohols into alkenes and water. Adapted from [166].

Figure I-20 shows how, in the dehydration process of C_2-C_6 aliphatic primary alcohols, the weakly acidic -OH groups capture an electron deficient β-H in a four-center transition state ring. When the C-O bond cleavage occurs, the remaining electronic density leads to the formation of alkenes species (e.g., 1-ethene, 1-propene, etc.) and water molecules [166, 179]. Despite the fact that the BDE of β-H atoms are higher than for α-H atoms (Figure I-18), four-center reactions are generally thermodynamically the most favored due to steric hindrance. However, it has been suggested in the case of propanol that three-center transition rings involving α-H atoms were thermodynamically favored [180].

Production of water during unimolecular elimination reactions is generally estimated by monitoring alcohol to alkene conversion as a function of temperature, pressure, etc. and kinetic rates usually by monitoring alkene conversion in time-resolved measurements, admitting whether alkene formation is fully or partially generated by water elimination reactions. Most studies realized on one or many different alcohols agree on the fact that in similar experimental conditions, the longer the aliphatic alcohol the lesser water tends to be generated through elimination reactions. In the case of ethanol conversion was estimated to be ≈ 19 % [176]; ≈ 17 % in the case of n-propanol; ≈ 7.6 % for butanol [181, 182, 183]; and ≈ 4% in the case of n-pentanol [175, 184, 185]. The temperature range was systematically higher than each alcohol's critical temperature, and most studies agreed that pressure variations explored were rather insignificant in the conversion processes.

We have seen in Figure I-17 that in the case of C_2 to C_4 alcohols the values of dielectric constants tend to converge at the vicinity of the critical temperature ($\varepsilon \approx$ 2-5). It is therefore allowed to assume that these observations in relatively different conditions will be valid in our synthesis conditions [146, 176, 177].

I.6.2.2 Radical reactions

Radical decomposition and radical isomerization reactions are favored by the decrease of the solvent's dielectric constant and generate a pool of heterogeneous $C_nH_{2n}OH$ radical species [146, 166, 167, 168, 169]. In such conditions, the formation of water molecules may occur *via* dehydrogenation of radicals by OH groups [166, 180, 184, 185, 186, 187, 188]. High temperature n-propanol decomposition reaction experiments showed that H atom abstraction reactions by hydroxyl (OH) and hydrogen (H) radicals were the dominating reactions with 65 and 25% contribution, respectively [189].

Because so many works on alcohol decomposition reactions have been realized, the topic is too immensely vast to approach and not the purpose of this thesis. However, from these considerations on BDE and PES, and though in the absence of energy values for n-hexanol, it may seem that the main source of water molecules is generated by the dehydration of alcohols via elimination reactions which is commonly reported in most studies on decomposition reactions of alcohols and polyols regardless of the experimental technique [166, 168, 180, 184, 185, 186, 187, 190, 191, 192].

I.6.3 Solvent-solute interactions

Supercritical alcohols will be used in this work to initiate B.N.H.S.G. reactions as not only can they be thermally dehydrated, but also because alcohol dehydration occurs and is catalyzed at the surface of metal oxide nanoparticles [193, 194, 195, 196, 197, 198, 199, 200, 201, 202, 203]. Therefore, the following discussion will be centered on the alcohol dehydration kinetic rates catalyzed at the surface of metal oxides and more specifically ZrO_2 nanoparticles.

I.6.3.1 Solvent to alkoxide precursor molecule interactions

Upon dissolution in an alcoholic solvent, alkoxide precursors may undergo ligand exchange and result in a different alkoxide, thus changing the precursor's chemical properties, and lead to different reaction pathways and final crystalline structures [17, 130, 131, 204, 205, 206]. The substitution reactions occurring between the nucleophilic solvent (δ_O^-) and ligand (δ_{OPr}^-) molecules with electrophilic metal precursor ions (δ_{Zr}^+) depend on the partial charge of each entity as shown in Figures I-21 a and b where Zr and propoxide ligand (OPr) partial charge distributions δ_{Zr}^+ and δ_{OPr}^-, respectively, are impacted depending on the number of solvating molecules.

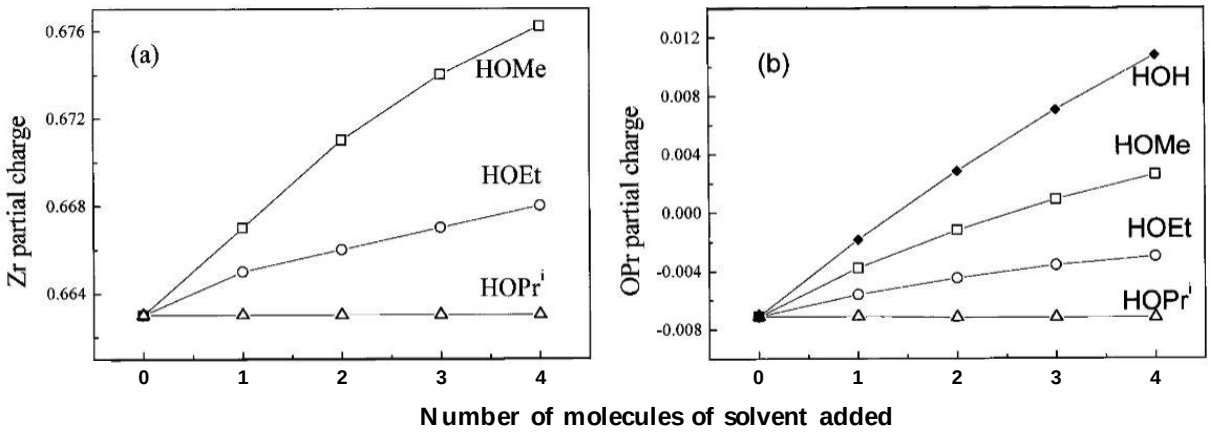

Figure I-21. Representation of the partial charge distributions around Zr and propoxide (OPr) species as a function of the number of solvent molecules per ZrOPr precursor molecule, with theoretical calculations based on the partial charge model [130].

As the relative number of solvent-to-precursor molecule increases, both δ_{Zr}^{+} and δ_{OPr}^{-} partial charge distributions may increase and favor ligand exchange if δ_{OPr}^{-} becomes positive. Since δ_{Zr}^{+} and leaving δ_{OPr}^{-} must be positively charged for the substitution to be successful, the ligand exchange may occur when 3:1 and 2:1 methanol (HOMe) to Zr and water (HOH) to Zr ratios are reached, respectively. However, as the increase in δ_{OPr}^{-} is only moderate and almost not perceptible when ethanol and isopropanol are used as solvents, respectively, ligand exchange should therefore probably be negligible in the case of ethanol and longer chain aliphatic alcohols.

I.6.3.2 Solvent to nanoparticle surface interactions

ZrO_2 is an amphoteric metal oxide, meaning its surface properties enable bifunctional acid-base catalytic mechanisms of balanced strength [203, 207, 208, 209]. It should therefore be important to consider the catalytic activity of ZrO_2 to convert alcohols through dehydration and dehydrogenation reactions occurring specifically on surface acidic and basic sites, respectively [193, 195, 197, 198, 200, 201, 202, 203, 210]. Investigation on the relative acidic and basic site concentrations for ZrO_2 as well their relative strength revealed that in the 170-400°C temperature range, m-ZrO_2 presented slightly higher concentrations in acidic surface sites available for dehydration than t-ZrO_2 [203]. Therefore, as dehydration occurs *via* E_2 elimination reactions more readily on Lewis acidic sites, m- and t-ZrO_2 nanoparticles should present different reactivities during the homogeneous nucleation stage, depending on surface contribution of the exposed facets in

adsorption of alcohol molecules [203, 208]. Figures I-22 a and b show, for amphoteric metal oxide nanoparticles, possible ethanol surface dehydration and dehydrogenation mechanisms, respectively [207].

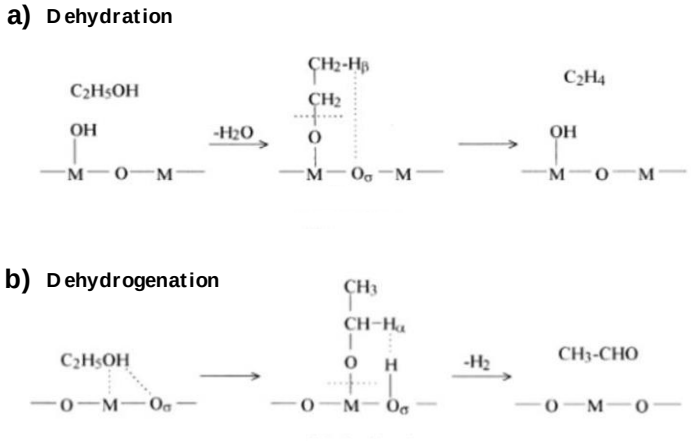

Figure I-22. a and b, possible mechanisms for ethanol dehydration and dehydrogenation at the surface of metal oxide materials, respectively.

In the dehydration mechanism in Figure I-22 a, proposed for the amphoteric Al_2O_3 metal oxide, an alcohol molecule (ethanol) adsorbs on a Brønsted acidic site (e.g., a surface hydroxyl group), hence generating an alkoxy specie (ethoxy group) and a water molecule. A β-H atom from the ethoxy group can then shift on a basic oxide site to form a new Brønsted acidic site and alkene specie (ethylene). In this process, a water molecule and a surface hydroxyl are generated to ensure continuity of the alcoholysis and condensation processes.

In the dehydrogenation process proposed in Figure I-22 b surface metal and oxide ions concertedly interact with the O and H atoms from the ethanol hydroxyl resulting in an alkoxy and a proton linked to the surface metal and oxide, respectively. An α-H atom from the alkoxy can then be abstracted by the surface proton, leading to the formation of an aldehyde (acetaldehyde) and desorption of molecular hydrogen. It is important to note that during the dehydrogenation process, no Brønsted acidic sites nor water molecules are generated to allow further condensation to larger particles, meaning that the competition between both mechanisms can lead to different behaviors in the nanoparticle nucleation and growth processes.

I.6.3.2.1 Activation energies at the surface of nanoparticles

Many works have emphasized the role of t- and m-ZrO_2 activation energies (E_A) in the stabilization process and the general trend observed is that the activation energy for the tetragonal structure is generally lower than that of the monoclinic structure with E_A = 13 and 27 kJ/mol for t- and m-ZrO_2, respectively, regardless of the synthesis procedure or the starting materials [35, 211, 212, 213]. These low activation energies indicate that solvolysis must readily occur at very low temperatures, typically from temperatures as low as 25-75°C [214], but also the general tendency of t-ZrO_2 to crystallize before m-ZrO_2 in many studies.

I.7 ZrO_2 synthesized in supercritical fluids

I.7.1 Continuous flow synthesis of ZrO_2 in supercritical fluids

As ZrO_2 is an extremely interesting material for its catalytic properties and applications, the interest in synthesizing ZrO_2 in supercritical fluids has increased over the last decades as the technology has the ability to rapidly produce ultrafine and uniform nanoparticles due to the accelerated nucleation rates allowed by supercritical solvothermal conditions and supersaturation conditions [215]. As in other more conventional synthesis routes, ZrO_2 nanoparticles can be produced in supercritical water [15, 17, 108, 153, 215, 216, 217], as well as in supercritical alcohols [15, 17, 18, 19] and the nanoparticle size can easily be lowered uniformly, making this synthesis route a great candidate to study the size effect and metastable t-ZrO_2 stabilization.

A wide variety of experimental set-ups may be used during supercritical solvothermal synthesis of ZrO_2 nanoparticles, such as those presented in Figures I-13 and 14, and in Figure I-23.

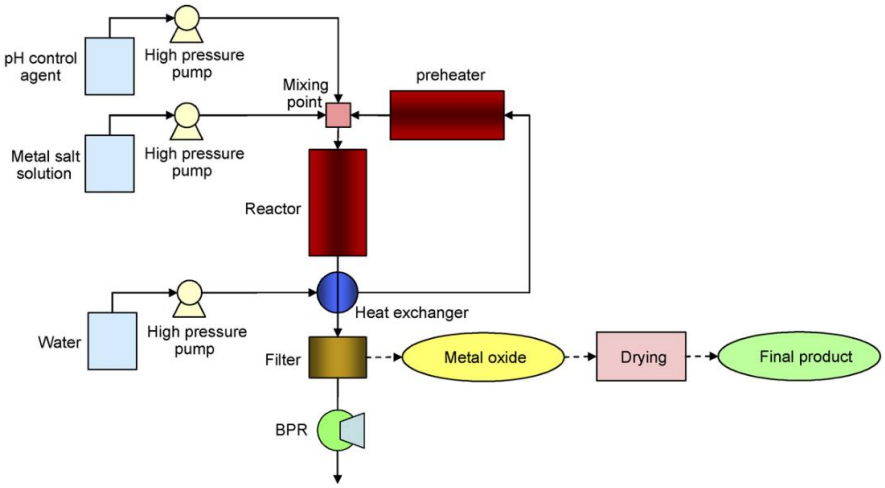

Figure I-23. Typical supercritical solvothermal continuous flow reactor used for the synthesis of ZrO_2 nanoparticles in supercritical water [115].

The reactor presented in Figure I-23 typically allows the formation of ZrO_2 nanoparticles with various m- to t-ZrO_2 molar fractions, as we have seen in Figures I-5 b and c that controlling the pH could influence the formation of either majorly m- or t-ZrO_2 crystal structures at low and high pH values, respectively. Table I-4 lists the various structures obtained during ZrO_2 syntheses performed in supercritical fluids along with the characterization techniques that enabled to study the crystal structures of synthesized ZrO_2 nanoparticles.

Table I-4. Crystalline structure for ZrO_2 nanoparticles synthesized in supercritical fluids depending on the input experimental parameters, along with the characterization techniques used.

Solvent	Precursor source	$[Zr^{4+}]$ mol/L	T (°C)	P (MPa)	A.C.S. (nm)	Crystalline structure	Characterization technique	Ref
Methanol	$ZrO(NO_3)_2.2H_2O$	1	250	25	5	m- and t-ZrO_2	WAXS	[17]
Methanol	$ZrO(NO_3)_2.6H_2O$	1	250	23	4	m- and t-ZrO_2	WAXS, SAXS, TEM	[218]
Isopropanol	$Zr(OCH_2CH_3)_4$	0.015	200-450	15-45	5-6	t-ZrO_2 (LP, LT)	PXRD, SAXS,	[15]
Water	$Zr(ac)_4$	0.11-0.55	300-400	10-45		m-ZrO_2 (HP, HT)	TEM	
Water	$ZrOCl_2$	0.038	400-490	30	10	c-ZrO_2	XRD	[219]
Water	$ZrOCl_2$	0.02	400-490	30	20-50	m- and t-ZrO_2	XRD, TEM	[215]
Water	$ZrO(CH_3COO)_2$ $ZrO(NO_3)_2$	0.05	400	30	3-7	m- and t-ZrO_2	XRD, TEM, BET	[220]
Water	$ZrO(NO_3)_2$	0.02	400	25	10	m-ZrO_2	XRD, TEM	[115]
Water	$ZrO(NO_3)_2.2H_2O$	0.01-0.1	400	30	4-5	m- and t-ZrO_2	XRD, TEM, TG	[221]

From Table I-4, one can easily observe the systematic absence of Raman spectroscopy to clearly identify the obtained ZrO_2 structures.

In supercritical solvothermal conditions, ZrO_2 nanoparticles are usually obtained with A.C.S. encompassed between 4 to 10 nm [15, 204] or larger if desired by varying residence times or precursor concentrations [108, 115, 150, 217]. Moreover, playing on ZrO_2 polymorphism in supercritical fluids may be performed in two evident ways. Probably the easiest is varying initial pH conditions when water is used as a solvent [108, 153], as metastable t-ZrO_2 will preferably form at high pH conditions (pH>9), where entrapped hydroxyl functions are believed to be responsible in the stabilization mechanism [80, 216]. The other method is by reducing the crystallite size and cross the energetic barrier of the critical size as stated previously in this chapter.

I.7.2 *In situ* measurements of ZrO_2 formation in supercritical fluids

In the recent years, new methods to visualize *in situ* the formation of nanoparticles from the precursor configuration to the final nanoparticles have been developed with the aim to unravel the formation mechanisms. One of these methods, associated with its analysis technique is total X-ray scattering coupled to pair distribution function analysis. The technique, as we will detail in Chapter II, allows to perform syntheses of metal oxides in ultra-small closed-systems similar to batch reactor configurations and collect the total X-ray scattering intensity from the reaction media at relatively fast rates (typically, down to seconds) [15, 17, 19, 216, 222].

The fast precipitation and thermal decomposition of zirconium precursors and their subsequent slow crystallization to 5 to 10 nm ZrO_2 nanoparticles were observed *in situ* in supercritical fluids with an apparatus we will introduce in the Chapter II, during SAXS and WAXS crystallization studies [19, 222,] . PDF analysis of the experimental data showed that their formation was the result of amorphous octahedrally coordinated nanoclusters agglomerating within 20 seconds and the subsequent slow crystallization of these nanoclusters leading to both t- and m-ZrO_2 nanoparticles whether syntheses were performed in supercritical water [15, 17, 216] or alcohols [15, 17, 19]. This method opens new horizons and a step forward in the understanding of ZrO_2 formation mechanisms like demonstrating the topotactic character of ZrO_2 crystallization [17], etc. and will be the one tool used throughout this thesis to understand metastable t-ZrO_2 formation mechanism.

Figure I-24 shows the evolution of the nanoparticle size obtained from PDF analysis for ZrO_2 from zirconium nitrate precursors in supercritical methanol.

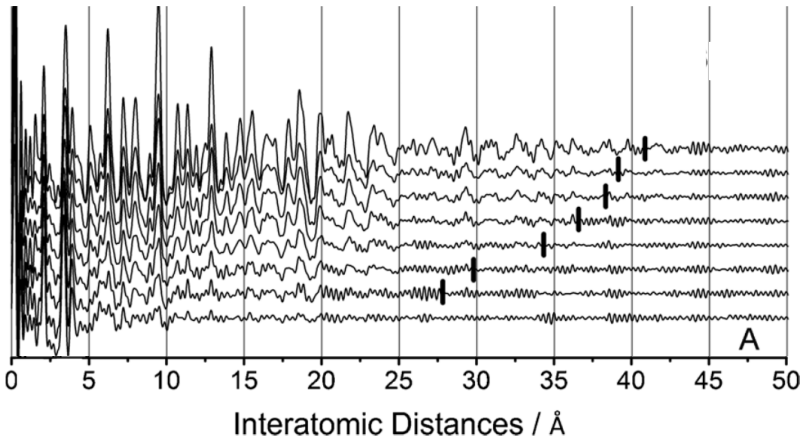

Figure I-24. PDF of ZrO_2 formation in supercritical methanol, from a zirconium nitrate precursor source [204].

In Figure I-24, each PDF is represented with a time gap of 50 seconds, thus showing almost each minute the evolution of ZrO_2 formation from a given precursor source and in a given solvent.

However, synthesized ZrO_2 nanoparticle A.C.S. were generally above the lower limit for the critical size (≈ 3 nm) [26], and therefore structural segregation due to the nanoparticle size has yet not been properly performed. Therefore, we strongly believe that synthesis of ZrO_2 nanoparticles in supercritical B.N.H.S.G. reactions may produce optimum conditions to study the impact of the critical size in stabilizing metastable t-ZrO_2. Table I-5 lists, non-exhaustively, the pros and cons, but also the A.C.S. obtained with the various synthesis routes used to produce ZrO_2 mentioned in this section.

Table I-5. Pros and cons of different syntheses routes for the formation of ZrO_2 nanoparticles.

Processes	Duration	Post synthetis step	A.C.S. (nm)	Homogeneity	Reference
Dry					
Solid state	Long	Milling, annealing	7-17	Low	223,
Deposition	Long	Drying, annealing	4-40	Medium	54, 224, 225
Wet					
Hydrothermal	Moderate	Drying	8-30	High	80, 147
Sol gel	Long	Drying, annealing	7-500	High	51, 66, 67, 78, 79, 127,
N.H.S.G.	Long	None	2-4	Very high	138, 143, 226
Supercritical fluids	Short	None	5-50	Very high	15, 17, 220, 221, 227, 228

It appears from Table I-5 that both N.H.S.G. reactions and the supercritical fluids technology offer the possibility to synthesize ultra-fine ZrO_2 nanoparticle exhibiting very high size homogeneity and no post-synthesis step to finalize nanoparticle formation. However, though N.H.S.G. reactions allow the formation of the finest ZrO_2 nanoparticles, the synthesis procedure is nevertheless relatively long in comparison to the supercritical fluid method.

I.7.3 Metastable cubic ZrO_2 stabilization

Very few works have reported the stabilization of 3.5 to 10 nm metastable c-ZrO_2 nanocrystallites in supercritical water, synthesized within 2 s [219, 229]. Figure I-25 shows an XRD pattern of ZrO_2 referenced as cubic with the major $(111)_c$, $(200)_c$, $(220)_c$ and $(311)_c$ Bragg reflections at $2\theta \approx 30$, 35, 51 and 60°, respectively.

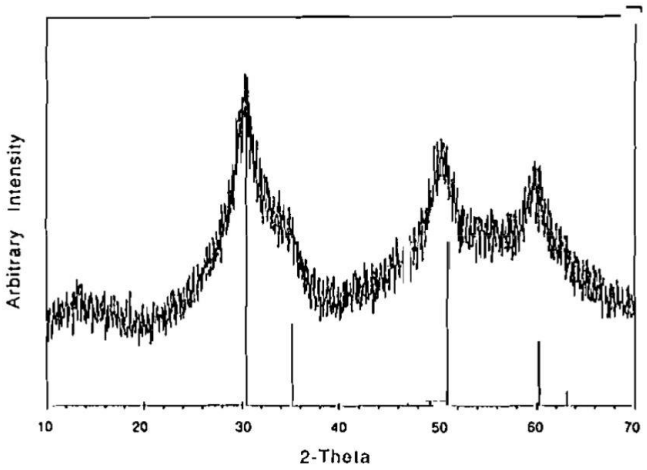

Figure I-25. X-ray diffraction pattern of ≈ 3.5 nm metastable c-ZrO_2 with (111), (200), (220) and (311) enlarged Bragg reflections due to the small crystallite size of the nanocrystallites [229].

Pure zirconia cubic to tetragonal phase transition has been estimated at size of approximately 2 nm by first principle calculations in support of experimental TEM imagery [230]. From the TEM diffraction patterns, lattice constants were estimated to be a_t = 0.351(4) nm and c_t = 0.515(4) nm for the tetragonal phase, and a_c = 0.506(6) nm for the cubic phase. Total energy for cubic and tetragonal clusters were simulated by means of first principles quantum mechanical molecular dynamics. Their hypothesis, based on hydrostatic and non-hydrostatic stresses, were computed for 1.5 to 2.5 nanocrystallites with the tetragonal and fluorite-type structures and compared to TEM images. The computed results estimated that the phase transition, from cubic to tetragonal could occur between two clusters of different, but very close dimensions: $Zr_{116}O_{208}$ and $Zr_{201}O_{360}$, which means for a particle size of approximately 2.05 ± 0.15 nm and for c-ZrO_2 and t-ZrO_2 phases, 10.45 and 10.34 % oxygen sub-stoichiometries, respectively. Moreover, computed effective Zr valence was found to be 3.6 for a 2 nm crystallite with one eight of missing oxygen and the remaining displaying an effective valence of |1|, strongly suggesting that surface oxygens combine with protons to form surface hydroxyl groups.

I.8 Conclusion of Chapter I

This chapter has focused on the main properties to likely enable metastable t-ZrO_2 stabilization in order to condense knowledge of some of the many mechanisms proposed throughout the past decades gathered on the particle size effect of ZrO_2 and elaborate, if possible, in the chapters to come a stabilization mechanism in our synthesis conditions. To answer this question, among the many theoretical mechanisms, two have been outlined based on either the critical size (the most commonly highlighted to this day) and the generation of structural defects such as lattice oxygen vacancies.

It has been decided to transpose the non-hydrolytic sol-gel process (N.H.S.G.) to the supercritical fluid method as both have shown great potential in achieving the smallest possible nanocrystallites independently. This is due to two major factors: (i) the N.H.S.G. process enables a higher degree of control and homogeneous reaction rates than conventional sol-gel syntheses, and (ii) the reaction rates in supercritical fluids enable ultrafast precipitation or hydrolysis and condensation of precursor molecules to form isolated nanoclusters with a low degree of subsequent condensation.

Many studies on low temperature metastable tetragonal zirconia have now estimated a critical size for metastable tetragonal ZrO_2 below 3 nm, with an achievable size limit in many studies comprised between 3 and 4 nm. It is therefore necessary to opt for optimized characterization techniques and data analysis as in this size range, the reliability of conventional diffractometers tends to fade out.

Understanding the underlying processes during nanoparticle formation in supercritical fluids has only started to become possible to experimenters given the latest *in situ* total X-ray scattering WAXS and SAXS experiments coupled to PDF data analysis. These latest works unraveled some of the characteristics in crystallite formation, kinetic rates of precursors consumption, as well as nucleation and growth profiles in the time dimension.

Also, new insights on a possible metastabilization of a c-ZrO_2 structure below a critical size of 2 nm opens new perspectives of research in the t- to c-ZrO_2 transformation for nanocrystallites below that possible critical size.

Therefore, and considering the results highlighted in this first chapter, this thesis will focus on:

- Combining borderline non-hydrolytic sol-gel alkoxide-based reactions and the supercritical fluids routes and study the influence of operating parameters on the obtained nanocrystallite characteristics;

- Stabilization of the metastable tetragonal ZrO_2 phase using an optimized supercritical fluids synthesis process and estimate a critical size for t-ZrO_2 nanocrystallite stabilization;
- Unravel the stabilization mechanisms of tetragonal ZrO_2 highlighted in this first chapter using pair distribution function analysis of time resolved *in situ* total X-ray scattering experiments.

Chapter II

Experimental set-ups, synthesis procedures and characterization techniques

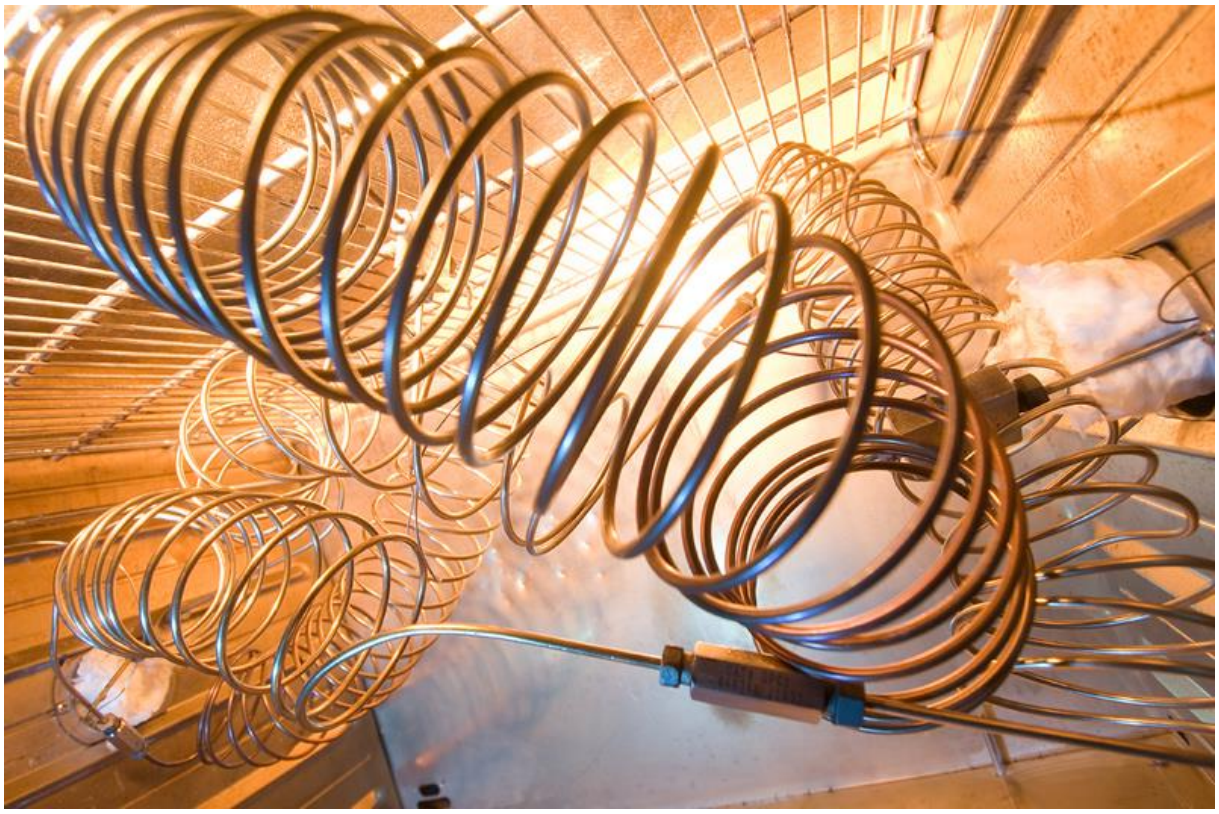

II.1 Introduction

In the previous chapter we have highlighted the advantages of the supercritical fluid method in its ability to promote fast reaction kinetics in comparison to other hydrothermal techniques. Indeed, the technology can cope with relatively high operating temperatures and pressures and therefore achieve high levels of supersaturation, but also continuous flow reactors enable precise control over reaction times and thus control of the uniformity of very small nanoparticles.

Nevertheless, knowledge in formation of such small nanocrystallites must be brought to a new level of understanding regarding the reaction processes, and the case of ZrO_2 nanoparticle formation is a very good example since the influence of the crystallite size is believed to be a key parameter to control the crystal structure, though it still does not find a consensus in the scientific community on whether size or initial experimental parameters are responsible for the stabilization of metastable t-ZrO_2. The main core of this thesis is therefore to gain a better understanding in metastable t-ZrO_2 stabilization mechanisms.

To do so, a synthesis set-up optimized to catch *in situ* a picture of the whole synthesis steps with a time resolution down to one second will be used [222]. This set-up will be introduced later in this chapter after the *ex situ* experimental set-ups used to validate the feasibility of borderline non-hydrolytic sol-gel (B.N.H.S.G.) reactions in supercritical fluids are introduced. Both reactor types, their characteristics and limitations will be discussed in a following section. This chapter will also introduce the techniques used to characterize the materials synthesized *ex situ* and *in situ* to investigate the nucleation and growth phenomena occurring during the formation of ZrO_2 nanoparticles.

While syntheses of nanoparticles were realized in continuous flow reactors and characterized *ex situ*, *in situ* observations on ZrO_2 nanoparticles nucleation and growth were performed in synchrotron under a high energy hard X-ray beam source in closed batch-type reactors. Indeed, the observation of such phenomena *in situ* during continuous flow syntheses still remains to this day a technical challenge to overcome. Though the main challenge in batch synthesis conditions is an accurate control of the residence time, continuous flow synthesis conditions do however allow to quench instantly nanoparticle growth within seconds after reaction has started. Nevertheless, the general approach behind nanomaterial synthesis in supercritical fluids remains the same in both batch and continuous flow configurations [115, 217, 219, 231, 232, 233, 234, 221].

II.2 Continuous flow synthesis of ZrO_2 nanoparticles in supercritical fluids, synthesis and characterization procedures

II.2.1 Synthesis procedure to produce ZrO_2 nanoparticles

We have briefly overviewed in chapter I the major differences between batch and continuous flow syntheses in sub- and supercritical fluids and identified the necessity to carry out this work in supercritical fluids. Thus, this chapter will focus only on the aspects of continuous flow syntheses in supercritical fluids.

Full solvation of the precursors will be guaranteed by an intermediate state of molecular aggregation of the supercritical solvents [156, 158] in order to maintain a high level of supersaturation and homogeneous nucleation conditions in our synthesis apparatus, as discussed in Chapter I-5.1.2. Similar experiments were conducted in both continuous flow reactors and during *in situ* measurements to facilitate our understanding of nucleation and growth phenomena. In order to keep as many constant operating parameters as possible, pressure and temperature conditions for all syntheses were chosen to be higher than the critical pressure of the highest of all investigated solvents, thus that of water, and were set to 25 MPa and 400°C for every experiment presented in Chapter III.

II.2.1.1 Starting materials

II.2.1.1.1 Solvents used

In this thesis, focus was made on solvothermal and sol-gel like reactions, thus implying the use of various types of solvents: water for the supercritical hydrothermal synthesis of pure m-ZrO_2 nanoparticles (used as a reference); also, and based on previous works performed in our research group [5, 52, 235] a 50/50 wt.% water/ethanol mixture was used for the supercritical sol-gel like synthesis of ZrO_2; finally anhydrous ethanol to study B.N.H.S.G. synthesis of ZrO_2 ultrafine nanoparticles in supercritical fluids, with the aim to find a reactional media that can allow the formation of pure t-ZrO_2 nanoparticles.

Table II-1 lists all the solvent conditions followed during continuous flow reactions to study nucleation and growth phenomena of ZrO_2 nanoparticles along with their corresponding thermophysical properties, necessary to determine the residence time for each continuous flow reaction performed throughout this thesis.

Table II-1. Solvent pressure and temperature conditions and associated thermophysical properties.

Solvent	Temperature (°C)	Pressure (MPa)	Density (g/cm^3)	Viscosity (µPa.s)	Dielectric constant	Critical point {°C; MPa}
Water	25	0.1	997.05	890.02	78.408	{374; 22.06}
	25	25	1008	887.59	79.323	
	400	25	166.54	29.287	2.504	
Water/ethanol (50/50 wt.%)	25	0.1	905.59			{339.88; 20.12}
	25	25	924.34			
	400	25	190.33			
Ethanol	25	0.1	785.13	1082.3	23.6[a]	{241.56; 6.29}
	25	25	805.14	1243.4		
	400	25	289.85 *	44..447 *		

* extrapolated density and viscosity values for supercritical ethanol. All values obtained via NIST Reference Fluid Properties – REFPROP, except **a** [236].

II.2.1.1.2 Zirconium metal precursors

The influence of the precursor type: either a metal salt in the case of nitrates; a metal complex with acetylacetonate organic ligands; or alkoxides, was investigated in order to choose the precursor and solvent types for further *in situ* measurements to investigate the possibility to fully stabilize the metastable t-ZrO_2 structure at low temperature.

First of all, the hydrothermal synthesis of ZrO_2 in supercritical water was performed using zirconium oxynitrate precursors. To perform the sol-gel synthesis of ZrO_2 in a continuous flow reactor, zirconium propoxide precursors were dissolved in ethanol and then mixed with water in the process to initiate the sol-gel reaction in the supercritical ethanol/water mixture. Foremost, B.N.H.S.G. reactions were performed with both zirconium acetylacetonate and zirconium propoxide in supercritical ethanol. Hexanoic acid (HA) was also used for surfactant assisted B.N.H.S.G. reactions with zirconium propoxide. Table II-2 summarizes all types of syntheses undergone throughout this thesis.

Table II-2. Listing of all the different types of reactions realized during continuous flow syntheses.

Reaction type	***Solvent***	***Precursor source***
Hydrothermal	*Sc-water*	*Zirconium oxynitrate* ($ZrO(NO_3)_2.xH_2O$)
Sol-gel	*Sc-water/ethanol*	*Zirconium propoxide* ($Zr(OCH_2CH_2CH_3)_4$)
B.N.H.S.G.	*Sc-ethanol*	*Zirconium propoxide* *Zirconium acetylacetonate* ($Zr(C_5H_7O_2)_4$)

II.2.1.2 Experimental set-up used to produce ZrO_2 nanoparticles

It has been decided to use continuous flow reactor experimental set-ups as they are being elaborated and used on a daily basis in our research group since control over temperature, pressure and residences time is greatly flexible in such systems, but also because they allow the fast synthesis of very fine and uniform nanoparticles in various supercritical solvents [5, 52, 25, 164, 22, 21, 162, 237, 238].

The reactor used for both hydrothermal and B.N.H.S.G. syntheses of the ZrO_2 nanoparticles presented in Chapter III is shown in Figure II-1. The sol-gel like synthesis of ZrO_2 nanoparticles in the 50/50 wt. % supercritical ethanol/water mixture was performed in a second reactor, similar to the one presented in Figure II-1, equipped with a secondary line to inject preheated water (inside the blue dashed-line perimeter in Figure II-1).

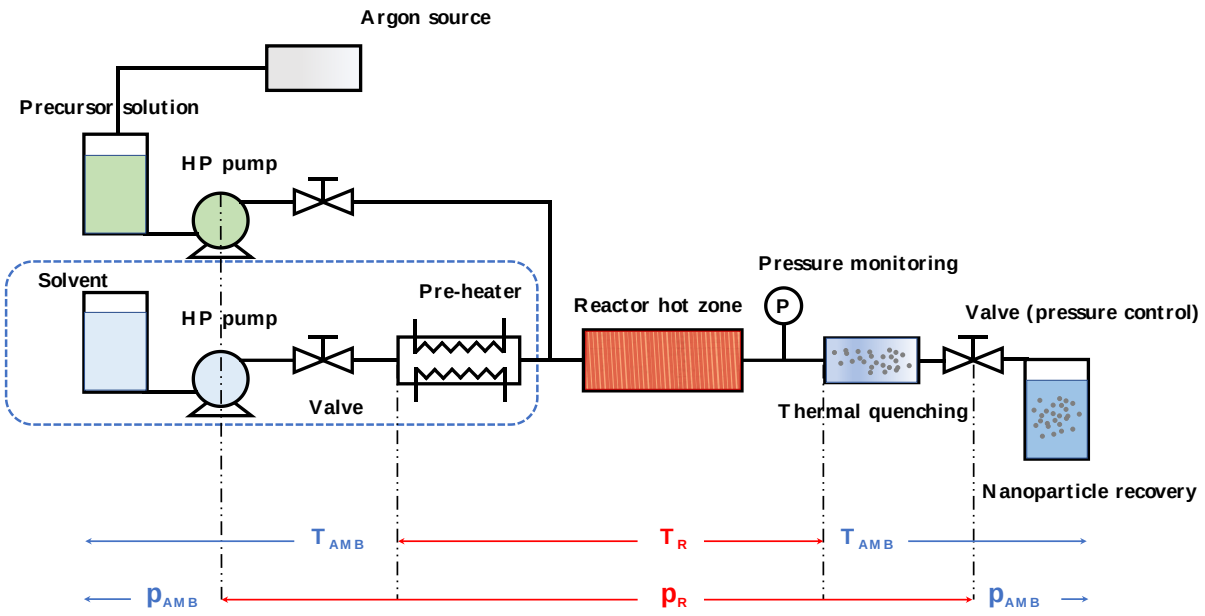

Figure II-1. Schema of the continuous flow reactor used for the synthesis of ZrO_2 nanoparticles during this thesis.

Basically, the experimental set-up represented in Figure II-1 consists of a precursor solution tank, a high-pressure liquid chromatography (HPLC) pump, a hot zone reactor where nucleation and crystallization processes occur, an ice bath to thermally quench the nanoparticle growth, a back-pressure regulator valve (Tescom®) to maintain a constant pressure in the whole system and a solution tank to recover the nanoparticles at the end of the line. The overall pressure inside the whole reactor is monitored just before and after the reactor.

The only difference when the sol-gel like synthesis is performed is a second injection line, represented inside a blue dashed-line perimeter in Figure II-1, in which pre-heated water ($T_{PREHEATER}$ = 225°C) was mixed to the precursor solution at the mixing point (T_{MIX} = 150°C) a few centimeters before the reactor hot zone entrance ($T_{REACTOR}$ = 400°C).

Tubing junctions between each part of the reactor are made of stainless-steel tube (SS-316L) with an inner diameter of 1.58 mm. The reactor itself, in which take place the nucleation, growth and crystallization of nanoparticles, consists of a 5-meter-long and 1.58 mm inner diameter stainless steel (SS-316L) tube coiled around a tubular support. The reactor is then placed inside a heating clamp equipped with both temperature controller and monitoring. A vermiculite® isolating compartment is used to minimize heat loss around the heating clamp at high operating temperatures and K-type thermocouples are placed at various locations of the reactor for an accurate control of the synthesis temperature, hence accurate residence time estimations. However, when alkoxide precursors were used the precursor solution tank was kept under constant argon flow to avoid air contamination of the precursors.

The nanoparticles recovered after hydrothermal and sol-gel syntheses were subsequently filtered from the reaction media using a Büchner filtration apparatus equipped with 100 nm pore size filters, washed several times using de-ionized water and ethanol, dried and stored for further characterization. However, powders recovered from B.N.H.S.G. syntheses were only slightly aggregated and could therefore not be filtered. They were thus separated from their solvent by a slow evaporation process inside a low temperature furnace (T = 85°C) and no further cleaning was performed to leave their surface and structure unaltered.

Production of these ZrO_2 powders was a preliminary step before investigating their nucleation and growth mechanisms during time resolved *in situ* wide angle X-ray scattering (WAXS) measurements under a high energy X-ray radiation source.

II.2.1.2.1 Experimental conditions

During a continuous flow synthesis, a turbulent flow hydrodynamic regime needs to settle inside the reactor to ensure a homogeneous concentration and dispersion of the solubilized precursor molecules, and thus homogeneous nucleation and produce uniform very small highly crystallized ZrO_2 nanoparticles across the whole reactor volume where the residence time is generally estimated as expressed in Equation $(II - 1)$ [23],

$$t_R = \frac{V_R \cdot \rho_{(HP,HT)}}{Q_V \cdot \rho_{(HP,LT)}} \qquad (\text{II} - 1)$$

where t_R is the residence time, V_R the volume of the reactor hot zone, $\rho_{(HP,HT)}$ and $\rho_{(HP,LT)}$ the solvent densities at high pressure-high temperature and high pressure-low temperature, respectively. Therefore, statistically each particle is subject to share the same residence time inside the reactor, resulting in uniform size distributions for each synthesis.

In order to maintain these conditions and avoid nanoparticle deposition on the inner walls of the reactor, knowing the hydrodynamic flow regime is mandatory and is characterized by the Reynolds number (Re), as expressed in Equation ($II - 2$),

$$Re = \frac{\rho * \upsilon * D}{\eta} = \frac{4 * d_m}{\pi * D * \eta} \qquad (II - 2)$$

where ρ is the fluid density [kg.m^{-3}], υ the fluid velocity [m.s^{-1}], η the fluid dynamic viscosity [Pa.s], D the inner diameter of the reactor [m], and d_m the fluid mass flow [kg.s^{-1}]. Fluid densities and dynamic viscosities were both estimated from Refprop© software developed by the National Institute of Standards and Technology (NIST).

The Reynolds number allows, in our synthesis conditions, 3 different regimes: laminar flow with Re < 2000; intermediate flow with 2000 < Re < 3000; and turbulent flow with Re > 3000.

II.2.2 *Ex situ* characterization of synthesized ZrO_2 nanoparticles

Several *ex situ* characterization techniques were used to understand the differences in morphologies, structures and state of aggregation of the produced powders, and gain deeper understanding of the processes occurring during supercritical fluids syntheses of ZrO_2.

II.2.2.1 Powder X-ray diffraction (PXRD)

X-ray diffraction patterns were systematically performed by Eric Lebraud, at the ICMCB, on the synthesized powders to analyse the obtained crystal structure. Figure II-2 schematizes briefly the Bragg formulation of X-ray diffraction.

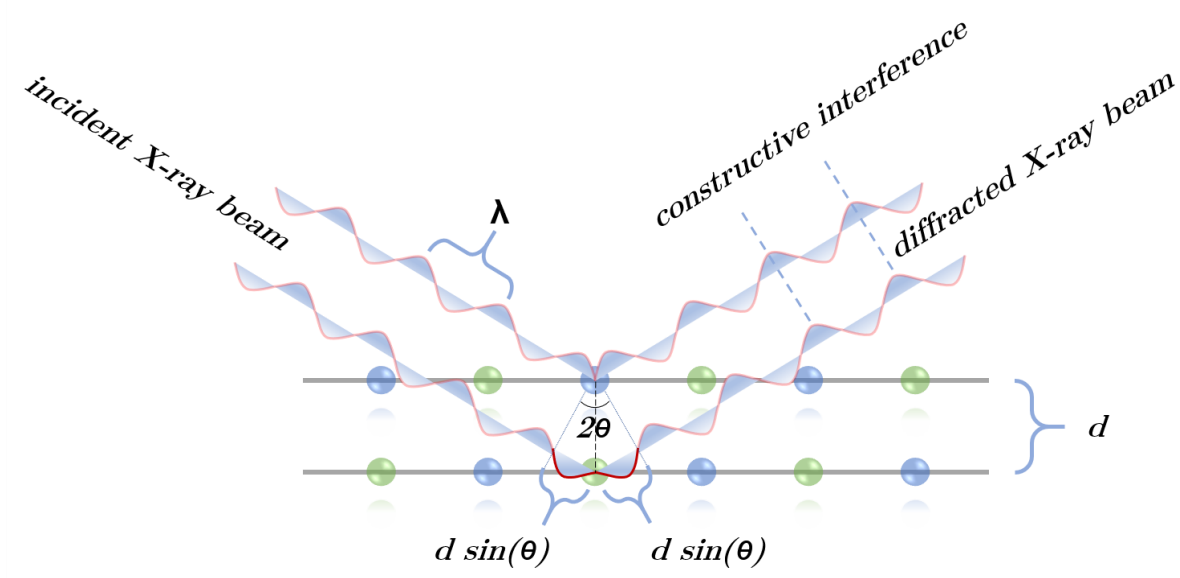

Figure II-2. Depicts the fundamental diffraction principle, namely the Bragg formulation of X-ray diffraction.

In Figure II-2, when an incident wavelength interacts with the atoms of a crystal and the lattice plane distances and scattering angles meet the Bragg condition for diffraction ($2dsin(\theta) = n\lambda$), the scattered wavelengths between the electronic densities of two distant atomic planes will interfere constructively with an intensity depending mainly on the scattering factor of the atoms but also on the atomic density of the diffracting planes.

II.2.2.1.1 PXRD measurements

Routine room temperature PXRD patterns were recorded on a PANalitycal MPD diffractometer with the Bragg-Brentano $\theta - \theta$ geometry over an angular range of $10 < 2\theta < 80°$ with a step of 0.0167°. The diffractometer was equipped with a secondary monochromator and the Cu $K\alpha_1$ = 1.5418 Å radiation was generated at 40 kV and 40 mA.

Room temperature powder X-ray diffraction patterns for Rietveld analysis were recorded on a PANalitycal MPD-PRO diffractometer with the Bragg-Brentano $\theta - 2\theta$ geometry over an angular range of $10 < 2\theta < 130°$ with a step of 0.0167°. The diffractometer was equipped with a secondary monochromator and the Cu $K\alpha_1$ = 1.5418 Å radiation was generated at 45 kV and 40 mA. Prior to measurements, powders were ground and were sieved to 40 µm maximum aggregates.

II.2.2.1.2 Rietveld analysis of PXRD patterns

Though the A.C.S. of ZrO_2 nanoparticles was at the limit or below the instrumental resolution of the diffractometer, Rietveld analysis was nevertheless performed to extract crystal structural information using the least-squares approach to minimize the weighed sum of difference between the experimental data and the models.

The refinements were performed using the FullProf_Suite software with the Thompson-Cox-Hastings model to describe the peak profiles. The scale factor for each structure, background, instrumental zero, unit cell parameters, Gaussian and Lorentzian contributions to the total peak broadening, and the microstructural strain parameter were systematically refined.

The "goodness of the fits" were estimated according to the weighed and expected weighed profile residual functions R_{wp} and R_{exp}, as expressed in Equations $(\mathrm{II}-3)$ and $(\mathrm{II}-4)$,

$$R_{wp} = \sqrt{\frac{\sum_{i=0}^{n-1} \omega_i \left|Y_{obs_i} - Y_{calc_i}\right|^2}{\sum_{i=0}^{n-1} \omega_i Y_{obs_i}^2}} * 100 \qquad (\mathrm{II}-3)$$

$$R_{exp} = \sqrt{\frac{N-P}{\sum_{i=0}^{n-1} \omega_i Y_{obs_i}^2}} * 100 \qquad (\mathrm{II}-4)$$

where $\omega_i = (\sigma_i^2)^{-1}$ the statistical weight, σ_i^2 the variance in observed intensity and, σ_i the standard deviation from the model on the i^{th} data point. Also, N and P are the number of data points and refined parameters, respectively. However, the reduced χ^2 function best indicates the quality of a refinement, as expressed in Equation $(\mathrm{II}-5)$,

$$\chi^2 = \left[\frac{R_{wp}}{R_{exp}}\right]^2 \qquad (\mathrm{II}-5)$$

Thus, the lower the value of χ^2, the closest the expected structure is to the model. Unfortunately, conventional X-ray diffraction cannot differenciate unequivocally c- and t-ZrO_2 structures in ultrafine nanoparticles as the coherence length is approximately 4-5 nm for this technique. Raman spectroscopy is however sensitive enough to assess the local symmetry in coherent diffracting domains of less than 2 nm and therefore cannot be overlooked when it comes to differenciate c-ZrO_2 and t-ZrO_2, or even estimate structural proportions of small nanoparticles

inside a powder mixture. It will therefore be used to infirm or confirm observations made by Rietveld analysis. Also, information on local order/disorder or deviation from the perfect lattice can only be obtained using more powerful techniques that are able to treat on an equal basis both X-ray diffraction and diffuse scattering. This kind of information is extremely valuable for particles of very small size and can only be accessed in total X-ray scattering measurements, which will be introduced later along with pair distribution functions analysis.

II.2.2.2 Spectroscopy measurements

Two spectroscopy techniques were used to characterize the structural and surface properties of ZrO_2 nanoparticles. Raman spectroscopy was used to determine the structure of very small ZrO_2 nanocrystals as well as to estimate the structural proportions when the powders were a mixture of t- and m-ZrO_2, while Fourier transform infrared (FTIR) spectroscopy was used to characterize the surface properties of the functionalized ZrO_2 powders.

II.2.2.2.1 Raman spectroscopy

Variations in local symmetries can theoretically easily be observed using Raman spectroscopy according to the correlation method [239], therefore this technique cannot be circumvented for precise determination of the crystal structure of ZrO_2 [240, 241, 242, 243, 244]. Table II-3 displays all possible Raman vibrational active modes for c-, t- and m-ZrO_2.

Table II-3. List of all the possible Raman vibrational active modes for c-, t- and m-ZrO_2 polymorphs.

Atom	Type	N_B	Site	Symmetry
Cubic ZrO_2 (c-ZrO_2), Fm-3m ≡ O_h^5 (225), Z = 4				
Zr		1	Oh	F_{1u}
O		2	Td	$F_{1u} + F_{2g}$
Total				$2F_{1u} + F_{2g}$
Acoustic				F_{1u}
Optical	Raman			F_{2g}
	FTIR			F_{1u}
Tetragonal ZrO_2 (t-ZrO_2), $P4_2/nmc$ ≡ D_{4h}^{15} (137), Z = 2				
Zr		2	D_{2d}	$B_{1g} + E_g + 2\,A_{2u} + E_u$
O		4	C_{2v}	$A_{1g} + B_{1g} + 2\,E_g + A_{2u} + B_{2u} + 2\,E_u$
Total				$A_{1g} + 2\,B_{1g} + 3\,E_g + 2\,A_{2u} + B_{2u} + 3\,E_u$
Acoustic				$2\,A_{2u} + E_u$
Optical	Raman			$A_{1g} + 2\,B_{1g} + 3\,E_u$
	FTIR			$A_{2u} + B_{2u} + 3\,E_u$
	Inactive			$A_{1g} + 2\,E_u$
Monoclinic ZrO_2 (m-ZrO_2), $P2_1/c$ ≡ C_{2h}^5 (14), Z = 4				
Zr		4	C_1	$3\,A_g + 3\,B_g + 3\,A_u + 3\,B_u$
$O_{(I)}$		4	C_1	$3\,A_g + 3\,B_g + 3\,A_u + 3\,B_u$
$O_{(II)}$		4	C_1	$3\,A_g + 3\,B_g + 3\,A_u + 3\,B_u$
Total				$9\,A_g + 9\,B_g + 9\,A_u + 9\,B_u$
Acoustic				$A_u + 2\,B_u$
Optical	Raman			$9\,A_g + 9\,B_g$
	FTIR			$8\,A_u + 7\,B_u$

Group theory predicts that as the symmetry of a crystal system decreases, the predicted number of Raman active modes increases, thus while only one characteristic optical mode is active for c-ZrO_2, six and eighteen are active for t- and m-ZrO_2, respectively, (Table II-3). However, though the Raman signature of m-ZrO_2 is usually a well-defined spectrum, the increasing structural defect concentration in t- and c-ZrO_2 is associated with broadening of the Raman vibrational modes, and thus resulting in less-defined Raman spectra.

Room temperature Raman spectra were collected, under supervision of Caroline Delhaye, at the ISM, using a XploRA HORIBA Scientific Raman spectrometer operating in backscattering geometry and equipped with an Andor CCD detector. The exitation wavelenght (λ_{exc}) was 532

nm over the 110-1700 cm^{-1} domain with a resolution of 4 cm^{-1} and experimental data were integrated using Labspec software.

II.2.2.2.2 Fourier transform infra-red (FTIR) spectroscopy

Though FTIR spectroscopy can, just as Raman spectroscopy, be used to characterize structural properties of metal oxides in the fingerprint domain, the technique was used to characterize the effectiveness of surface functionalization performed during B.N.H.S.G. synthesis of ZrO_2.
FTIR spectroscopy was performed on a Brucker equinox 55 spectrophotometer with a spectral absorption domain encompassed between 400 and 4000 cm^{-1}, over 32 scans with a spectral resolution of 4 cm^{-1} using a Globar radiation source. Nanoparticles were ground and dispersed into a KBr matrix prior to measurements.

II.2.2.3 Electronic microscopy

The size, uniformity, quality and morphology of ZrO_2 powders were examined by transmission electron microscopy. A transmission electron microscope was used to observe powders resulting from the hydrothermal synthesis of ZrO_2, while a high-resolution transmission electron microscope was used to observe powders resulting from the sol-gel and B.N.H.S.G. synthesis of ZrO_2, due to the decrease in A.C.S.

II.2.2.3.1 Transmission electron microscopy (TEM)

TEM imagery was performed at the PLACAMAT platform by Marion Gayot. The TEM JEOL 2100 transmission electron microscope was equipped with a specific diffraction camera and an acceleration voltage of 100 keV.

II.2.2.3.2 High resolution transmission electron microscopy (HRTEM)

HRTEM imagery was performed at the PLACAMAT platform by Sonia Buffière. The HRTEM-FEG JEOL 2200FS high resolution transmission electron microscope was equipped with a high-resolution camera. The accelerating voltage used was 200 keV.
Digital Micrograph software was used to acquire the images issued from both microscopes. Powders were dispersed in ethanol and ultrasonicated prior to being placed on 200 mesh carbon-supported copper grids.

II.2.3 The supercritical fluid reactor, a black box

As the type of reactor used during this thesis was made out of thick and opaque stainless-steel material, following the different steps occurring during a synthesis is a difficult task. Circumventing this problem as only recently become possible owing experimental set-ups designed and optimized at the University of Aarhus in the Center for Material Crystallography (CMC) research group directed by Prof. Bo Iversen and will be introduced later in this chapter. While for well-ordered crystal structures of thousands to billions of atoms Bragg's law is an extremely powerful and simple law that reduces their spatial representation into only very few atoms by specifying both the lattice symmetry and atomic positions within a unit cell, when the nanoparticle size becomes very small or when structural order extends to over only a few nanometers within the material, the Bragg formulation of X-ray diffraction becomes less reliable. This problem, commonly known as the "nanostructure problem", has become an increasing subject of research in nanomaterial science [245, 246, 247]. Figure II-3 represents the limits of Bragg's law for ordered, disordered and amorphous materials.

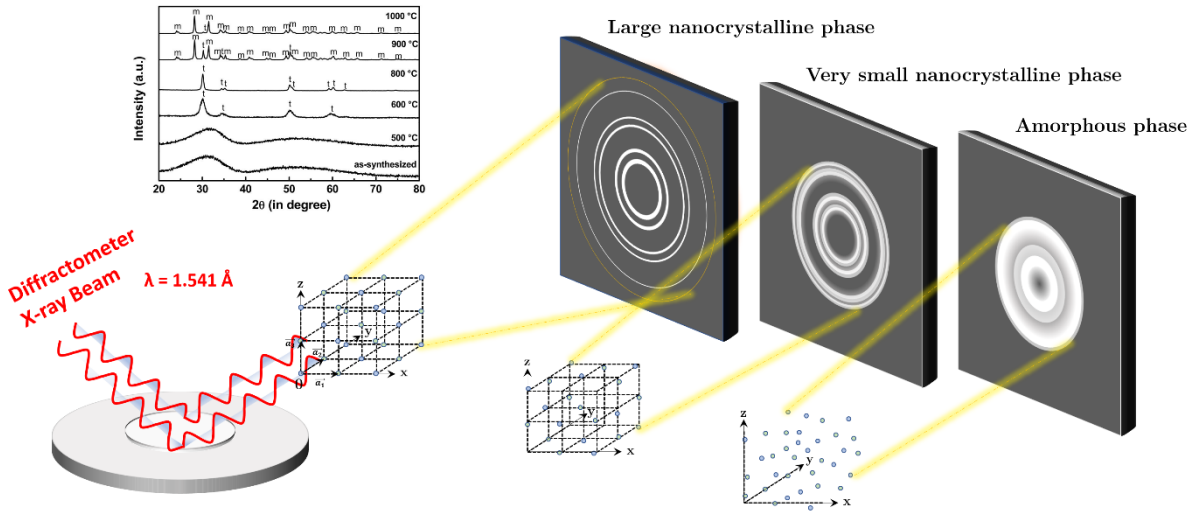

Figure II-3. Representation of the variation in X-ray scattering patterns for large nanoparticles, small nanoparticles and amorphous ZrO_2. The structural variations in the multiple XRD pattern correspond to amorphous zirconium hydroxide heated from 400 to 1000°C [248].

In Figure II-3 is represented the difference between diffraction and diffuse scattering of well-ordered and amorphous phases, respectively.

The concept of lattice defects or elasticity theory can be useful for discussion if deviations from the perfect lattice are relatively small, or if these deviations vary smoothly with space, but at some point different approaches become more useful and reliable to describe quasi-periodic nanostructures or easily differentiate crystallite and particle size through modeling. Therefore, total X-ray scattering measurements are more appropriate to understand local ordering in very fine nanoparticles. Figure II-4 shows all the information available from a scattering experiment.

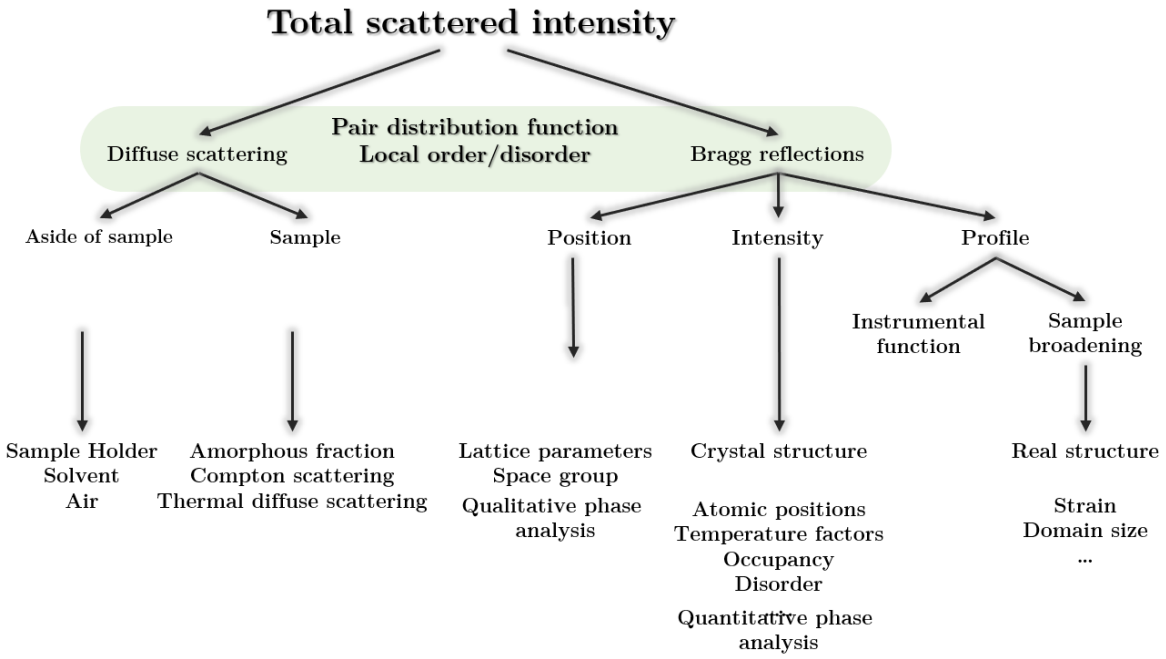

Figure II-4. Visualization of the information available from either total X-ray scattering experiments (diffuse scattering and Bragg reflections) or diffraction experiments (Bragg reflections).

From Figure II-4, we can see that from the interactions between an incident X-ray beam and a coherently organized set of atoms, the total X-ray scattered intensity (SAXS and WAXS) contains all the structural information. However, while only part of the information may be refined by the Rietveld method on laboratory diffractometer measurements, PDF analysis encompasses both Bragg reflections and diffuse scattering. For this reason, combining total X-ray scattering measurements to pair distribution function (PDF) analysis allows the experimenter to gain structural information on local ordering in ultrafine nanocrystallites.

II.3 *In situ* investigation on the formation mechanisms of ZrO_2 nanoparticles, synthesis and analysis procedures

II.3.1 Synthesis procedure during *in situ* measurements of ZrO_2 formation

All experiments presented in this chapter were performed at PETRA III in Hamburg, beamline P02.1 in the framework of a collaboration with Prof. B. Iversen from the Center for Materials Crystallography (CMC) at the university of Aarhus in Denmark. During *in situ* measurements, the pressure was 25 MPa and the reference temperature was 400°C, though changes in temperature were performed to vary kinetic conditions during *in situ* measurements presented in Chapter IV.

II.3.1.1 Starting materials

It was decided to perform *in situ* measurements on B.N.H.S.G. synthesis of ZrO_2 nanoparticles, as we will see in Chapter III that this synthesis route allowed to form t-ZrO_2 ultrafine nanoparticles with the highest degree of purity.

II.3.1.1.1 Solvents used

Synthesis of ZrO_2 during *in situ* measurements was investigated in many supercritical C_1 to C_6 primary alcohols, though analogous continuous flow syntheses were not conclusive for technical reasons, and would necessitate, to succeed, persevering in a dimensional study of an optimized continuous flow reactor system. However, as the amount of water generated *in situ* from supercritical ethanol decomposition increases almost linearly with temperature above the critical temperature [146], B.N.H.S.G. reaction kinetics will be investigated in supercritical ethanol at 300, 350, and 400°C, all above the supercritical temperature of pure ethanol (p_C = 6.29 MPa; T_C =241.56 °C), while in the other alcohols measurements will only be performed at 400°C.

Table II-4 lists all the solvent conditions chosen during the *in situ* measurements on nucleation and growth of ZrO_2 nanoparticles along with their corresponding thermophysical properties.

Table II-4. Pressure and temperature conditions and thermophysical properties of the solvents used during *in situ* measurements.

Solvent	Temperature (°C)	Pressure (MPa)	Density (g/cm^3)	Viscosity (µPa.s)	Dielectric constant	Critical point {°C; MPa}
Ethanol	25	25	805.14	1243.4		{241.6; 6.3}
	300	25	466.14	64.927		
	350	25	365.14	50.905		
	400	25	289.85 *	44..447 *		
Butanol	25	25	820.6 [b]		18 [c]	{288.8; 4.5}
	400	25				
Pentanol	25	25				{306.8; 3.9}
	400	25				
Hexanol	25	25				{337.3; 3.4}
	400	25				

* extrapolated density and viscosity values for supercritical ethanol. All values obtained via NIST Reference Fluid Properties – REFPROP, except **b** [249] and **c** [250].

II.3.1.1.2 Zirconium metal precursors

Only B.N.H.S.G. reactions were performed *in situ* with zirconium propoxide precursors in supercritical alcohols. However, two different surfactants were used: hexanoic acid (HA) and trioctylphosphine (TOP) in various precursor to surfactant molar ratios to investigate the possibility to decrease the nanoparticle A.C.S.

II.3.1.2 Sample preparation procedure

Samples were prepared inside a dedicated glovebox under a controlled argon atmosphere where proper volumes of $Zr(OCH_2CH_2CH_3)_4$ were inserted inside 10 mL test tubes using a 1 mL adjustable micropipette to reach concentrations of 1, 0.5, and 0.25 mol/L. The same procedure was used to insert the hexanoic acid (HA) and trioctylphosphine (TOP) during the surfactant assisted syntheses with the desired precursor to surfactant molar ratios, typically $[Zr(OCH_2CH_2CH_3)_4]$:[surfactant] = 2:1 and 1:1.

Inside the glovebox, the precursor solution was injected at one end of the sample holder, while at the other end the lock nut was tightened when the first drops of precursor solution came out. The sample holder was then directly taken to the experimental hatch of beamline P02.1 and mounted to be measured. A HPLC pump was connected to the sample holder to provide the proper solvent was supplied to maintain a constant pressure. The cleaning of the sample holder was then realized using anhydrous alcohol and inserted inside the vacuum chamber for the next synthesis.

II.3.1.3 Experimental set-up used during *in situ* measurements

In order to gain deeper understanding of nanoparticle formation mechanisms, an experimental set-up has been designed and elaborated by Prof. B. Iversen's research group at Aarhus University (Denmark), allowing to study *in situ* X-ray scattering processes [222]. This set-up, represented in Figure II-5, consists of a sample holder exposed under a hard X-ray collimated beam. The pressure and temperature ranges allowed by the set-up do not exceed 27.5 MPa and 450°C, comfortable conditions to visualize and study nucleation and growth processes in most commonly used supercritical solvents and with a time resolution close to the second, depending on the scattering power of the chemical compounds of interest.

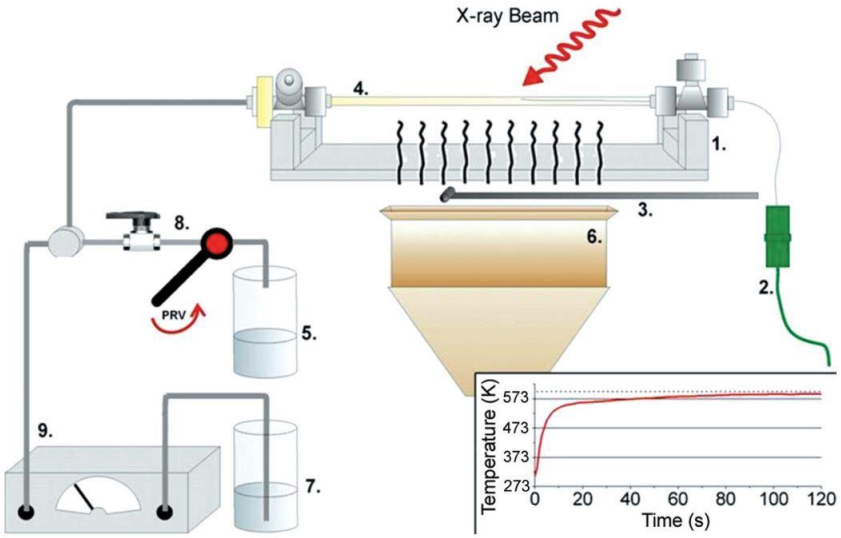

Figure II-5. Key parts illustrating the apparatus used throughout this thesis to visualize *in situ* particle formation during WAXS measurements. The set-up is composed of: 1, fastening shoe; 2, thermocouple; 3, beam-stop; 4, silica fused capillary; 5, solvent waste container; 6, heater mouthpiece; 7, solvent injection; 8, ball- and pressure regulator valves; 9, HPLC pump and manometer. The inset on the bottom right part of the illustration represents classical temperature profiles during heating.

This experimental set-up has been intensively used in both SAXS and WAXS measurements and coupled to pair distribution function (PDF) analysis over the past years to unravel formation mechanisms of many types of compounds [17, 19, 216, 251, 252, 253, 254, 255], and can be considered as a reliable apparatus for the quality of the data collected.

Figure II-6 displays camera pictures of the sample holder location presented schematically in Figure II-5, where the two-dimensional area detector is placed behind the beam stop and protected by a plexiglass window.

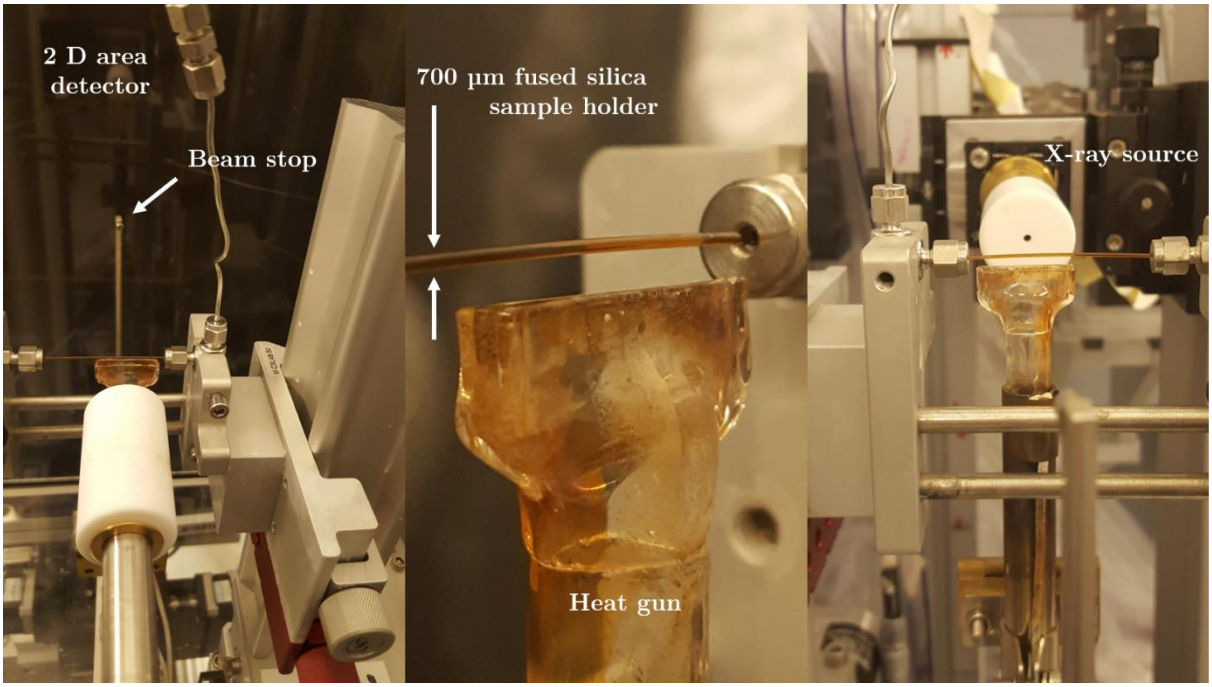

Figure II-6. Pictures of the *in situ* experimental set-up used to investigate ZrO_2 nanoparticle crystallization mechanisms. One can see in line the collimated X-ray source, sample holder, beam stop and finally the 2-D area detector.

At this stage it is important to note that experimental conditions met in both continuous flow syntheses and *in situ* measurements differ in three ways: first of all, the rate of heating is slower during *in situ* experiments (typically one order of magnitude); secondly, *in situ* experiments are run in closed reactor systems and lastly, in order to collect significant scattering intensity from the sample, precursor concentrations are increased by almost a factor 10 during *in situ* measurements, thus in the order of 1 mol/L.

II.3.1.3.1 Experimental conditions

During *in situ* measurements, four different parameters were chosen to be varied to stabilize metastable t-ZrO_2:

1. The effect of the temperature;
2. The effect of the precursor concentration;
3. The effect of addition of surfactants;
4. The effect of the alkyl carbon chain of alcohols.

In a first series of experiments, the influence of temperature on the crystal structure of ZrO_2 was investigated in supercritical ethanol at 300, 350, and 400°C while the impact of the precursor concentration was studied for three concentrations: 0.25, 0.50 and 1 mol/L. Also, two different surfactants were used: hexanoic acid (HA) and trioctylphosphine (TOP) and the precursor to surfactant molar ratios were varied.

In a second series of experiments, the impact of the alkyl chain length of alcohols on ZrO_2 nanoparticle synthesis was investigated in supercritical alcohols such as: methanol, propanol; isopropanol, butanol; pentanol; and hexanol. Special focus, in these experiments was directed towards stabilizing metastable t-ZrO_2 during B.N.H.S.G reactions. The synthesis pressure was maintained at 25 MPa for all syntheses. These syntheses will be further detailed in Chapter IV.

II.3.2 Measurement and analysis procedures used to investigate *in situ* ZrO_2 formation mechanisms

II.3.2.1 Total X-ray scattering measurements

Though the total X-ray scattered intensity encompasses both small (SAXS) and wide (WAXS) angle X-ray scattering intensities, *in situ* measurements conducted in order to gain information on the local structure of nanoparticles during this thesis were performed only at wide angles (WAXS). The following section will briefly overview the basics of scattering theory necessary for further PDF analysis of the obtained results which will be presented in Chapter IV.

II.3.2.1.1 Total scattered intensity

In a scattering experiment, interactions occurring between the sample and the beam source result in scattered intensities which vary as a function of the incident beam angle and of course, the nature of the source (electrons, X-rays, neutrons) and therefore the total scattered intensity (I_T) is thus composed of several contributions as seen in Figure II-4 and is expressed in Equation (II − 6),

$$I_T = I_C + I_{IC} + I_{MC} + I_{BG} \qquad \text{(II} - 6\text{)}$$

where I_C, I_{IC}, I_{MC} and I_{BG} are the coherent, incoherent, multiple coherent and background scattering intensities, respectively. Coherent scattering (I_C) contains basically most of the

structural and lattice dynamics information. Incoherent scattering (I_{IC}) is mainly the result of Compton scattering and multiple coherent scattering (I_{MC}) occurs when photons propagate through multiple scatterers inside the material. The background scattering intensity (I_{BG}) contains contributions of the sample holder, solvent, air, optical systems, etc., but also extremely valuable information on the material local structure.

Bragg scattering is a coherent and elastic process while thermal diffuse scattering is a coherent and inelastic process, meaning the scattered waves can interfere either constructively or destructively for both processes and thus their intensity is the squared sum of the amplitude of each wave: i.e., for n scattered waves, the scattered intensity can be as expressed in Equation (II − 7),

$$I_T = |\,\psi_1 + \psi_2 + \ldots + \psi_n\,|^2 \qquad \text{(II} - 7\text{)}$$

where ψ_1, ψ_2, ψ_n are the amplitude of the 1st, 2nd and nth scattered waves and I_T the total scattering intensity as in Equation (II − 6).

II.3.2.1.2 Total scattering structure function

The total-scattering structure function S($\boldsymbol{Q}$) is a function of the momentum transfer $\boldsymbol{Q}$ [Å^{-1}] and can be expressed for a single crystal as the sample's total scattering amplitude as in Equation (II − 8),

$$S(\boldsymbol{Q}) = |\,\psi(\boldsymbol{Q})|^2 = 1 + \frac{1}{N\langle f\rangle^2}\sum_{i\neq j} f_j^{*}\, f_i \frac{sin[\boldsymbol{Q}(\boldsymbol{r}_{ij})]}{\boldsymbol{Q}(\boldsymbol{r}_{ij})} \qquad \text{(II} - 8\text{)}$$

where $\psi(\boldsymbol{Q})$ is the sample's total scattered amplitude, $\boldsymbol{Q} = |\boldsymbol{k}\text{-}\boldsymbol{k_0}| = 4\pi sin(\theta)/\lambda$ the difference between the incident and scattered wavevectors, λ the incident beam wavelength and θ half of the diffraction angle 2θ.

Though scattering of a single crystallite is not isotropic, scattering from an ensemble of crystallites can be considered as isotropic and the resulting S($\boldsymbol{Q}$) depends only on the magnitude of the scattered wavevector, and not its direction. Therefore, Equation (II − 8) implies that for an isotropic sample containing N atoms with every orientation of equal probability, and where f_i and f_j are the scattering factors of atoms i and j and $\langle f\rangle^2$ the squared average atomic form

factor, all $\boldsymbol{r}_{ij}$ orientations in space are of equal probability and therefore all values are taken with equal probability for every θ position.

II.3.2.2 *In situ* Total scattering measurements procedure

In situ measurements presented in this work were performed at PETRA III, Hamburg, Germany.

II.3.2.2.1 Beamline P02.1

PETRA III is a high brilliance third Generation Synchrotron Radiation Source at the Deutsches Elektronen-Synchrotron complex (DESY). It is a 2.3 km circumference accelerator operating a 6 GeV beam source redistributed to 20 beamlines. The beamline P02.1 in the Max von Laue experimental hall is dedicated to high resolution powder diffraction experiments and provides hard X-rays of 60 keV ($\lambda \approx 0.2$ Å) and a 100 mA current allowing total X-ray scattering data to be collected on a Perkin Elmer XRD1621 two-dimensional fast area detector. Figure II-7 is a representation of the beamline P02.1 optical train were all *in situ* measurements were performed during this thesis.

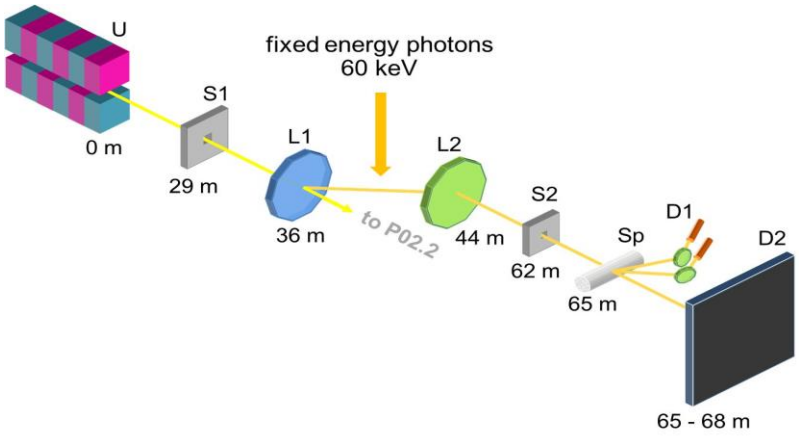

Figure II-7. Schematic of the beamline P02.1 optical train with: the undulator U23 (U); C(111) and Si(111) crystals Laue monochromators (L1 and L2), slit systems (S1 and S2); Sample (Sp) and detectors (D1 and D2).

II.3.2.2.2 Technical specifications of beamline P02.1

The main technical specifications of beamline P02.1 are listed in Table II-5.

Table II-5. Technical specifications for beamline P02.1

Photon source	Undulator U23, 2 m long
Photon source energy	60 keV (fixed)
Operated wavelength	0.207 Å
Grating properties	Double Laue monochromator, diamond (111) and Si (111) crystals
Maximum flux on sample	5.10^{10} ph/s
Hard X-ray spot size (on sample)	0.6 (H) x 0.9 (V) mm² (FWHM)
2-Theta range (SDD* = 200 mm)	Qmax = 25 $Å^{-1}$
Fast area detector type	XRD1621 (Perkin Elmer). CsI bonded amorphous silicon detector
Temperature range	90-1200 K

SDD*: Sample to detector distance (mm)

II.3.2.2.3 Detector

The Perkin Elmer detector is a 2-dimensional amorphous Si sensor with CsI scintillator consisting of 2048 x 2048 pixels, each of 200 x 200 µm² in size for a total area of 40 x 40 cm². The detector is mounted orthogonally to the incident beam for transmission experiments at a sample to detector distance of ≈ 200 mm, allowing a large momentum transfer of ≈ 25 $Å^{-1}$. Its fast readout rate (67 ms) allows a maximum exposure time of more than 1 frame per second, making it suitable for *in situ* and *ex situ* XRD and PDF measurements with good statistics. Due to the large accessible Q-space and high angular resolution of the Perkins Elmer XRD1621 detector, the X-ray photon energy source at beamline P02.1 is particularly well suited for the study and characterization of local ordering in nanocrystalline and disordered materials.

Another interesting feature of PDF analysis is that X-ray scattering measurements can easily be monitored in the time dimension due to the combination of high energy X-ray beam sources, fast area detectors and powerful microcomputers. The PDF analyses carried out in this thesis will greatly take advantage of these features during *in situ* measurements with a time resolution of one to two seconds.

The collected WAXS data were further analyzed using the PDF analysis method.

II.3.2.3 Operating conditions

For all *in situ* experiments, the sample to detector distance (SDD) was ≈ 200 mm, thus allowing reliable data collection up to a maximal momentum transfer $Q \approx 23$ $Å^{-1}$ for a wavelength $\lambda \approx$ 0.2 Å. During total X-ray scattering measurements, before the heat was turned on to initiate the

reactions, data were collected for 1 minute at room temperature with the pressure set to 25 ± 1 MPa to observe the precursor molecular configuration as a function of the precursor concentration, the presence of surfactants, and the type of solvent.

II.3.2.3.1 Temperature profile

Temperature profiles are determined in the beginning of each beamtime in order to monitor the heating rate for each targeted temperature. They were realized by fitting a 0.5 mm K-type thermocouple inside a sapphire capillary filled with the desired solvent. The following temperatures were used for the calibration as well as for the sequential PDF refinements: 100; 150; 200; 250; 300; 350; 400 and 450°C. Figure II-8 shows the temperature rate profile for the experimental set-up used during *in situ* measurements performed in supercritical ethanol.

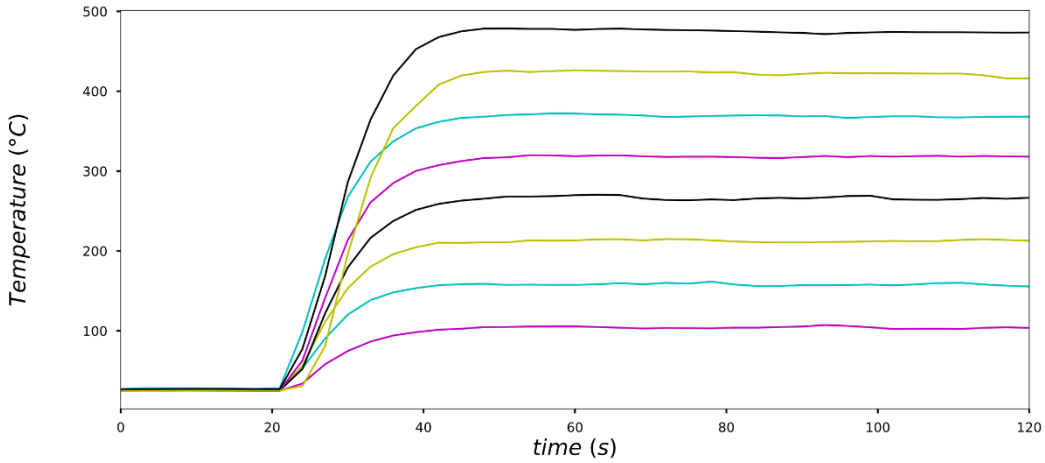

Figure II-8. Temperature heating rate profiles during *in situ* experiments conducted in supercritical ethanol (first set of measurements). From bottom to top curves are the following target temperatures: 100; 150; 200; 250; 300; 350; 400 and 450°C.

Figure IV-8 shows the difference between the inset and outset temperatures inside the sapphire capillary, necessary information to define and readjust properly the inset temperature for each synthesis. The temperature rate profiles also give the valuable information that 95 % of the final temperature is reached within twenty seconds for every temperature.

II.3.2.4 Instrumental calibration for measurements preformed in supercritical ethanol

For this set of measurements, the time resolution was one frame per second to determine if it was possible to catch the instant of nucleation as one frame per second was the maximum time resolution to follow reactions while still maintaining a reliable scattering signal quality. Table II-6 lists the main technical specifications for the instrumental set-up during measurements performed in supercritical ethanol.

Table II-6. Operating conditions for the collection of total X-ray scattering intensity 2-D data files.

Sample exposure time (s)	*1*
Camera gain (pF)	*1*
X-ray wavelength (Å)	*≈ 0.2*
Q_{Damp} ($Å^{-1}$)	*0.0321*
SDD (mm)	*≈ 200*

II.3.2.5 Instrumental calibration for measurements preformed in supercritical alcohols

The time resolution chosen for the measurements in supercritical alcohols was one frame every two seconds to improve the signal to noise resolution while still following precisely the reaction kinetics. Table II-7 lists the main technical specifications for the instrumental set-up during measurements performed in the other supercritical alcohols.

Table II-7. Operating conditions for the collection of total X-ray scattered intensity 2-D data files.

Sample exposure time (s)	*2*
Camera gain (pF)	*2*
X-ray wavelength (Å)	*≈ 0.2*
Q_{Damp} ($Å^{-1}$)	*0.0319*
SDD (mm)	*≈ 200*

The collected WAXS data were further analyzed using the PDF analysis method.

II.3.2.6 Atomic pair distribution function analysis procedure

Pair distribution functions (PDF) are one-dimensional functions giving the extent of the interatomic positional correlations structuring multi-dimensional single crystals, isotropic or anisotropic crystalline powders, amorphous or even liquid materials [256, 257 258, 259, 260, 261].

The formalism structuring the PDF theory dates back to almost 100 years ago, in the wake of crystallography as can be seen in Figure II-9, but the challenge in collecting experimental data to qualitative high momentum transfer values (Q [Å^{-1}]) highly limited its application fields to studies on material with no long range order (e.g., liquids and glasses).

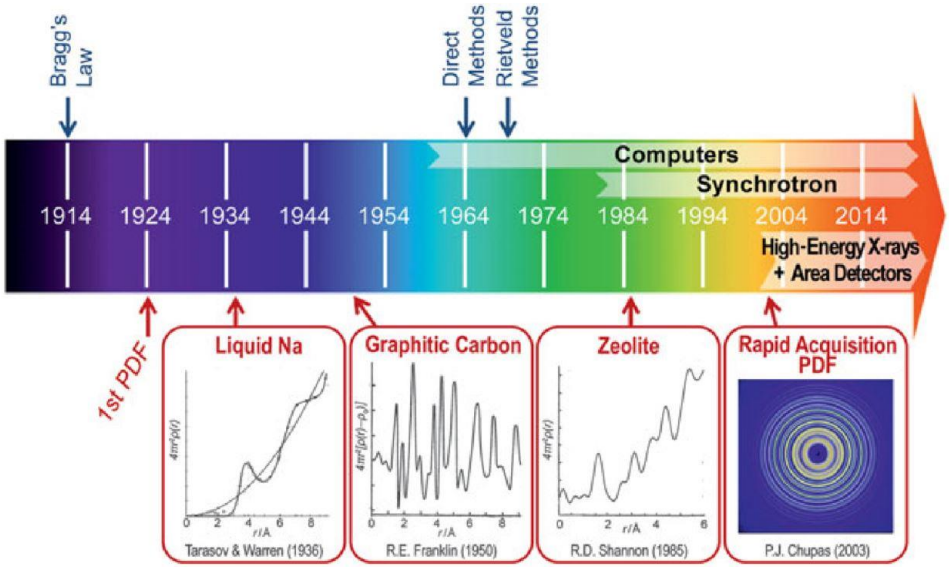

Figure II-9. Evolution of the PDF technique over a full century of crystallographic analysis [262]

Nowadays, third-generation high-energy (i.e., short wavelengths) X-ray, electron and neutron sources and large-area fast detectors coupled to ultra-fast computers allow totally new approaches in nanomaterial formation understanding where, during a single beamtime of only a few days, comparative studies may be performed on either complex structures, or complex physical and chemical processes occurring due to external parameters chosen by the experimenter [263].

The major feature of PDF analysis relatively to the conventional XRD method is its capacity to treat both Bragg diffraction and diffuse scattering on an equal basis as seen in section II-3.4, thus resulting in precise information on the structure and lattice dynamics of the real crystalline structure as illustrated in Figure II-10.

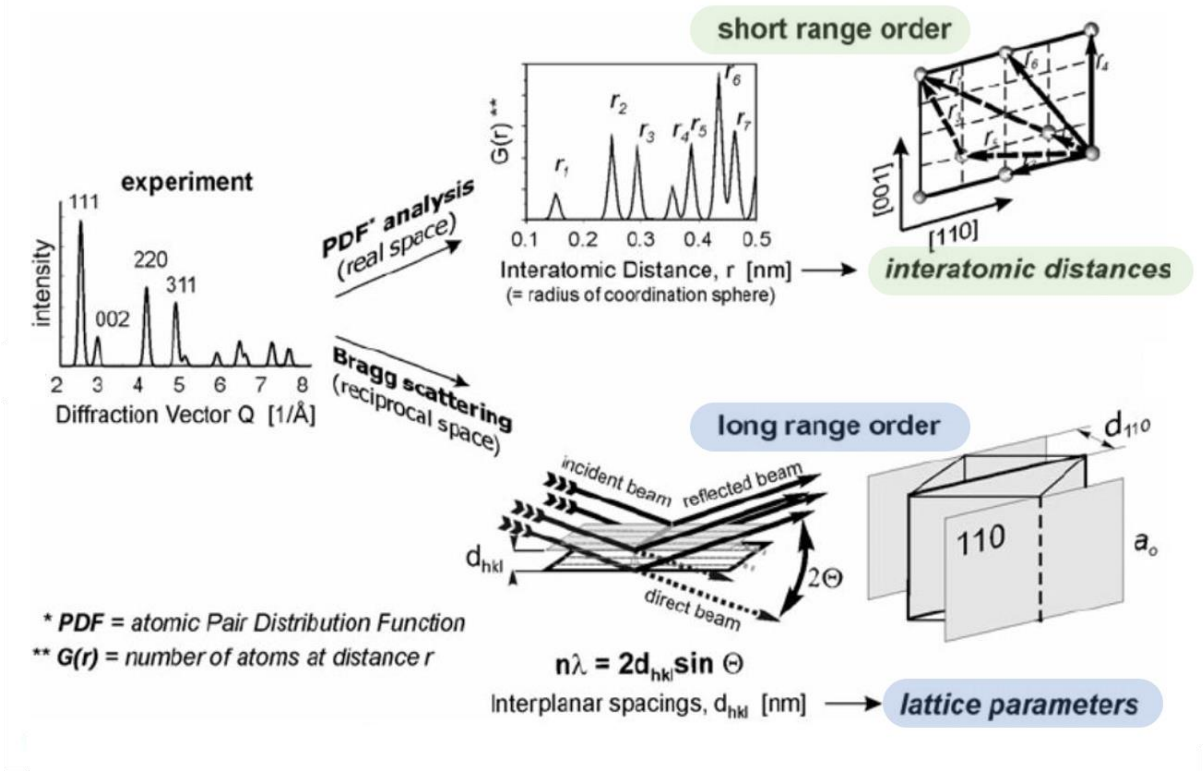

Figure II-10. Representing the difference in structural information available from the Bragg reflections alone, or when combined to diffuse scattering during PDF analysis. Adapted from [264, 265].

Figure II-10 shows how unlike during conventional XRD analysis where only the diffraction of lattice planes may be observed, it is the distance between the atoms constituting lattice planes that may be observed through PDF analysis of total X-ray scattering measurements. Thus, information on the local structure but also on the intermediate to long-range structure may be obtained. Though this information could theoretically be available through Rietveld analysis performed on classical diffractometers, the instrumental contribution on the line shape is far too important to enable reliable analysis of microstructural properties for very small diffracting domains.

II.3.2.6.1 Pair distribution functions

Pair distribution functions are basically the Fourier transform of the total scattering function S(***Q***) and may be written as in Equation (II − 9),

$$G_{obs}(r) = \frac{2}{\pi}\int_{Q_{min}}^{Q_{max}} Q[S(\boldsymbol{Q}) - 1]\sin(Qr)\,dQ \qquad \text{(II} - 9\text{)}$$

Where $G_{obs}(r)$ is the observed PDF, Q is the magnitude of the momentum transfer and S($\boldsymbol{Q}$) the corrected and normalized total scattering intensity from Q_{min} to Q_{max}, the experimental limitations to the momentum transfer allowed by the experimental set-up [263]. After derivation, the $G(r)$ function can be expressed as a function of atom-pair density and a characteristic shape function as in Equation (II − 10) [266, 267],

$$G(r) = 4\pi r[\rho(\boldsymbol{r}) - \rho_0\, \gamma_0(\boldsymbol{r})] \qquad (\text{II} - 10)$$

Where ρ_0 is the material's atomic number density, $\rho(\boldsymbol{r})$ the average pair density, or in other words the weighed density of neighboring atoms separated by the distance r, and γ_0 a characteristic shape function. Several γ_0 functions have already been implemented to refine nanoparticles of cubic, spherical, ellipsoids, or even rod-like shapes taking even into account the anisotropic character of small nanoparticles [258]. In terms of physical measurements $\rho(r)$ is generally expressed as in Equation (II − 11),

$$\rho(r) = \frac{1}{4\pi r^2 N} \sum_i \sum_{j \neq i} \left[\frac{f_i f_j}{\langle f \rangle^2} \delta(r - r_{ij}) \right] \qquad (\text{II} - 11)$$

where i and j run over all N atoms, f_i and f_j are the scattering factors of atoms i and j, respectively, $\langle f \rangle$ the averaged scattering factor of the sample, and r_{ij} in the Dirac function $\delta(r - r_{ij})$ the distance between two atoms i and j. Therefore, experimental PDF may be calculated, for a known structure, and given all input information, as in Equation (II − 12),

$$G_{calc}(r) = \frac{1}{Nr} \sum_i \sum_{j \neq i} \left[\frac{f_i f_j}{\langle f \rangle^2} \delta(r - r_{ij}) \right] - 4\pi r \rho_0 \qquad (\text{II} - 12)$$

where the first term of Equation (II − 12) is equal to $4\pi r\rho(\boldsymbol{r})$ in Equation (II − 10).

II.3.2.7 Data processing

II.3.2.7.1 2D data integration process

Integration of the 2D total X-ray scattered intensity measured data sets was performed on FIT2D software. The instrumental calibration for the synthesis set-up was realized using a LaB_6 standard to refine the values of the incoming wavelength, sample-to-detector distance, the central position of the Debye-Scherrer rings on the detector, the detector tilt angles and non-orthogonality.

Once the instrumental calibration was realized, the refined values were applied to the raw X-ray intensity data files in a sequential integration process to the desired dimension: e.g., $2\,\theta$ and Q-space for Rietveld refinements and PDF analysis, respectively.

II.3.2.7.2 PDF file generation

The xPDFuite software was used to transform the integrated one-dimensional raw data to pair distribution functions using PDFgetX3 where background subtraction and Q range were cut off to decrease the contribution of noise in the PDF as shown in Figure II-11 where correlation between the raw X-ray total scattered intensity I(***Q***) and the final PDF G(***r***) obtained.

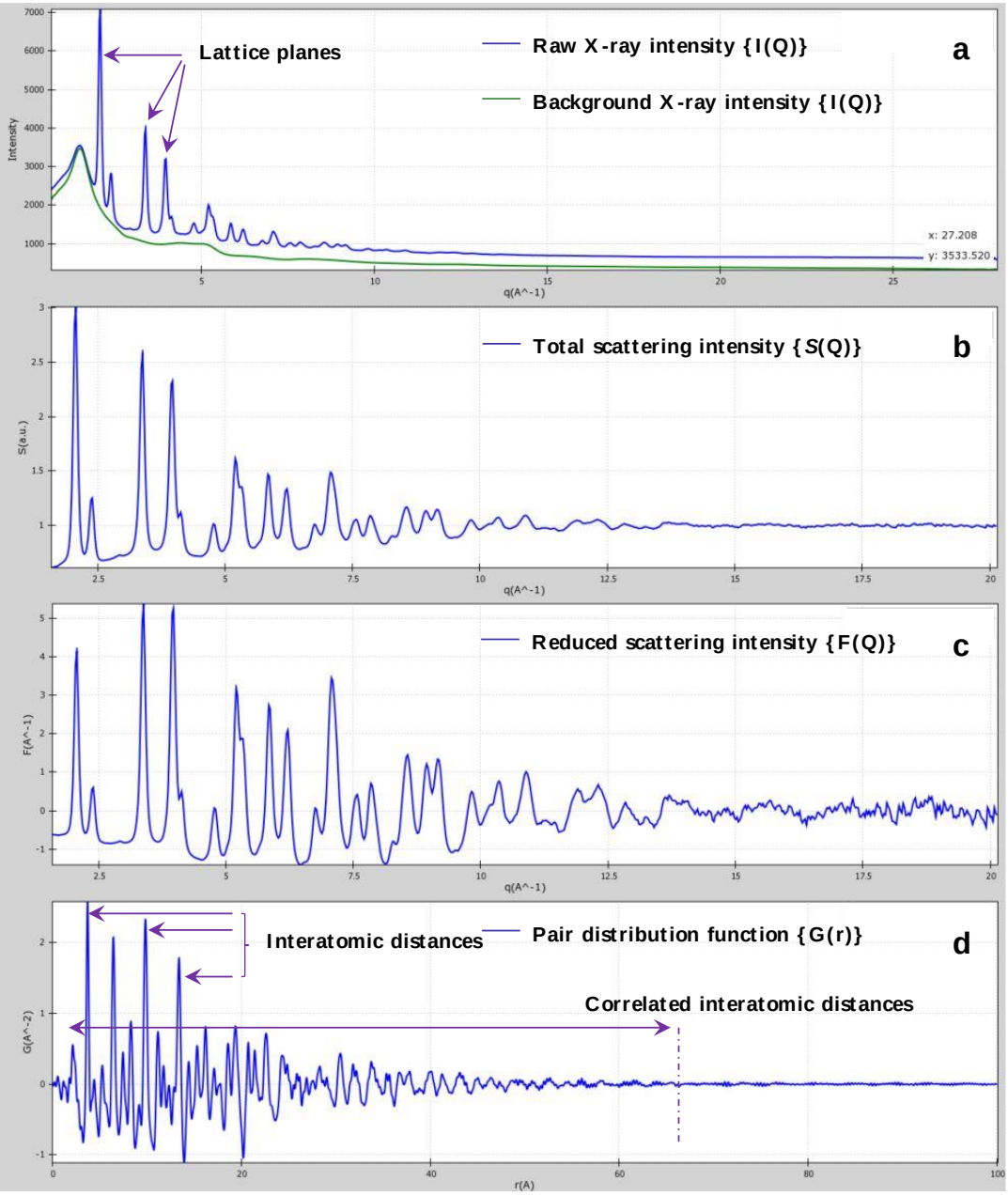

Figure II-11. Representing for a single measurement on a ≈ 60 Å ZrO_2 nanoparticle: a, the raw X-ray scattering intensity; b, the total scattering intensity; c the reduced scattering intensity and d, the pair distribution function.

The total scattering intensity S(***Q***) in Figure II-11 b corresponds to the scattering intensity of the sample I(**Q**) (Figure II-11 a) after the background was discarded (green line), while the reduced scattering intensity F(***Q***) = ***Q***[S(***Q***)-1] (Figure II-11 c). Also, though S(***Q***) and F(***Q***) must converge to 1 and 0 at high Q values, respectively, both functions are nevertheless equivalent in obtaining the final G(***r***) functions (Figure II-11 d) [263].

II.3.2.7.3 Background removal

In order to remove the fuse silica sample holder, solvent and air scattering contributions (green intensity in Figure II-11 a) for accurate analysis of only Bragg reflections and diffuse scattering from the sample (Figure II-11 b), measurements were performed on the sample holder containing the solvent for many temperatures along the course of the increase in temperature so that in the first 20 to 30 seconds during heating, the proper background contributions could be accurately removed when generating the PDF files.

II.3.2.8 Small box modelling

The "Small Box" modeling approach was chosen to refine time-resolved PDF measurements performed in this work and presented in Chapter IV. This choice was governed by the fact that the nanoparticle size range was approximately 20 to 60 Å, thus not too large in comparison of the average unit cell described by crystallographic information files (CIF) which contain all the possible interatomic distances and thus crystallographic information through translational symmetry repeated over multiple cells to the extent of experimental r_{max}.
The PDF of a nanoparticle $G_{nano}(r)$ may then be calculated theoretically using atomic models as in Equation $(\mathrm{II}-13)$ [268],

$$G_{nano}(r) = \gamma(r) G_{bulk}(r) \qquad (\mathrm{II}-13)$$

where $\gamma(r)$ is the characteristic function and $G_{bulk}(r)$ the PDF of a bulk material calculated using periodic boundary conditions. In this method, a characteristic spherical function $\gamma(r)$ is already implemented in PDFgui to account for the nanoparticle finite size and shape [268, 269, 270, 271, 272, 273] as expressed in Equation $(\mathrm{II}-14)$,

$$\gamma_{\text{sphere}}(r) = \left[1 - \frac{3}{2}\frac{r}{D} + \frac{1}{2}\frac{r^3}{D^3}\right] \theta(D - r) \qquad (\text{II} - 14)$$

with $\theta(D - r)$ the boundary conditions expressed in Equation (II − 15),

$$\theta(D - r) = \begin{cases} 0, & D < r \\ 1, & D > r \end{cases} \qquad (\text{II} - 15)$$

and where D is the diameter of a sphere, and r the distance separating two spheres. Using this characteristic function to refine spherical nanoparticles, if two spheres are separated by a value greater than D, there is no overlap between the two spheres and $\theta(D - r) = 0$. On the other hand, if two spheres overlap, the common volume varies between 0 and 1.

In analogy to the Rietveld refinements process, "Small Box" modeling integrates sample-dependent parameters including the unit cell parameters, atomic fractional coordinates, isotropic or anisotropic thermal ellipsoids and atomic occupancies to be refined. The local structural parameters are refined in the real space (Å) rather than the reciprocal space, where the average structural parameters may be obtained with more accuracy.

II.3.2.8.1 Quality of the refinement

Small box modelling of PDF allows the refinement of multiple structures at once in a least-squares minimization procedure to yield the model parameters with estimated standard deviations where the PDF weighed agreement factor R_W, corresponding to the "goodness of the fit", is equivalent to the Rietveld residual parameter and is expressed as in Equation (II − 16),

$$R_W = \sqrt{\frac{\sum_{i=1}^{N} \omega(r_i)[G_{obs}(r_i) - G_{calc}(r_i)]^2}{\sum_{i=1}^{N} \omega(r_i) G_{obs}^2(r_i)}} \qquad (\text{II} - 16)$$

where $\omega(r_i) = (\sigma^2(r_i))^{-1}$ is the weighing factor, σ the estimated standard deviation on the i^{th} data point at position r_i , and with G_{obs} and G_{calc} the observed and calculated PDF, respectively. However, as data points in a PDF that are not separated by a value of $\Delta r \approx \pi/Q_{max}$ cannot be considered as statistically independent, a reasonable qualitative measure of the "goodness of the fit" can be expressed by χ^2 as in Equation (II − 17),

$$\chi^2 = \frac{R_{wp}^{PDF}}{\frac{(r_{max} - r_{min})Q_{max}}{\pi} - P} \qquad (II - 17)$$

where R_{wp}^{PDF} is the weighed agreement factor (R_W) and P the number of refined parameters in the PDF refinement [263].

II.3.2.8.2 Momentum transfer resolution

Due to the finite Q resolution in X-ray scattering measurements, the scattered amplitude $\psi(\boldsymbol{Q})$ decreases with increasing Q (or 2θ), and thus the envelope of the scattered intensity is attenuated. This dampening factor (Q_{Damp}) is characteristic of a particular set-up and must be accounted for during PDF refinements. Experimentally, Q_{Damp} is obtained by measuring a large and highly crystallized LaB_6 standard (NIST SRM 660) in similar conditions as all subsequent experiments. The decrease in the standard's scattered intensity along Q results in a Gaussian like shape function $B(r)$, described as in Equation $(II - 18)$,

$$B(r) = exp\left(-\frac{(r.Q_{Damp})^2}{2}\right) \qquad (II - 18)$$

corresponding to the maximum range the experimental set-up may reliably interpret a single coherent diffracting domain. It is then important to use a high Q resolution to obtain structural correlations over large r-distances as for increasing r values, while B(r) decreases and gives reliable structural information, beyond the instrumental envelope no structural information may be truly reliable as shown in Figure II-12.

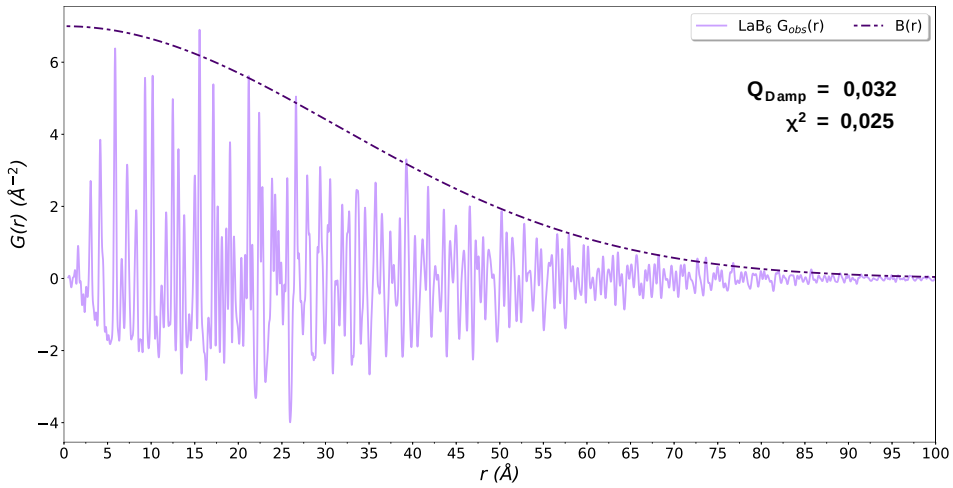

Figure II-12. Representing a LaB_6 standard PDF measured on beamline P02.1 and the instrumental envelope B(r) for the set-up used in experiments presented in chapter IV.

Figure II-12 represents the PDF of a LaB_6 standard refinable to ICSD-40947 model (Pm-3m, space group 221). Scale factor, lattice constants, correlated motion, isotropic thermal factors, along with the Q_{Damp} were refined for our experimental set-up. Also, $B(r)$ was calculated from Equation $(\mathrm{II}-18)$ and superposed to the LaB_6 PDF.

As one of the limitations of the technique is that Q_{max} can never be larger than $4\,\pi/\,\lambda$, a conventional diffractometer operating a Cu Kα_1 X-ray source will never be able to allow a scattering vector larger than 8 $Å^{-1}$ while large synchrotron X-ray sources allow up to 20 and even 40 $Å^{-1}$. A further limitation also in achievable Q values is the total area of the detector used for data collection.

II.3.2.8.3 Statistical errors

In the case of a high energy X-ray monochromatic beam, Q-resolution (ΔQ) is quasi constant with Q and termination errors can be eliminated with detectors allowing a high enough momentum transfer. However, as noise is cumulative, a large extension in the Q range increases the risk of including statistical noise to errors. This can be solved by a proper termination in the Q range in $S(\boldsymbol{Q})$ functions when integrating X-ray scattering intensity into $G(r)$ functions as we will see in the next section on the *in situ* characterization of samples.

II.3.2.9 PDF data modeling

In the scope of this thesis, we consider in first approximation that the synthesized nanoparticles have a uniform internal structure to model structural changes in time from finite pieces cut out of bulk structures and use the approach implemented in PDFgui.

The small box modeling approach chosen during PDF refinement is very similar to the Rietveld refinement approach where physical models used in the refinements include all structural parameters necessary to simulate the experimental data in a least-squares minimization procedure. All existing zirconium oxide CIF files were tested in single PDF refinements for all measurements and the least diverging were kept to initiate the final sequential refinements. When the model and experimental data would diverge, the sequential refinement would be stopped, the number of refined parameters usually be diminished until minima would converge and the sequential refinement be initiated again. This usually happened when some parameters became irrelevant, mathematically and moreover physically, to refine when variations in structures were too important.

II.3.2.9.1 PDF refinement procedure of ZrO_2 nanoparticle formation

Once all intensity data were reduced to PDF files, different crystallographic models were then implemented in the PDFgui calculation module and refined to the experimental PDF files and the "goodness of the fit" factor indicated the best model for each series of measurements. Sequential refinements were then realized on each sample to visualize their structural changes in time. The crystallographic information files (including unit cell parameters, atomic fractional coordinates and occupancies, isotropic thermal ellipsoids, etc.) used as models in the least-squares minimization method to yield the model parameters during real space refinements were ICSD #66781 and #157403 CIF files for t-ZrO_2 and m-ZrO_2, respectively with all initial parameters listed in Table II-8.

Table II-8. List of initial starting parameters used for the PDF refinements in this section on ZrO_2.

m-ZrO_2, $P2_1/c \equiv C_{2h}^5$ (14), Z = 4 Cif # 157403		**t-ZrO_2, $P4_2/nmc$ (Z) $\equiv D_{4h}^{15}$ (137), Z = 2** Cif # 66781	
a	*5.1514 (4) Å*	*a*	*3.5960 Å*
b	*5.2098 (4) Å*	*b*	*3.5960 Å*
c	*5.3204 (4) Å*	*c*	*5.1841 Å*
α	*90 °*	*α*	*90 °*
β	*99.171 (3) °*	*β*	*90 °*
γ	*90 °*	*γ*	*90 °*
Volume	*140.96 Å^3*	*Volume*	*67.04 Å^3*
Zr^{4+} B_{ISO}	*0.47*	*Zr^{4+} B_{ISO}*	*0.48*
Zr^{4+} Occ	*1*	*Zr^{4+} Occ*	*1*
Zr^{4+} CN	*[VIII]*	*Zr^{4+} CN*	*[VIII]*
O^{2-} B_{ISO}	*0.29*	*O^{2-} B_{ISO}*	*0.3*
O^{2-} Occ	*1*	*O^{2-} Occ*	*1*
O^{2-} CN	*[IV]*	*O^{2-} CN*	*[IV]*

PDF refinements were performed from these starting parameters to investigate the different steps in nanoparticle formation, from the precursor molecular organization to the final nanoparticle structures. Sequential refinements were performed using PDFgui with systematically both t- and m-ZrO_2 structures if possible, with for each structure, the scale factor, lattice parameters, single particle diameter (Spd). Depending on the experiment, atomic positions and ADPs were either partially or totally refined. However, Delta 2 values were generally kept constant during the refinements.

II.3.2.9.2 PDF modelling of molecular clusters

As very small nanoparticles generally contain many structural defects, the shape function approach usually fails. To overcome this problem, PDF calculations have been performed, over the past ten years, using the Diffpy complex modelling infrastructure (CMI) software over a wide variety of nanostructures [274, 275, 276, 277] due to the great flexibility offered by the library of Python modules. Diffpy-CMI offers the possibility to implement, in the small box modelling approach, various numerical characteristic shape functions in relatively computationally inexpensive PDF calculations [278, 279].

For this reason, the approach will be used for modelling and extracting information on the small nanoclusters present in the precursor solutions prior to heating.

The least-squares minimization mathematical procedure is the same as the one used in PDF analysis (e.g., PDFgui) where lattice parameters, atomic positions, bond lengths, spatial orientations, bond valence sums, etc. are refined while the overall structure is maintained by applying restraints (e.g., soft constraints) to refine very small clusters or large nanoparticles in a fitting framework combining multiple experimental inputs in a single optimization problem.

Figure II-13 shows simulated PDF for single ZrO_6 or multiple corner sharing ZrO_6 octahedra obtained from Diffpy CMI.

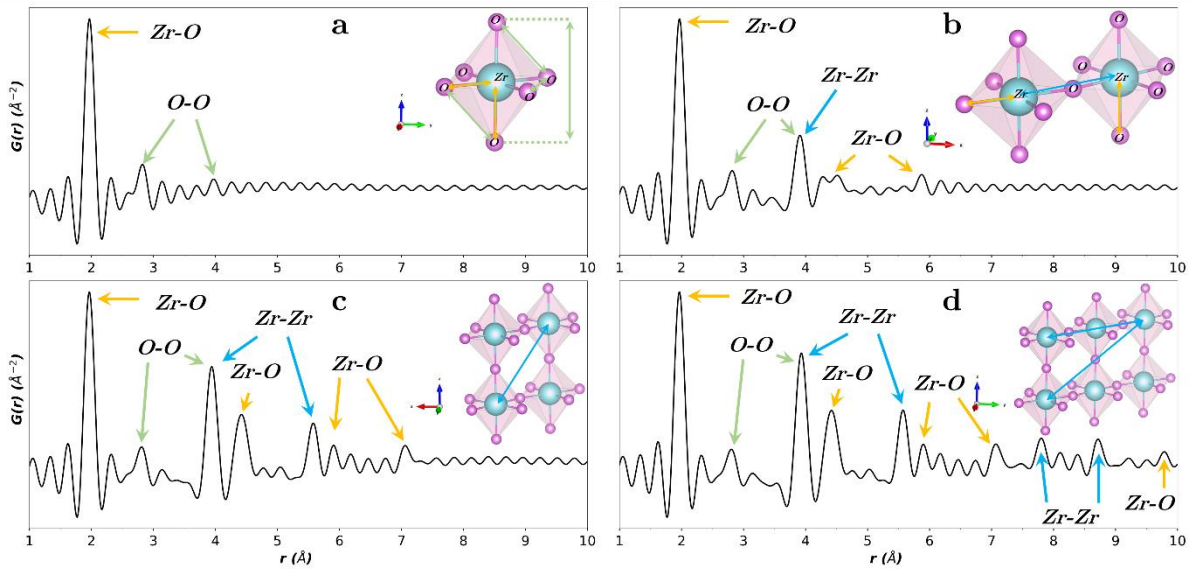

Figure II-13. Simulated PDF in the real space (Å) for: a, single ZrO_6 octahedron; b, c and d 2, 4 and 6 ZrO_6 corner sharing octahedra. Zr-O, O-O and Zr-Zr atomic correlations are marked with orange, green and blue arrows, respectively.

Figure II-13 shows visualization of the increasing cluster growth from a single octahedron (Figure II-13 a) to a larger nanocluster made of 6 single ZrO_6 octahedra (Figure II-13 d) performed using a *debyepdfcalculator* module from the *diffpy.srreal* package. The increasing number of atoms is observed in the PDF by the apparition of new peaks in the r range.

However, the *DebyePDFGenerator* module from the *diffpy.srfit.pdf* package was used to fit models to the experimental data and thus observe if there were any correlations between the precursor organization and the final structures in each experiment as it is believed that structural

similarities also could be responsible for the stabilization of metastable t-ZrO_2 as seen in Chapter I.3.2.

II.3.2.10 Information obtained from PDF refinements

As all other refinement parameters (scale factor, lattice constants, single particle diameter, atomic positions) are quite straightforward and similar to the Rietveld method, they are also generally less subject to dissension.

Figure II-14 represents a PDF pattern and the information that can be derived out of such functions in terms of atomic distances, coordination number, local disorder, coherent scattering domain size, etc.

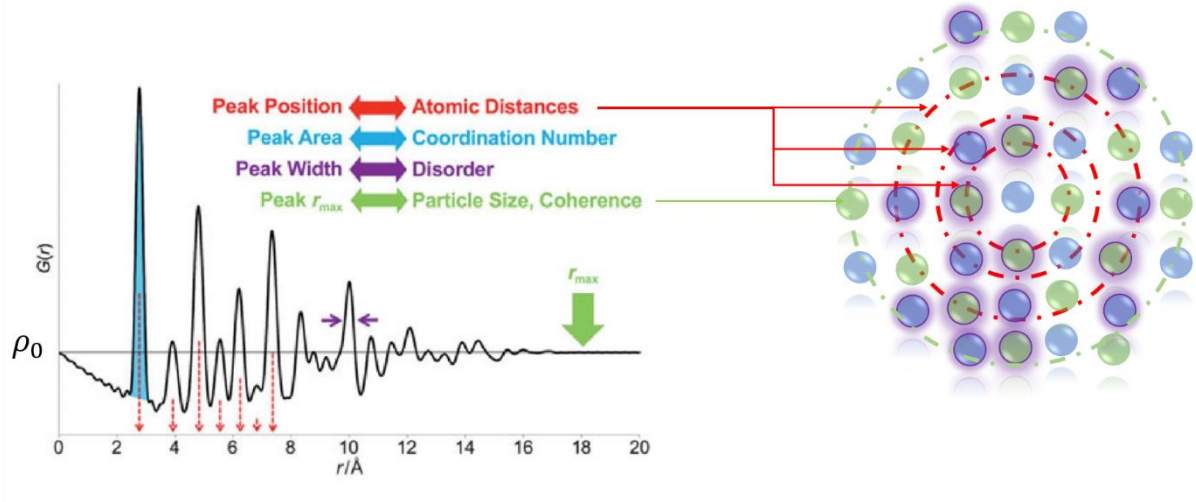

Figure II-14. Exemplifies how information can be deduced from a typical PDF fit from a model whose crystallographic characteristics are known. Adapted from [262].

The main source of structural information that can be obtained from PDF analysis lies basically on the peak positions, width, intensities and extension. From the peak positions and extent, one can directly and accurately observe as far as the instrumental envelope interatomic distances between correlated atomic pairs and crystallite size in real space. Information on the static and dynamic disorder can be obtained from the width of the peaks while atomic coordination numbers (CN) can be extracted from the integrated intensity of the peaks as expressed in Equation ($\mathrm{II}-19$),

$$N_C = \int_{r_1}^{r_2} R(r)dr \qquad (\mathrm{II}-19)$$

where $R(r) = 4\pi r^2 \rho(r)$, the radial distribution function, and r_1 and r_2 the integration limits of the considered coordination shell.

II.3.2.10.1Structural information

Figure II-15 represents simulated PDF obtained for ZrO_2 nanoparticles with sizes of 20, 30 and 60 Å.

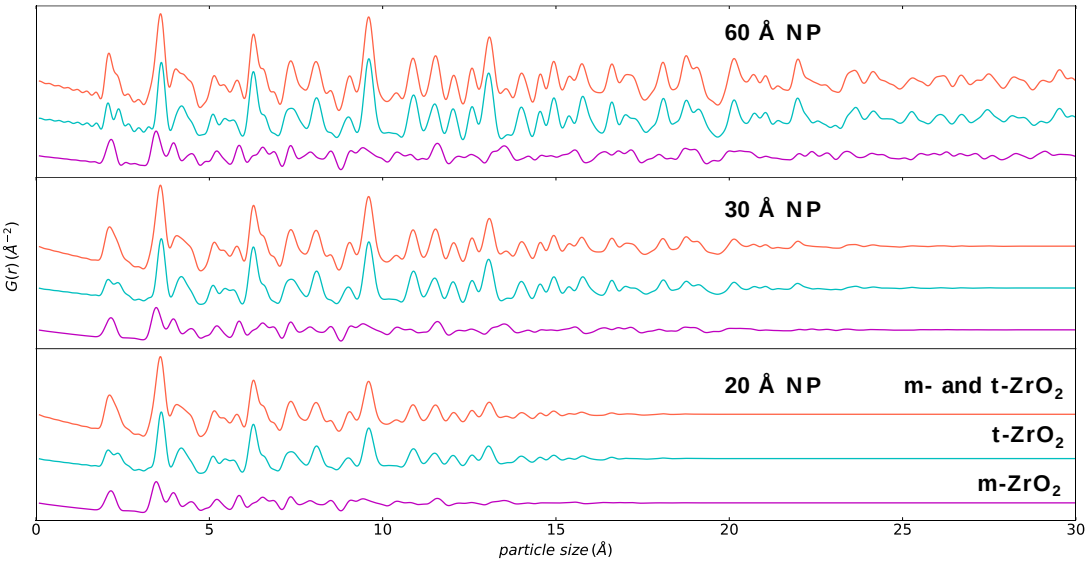

Figure II-15. Representation of 20, 30 and 60 Å nanoparticles, with: in magenta m-ZrO_2; in cyan t-ZrO_2 and in light red a 50/50 vol.% mixture of m- and t-ZrO_2.

The PDF simulations on 20, 30 and 60 Å ZrO_2 nanoparticles were performed using PDFgui from CIF files and with fixed initial parameters. It is important to notice the difference in intensity between t-ZrO_2 and m-ZrO_2 $G(r)$ functions, meaning that to the eye, while the structure may seem to be purely tetragonal, relatively large amounts of monoclinic structure will be necessary in the case of a phase mixture before being visible. However, it will be visible through observation of either a shift or shouldering in the first Zr-Zr distances, typically between 3.453 Å (m-ZrO_2) and 3.615 Å (t-ZrO_2). Also, PDFgui software is sensitive enough to detect these variations and mathematically interpret changes in phase proportions. It is noteworthy that sizes deduced from PDF analysis correspond to structural coherent scattering domains, thus crystallite sizes (A.C.S.).

II.3.2.10.2Interatomic local order/disorder

Figure II-16 shows how PDF analysis also differentiates between atomic pairs (e.g., Zr-Zr, Zr-O; O-O).

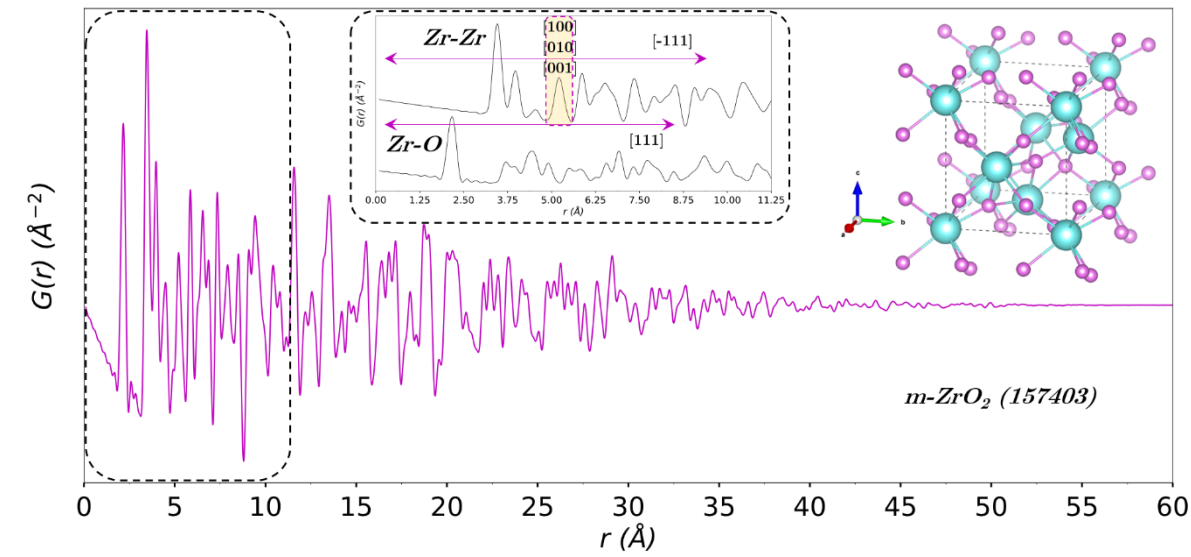

Figure II-16. PDF of ≈ 60 Å m-ZrO_2 nanoparticle simulated from ICSD 157403 CIF file. The insets represent a deconvolution of Zr-Zr and Zr-O atomic correlations in the 0-11 Å r range and a m-ZrO_2 unit cell.

In the inset presenting the atomic correlations in Figure II-16, the extent of the unit cell is visible between 5.15 and 5.32 Å in the [100], [010], [001] directions, but also between 8.56 and 9.53 Å in the [111] and [-111] directions, respectively.

II.4 Conclusion of Chapter II

The characterization methods presented in this chapter will be used in the following chapters to understand the key steps in metastable t-ZrO_2 stabilization in supercritical fluids by comparing results observed through *ex situ* and *in situ* experiments.

Optimizing the supercritical B.N.H.S.G. synthesis conditions to decrease the A.C.S. of ZrO_2 nanoparticles will be the object of Chapter III and the starting point of this work considering the importance of the crystallite size in maintaining the metastable t-ZrO_2 structure. X-ray diffraction and Raman spectroscopy analyses will be used as complementary characterization techniques to study the crystalline structure specificities of synthesized nanoparticles; transmission electron microscopy will be performed to analyze both morphology and surface characteristics of ZrO_2 nanoparticles while FTIR spectroscopy will be performed to validate surface functionalization in our synthesis conditions.

Chapter IV will present the *in situ* measurement results obtained during a study on nucleation and growth of ZrO_2 nanoparticles and, through a PDF analysis of the experimental results, understand the mechanisms responsible for metastable t-ZrO_2 stabilization. Finally, modeling of nuclei, prior to nucleation will be realized using Diffpy-complex modelling infrastructure to obtain the stable molecular configuration in the very first moments of ZrO_2 nanoparticle formation.

Chapter III

Synthesis of ZrO_2 nanoparticles in supercritical fluids: Design and control of the crystal structure

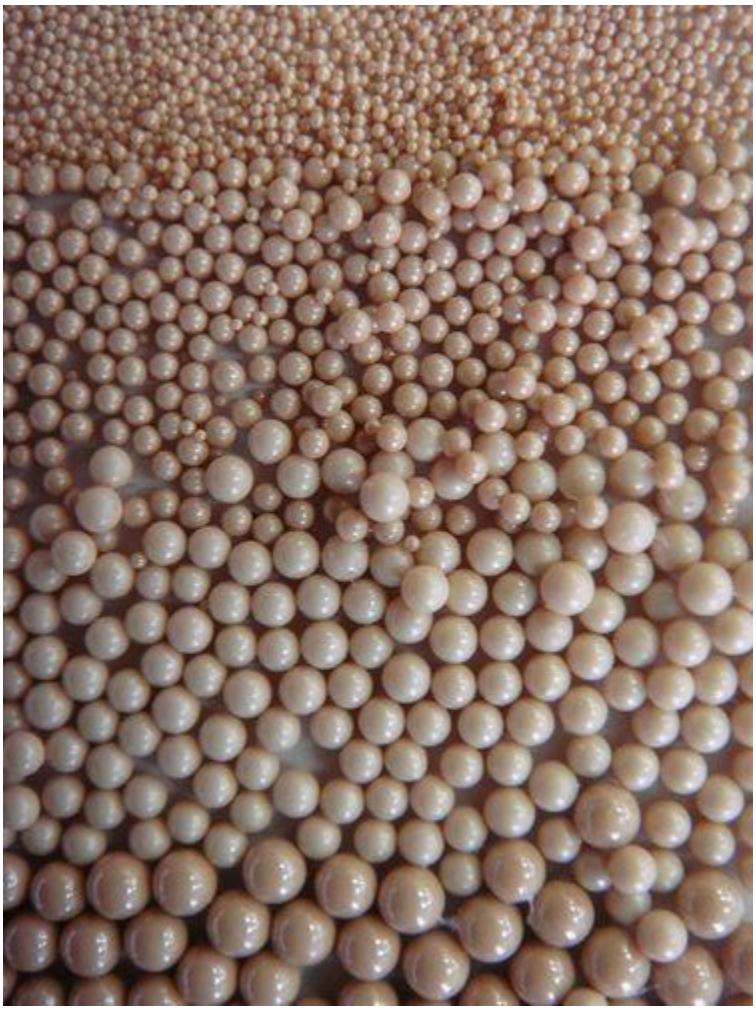

III.1 Introduction

As we have seen in chapter I, the possibility to stabilize both tetragonal (t-ZrO_2) and cubic (c-ZrO_2) ZrO_2 polymorphs at mild pressure and temperature conditions is generally achieved by substituting Zr^{4+} elements by either iso- or aliovalent elements [72, 280, 281, 282, 283]. The strain associated with the eightfold coordination is then relieved in a structure where Zr atoms tend to coordinate to 8 O atoms, thus inducing structural defects such as lattice oxygen vacancies (L.O.V.) [48, 49, 50, 61, 284].

However, the key role of size effect correlated to the nanocrystalline size in stabilizing metastable t-ZrO_2 at mild synthesis conditions for sizes ranging between 3 and 30 nm has found echo in many works [74, 285, 286, 287, 288, 289, 290]. In this size range, the combined surface free energy to the volume free energy is believed to be responsible for the stabilization of t-ZrO_2, in a crystallographic structure similar to the high temperature stable t-ZrO_2, as it tends to be lower than that of m-ZrO_2 as the particle size decreases down to 3 nm [69, 285, 291].

Other works have also emphasized that metastable t-ZrO_2 stabilization may be induced by structural similarities observed between the amorphous phase and the intermediate tetragonal crystalline structure, and that this tetragonal structure is only an intermediate to the thermodynamically stable monoclinic structure as increasing the temperature usually stabilize the monoclinic structure at temperatures far below its thermodynamic limit (≈600°C).

As stabilization of metastable t-ZrO_2 at low temperatures necessitates to adapt the proper synthesis conditions, we have therefore chosen the sol-gel chemistry as a pathway to achieve the stabilization of the metastable t-ZrO_2 structure and understand which main mechanism (creation of L.O.V., size effect or structural similarities) leads most certainly to the formation of metastable t-ZrO_2.

III.2 Synthesis of ZrO_2 nanoparticles in supercritical fluids

III.2.1 Experimental conditions

III.2.1.1 Choice in the starting materials

The choice in solvent type and metal precursor source is critical when aiming to stabilize metastable t-ZrO_2. Therefore, three types of precursors were carefully chosen after the literature

study for their ability to react differently regardless of the synthesis conditions as seen in Chapter II [15, 17, 19, 67, 217, 283, 292, 293].

Zirconium(IV) oxynitrate hydrate [$ZrO(NO_3)_2.xH_2O$] (Sigma-Aldrich, ≥ 99%); Zirconium(IV) propoxide solution, 70 wt.% in 1-propanol [$Zr(OCH_2CH_2CH_3)_4$] (Sigma-Aldrich); and zirconium(IV) acetylacetonate [$Zr(C_5H_7O_2)_4$] (Sigma-Aldrich, 97%) were used as precursors. The influence of a surface-active agent (surfactant) was also investigated with hexanoic acid [$CH_3(CH_2)_4COOH$] (Sigma-Aldrich, ≥ 99%).

Deionized water and absolute ethanol [C_2H_5OH] (Sharlau, ≥ 99.9%) were used as single solvents for the supercritical hydrothermal and B.N.H.S.G. syntheses of ZrO_2, respectively, or when mixed in a 50/50 wt. % for sol-gel like synthesis of ZrO_2, based on previous studies realized in our research group [52, 294].

The thermal decomposition of $ZrO(NO_3)_2.xH_2O$ was performed hydrothermally in supercritical water to generate a reference monoclinic structure for ZrO_2. Both $Zr(C_5H_7O_2)_4$ and $Zr(OCH_2CH_2CH_3)_4$ precursors were solvothermally decomposed in supercritical ethanol to evaluate the ability of both molecular precursors to provide metastable t-ZrO_2 in our synthesis conditions. Also, ZrO_2 was synthesized from $Zr(OCH_2CH_2CH_3)_4$ precursors in a supercritical 50/50 wt. % water/ethanol mixture to investigate the influence of pre-polymerization of an amorphous cluster network in the synthesis of ZrO_2.

III.2.2 Synthesis procedure

III.2.2.1 Preparation of the precursor solutions.

As both $ZrO(NO_3)_2.xH_2O$ and $Zr(C_5H_7O_2)_4$ solid precursor salts are not sensitive to air contamination in the course of the whole synthesis process, no special care was needed more than what is observed in the regular formal procedures followed inside a chemistry laboratory. However, as seen in Chapter I, the $Zr(OCH_2CH_2CH_3)_4$ metal alkoxide precursors are highly reactive to contamination from elements present in the surrounding atmosphere. Therefore, all reactants involved in $Zr(OCH_2CH_2CH_3)_4$ precursor solutions were stored inside a glovebox dedicated to $Zr(OCH_2CH_2CH_3)_4$ precursor solution preparations. Such precautions were systematic to avoid contamination of the injection pumps.

III.2.2.2 Apparatus and procedure

Synthesis of ZrO_2 nanoparticles from nitrate precursors was performed using the reactor presented in Chapter II-2.1.2. Proper precursor salts were weighed using a 10^{-4} g precision lab scale and inserted into a gauged flask. Deionized water was then slowly added to the precursor salts inside the flask and under moderate stirring to reach a total Zr^{4+} concentration of 10^{-2} mol/L. The chosen flow rate was equal to 8 mL/min, and p, T conditions set to 25 ± 1 MPa and 400 ± 2°C, thus a residence time for this reaction equal to 30 s, determined from Equation (II − 1). Thermal quenching of the nanoparticle growth was realized by flowing the nanoparticle suspension through an ice-cooled stainless-steel tubing downstream the reactor prior to recovering the powder in the polar solvent.

III.3 Results

III.3.1 Structural analysis of synthesized ZrO_2

III.3.1.1 Crystalline structure of ZrO_2 synthesized in supercritical water

ZrO_2 powder A recovered after the synthesis was filtered through a Büchner apparatus and washed several times using deionized water, centrifuged to rid the surface of impurities and finally dried. The obtained powders were then sieved using a 100 µm sieve prior to XRD analysis. The routine XRD pattern of powder A shown in Figure III-1 was collected at room temperature using the Cu Kα_1 wavelength.

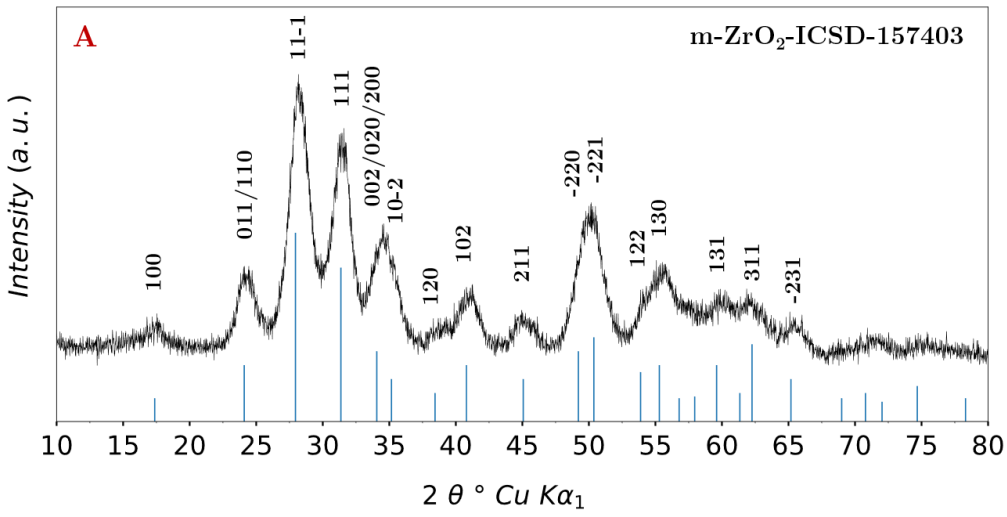

Figure III-1. XRD pattern for ZrO_2 synthesized in supercritical water from $ZrO(NO_3)_2.xH_2O$ at 25 MPa and 400°C. The residence time was 30 s. The Miller index and the main Bragg reflections are displayed above and below the XRD pattern, respectively.

The Reynolds number determined for this synthesis was ≈ 3100, thus indicating a turbulent flow regime during this synthesis. As expected, ZrO_2 synthesized in supercritical water exhibits purely the monoclinic crystal structure (m-ZrO_2) with no extra peaks arising from another phase. The A.C.S. determined from Rietveld analysis realized on the Fullprof_Suite package on this sample was 7.1 nm and the lattice constants a_m = 5.1522 ± 0.0011 Å, b_m = 5.1999 ± 0.0010 Å, and c_m = 5.3083 ± 0.0011 Å, and the angle β between the a and c directions equal to 98.966 ± 0.009°. The lattice constants for powder A are extremely close to those from the model (a_m = 5.1514(4) Å, b_m = 5.2098(4) Å, and c_m = 5.3204(4) Å, and β = 99.171(3)°), meaning that the nanoparticles are well crystallized.

III.3.1.2 Crystalline structure of ZrO_2 synthesized in supercritical water/ethanol mixture

Preparation of the alkoxide precursor solution was realized inside a dedicated glovebox under argon (Ar) atmosphere where the proper volume of precursor molecules was pipetted, using a micropipette, inside a gauged flask. The necessary volume of absolute ethanol to reach a total Zr^{4+} concentration of 10^{-2} mol/L was then added to the flask which was then recapped and left under moderate stirring inside the glove box until the reaction was started.

Synthesis of ZrO_2 nanoparticles in the supercritical water/ethanol mixture and from alkoxide precursors as starting material (powder B) was the only one performed using 2 injection lines as discussed in Chapter II-2.1.2. This 50/50 wt. % water-ethanol supercritical mixture is now commonly used in our research group to synthesize via the sol-gel method ≈ 20 nm large $BaTiO_3$, $Ba_{1-x}Zr_xTiO_3$ ($0 \leq x \leq 1$) and $Ba_{1-x}Sr_xTiO_3$ ($0 \leq x \leq 1$) nanoparticles at a relatively large scale [5, 52, 294, 163]. The p, T conditions inside the reactor were also set to 25 ± 1 MPa and 400 ± 2°C. The chosen flow rate for the precursor solution in absolute ethanol injected in the first line was 3.25 mL/min, while the flow rate of preheated water ($T_{PREHEATER}$ = 250°C) in the second injection line was 4 mL/min, thus a residence time of 30 s for this reaction to compare the crystal structure, size and dispersity of the nanoparticles in powder B with those in powder A obtained in supercritical water. At the mixing point right before the reactor hot zone, the temperature was T_{MIX} = 150 ± 2°C. During the reaction, the precursor solution was placed under magnetic stirring and argon flow to prevent contamination and thus prehydrolysis of the precursor solution inside the solution tank. Figure III-2 shows the XRD pattern of powder B collected at room temperature with the Cu Kα_1 wavelength.

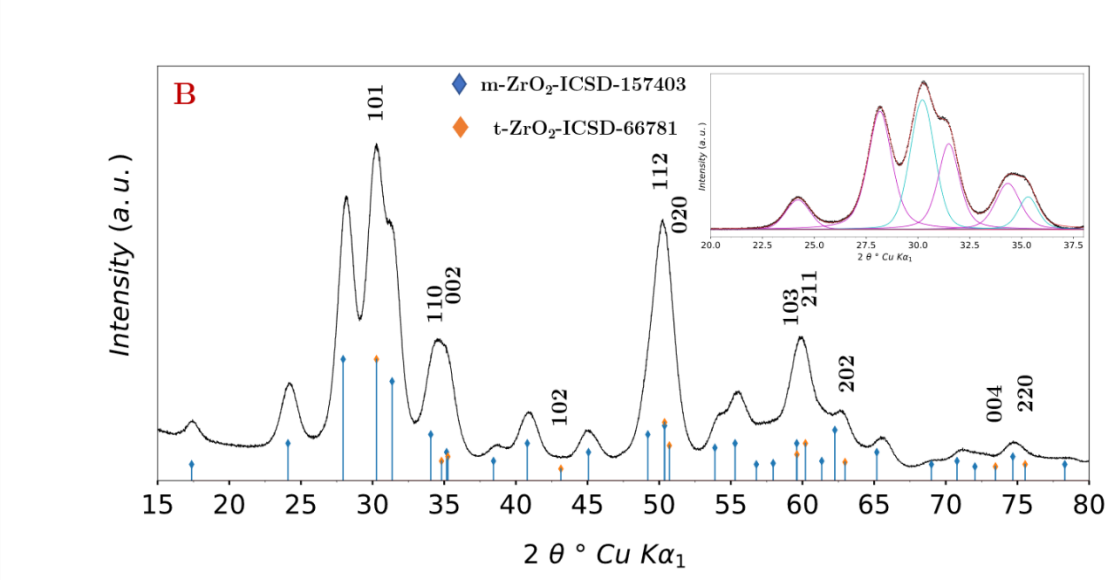

Figure III-2. XRD pattern for ZrO_2 synthesized in supercritical water/ethanol mixture, in 30 s and from $Zr(OCH_2CH_2CH_3)_4$ precursor at 25 MPa and 400°C. The Miller index and corresponding main Bragg reflections (orange diamonds) are displayed, for the t-ZrO_2 structure, above and below the XRD pattern, respectively. The main Bragg reflections for the m-ZrO_2 structure are displayed below the XRD pattern (blue diamonds). The inset in the $20 < 2\theta < 37.5°$ range is a decomposition of t-ZrO_2 (cyan) and m-ZrO_2 (magenta) contributions to the total diffraction signal collected.

The Reynolds number determined for this synthesis was ≈ 2600, thus indicating that the fluid was subject to an intermediate flow regime. This difference in hydrodynamic regimes was imposed by the experimental set-up used. The XRD pattern for powder B reveals the presence of two crystal structures identified as m-ZrO_2 (major phase) and t-ZrO_2 (minor phase). The presence of the tetragonal structure inside the final powder is clearly visible through the $(101)_t$ Bragg reflection at 30.3°. Rietveld analysis on this sample determined a m-ZrO_2 to t-ZrO_2 molar ratio of 2 between the two structures in the final powder mixture. The A.C.S. obtained for both m- and t-ZrO_2 were 6.1 and 4.7 nm, respectively, encompassed in the critical size range for the stabilization of metastable t-ZrO_2 [74, 285, 286, 287, 288, 289, 290]. The refined lattice constants of the major crystal structure, m-ZrO_2, are very close to those of the model used with a_m = 5.1548 ± 0.0003 Å; b_m = 5.2059 ± 0.0003 Å and c_m = 5.3271 ± 0.0004 Å. For t-ZrO_2, the refined lattice parameters are $a_t = b_t$ = 3.6002 ± 0.0002 Å, and c_t = 5.1867 ± 0.0003 Å, also very close to those of the model ($a_t = b_t$ = 3.5960(1) Å and c_t = 5.1841(2) Å).

The fit in the inset of the XRD pattern is a deconvolution of m-ZrO_2 and t-ZrO_2 contributions to the total diffracted signal. The fit was performed using the Fityk 1.0.2 software with Pseudo-Voigt type functions for each fitted diffraction peak after the baseline was subtracted from the signal. The following parameters were allowed to vary during the refinements: the integrated area underneath each peak; the position of the intensity maxima (2θ position); the half width at half max (HWHM) and the shape of the function. From the integrated areas obtained for the most intense Bragg reflections of each structure, the molar fraction of both monoclinic and tetragonal structures was determined using Equation (III − 1),

$$X_t = \frac{I\,(101)_t}{I\,(101)_t + I\,(11-1)_m + I(111)_m} \qquad \text{(III} - 1\text{)}$$

where X_t is the t-ZrO_2 molar fraction inside the synthesized powder, $I\,(101)_t$ is the total integrated area under the (101) t-ZrO_2 Bragg reflection, $I\,(11-1)$ and $I\,(111)$ are the total integrated areas under the $(11-1)_m$ and $(111)_m$ m-ZrO_2 Bragg reflections, respectively. From this, the m-ZrO_2 molar fraction was estimated as $X_m = 1 - X_t$. The estimated t-ZrO_2 molar fraction was 30 (mol. %, giving a m-ZrO_2 to t-ZrO_2 ratio of 2.3 which is in relatively good agreement with 2 obtained from the Rietveld refinement performed on this powder.

As nanoparticles in powder B display lattice constants very close to those of the models, we may believe that they have achieved a high level of crystallinity. The large proportion of m-ZrO_2 in powder B is believed to result from the pre-polymerization of m-ZrO_2 clusters at the

mixing point (T_{MIX} = 150°C) where the presence of water at mild conditions (p = 25 MPa; T_{MIX} = 150°C) favors the formation of nuclei with local structures close to m-ZrO_2, thus facilitating ZrO_7 polyhedra packing [295]. Mixtures of m- and t-ZrO_2 structures have already been observed, but only qualitatively monitored through variations in $(101)_t$, $I\,(11-1)_m$ and $I\,(111)_m$ Bragg reflections, in a supercritical isopropyl alcohol and water mixture, where water was added in very small proportions to assure complete precursor condensation [15]. The authors concluded on the incapacity to synthesize pure t-ZrO_2 even when nanoparticles were only 5 to 6 nm, though however structural contents could be manipulated by varying experimental parameters such as temperature, pressure, solvent and precursor types.

III.3.1.3 Crystalline structure of ZrO_2 synthesized in supercritical ethanol

To achieve higher t-ZrO_2 proportions in the final powders, syntheses were performed in supercritical ethanol using $Zr(C_5H_7O_2)_4$ and $Zr(OCH_2CH_2CH_3)_4$ precursor sources for powders C and D, respectively. The aim was to find a precursor type that would allow us to obtain pure or quasi pure t-ZrO_2 nanoparticles. For this, two B.N.H.S.G. reactions with different kinetics expected were performed: synthesis through solvolysis and condensation of propoxide precursors, believed to be relatively slow compared to the one performed with acetylacetonate precursors where ligand exchange is expected. The same experimental p, T conditions as for the synthesis presented in III-3.1.1 were maintained, as well as precursor concentrations. While the use of acetylacetonates did not require special precautions during the preparation and synthesis, the use propoxide precursors did on the other hand as for the previous synthesis depicted above. Figures III-3 a and b show the XRD pattern of powders C and D, respectively. The XRD pattern for powder C (Figure III-3 a) was collected at room temperature with the Cu $K\alpha_1 K\alpha_2$ wavelengths. The one for powder D (Figure III-3-b) was collected at room temperature using the Cu $K\alpha_1$ wavelength only, however.

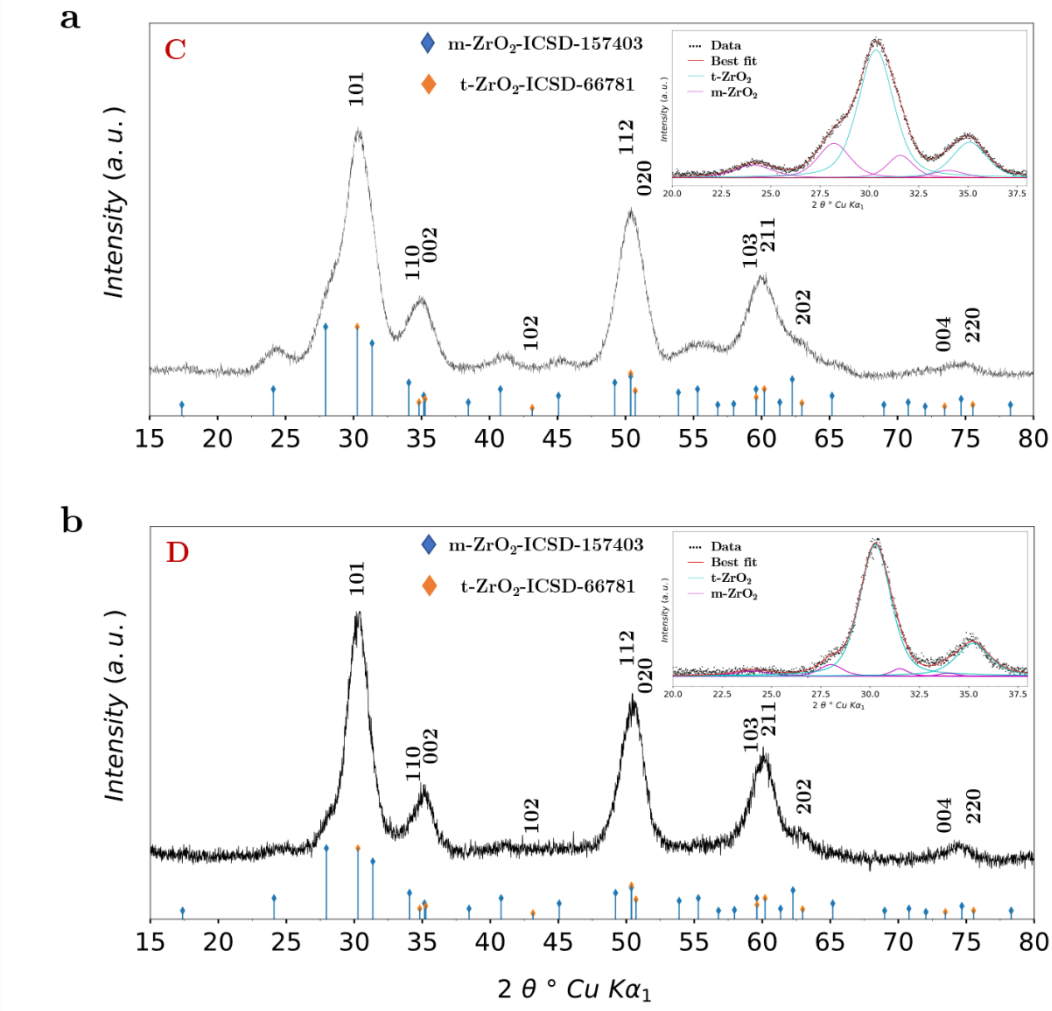

Figure III-3. a and b represent XRD patterns of ZrO_2 synthesized in supercritical ethanol from $Zr(C_5H_7O_2)_4$ and $Zr(OCH_2CH_2CH_3)_4$ precursors, respectively. Blue and orange diamonds represent the model Bragg reflections for m- and t-ZrO_2, respectively. For clarity, are only indexed the major t-ZrO_2 Miller indexes. The inset in the $20 < 2\theta < 37.5°$ range for each pattern is a deconvolution of t-ZrO_2 (cyan) and m-ZrO_2 (magenta) contributions to the total diffraction signal recorded.

The Reynolds number determined for this synthesis was ≈ 1500, thus indicating a laminar flow regime during this synthesis. This difference in hydrodynamic regime with the 2 previous syntheses is due to the difference in fluid densities under supercritical conditions and was imposed by the experimental set-up used. However, it is noteworthy that these conditions allowed formation of uniformly distributed ZrO_2 nanoparticles as will later be seen in section III-5.7.

The XRD patterns in Figure III-3 reveal a drastic change in m- and t-ZrO_2 structure proportions when comparing to ZrO_2 synthesized in the supercritical water/ethanol mixture. In both

experiments presented in Figure III-3 a and b, t-ZrO_2 is the major phase obtained in the powders. This observation is emphasized by the fits performed on Fityk 1.0.2 and displayed in the inset of each XRD pattern where, though the contribution of the $(011)/(110)_m$, $(11-1)_m$, $(111)_m$ and $(002)/(020)/(200)_m$ Bragg peaks at 24.1, 28.2, 31.6 and 34° are still largely present in powder C (Figure III-3 a), almost only the $(11-1)_m$ Bragg reflection is visible in the inset of Figure III-3 b. Also, for powder D (Figure III-3 b), the shape of the $(101)_t$ peak at 30.3° is quasi symmetrical and the only traces of m-ZrO_2 in those powders are slightly visible at 17.4, 24.1, 40.8 and 45.1°.

The t-ZrO_2 A.C.S. obtained from the Rietveld refinements were both 3.9 nm for powders C and D. Concerning the m-ZrO_2 A.C.S., 3.3 and 3.9 nm were reported for powders C and D, respectively.

For powder C, the lattice constants of the major phases are $a_t = b_t = 3.6038 \pm 0.0005$ Å and $c_t = 5.1698 \pm 0.0013$ Å. For the m-ZrO_2 structure, $a_m = 5.1680 \pm 0.0016$ Å, $b_m = 5.2024 \pm 0.0015$ Å and $c_m = 5.3306 \pm 0.0015$ Å.

The Rietveld refinement for powder D reveals lattice constants for the major phase of $a_t = b_t = 3.5985 \pm 0.0006$ Å and $c_t = 5.1476 \pm 0.0018$ Å, while those for m-ZrO_2 are $a_m = 5.1535 \pm 0.0055$ Å, $b_m = 5.1629 \pm 0.0056$ Å and $c_m = 5.3671 \pm 0.0045$ Å. It may be important to note the increasing uncertainties in the lattice parameters for both structures, which can be related to the smaller crystallite size of ZrO_2 nanoparticles and related increasing uncertainty of the Rietveld method on small nanoparticles.

Though the lattice parameters for m-ZrO_2 in powder C are very close to those of the model, those of powder D however tend to diverge from the model used. Also, for this structure, the difference in a_m and b_m lattice parameters is only 0.2 %, and the difference between the a_m/c_m and b_m/c_m is 4.1 and 3.9 %, respectively. This monoclinic structure could be similar to an enlarged tetragonal structure in the *a* and *b* directions and with a β-angle tilted of 99.99°. Also, for t-ZrO_2, estimated contractions in the c direction of 0.3 and 0.7 % are observed for powders C and D, respectively. These observations can directly be related to the lattice expansion and contraction phenomena that generally accompany the decrease in crystallite size [56, 62, 296].

The molar fractions for both syntheses where estimated by Rietveld refinements and Equation $(III-1)$. Regarding the Rietveld results, 53 and 82 mol % of t-ZrO_2 in powders C and D, respectively, while 58 and 74 mol. % were determined from Equation $(III-1)$ for powders C and D, respectively. The relatively good agreement between both quantification methods (difference of less than 10 %) allows us to believe that the propoxide precursor source is probably appropriate to stabilize preferentially the metastable t-ZrO_2 structure between the

chosen reactional systems. Indeed, many works have emphasized the importance of OH structural defects to stabilize metastable t-ZrO_2 [80, 216], and the fact that they may be provided in higher concentrations during sol-gel syntheses [29, 126].

III.3.2 Local probing of synthesized ZrO_2 nanoparticles

As Raman spectroscopy is sensitive to the displacement of light elements such as oxygen inside the crystal lattice, it is therefore a reliable technique to characterize precisely crystal structures locally. Hence, to corroborate structural observations made by Rietveld analysis and Equation (III − 1), Raman spectroscopy was performed on ZrO_2 powders A, B, C and D. As it was discussed in Chapter II, according to group theory 18 Raman active modes are predicted for the monoclinic structure ($9A_g + 9B_g$) and only six for the tetragonal structure of ZrO_2 ($1A_g + 2B_g + 3E_g$). Many works on structural characterization of ZrO_2 have been realized [74, 297, 298, 299, 300] and were the basis for the assignment of our Raman spectra.

III.3.2.1 t-ZrO_2 purity

In analogy to XRD structural determination, t- and m-ZrO_2 proportions can be well estimated by the intensity of the two main and most intense active modes of each structure. These are located for t-ZrO_2 at ≈ 150 and 270 cm^{-1}, and ≈ 180 and 190 cm^{-1} for m-ZrO_2. The molar fraction of t-ZrO_2 can be estimated by Raman spectroscopy using Equation (II − 2) [301]:

$$X_t = \frac{I_t\,(150\ cm^{-1}) + I_t\,(270\ cm^{-1})}{I_t\,(150 cm^{-1}) + I_t\,(270\ cm^{-1}) + I_m\,(180\ cm^{-1}) + I_m\,(190\ cm^{-1})} \qquad (\text{III} - 2)$$

where X_t is the t-ZrO_2 molar fraction inside the synthesized powder, $I_t\,(150\ cm^{-1})$ and $I_t\,(270\ cm^{-1})$ the total integrated areas under the active modes at the corresponding wavenumbers for t-ZrO_2, $I_m\,(180\ cm^{-1})$ and $I_m\,(190\ cm^{-1})$ those for m-ZrO_2. From Equation (II − 2), the m-ZrO_2 molar fraction was estimated as X_m = 1-X_t. Figure III-4 shows the Raman spectra of powders A, B, C and D in the 125-915 cm^{-1} range.

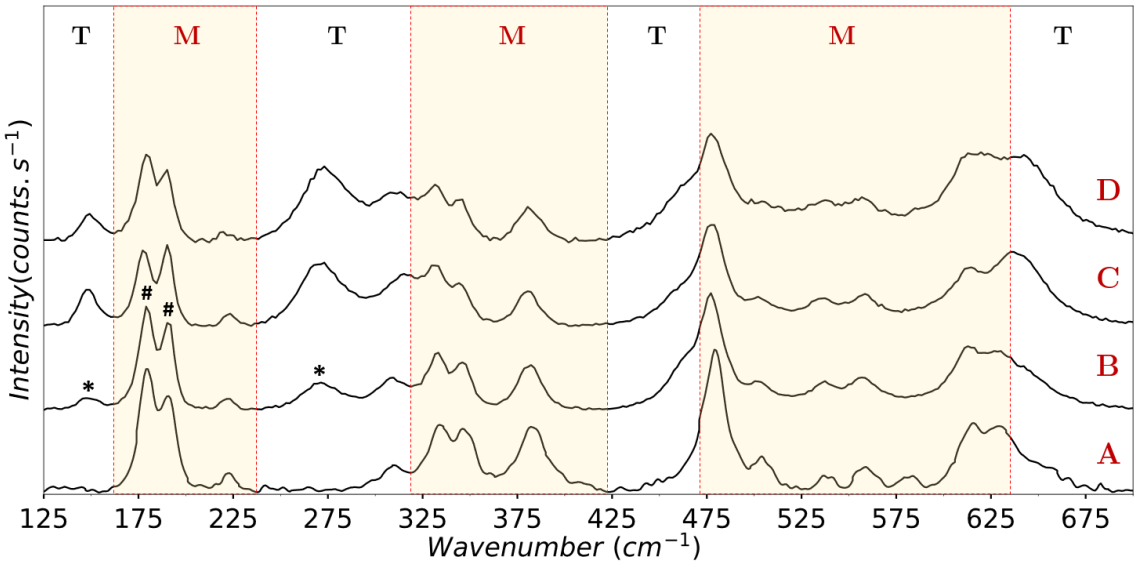

Figure III-4. Raman spectra for powder A; B, C and D. Tetragonal and monoclinic domains are labeled as T and M, respectively, and Raman active modes used for the structural proportions quantification indexed with **(*)** and **(#)** for the t- and m-ZrO_2 structures, respectively.

In Figure III-4, all powders exhibit a mixture of t- and m-ZrO_2 structures except powder A, which displays purely the monoclinic structure with active modes located at 180,190, 215, 330, 34, 380, 475, 500, 530, 555, 575, 610 and 620 cm^{-1} and no active modes visible in all tetragonal domains (150, 270, 310, 460, 630 cm^{-1}). However, powders B, C and D are all characterized by different weights on t-ZrO_2 active mode intensities at 150 and 270 cm^{-1} relatively to m-ZrO_2 modes at 180 and 190 cm^{-1}. Also, in the 250-400 cm^{-1} domain, all three m-ZrO_2 mode intensities dramatically decrease while both tetragonal modes at 270 and 310 cm^{-1} increase.

The broadening of the peaks in Figure III-4 is attributed to disorder inside the crystal structure as the result of the small crystallite size, and this even for the monoclinic structure. Also the increasing background as the proportion of t-ZrO_2 increases may be related to the increase of disorder in the oxygen sublattice [301], which generally results in m-ZrO_2 modes converging in pairs to become doubly degenerate E modes. This phenomenon is clearly visible in the 300-350 and 500-580 cm^{-1} domains.

Refinements shown in Figure III-5 were performed on Fityk software with Pseudo-Voigt type functions and areas were determined using Equation (II − 2).

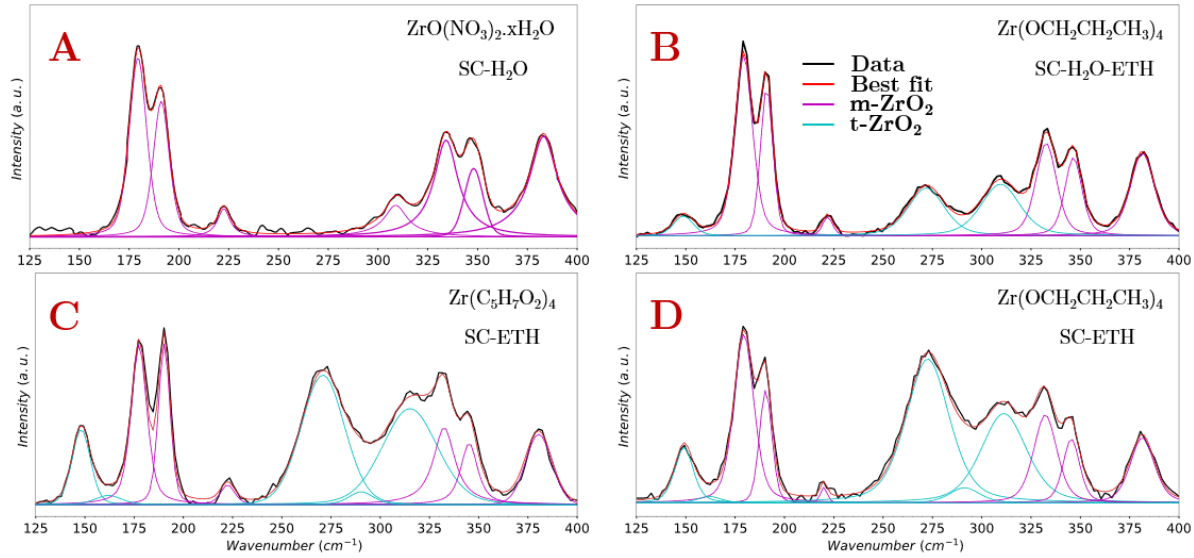

Figure III-5. Fits performed on Fityk for powders A, B, C, and D to estimate the t- and m-ZrO_2 structure proportions in each powder.

The estimated t-ZrO_2 molar fractions determined from Raman quantification using Equation (II – 2) were 0, 30, 53 and 71 mol. % for samples A, B, C and D, respectively. These estimations are relatively in good agreement with mol. % obtained for samples A, B, C and D from both Rietveld refinements and Equation (II – 2).

III.3.3 Size and size distribution of ZrO_2 nanoparticles

To understand if these structural variations may be in some way correlated to the nanoparticle size or synthesis procedure, the A.C.S were observed under a transmission electron microscope (powder A) and high-resolution transmission electron microscope (powders B, C and D) as shown in Figure III-6.

In Figure III-6, under each microscope image are represented individual particles and below, on the left-hand side is a plot of the A.C.S. and corresponding standard deviations for each powder while on the right-hand side is a diffraction image of powder B nanoparticles. Particle counts were performed on ImageJ software on a minimum of 70 diffracting domains in order to decrease the uncertainty on A.C.S.

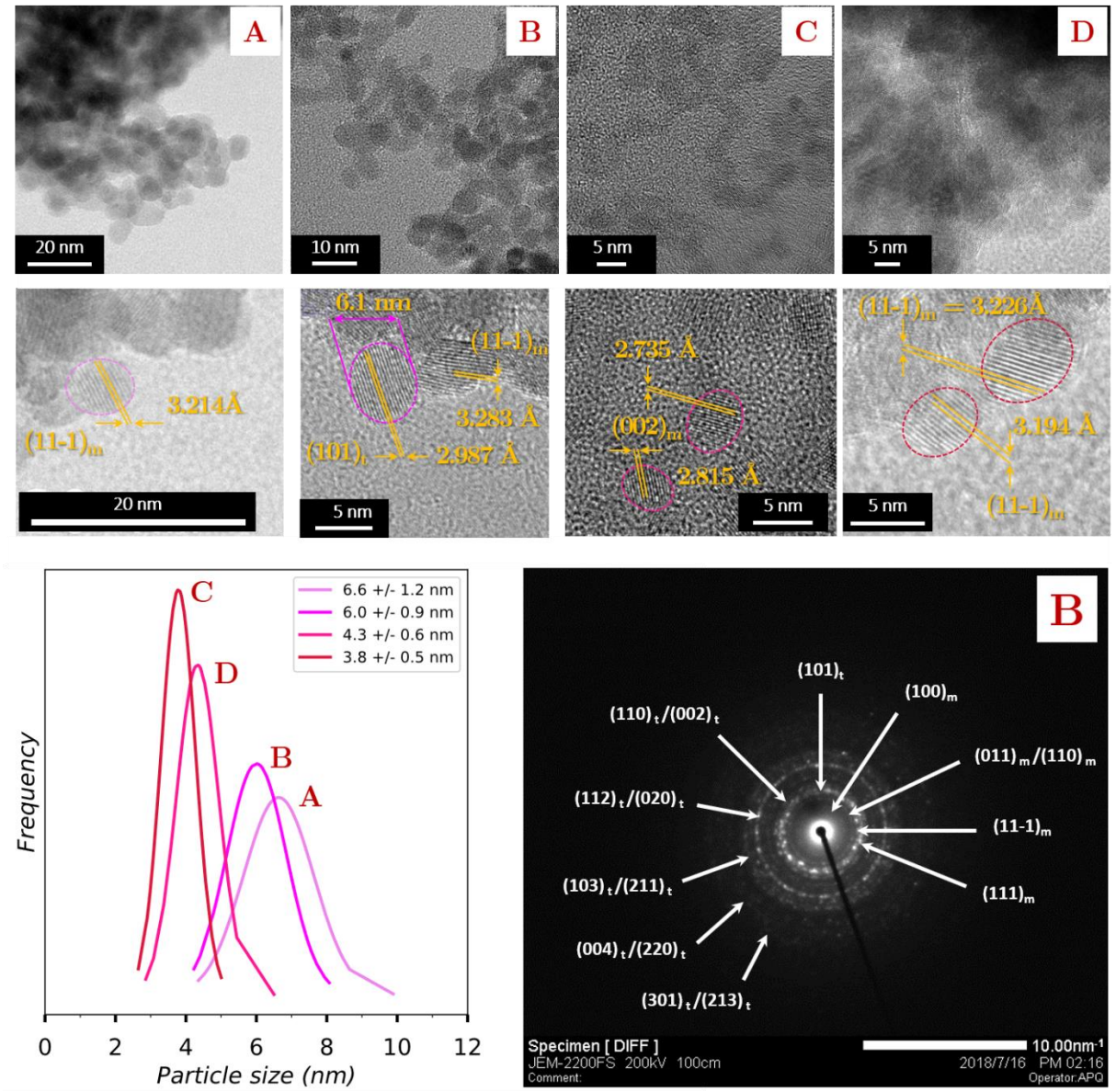

Figure III-6. A: TEM image of powder A; B, C and D: HRTEM images of powders B, C and D; zooms on individual nanoparticles corresponding to each powder and their corresponding A.C.S. and standard deviations plotted. A diffraction image for powder B is also displayed with both t- and m-ZrO_2 diffraction rings indexed.

The TEM images reveal that all ZrO_2 particles are quasi-spherical and exhibit a narrow size distribution and that the powders containing the largest proportions of m-ZrO_2, powders A and B, being those that exhibit the largest A.C.S and size distribution with 6.6 ± 1.2 nm and 6.0 ± 0.9 nm, respectively. The smallest correspond to powders C and D with 3.8 ± 0.5 nm and 4.3 ± 0.6 nm, respectively. Also, the A.C.S. obtained from both Rietveld analysis and TEM match nicely, indicating the nanocrystalline nature of the particles. Though, in Figure III-6, the zoomed and indexed nanoparticles display for the majority the monoclinic $(11-1)_m$ and

$(002)_m$ lattice planes (powders A, C and D), a nanoparticle exhibiting the $(101)_t$ diffracting plane is visible for powder B.

Table III-1 lists all the structural and size observations made on samples A, B, C and D.

Table III-1. Summary of observations on powders A, B, C and D.

Powder	A.C.S.			m-ZrO_2 mol. %		
	TEM (nm)	Rietveld (nm)		Rietveld	Raman	Equation III-1
		m-ZrO_2	t-ZrO_2			
A	6.6 ± 1.2	7.1		100	100	100
B	6.0 ± 0.9	6.1	4.7	67	70	70
C	3.8 ± 0.5	3.3	3.9	47	47	42
D	4.3 ± 0.6	3.9	3.9	18	29	26

From Table III-1, one can clearly see that all three methods to determine m- and t-ZrO_2 proportions in powders A, B, C and D give similar results even though the amount determined by Rietveld analysis for powder D (18 mol. %) is significantly smaller than those obtained from Equations $(\mathrm{III}-1)$ and $(\mathrm{III}-2)$ with 26 and 29 mol. %, respectively. Also, A.C.S. obtained by both Rietveld analysis and TEM observations are in good agreement for all powders. Finally, between powders A and C the amount of m-ZrO_2 in the final powders decreases with decreasing A.C.S.; while powder C seems to contain more m-ZrO_2 than powder D for similar A.C.S.

From these first observations, it is difficult to conclude on the metastable t-ZrO_2 stabilization mechanism from either the size effect or reactional pathway considerations. Indeed (i), all samples are in the 3-30 nm size range generally reported as necessary to favor the formation of metastable t-ZrO_2 nanoparticles [286, 290, 302, 303] (ii), a general tendency to favor t-ZrO_2 formation as the A.C.S. decreases seem plausible from these first observations but (iii), all powder result of different synthesis conditions

It seems that if only the decrease in A.C.S. was a preponderant factor in choosing a reactional system, synthesis of ZrO_2 nanoparticles would be performed in supercritical ethanol and with $[Zr(C_5H_7O_2)_4]$, however, as both Rietveld analysis and Raman spectroscopy distinguish powder D as the one containing the least m-ZrO_2 proportions, $Zr(OCH_2CH_2CH_3)_4$ and supercritical ethanol were chosen as the precursor and solvent types for all subsequent experiments in this work. Even though the alkoxide precursor source did not allow the formation of the smallest nanocrystallites, it nevertheless enabled the formation of ZrO_2 ultrafine nanoparticles exhibiting

the highest tetragonal structure proportions, which is generally reported in literature concerning N.H.S.G. synthesis of ZrO_2 [75, 127, 135, 138, 286].

III.4 Downsizing ZrO_2 nanoparticles

III.4.1 Overview of the strategy

In the previous section, we identified both precursor and solvent types to further study the mechanisms responsible for metastable t-ZrO_2 stabilization at low p and T conditions. $Zr(OCH_2CH_2CH_3)_4$ and ethanol (powder D) were thus chosen among other reactants and solvents to further the study by (i), changing the precursor concentration and (ii), functionalizing the nanoparticle surfaces using surfactants. These two strategies will be presented in next sections, where the same nanoparticle characterization procedure will be followed. Figure III-7 shows the two strategies followed to obtain the smallest possible ZrO_2 nanoparticles in our synthesis conditions.

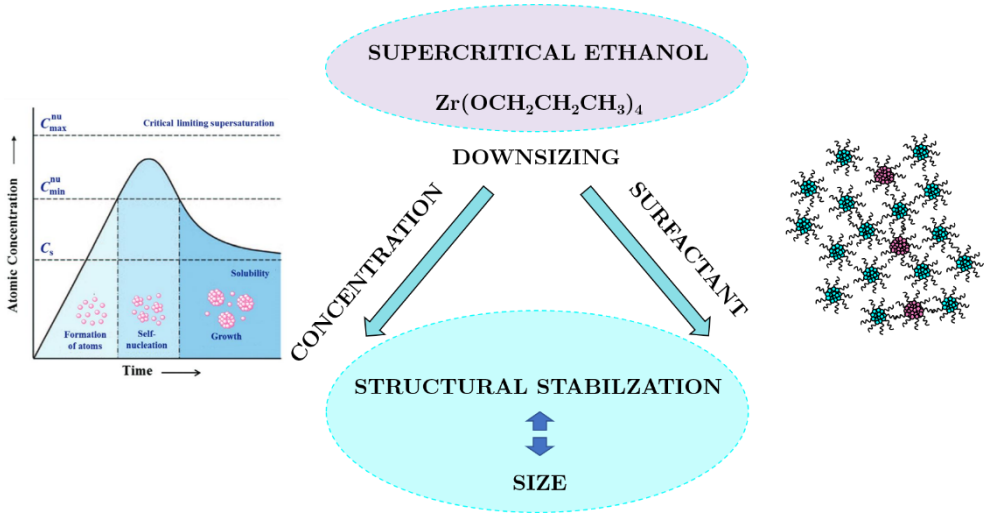

Figure III-7. Strategy chosen to identify the mechanism responsible for stabilization of metastable tetragonal ZrO_2.

Two types of routes were followed to synthesize ZrO_2 nanoparticles below the estimated critical size encompassed in the rather large 3-30 nm size range [18, 64]. First of all, varying the precursor concentration was investigated to favor self-nucleation in supercritical conditions. This method allows to maintain the system in supersaturation conditions in the given period of reaction time (residence time). As the LaMer model tells us, maintaining supersaturation conditions in the

reaction media can be realized by varying both precursor concentration or residence time. Therefore, varying the reaction residence time was also investigated. In addition to the 30 seconds residence time presented previously, 15 and 45 seconds were investigated. Unfortunately, while 15 s were not sufficient for the reaction to occur at the different concentrations, 45 s led inevitably to clogging of the reactor within minutes for the lowest concentration investigated. Therefore, a 30 s residence time was maintained for all subsequent experiments.

The second route tested was grafting surface modifiers and thus, hinder the growth of ZrO_2 nanoparticles. For this, carboxylic acids proved to be effective throughout many works [67, 75, 127], thus hexanoic acid (HA) was chosen rather than oleyamine or trioctylphosphine (TOP), to impede progress in the early stages of ZrO_2 nanocrystallite growth as it has not yet been reported. However, *in situ* measurements will be introduced in Chapter IV where TOP was introduced in the reactional media to act as a surface modifier.

III.4.2 Playing with the supersaturation conditions

III.4.2.1 Influence of concentration on the evolution of ZrO_2 structure

Four different concentrations were investigated: 0.01, 0.033, 0.066 and 0.1 mol/L. However, the 0.1 mol/L concentration induced clogging of the reactor within minutes and therefore the resulting powders could not be characterized owing the insignificant quantities obtained. Figure III-8 displays the XRD patterns for ZrO_2 synthesized from starting precursor concentrations of 0.01, 0.033 and 0.066 mol/L, further labeled as powders D, E and F, respectively. P and T conditions of 25 MPa and 400°C were maintained to compare the following results to powder D obtained in the previous section.

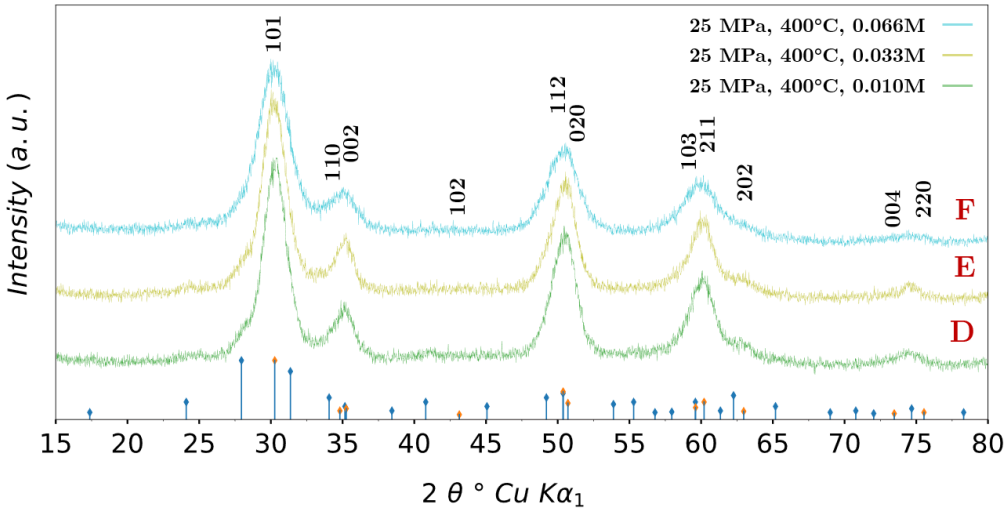

Figure III-8. XRD patterns of ZrO_2 powders synthesized in our synthesis conditions by varying the precursor concentration. The synthesis of powders D, E, and F were performed with precursor concentrations of 0.01, 0.033 and 0.066 mol/L, respectively.

All three XRD patterns displayed in Figure III-8 exhibit both intense t-ZrO_2 and weak m-ZrO_2 Bragg reflections. However, the change in peak breadth between powders D and E is relatively insignificant while clearly visible between powders D and F on all ZrO_2 Bragg reflections meaning a small decrease in A.C.S. achieved for powder E but larger in powder F. Also, the $(11-1)_m$ m-ZrO_2 reflection at 27.9° remains strongly visible only in powders D and E while the $(011)_m/(110)_m$, $(102)_m$ and $(400)_m/(014)_m$ m-ZrO_2 reflections at 24.1, and 40.7, and 74.6°, respectively seem to disappear with increasing precursor concentration. A.C.S. obtained by Rietveld refinements on powders E were 4.2 and 3.7 nm for m- and t-ZrO_2, respectively, while those obtained for powder F were 3.9 and 2.8 nm for m- and t-ZrO_2, respectively. The m-ZrO_2 proportions estimated by Rietveld analysis were 17 and 15 mol. % for powders E and F, respectively compared to 18 mol. % obtained for powder D.

These first results clearly show that the increase in $[Zr^{4+}]$ only has a slight impact on t-ZrO_2 A.C.S of powder E but clearly impacted that of powder F. Also, and though we must remain critical of the absolute validity of Rietveld analysis on such small nanoparticles and data quality, increasing supersaturation conditions attained inside the reactor for these syntheses favored homogeneous nucleation relatively to growth, leading to a general decrease in the crystallite size, thus favoring furthermore the formation of t-ZrO_2 as we were expecting as this phenomenon is generally observed in supercritical syntheses.

III.4.3 Surfactant assisted syntheses of ZrO_2

Fourier transform infra-red spectroscopy (FTIR) measurements were performed to evaluate the effectiveness and impact of surface functionalization over the synthesized ZrO_2 nanoparticles**.** Figure III-9 shows the FTIR spectra obtained for powders E, G and H containing 1:0, 1:6 and 1:12 $[Zr^{4+}]$:[HA] molar ratios, respectively.

The introduction of surfactants to the precursor solution should favor even further a decrease in A.C.S. From the concentration series (powders D, E and F), we have seen that a Zr^{4+} concentration of 0.066 mol/L enabled the formation of the smallest nanoparticles since further increase in $[Zr^{4+}]$ could not be achieved in our synthesis conditions. However, for technical reasons, further investigations were pursued on the basis of powder E ($[Zr^{4+}]$ = 0.033mol/L).

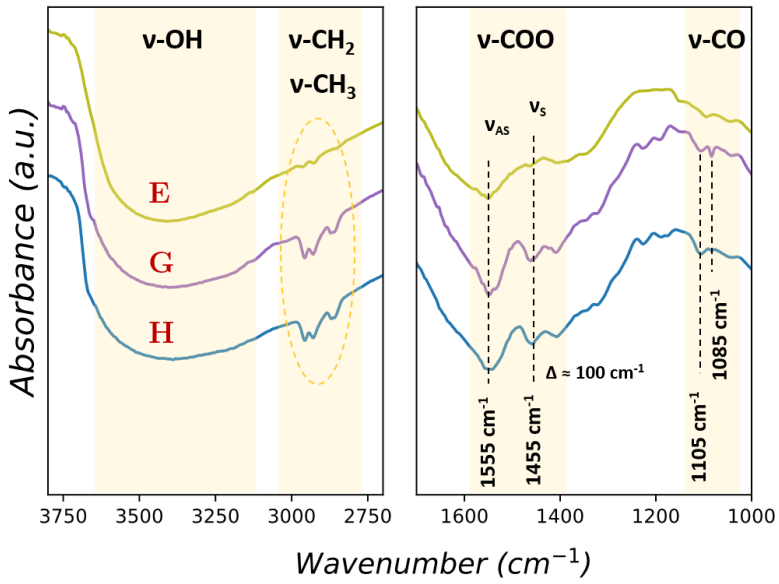

Figure III-9. FTIR spectra, in the 2700-3800 cm^{-1} and 1000-1700 cm^{-1} domains, obtained for powders E, G and H.

The effectiveness of functionalization is clearly visible in the 2800-3000 cm^{-1} region where CH_2 and CH_3 stretching vibrations are more intense on the functionalized powders (G and H) while they are hardly visible for the non-functionalized powder (E). However, between powders G and H, the intensity of the stretching vibrations does not differ as the amount of hexanoic acid is increased from 1:6 to 1:12. The 1400-1600 cm^{-1} and 1080-1120 cm^{-1} domains, which are representative of -COO and -CO stretching vibrations, respectively also indicate the effectiveness of the functionalization procedure. The difference Δ_ν of ≈ 100 cm^{-1} between the

antisymmetric (ν_{AS}-COO) and symmetric (ν_S-COO) vibrations of the carboxylate groups at 1555 and 1455 cm^{-1}, respectively is the result of a chelating bidentate type interaction between the carboxylate function and surface oxides in metal oxides [21, 304, 305, 306]. The -CO stretching vibrations evidenced at the surface of functionalized powders at 1105 and 1085 cm^{-1} may be attributed to alkoxides bound to the surface of ZrO_2 nanoparticles [307, 308], resulting from either alcohol moieties (mainly ethoxides) or ligands from the precursor (propoxides).

III.4.3.1 Influence of the surfactant on the evolution of ZrO_2 structure

As carboxylic acids are commonly used with the purpose of decreasing A.C.S. by interacting with oxide surfaces, the use of hexanoic acid (HA) was investigated in a series of experiments based on $[Zr^{4+}]$ = 0.033 mol/L (powder E) as the reference concentration for this series of experiments. The following $[Zr^{4+}]$ to [HA] molar ratios were chosen for this set of experiments: [1:0]; [1:6] and [1:12], represented by powders E; G and H, respectively, and the respective XRD patterns obtained for this series of experiments are represented in Figure III-10.

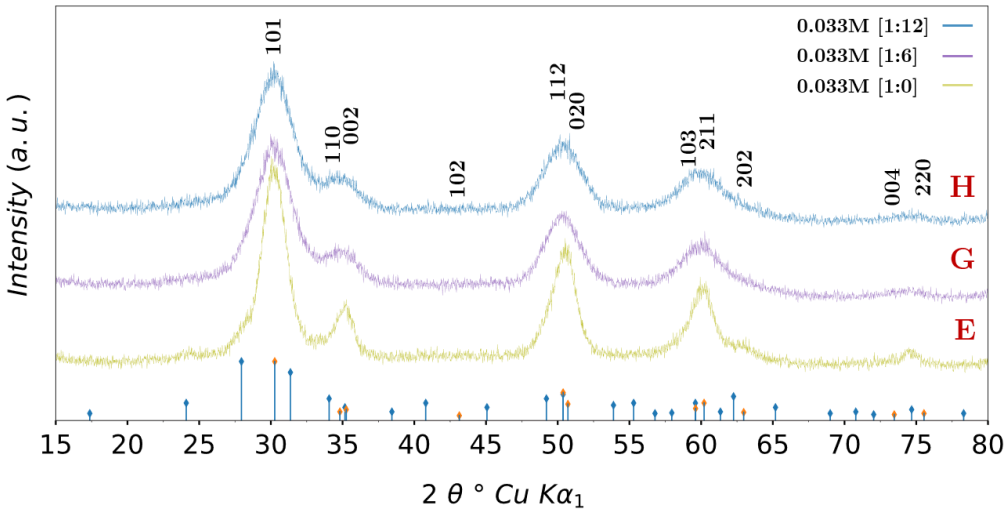

Figure III-10. XRD patterns of powders E, G and H synthesized in our synthesis conditions by varying the precursor to surfactant molar ratios.

The most striking difference between powders E, and both G and H is the total absence of Bragg reflections corresponding to m-ZrO_2 visible for powders that were synthesized in the presence of hexanoic acid (powders G and H). Also, each Bragg reflection is subject to a large increase in FWHM as the $[Zr^{4+}]$ to [HA] molar ratio decreases, meaning this could either be the result

of: (i), decreasing A.C.S. for both structures; (ii) increasing t-ZrO_2 proportions in the powders; (iii), poorly crystallized or large amorphous proportions of m-ZrO_2; or even that (iv), t-ZrO_2 stabilization by size effect occurs for a precursor concentration of 0.033 mol/L and a [Zr^{4+}] to [HA] molar ratio equal to [1:6] (powder G).

Indeed, Rietveld refinements reveal a large decrease in t-ZrO_2 A.C.S. with 2.3 and 2.2 nm for powders G and H, respectively, compared to 3.7 nm for powder E while that of m-ZrO_2 remains almost stable at 3.7 nm for both powders G and H. However, rather than a decrease in m-ZrO_2 proportions accompanying the decrease in nanoparticle size, Rietveld analysis reveals a stagnation in the structural proportions between powders E, G and H with 17, 15 and 17 mol. %, respectively.

When correlating FTIR spectra (Figure III-9) to XRD patterns in Figure III-10, it is possible to conclude that the decreased A.C.S. observed for powders G and H comparatively to powder E is the result of carboxylate species grafted at the surface of both t- and m-ZrO_2 nanoparticles. However, the grafting seemed more effective at the surface of t-ZrO_2 nanoparticles, as their A.C.S. was more impacted considering Rietveld analysis.

III.4.4 Rietveld structural analysis for optimized conditions

As the synthesis conditions for powder H ([Zr^{4+}] = 0.033 mol/L, [Zr^{4+}]:[HA] = 1:12) enabled to recover sufficient amounts of powder in just one synthesis, a very precise “Rietveld” XRD pattern could be obtained and is shown in Figure III-11.

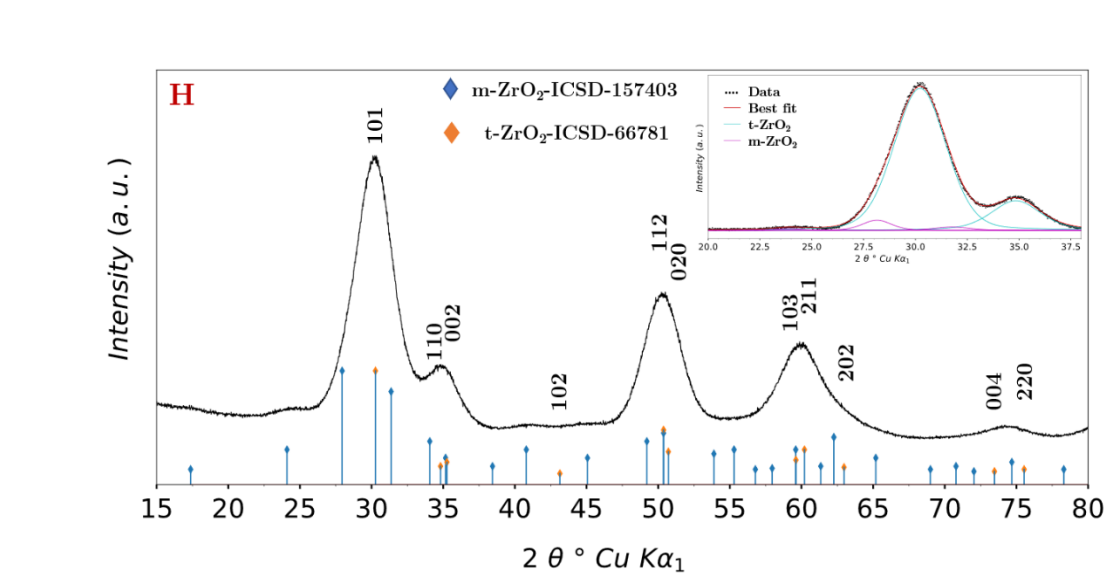

Figure III-11. XRD pattern of powder H ([Zr^{4+}] = 0.033 mol/L and [Zr^{4+}]:[HA] = 1:12). Blue and orange diamonds represent the Bragg reflections for m- and t-ZrO_2, respectively. Only the major t-ZrO_2 Miller indexes are displayed for clarity. The inset in the $20 < 2\theta < 37.5°$ range is a deconvolution of t-ZrO_2 (cyan) and m-ZrO_2 (magenta) contributions to the total diffraction signal recorded.

Though only slightly, all major Bragg reflections for m-ZrO_2 are visible up to $2\theta = 45°$ while none were visible in Figure III-10. These were not observed on the routine XRD pattern for powder H previously displayed, due to the relatively large signal-to-noise ratio. We clearly see here that the very large $(101)_t$ Bragg reflection completely overlaps both $(11-1)_m$ and $(111)_m$ Bragg reflections. Rietveld analysis of these powders revealed that the A.C.S. of t- and m-ZrO_2 structures were 2.5 and 2.7 nm, respectively, and that 80 mol. % of the powders were t-ZrO_2. However, from Equation $(III-1)$, 95 mol. % t-ZrO_2 was estimated inside powder H represented in Figure III-11. Therefore, Raman spectroscopy cannot be circumvented in this case to estimate more accurately m- and t-ZrO_2 contents inside the synthesized powders.

Figure III-12 is a zoom around the $(101)_t$ reflection at $2\theta \approx 30.2°$ for powders E, F, G and H where contribution of both t- and m-ZrO_2 structures were fitted using the Fityk software.

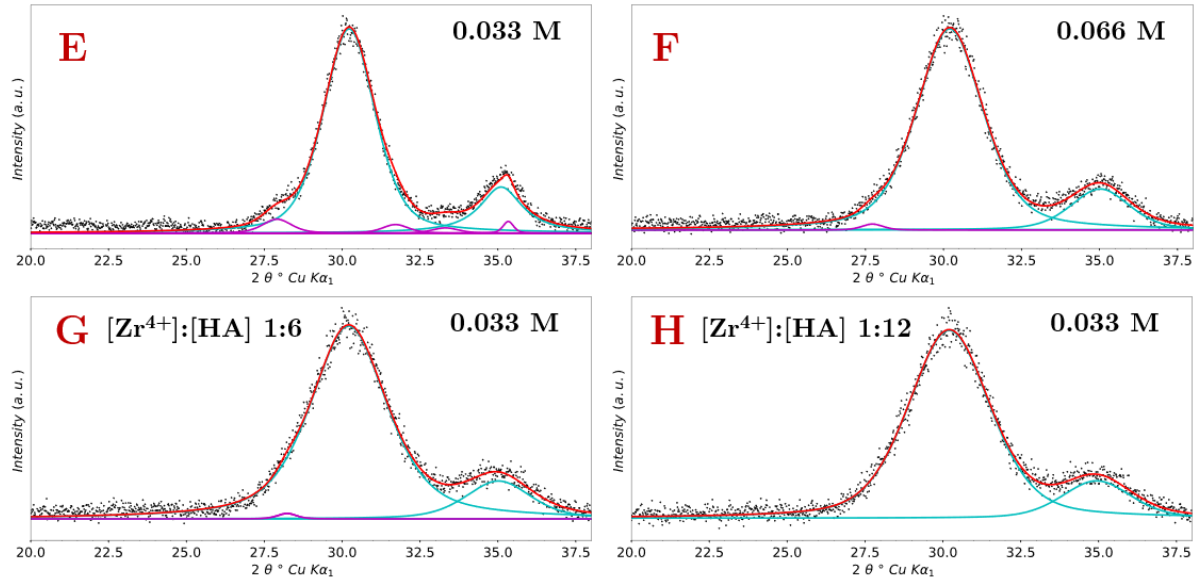

Figure III-12. XRD patterns in the $20 < 2\theta < 37.5°$ range of powders E, F, G and H. Each pattern is a deconvolution of the XRD data, represented in black dots, where t- and m-ZrO_2 contributions to the total diffraction signal recorded are represented in cyan and magenta lines, respectively. The red line is the best fit obtained, or sum of all t- and m-ZrO_2 contributions.

We can see in Figure III-12 that while for powder E, all $(11-1)_m$, $(111)_m$, $(002)_m/(020)_m/(200)_m$ and $(10-2)_m$ reflections could be refined, in powders F and G only the $(11-1)_m$ reflection remained visible but was no longer in powder H. A constant increase in the $(101)_t$ and $(110)_t/(002)_t$ reflections breadth also was visible between powders E and F, meaning that a decrease in the A.C.S. was observed for at least the t-ZrO_2 nanoparticles as the [Zr^{4+}]:[HA] molar ratio was decreased. Figure III-12 also clearly shows that, for powder E, G and H, the successive decrease in [Zr^{4+}]:[HA] molar ratio led to an increase in $(101)_t$ FWHMs, thus a decrease in t-ZrO_2 A.C.S. at least in the final powders. All these observations tend to support the results obtained by Rietveld analysis on the refined A.C.S.

Form these fits, 94, 99, 99 and 100 mol.% t-ZrO_2 were estimated to be present in powders E, F, G and H, respectively using (Equation III − 1).

This drastic change observed when HA is used to hinder the crystal growth and that seems to stabilize the pure t-ZrO_2 structure will be discussed later in a section dedicated to functionalization. However, to be clearly certain of these results, Raman spectroscopy was performed on powders E, F, G and H to investigate structure proportions with a complementary approach.

III.4.5Local structure analysis for powders E, F, G and H

While for the first set of powders (A, B, C and D) the crystallite size was just above or at the vicinity of the instrumental resolution limit of conventional diffractometers, the A.C.S. for this set of powders are clearly encompassed below that limit. Therefore, Raman spectroscopy was more than necessary to characterize accurately the presence and molar fraction of each structure inside the powders E, F, G and H. Figure III-13 shows the Raman spectra collected for powders E, F, G and H along with that of powder D.

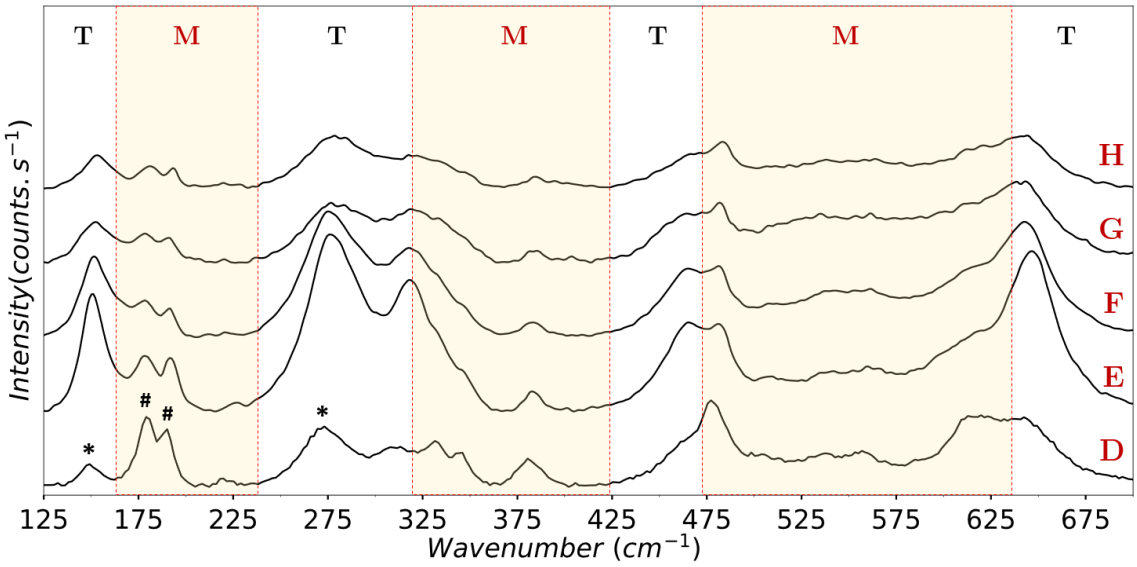

Figure III-13. Raman spectra for all powders D, E, F, G and H. Tetragonal and monoclinic domains are labeled as T and M, respectively, and Raman active modes used for the structural proportion quantification are indexed with (*****) and (**#**) for the t- and m-ZrO_2 structures, respectively.

Raman spectra in Figure III-13 show that all powders contain a mixture of t- and m-ZrO_2, as it was observed in Rietveld analysis. However, the intensity at 150 cm^{-1}, and those at 180 and 190 cm^{-1} are inverted between powder D and all other powders, revealing clearly a drastic variation into and m- and t-ZrO_2 proportions. Also, while powders E and F exhibit relatively well-defined Raman active modes, powders G and H suffer a lack of spectral definition. This may be attributed to the very small size of nanocrystals observed in Rietveld analysis and the structural defects that usually accompany such small particles (L.O.V.C., lattice expansion, etc.).

Raman spectra of powders E, F, G and H were also refined using Fityk to obtain the m-ZrO_2 molar fractions and the resulting fits are displayed in Figure III-14.

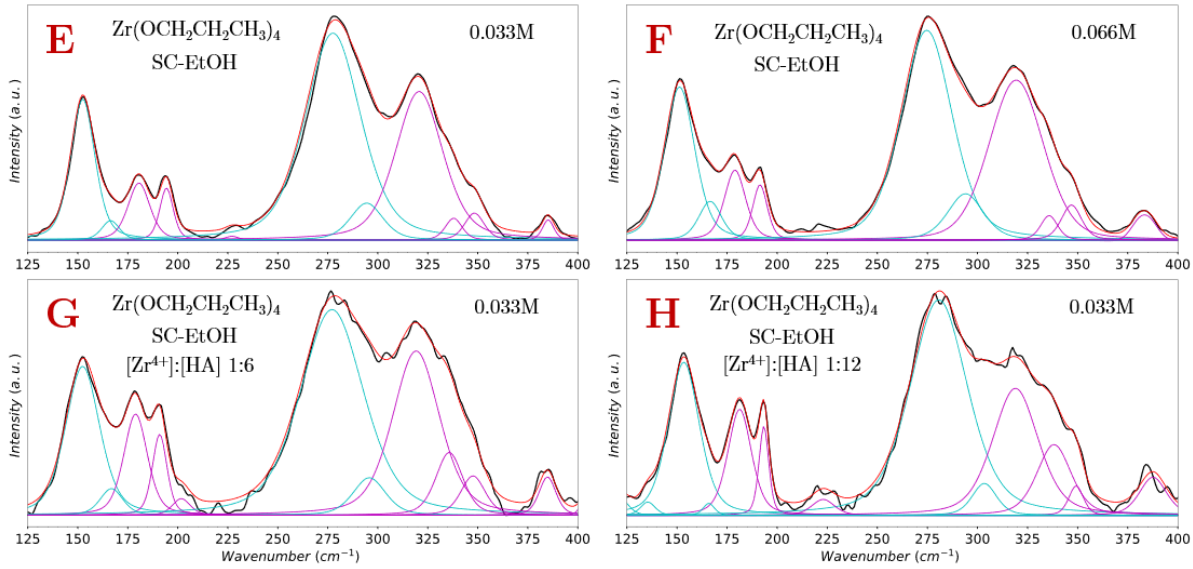

Figure III-14. Fits performed on Fityk for powders E, F, G, and H to estimate the t- and m-ZrO_2 molar fractions inside each synthesized powder.

From Equation (III − 2), 11, 12, 15 and 16 mol % m-ZrO_2 was estimated for powders E, F, G and H, respectively, which are in relatively good agreement with 17, 15, 15 and 17 mol % obtained by Rietveld refinements.

Though, for sizes below ≈ 4-5 nm, uncertainty of Rietveld analysis results tends to increase due to the increase in diffusion relatively to diffraction processes, we have seen that for powders A, B, C and D, structural proportions obtained by Rietveld analysis were in relatively good agreement with those estimated by Raman spectroscopy. Therefore, the same procedure was performed to characterize powders E, F, G and H and both Rietveld analysis and Raman spectroscopy gave similar results.

III.4.6 Investigation of ZrO_2 nanoparticle size

HRTEM observations were realized on powders E, F, G and H to gain deeper understanding of the mechanism responsible for t-ZrO_2 stabilization at the nanoscale as previous results do not seem to corroborate with the size effect theory as the molar fractions do not vary inversely to the A.C.S. observed. However, we have highlighted, with the use of surfactants in the synthesis of ZrO_2 nanoparticles and in our synthesis conditions, the fact that the number of crystallites must increase in order to maintain a certain structural proportion equilibrium roughly ≈ 85 mol. % t-ZrO_2. Figure III-15 shows the HRTEM images of powders E, F, G and H and their

respective diffraction images. Particle counts were performed on ImageJ software on a minimum of 70 nanoparticles.

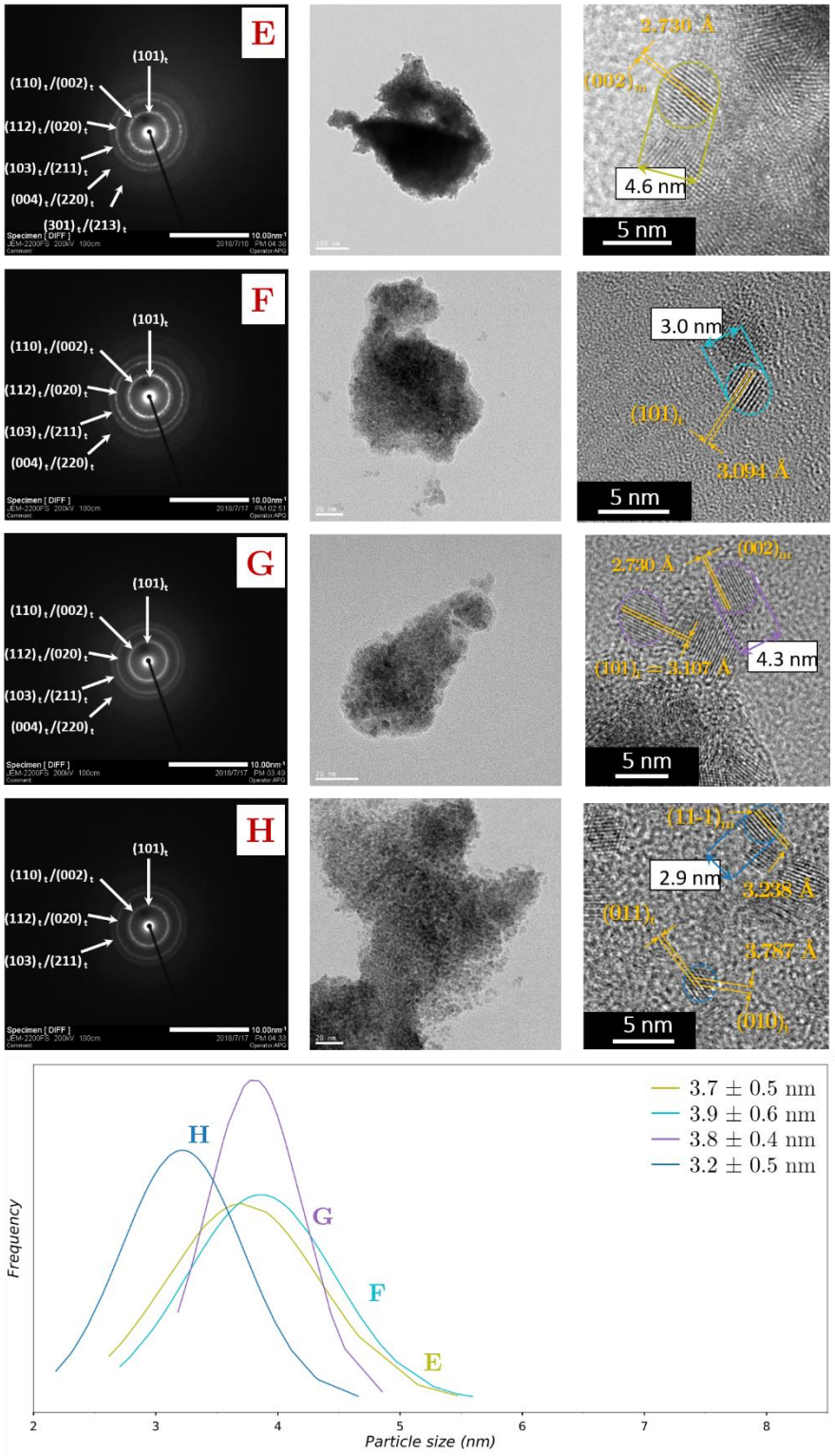

Figure III-15. Electron diffraction on powders E, F, G and H and their Miller indexes for each diffracting ring; their respective diffraction area and images of individual isolated ZrO_2 nanoparticles, along with their respective size distributions.

When comparing the diffraction patterns of powders E, F, G and H with that of powder B, the absence of diffraction rings for m-ZrO_2 is observed for each powder, though traces of $(011)_m/(110)_m$ are hardly visible for powder E. The corresponding diffracting areas are displayed next to the diffraction images and we can observe that the nanoparticles are highly aggregated in all powders. Also, next to the nanoparticle HRTEM images are displayed isolated individual ZrO_2 nanoparticles with diffracting lattice planes indexed and measured. The first observation that can be made is that the nanoparticle A.C.S. match nicely with those obtained from Rietveld analysis for each powder. In the case of powder E, a 4.6 nm m-ZrO_2 nanoparticle aggregated to other nanoparticles is displayed, exhibiting the $(002)_m$ regular diffracting lattice planes of medium intensity ($I\ (002)_m \approx 0.2\ I\ (11-1)_m$). The distance observed between two $(002)_m$ planes on the m-ZrO_2 nanoparticle in powder E is 2.730 Å, versus 2.626 Å in the model (ICSD#157403). For powder F, an isolated t-ZrO_2 nanoparticle of ≈ 3.0 nm exhibits the $(101)_t$ lattice planes distant of 3.094 Å, while the average distance observed in the tetragonal model (ICSD#66781) between two $(101)_t$ lattice planes is 2.955 Å.

The two isolated nanoparticles shown for powder G in Figure III-15 also exhibit the tetragonal and monoclinic structures with the $(101)_t$ and $(002)_m$ planes distant of 3.107 and 2.73 Å, respectively. The individual nanoparticles exposed in Figure III-15 for powder H, are both t- and m-ZrO_2 nanoparticles of less than 3 nm with one of them exhibiting the $(11-1)_m$ plane ≈ 3.238 Å and the other with the $(010)_t$ plane ≈ 3.787 Å, both larger compared to the models.

III.4.6.1 Crystalline defects in ZrO_2 nanoparticles

Further HRTEM observations focused on the structural defects exhibited by nanoparticles from powders G and H as they exhibit the smallest A.C.S. and size dispersity, but also because their higher dispersity enabled easier observations.

As the atomic layout in the t- and m-ZrO_2 lattice planes previously displayed for nanoparticles in Figure III-15 are extremely tight, the low contrast and the brightness in the HRTEM images increase the difficulty to locate precisely point defects in the structure. However, observations in the $(100)_t$, $(010)_t$ and $(001)_t$ lower atomic-density lattice planes favor better compromise in contrast and brightness due to the larger bond distances between Zr atoms. Figure III-16 shows a t-ZrO_2 nanoparticle from powder H with an atomic layout clearly identifiable as either the $(100)_t$ or $(010)_t$ identical lattice planes.

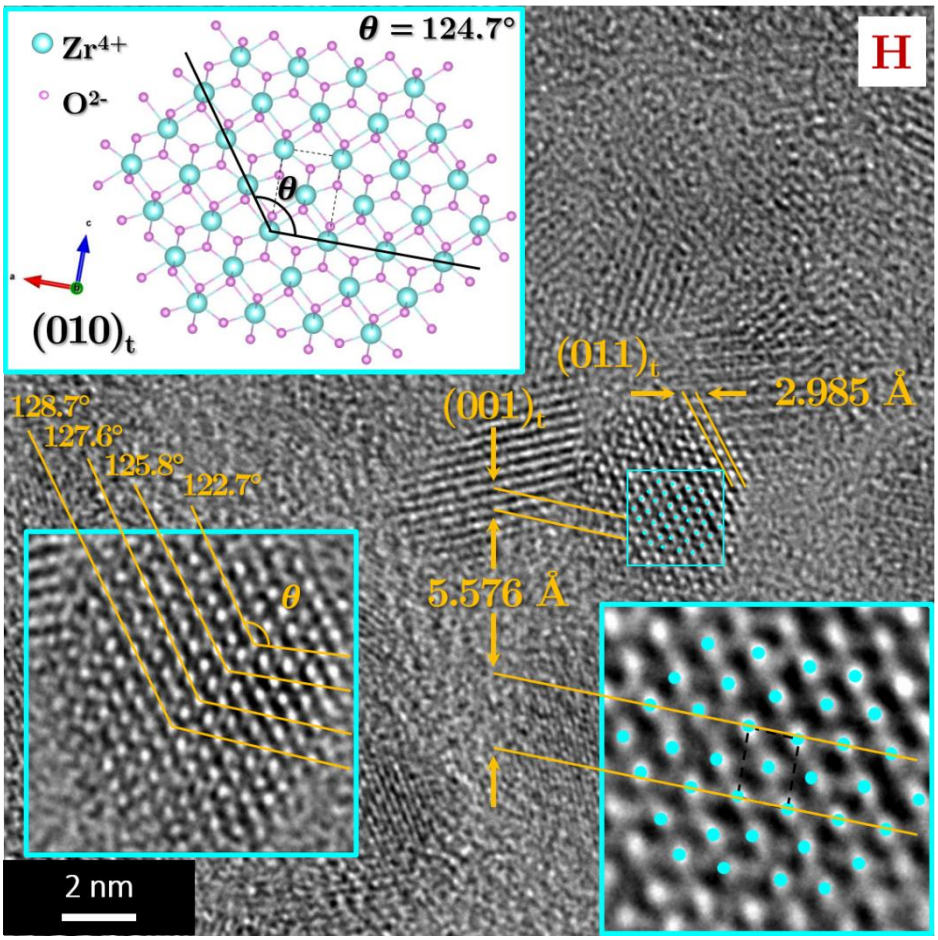

Figure III-16. Zoom highlighting disordered Zr atomic layout in an ≈ 4.5 nm t-ZrO_2 nanoparticle with Zr atoms represented in cyan and the same ordered domain represented on Vesta software in the $(010)_t$ plane.

Disorder in the atomic arrangement occurring in the nanoparticle in Figure III-16 is emphasized by the presence of large dark areas and irregularities in the atomic layout in opposition to highly ordered metal oxide materials which are generally recognizable by the oxide electronic density linking metal centers in atomic arrays [309, 310, 311]. In Figure III-16, the disorder in the structure generates d-spacings between the $(001)_t$ lattice planes of ≈ 5.576 Å while those observed in the model are 5.184 Å, thus representing a 7.6 % expansion in the *c* direction and in the $(100)_t$ plane, the average distance between Zr atoms is 3.866 Å vs 3.565 Å in the model, resulting in an 8.4 % expansion in the *a* direction. Also, the angle θ between the $(011)_t$ and $(001)_t$ planes varies between 128.7 and 122.7° as highlighted in Figure III-16, which is the direct consequence of disorder caused by the presence of oxygen vacancies. Lattice expansion and contraction phenomena occurring in metal oxide structures can be distinguished by either neutral or charged oxygen vacancies, respectively [60], meaning it may be wise to consider in the case of this nanoparticle that lattice expansion is generated by the presence of neutral oxygen vacancies.

III.4.6.1.1 Lattice oxygen vacancies

Figure III-17 shows two t-ZrO_2 nanoparticles from powder G with the $(100)_t$ or $(010)_t$ lattice plane exposed under the HRTEM electron beam.

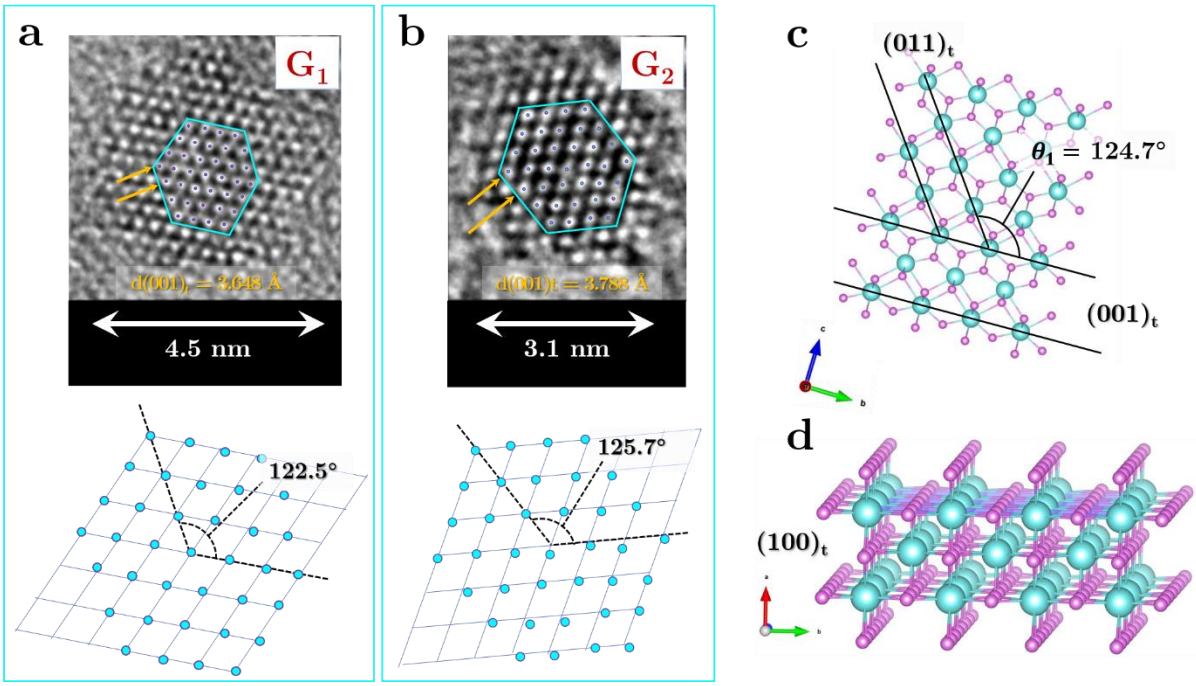

Figure III-17. a and b, zooms highlighting two nanoparticles from powder G exhibiting different levels disorder and their respective atomic layout in the (100) plane transposed below; c and d, the same ordered domain represented on Vesta software in the $(100)_t$ plane.

The nanoparticle G_1 (Figure III-17 a) is representative of large t-ZrO_2 nanoparticles observed in powder G with an A.C.S. of ≈ 4.5 nm, a lattice parameter of ≈ 3.648 Å, slightly larger than expected from the model (3.565 Å), and an angle θ between the $(011)_t$ and $(001)_t$ planes of 122.5° versus 124.7° for the model (Figure III-17 c). Though the lattice parameter is larger, the narrower angle results in relatively well-organized ZrO_2 nanoparticles exhibiting a low density of point defects in the considered plane as can be seen in the transposition of Zr atomic positions from the nanoparticle to the $(100)_t$ grid below the HRTEM image of G_1 (Figure III-17 a). On the other hand, the nanoparticle G_2 (Figure III-17 b) from the same powder exhibits a smaller size of ≈ 3.1 nm and a lattice parameter a = 3.788 Å which is 6.3 % larger than the model. Also, the angle θ between the $(011)_t$ and $(001)_t$ planes is 125.7°, slightly larger than the model's. These larger lattice parameter and angle result in a higher degree of disorder in the atomic array as can be seen in the $(100)_t$ grid below the HRTEM image of G_2 (Figure III-17 b). The G_2

highly disordered t-ZrO_2 nanoparticle is characterized by a high density of structural defects, believed to be neutral oxygen vacancies like the ones displayed in Figure III-16. These observations are in a way representative of the majority of isolated t-ZrO_2 nanoparticles obtained throughout the various syntheses presented in this work. Therefore, oxygen vacancies will be considered the most impacting phenomenon to take place in the t-ZrO_2 formation mechanism further developed. Table III-2 lists all the structural and size observations for powders E, F, G and H.

Table III-2. Summary of structural and size observations on powders E, F, G and H.

POWDER	TEM (nm)	A.C.S. Rietveld (nm)		m-ZrO_2 mol. %		
		m-ZrO_2	t-ZrO_2	Rietveld	Raman	Equation III-1
E	3.7 ± 0.5	4.2	3.7	17	11	5
F	3.9 ± 0.6	3.9	2.8	15	12	1
G	3.8 ± 0.4	3.7	2.3	15	15	1
H	3.2 ± 0.5	3.7	2.2	17	16	0
H(R)		2.7	2.5	20		5

H and H (R) powders were obtained in the same experiment. The only difference lies in the XRD pattern data collection, where H is a routine measurement whereas H (R) a Rietveld measurement, thus the signal-to-noise ratio is thus greatly reduced. Therefore, we may believe that the size reduction may occur on both m- and t-ZrO_2 structures as revealed by the Rietveld X-ray diffraction pattern.

From Table III-2, the difference in structural proportions obtained by Raman analysis from Equation (III − 2) and Rietveld analysis is very small, whereas they greatly differ from result obtained using Equation (III − 1). Though all 3 methods revealed very similar results, as listed in Table III-1, we must consider that Equation (III − 1) does not hold anymore for very small nanoparticle sizes, where the intensity of one structure may completely overlap the other structure's intensity as observed in routine XRD measurements displayed Figure III-10 for powders G and H. Also, A.C.S. obtained from both Rietveld analysis and HRTEM observations are in relatively good agreement on the overall size decrease. Therefore, we will not refer to results obtained from Equation (III − 1), but rather consider that the structural percentages remain almost constant in powders E, F, G and H as revealed by Raman spectroscopy and Rietveld analysis.

HRTEM images on the $(100)_t$ or $(010)_t$ diffracting planes of these powders revealed discrepancies in lattice plane distances and irregularities concerning the tetragonal nanocrystallites, probably generated by structural and surface oxygen vacancies. These discrepancies in lattice planes between HRTEM observations and the models are the result of lattice expansion phenomenon generally observed in the formation and stabilization of small nanoparticles as discussed in Chapter I. This generally results in expansion or contraction of bond distances, which are direct consequences of the formation of oxygen vacancies and stabilization of stable t-ZrO_2 and c-ZrO_2. We therefore believe that the mechanism responsible for the metastable t-ZrO_2 is based on the generation of oxygen vacancies, which we will briefly overlook in the next section, prior to a deep discussion on formation of ZrO_2 in supercritical alcohols in the next chapter.

In the light of these results, the stabilization of metastable t-ZrO_2 at the nanoscale cannot be considered as a direct effect of nanoparticle size only. Though it is certain that the size plays a key role in the stabilization process, we have seen that between 4 and 2 nm, the m- and t-ZrO_2 structural proportions no longer vary, with a limit of ≈ 85 mol. % t-ZrO_2 attained for both 4 and 2 nm when considering our reactional system. However, as it is molar fractions that are estimated, the large decrease in the t-ZrO_2 A.C.S. along with constant molar fractions observed from powder E to H are the reflect of a greater number of t-ZrO_2 nanoparticles crystallized. The correlation between A.C.S. and possibility to produce only pure t-ZrO_2 will be discussed further in this chapter.

III.5 Metastable tetragonal ZrO_2 formation mechanism

Based on the previously made observations and assumptions, a mechanism is proposed to understand ZrO_2 nanoparticle formation in powders C, D, E, F, G and H in our synthesis conditions and will be discussed all through the following section. The mechanism is based on the generation of defects in the preliminary nucleation stage, impacting thus the subsequent growth stage. We consider that in our synthesis conditions preliminary clusters exhibiting large amounts of trapped OH will lead to the formation of t-ZrO_2 nanoparticles exhibiting large oxygen vacancy concentrations as this is generally reported as the main mechanism stabilizing bulk and large nanoscale t-ZrO_2 [15, 83, 84, 85, 87], whereas clusters exhibiting low amounts of trapped OH will *in fine* lead to lower oxygen vacancy concentrations and to the formation of the more thermodynamically stable monoclinic structure.

III.5.1.1 ZrO_2 nucleation in supercritical conditions

Figure III-18 shows, eventual preliminary nucleation stages to form either monoclinic or tetragonal ZrO_2 nanoparticles.

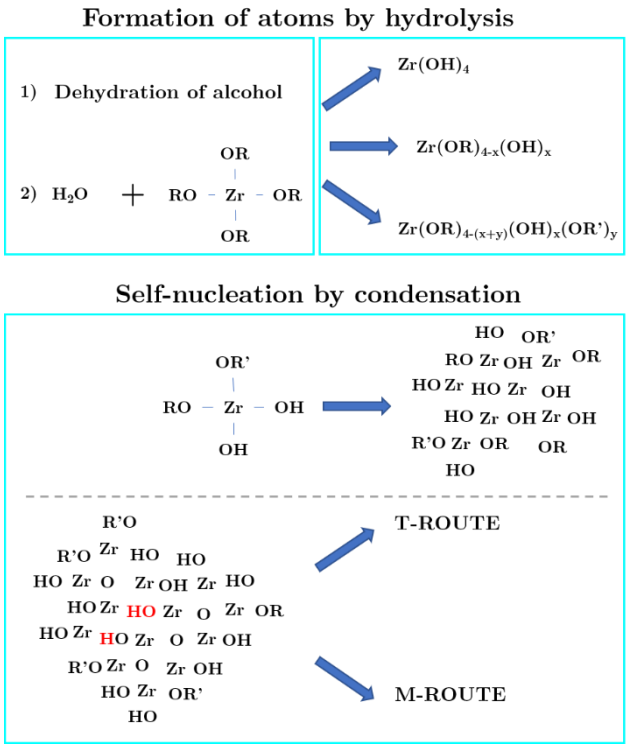

Figure III-18. Display of a possible formation mechanism of ZrO_2 clusters.

As shown in Figure III-18, the major molecules present are $Zr(OR)_4$, with R being propoxide ligands as when ethanol is used as a solvent as its ability to substitute to propoxide ligand molecules is minimal as we have seen in Chapter I.

Once inside the reactor ($p > p_C$; $T > T_C$), the drop in dielectric constant leads to supersaturation conditions ($\varepsilon_2 << \varepsilon_1$). The energy barrier to activate dehydration of ethanol is overcome and nucleation can proceed. During this self-nucleation step, hydrolysis enabled by alocoholysis generates unstable $Zr(OR)_{4-x}(OH)_x$ molecules which then condense to form very small $ZrO_{2-x}(OH)_x$ clusters and as long as supersaturation conditions are maintained. However, because of the drastic environmental unstable self-nucleation conditions, small clusters may begin to form either with high- or low-density structural defects simultaneously. Clusters exhibiting high-density structural defects will lead to the formation of metastable t-ZrO_2 nanoparticles while those exhibiting low-density structural defects to m-ZrO_2 nanoparticles.

III.5.1.2 ZrO_2 growth in supercritical conditions

The T- and M-routes presented in Figure III-19 a and b, respectively, are believed to occur simultaneously during the formation of ZrO_2 nanoparticles as the joint presence of both structures has been observed in each synthesis (except powder A) in this work, but also in numerous works realized on ZrO_2 formation with various precursors, solvents or even synthesis methods [62, 74, 298].

III.5.1.2.1 Growth along the tetragonal pathway (T-route)

Considering the T-route, the incomplete condensation of $Zr(OR)_{4-x}(OH)_x$ molecules during stage (i) is favored by the alcohol dehydration kinetic rates. We have seen in Chapter I that in our synthesis conditions (25 MPa; 400°C), relatively large amounts of water are generated *in situ* for hydrolysis to occur at relatively fast rates [146]. Precursor molecules thus stabilize in a relatively regular ordering to minimize Gibbs free energy in a burst nucleation process during which $ZrO_{2-x}(OH)_x$ clusters that contain large amounts of entrapped structural hydroxyl groups condense into larger defective structures (Figure III-19 a). The condensation of internal hydroxyl groups in these $ZrO_{2-x}(OH)_x$ clusters is accompanied with the formation of oxygen vacancies and diffusion of water molecules outside the structure [29]. The formation of these vacancies will, if their concentration is satisfactory, relieve the strain associated with the eight-fold coordination around Zr atoms and stabilize the metastable t-ZrO_2 structure in the early homogeneous nucleation stage (T-route). However, has the rapid precursor consumption by condensation results in a drastic drop in concentration below C_{min}^{nu}, the nucleation process ends. At this point, further condensation of $Zr(OH)_4$ monomers in solution supplies the surface of nanocrystallites during heterogeneous nucleation, or growth of already formed particles.

III.5.1.2.2 Growth along the monoclinic pathway (M-route)

Considering the M-route (Figure III-19 b), it is the pathway followed by the most stable clusters that underwent full or almost full condensation of $Zr(OH)_4$ molecules into ZrO_7 polyhedral packing where Zr atoms are coordinated to 7 O atoms. This structuration, thermodynamically favored, then undergoes very low density of structural defects to form m-ZrO_2 nanoparticles [29].

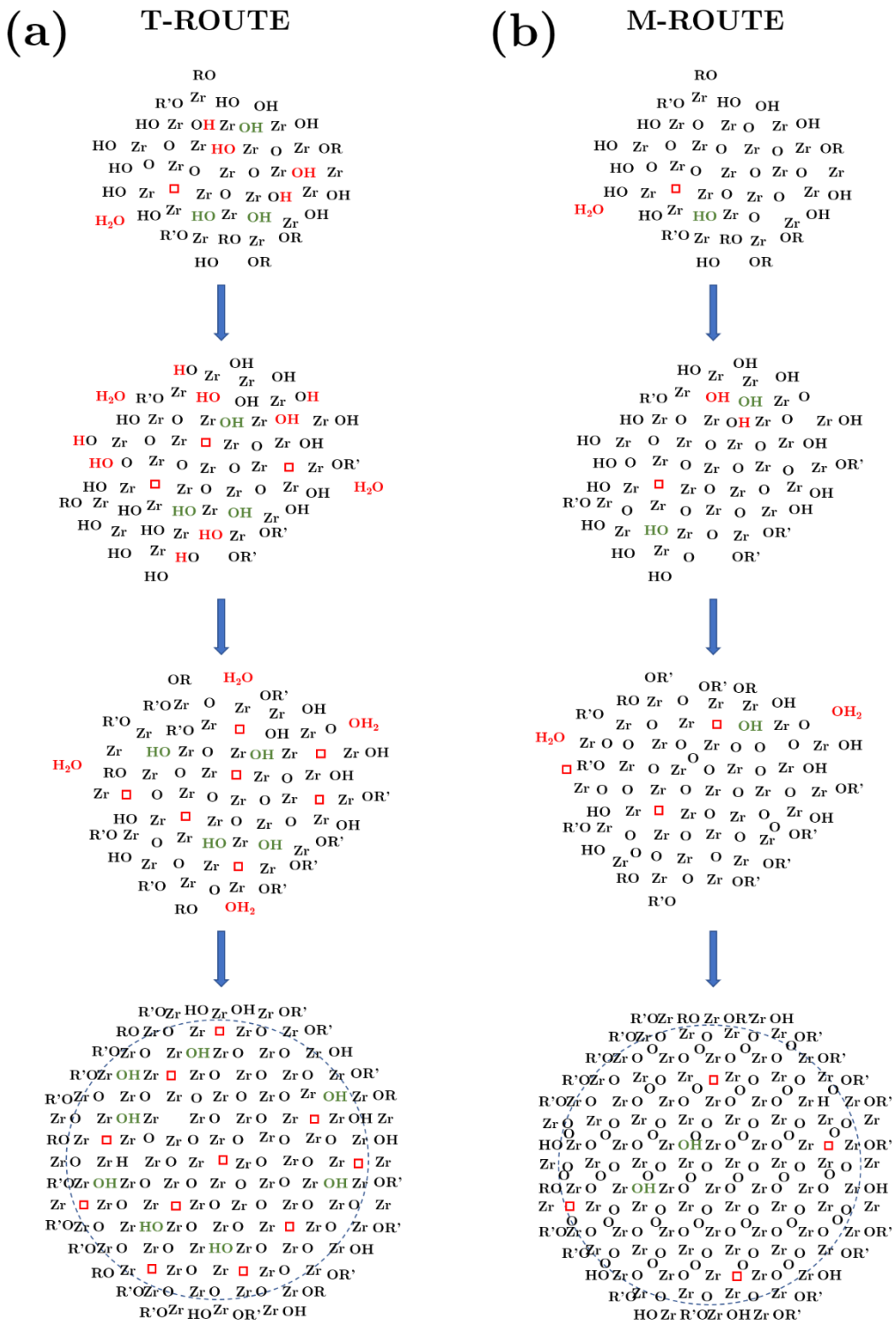

Figure III-19. Representing: a, the formation of a t-ZrO_2 nanoparticle from a cluster exhibiting high-density defects; and b, the formation of a m-ZrO_2 nanoparticle from a cluster exhibiting low-density defects. □ are oxygen vacancies, OH and OH internal or surface hydroxyls that react to generate oxygen vacancies, H_2O a water molecule generated from the combination of non-condensed hydroxyl groups, and OH a structural or surface trapped hydroxyl.

III.5.1.3 Structural equilibrium

Though it has been clearly deduced from both Rietveld analysis and Raman spectroscopy that powders exhibiting the smallest A.C.S. also contained the highest amounts of t-ZrO_2, an equilibrium in structure proportions seems to have been reached at ≈ 85 mol. % t-ZrO_2 as no matter the decrease in A.C.S. observed between powders E and H, molar fractions did not vary anymore. Figure III-20 schematizes this phenomenon by representing in a figurative fixed quantity of powders, the evolution of m- and t-ZrO_2 structural proportions and particle size observed in this chapter.

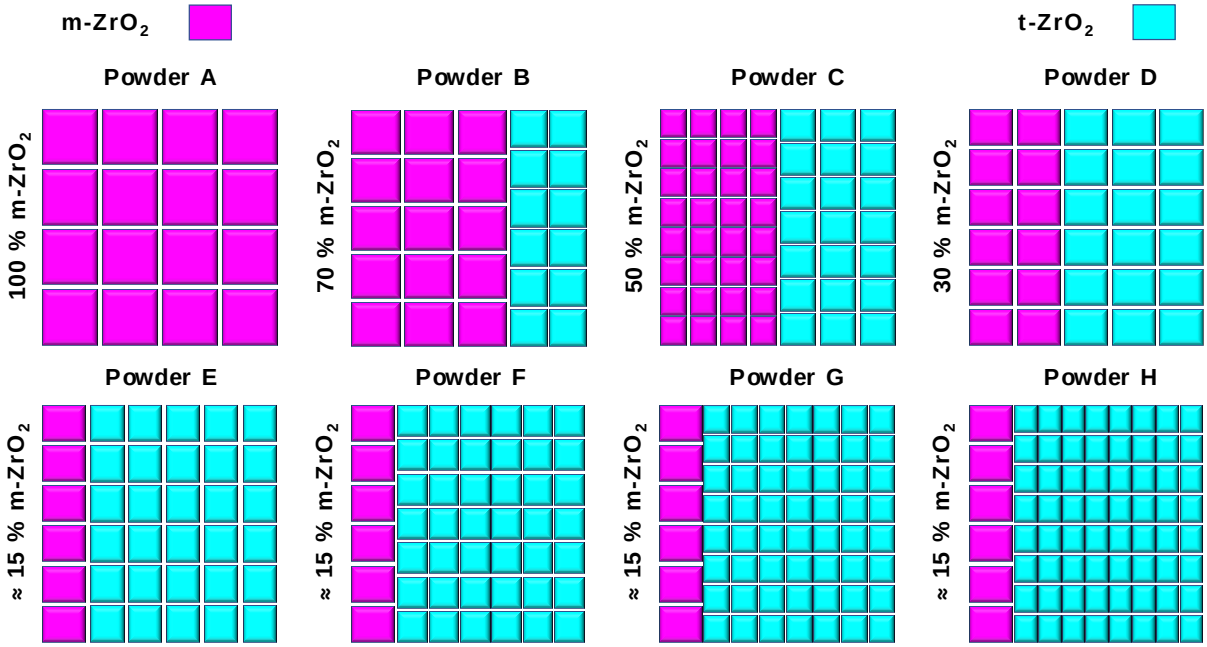

Figure III-20. Representation of the evolution of proportions and A.C.S. of each structure for all powders synthesized and presented in this chapter. m- and t-ZrO_2 nanoparticles are represented in magenta and cyan squares, respectively.

Figure III-20 summarizes the results on structural proportions and A.C.S. obtained from Rietveld refinements and Raman observations on each powder presented in this chapter. The fixed quantity of each synthesized powder (A to H) is schematized by the total area of each of all 8 squares (either all magenta for pure m-ZrO_2 or magenta and cyan for mixtures of m- and t- ZrO_2 in the synthesized powders, respectively). In each of all 8 squares, m- and t-ZrO_2 structural proportions are schematized by magenta and cyan colored quadrilaterals and the relative size of each individual quadrilateral represents the A.C.S. of both m- and t-ZrO_2 nanocrystallites. Figure III-20 thus illustrates the correlation between nanoparticle A.C.S. and structural proportion variations for each synthesized powder in this study.

In the first row of Figure III-20 (powders A to D) the choice in the reaction system clearly has an impact on both A.C.S. and structure proportions obtained *in fine* and we clearly see a link between the decrease in A.C.S. and decrease in m-ZrO_2 content inside the powder mixtures in the following order: 100; 70; 50; and 30 mol. % for powders A (pure m-ZrO_2), B, C and D, respectively, as in the same time the A.C.S. follow a general decrease. As all A.C.S. are above the lower boundary of critical size generally admitted (≈ 3 nm) but tend to it, the increase in t-ZrO_2 mol. % content can be explained by the critical size theory.

On the other hand, in the second row of Figure III-20 (powders E to H) the same trend as for powders A to D is not observed though between powders D and E, the amount of m-ZrO_2 decreased (almost divided by a factor 2 for H versus E) as the A.C.S. decreased by increasing the precursor concentration from 0.01 to 0.033 mol/L. Indeed, though both t- and m-ZrO_2 A.C.S. are at the vicinity or even below the critical limit generally admitted for t-ZrO_2, t- and m-ZrO_2 structural proportions stagnate at ≈ 15 mol. % m-ZrO_2 in each powder even when increasing the precursor concentration from 0.033 to 0.066 mol/L or increasing the amount of HA leads to a general decrease in A.C.S. It is important to notice that for powders E and H where m-ZrO_2 A.C.S. are very similar, t-ZrO_2 A.C.S. on the other hand is almost divided by 2 (from 4 nm (powder E) to 2 nm (powder H)), but as t-ZrO_2 mol. % are identical for both XRD and Raman observations, 4 times more t-ZrO_2 nanocrystals are therefore formed in powder H than in powder E. Therefore, it seems that decreasing A.C.S. kinetically favors nucleation of t-ZrO_2 in terms of nuclei and nanoparticle numbers, but not in terms of molar fractions like it is commonly believed.

Therefore, Figure III-20 clearly emphasizes the fact that t-ZrO_2 formation is favored as the A.C.S. decreases but only down to a limit of ≈ 85 mol. %, thus showing the limit of the size effect on the synthesis of pure t-ZrO_2 nanoparticles. Also, we may believe that in our synthesis conditions, and probably in a general manner, t- and m-ZrO_2 nuclei are formed concomitantly and that a t- to m-ZrO_2 structural transformation occurs when particles display A.C.S. larger than 2 to 3 nm as generally admitted. However, *in situ* studies focused specifically on ZrO_2 nucleation would be necessary to validate the hypothesis on the simultaneity in t- and m-ZrO_2 nucleation followed by reverse transformation and will be the object of Chapter IV.

Though this work focused on the possibility to synthesize pure t-ZrO_2 by decreasing the particle size below the reported critical size, this was unfortunately not possible with the chosen set of experiments presented here. We therefore believe that the mechanism responsible for metastable t-ZrO_2 stabilization is the control in the formation rates of oxygen vacancies. Thus,

by choosing the appropriate experimental parameters, it may be possible to increase the number of defective nuclei rather than segregate m- and t-ZrO_2 crystal structures by size effect.

Conclusion of Chapter III

The present chapter has focused on the structural control of ZrO_2 by designing very small nanocrystallites based on the hypothesis that control of the nanocrystallite size could advantage the nucleation and growth of pure t-ZrO_2 when the A.C.S. is maintained below the critical size encompassed between 3 and 30 nm. However, we have demonstrated by combining both Rietveld analysis and Raman spectroscopy that only a limit of ≈ 90 mol. % of t-ZrO_2 could be achieved in structural segregation by decreasing the nanoparticle size down to 2 nm and that no major difference was observed between nanoparticles of 2 and 4 nm. These very small ZrO_2 nanoparticles were designed with a new process where the alcoholysis/hydrolysis occur owing the dehydration of ethanol in supercritical conditions and where hydrolysis is limited mainly by the supply of water molecules generated from the dehydration of ethanol. Condensation in our synthesis conditions statistically leads to both metal oxide defective and non-defective $ZrO_{2-x}(OH)_x$ integrated networks. From this point, two main parallel reaction pathways coexist where one leads to the formation of a metastable t-ZrO_2 structure with a high density of oxygen vacancies, while the other pathway followed by quasi flawless particles leads, through ZrO_7 polyhedral packing, to the formation of the thermodynamically stable m-ZrO_2 structure.

The presence of these structural defects has been clearly identified by HRTEM observations on both t- and m-ZrO_2 nanoparticles, where large amounts of defects in the $(100)_t$ and $(010)_t$ planes were observed while all m-ZrO_2 lattice planes observed showed very little structural or surface defects.

The efficiency of functionalization with hexanoic acid was also evidenced by FTIR analysis where strong vibration bands could be observed on the functionalized samples, revealing that the decrease in A.C.S. realized by grafting carboxylic functions at the surface of ZrO_2 nanoparticles failed to increase the relative t-ZrO_2 molar fraction in the final powders.

Also, the very small size of ZrO_2 nanoparticles and their very narrow size distribution support the fact that optimal conditions for the synthesis of extremely small nanocrystallites were guaranteed in this work to properly study the impact of the size on stabilization of the metastable t-ZrO_2 structure. Therefore, either the critical size for zirconia must be below the limit of 2 nm and high energy X-ray sources are necessary to define clearly its limit, either its stabilization depends more on structural similarities or reaction kinetics and thus, in our conditions, on water release rates to produce varying oxygen vacancy concentrations.

Finally, simultaneity in m- and t-ZrO_2 nucleation was not highlighted in this chapter, but only supposed. For this reason, the next chapter will be dedicated to the *in situ* study of the formation

of ZrO_2 nanoparticles with the aim to unravel the very first steps differentiating the nucleation of monoclinic and tetragonal structures and validate the formation mechanism proposed in this chapter. Further investigations on the nucleation and growth processes necessitate the use of more powerful photon sources and analysis procedures, therefore, the next chapter will focus on the observation *in situ* of ZrO_2 formation in supercritical fluids under a hard X-ray photon source and pair distribution function analysis of the scattered intensity of the data collected.

Chapter IV

In-situ investigation of the nucleation and growth of ZrO_2

IV.1 Introduction

Many different *ex situ* and *in situ* experimental studies have been performed on the formation mechanisms and structural evolution of ZrO_2 polymorphs as we have seen in Chapter I. While most *ex situ* studies focused either on the structural changes occurring during the formation of ZrO_2 or structural changes induced by external perturbations on ZrO_2 polymorphs, *in situ* studies allowed direct visualization of the changes in interatomic interactions when external perturbations were applied (i.e. increase/decrease in temperature, pressure, oxygen partial pressure) [91, 312, 313 314]. However, it is only in the recent years that experimental set-ups enabled visualization of the formation steps during nanoparticle synthesis using time resolved total X-ray scattering measurements, giving more insight into nanoparticle formation mechanisms [125, 204, 315, 316, 317, 318].

In this chapter, we will try to bring more insights to the formation mechanisms undergoing in the first moments during the synthesis of ZrO_2 nanoparticles. We have seen in Chapter II that PDF analysis of total X-ray scattering intensity treats both Bragg and diffuse scattering processes on equal footing, allowing the study of disordered and partially ordered nanomaterials [245, 246, 247, 319]. Thus, we will observe the evolution of the reaction media (solvent, precursors and additives) from the precursor molecular configuration to the final crystallized ZrO_2 structures.

Two aspects will be considered to explain the observed results: the critical size of the metastable t-ZrO_2 nanoparticles, though we have in Chapter III pointed out their indirect impact on stabilization, and the reaction kinetics, which we believe are responsible for the formation of lattice oxygen vacancies (L.O.V.) formation and concentration, and thus stabilization of the metastable t-ZrO_2 structure. These reaction kinetics as we have seen in Chapter I, strongly depend on the dehydration of alcohols: (i) at supercritical conditions; and (ii) probably at the surface of nanoparticles, catalyzed by the newly formed metal oxide nanoparticles.

PDF analysis will allow observation of the precursor molecular organization in the different systems investigated, the final particle sizes, the nucleation and growth rates, but also metal coordination number of the final structures and finally give more insight in the mechanisms responsible for stabilization of metastable t-ZrO_2.

Therefore, the aim of this chapter is to unravel the formation mechanisms of nanocrystalline ZrO_2 with sizes below and around the commonly smallest values admitted for the critical size under which t-ZrO_2 can be stabilized rather than the more thermodynamically stable m-ZrO_2 crystal structure.

Pair distribution function analysis of total X-ray scattering measurements using the PDFgui software is often considered an easy "plug and play" technique and therefore sometimes highly underestimated. However, we will see in this chapter that most valuable information can be obtained on nanoparticle formation even for very small nanoparticles.

Investigation of this phenomena was led through different sets of experiments: the first set of experiments was realized in supercritical ethanol, and analysis of the variation of experimental parameters such as, temperature, precursor concentration and the use of surfactants while the second one was realized in supercritical alcohols, displaying increasing supercritical temperatures (T_C) with an increase in the alkyl chain length to investigate the formation kinetics through gradual increase in water release as seen in Chapter I.

IV.1.1.1 Solvent critical coordinates

Figure IV-1 displays a plot of the evolution of the critical coordinates for all anhydrous alcohols used during *in situ* measurements presented in this chapter.

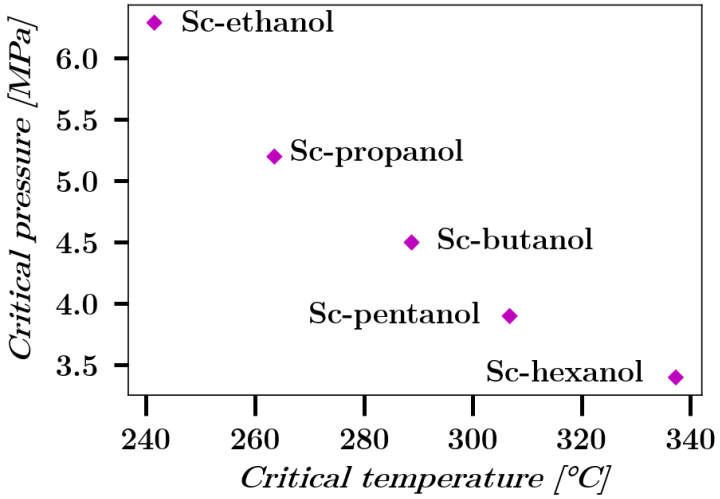

Figure IV-1. Representation of the critical coordinates for different anhydrous alcohols.

As the critical temperature of alcohols increases with the alkyl chain length for the different anhydrous alcohols, it should thus be possible to take advantage of their ability to generate water *in situ* at different rates at 400°C and allow relatively good control on dehydration kinetics during borderline non-hydrolytic sol-gel (B.N.H.S.G.) reactions. Also, while the critical pressure does not significantly vary from one alcohol to the other, the constant pressure of 25

MPa chosen for all measurements should maintain a comparable solvent state of aggregation [158].

The reference temperature and concentration chosen were 400°C and 1 mol/L, respectively. Also, to kickstart the study, the increase in precursor concentration ($[Zr^{4+}]$) by a factor 10 compared to syntheses realized in continuous flow reactors is determined in order to ensure sufficient scattering signal on the detector during in situ measurements as zirconium is a relatively poor scatterer. In the first set of *in situ* measurements, reaction kinetics were investigated by varying the temperature, while in the second set of *in situ* measurements reaction kinetics were investigated by varying primary alcohols.

The influence of varying initial experimental parameters on the nanoparticle final crystal structure will be discussed in this chapter along with mechanisms responsible for the stabilization of metastable t-ZrO_2.

IV.2 Structural characterization of ZrO_2 formation measured in supercritical ethanol

The first set of *in situ* measurements was performed in supercritical ethanol (considered as the reference solvent) where the evolution of ZrO_2 systems was observed when the synthesis temperature was varied between the reference temperature (400°C), down to just above the critical temperature of ethanol (≈ 250°C). As we have seen in Chapter I-5.1.6, water production from ethanol decomposition may be increased quasi linearly by increasing the temperature between 250 and 400°C, and thus temperature may be used as a kinetic lever to play on reaction kinetics during B.N.H.S.G. syntheses and enable to observe structural variations resulting from each temperature.

IV.2.1 Sample preparation

IV.2.1.1 Materials

Zirconium(IV) propoxide solution 70 wt. % in 1-propanol [$Zr(OCH_2CH_2CH_3)_4$] was used as the metal precursor source, absolute ethanol (C_2H_5OH) as the solvent, while hexanoic acid ($CH_3(CH_2)_4COOH$) and trioctylphosphine ($[CH_3(CH_2)_7]_3P$) were used as surfactants for ZrO_2 synthesized in sc-ethanol. All chemicals were purchased from sigma-Aldrich and used as received.

IV.2.2 Procedure

Ethanol being of all alcohols investigated the one displaying the critical temperature the furthest to 400°C, this set of experiments allowed a wide range of temperatures between the critical temperature and the maximal possible temperature allowed by the experimental set-up (450°C). The idea behind these experiments was to define different ways of controlling the final structure and confirm the influence of water release on ZrO_2 formation mechanism.

IV.2.3 Measurements conducted in supercritical ethanol

During *in situ* experiments conducted in supercritical ethanol, the influence of the temperature was investigated as we have seen in Chapter I and II that the dehydration rates are linearly proportional to the temperature for at least ethanol and isopropanol [146]. Also, the influence of the cationic concentration ($[Zr^{4+}]$) in the precursor solution was investigated as observations in Chapter III revealed that increasing the concentration played a key role in decreasing the final nanocrystallite size. However, we must remember that increasing the concentration did not seem to favor t-ZrO_2 in terms of molar fractions, but did favor t-ZrO_2 in terms of number of crystallites formed. Finally, the use of functionalizing agents to quench nanoparticle growth through surface adsorption in the early growth stage will also be discussed. Table IV-3 lists all the *in situ* measurements performed in supercritical ethanol.

Table IV-3. List of all measurements performed in supercritical ethanol.

Experiment	***Solvent***	***[Zr $^{4+}$] (mol/L)***	***T (°C)***	***[Zr $^{4+}$]:[HA]***	***[Zr $^{4+}$]:[TOP]***
		Temperature series			
1	*Sc-ethanol*	*1*	*400*		
2	*Sc-ethanol*	*1*	*350*		
3	*Sc-ethanol*	*1*	*300*		
		Concentration series			
4	*Sc-ethanol*	*0.5*	*400*		
5	*Sc-ethanol*	*0.5*	*350*		
		Surfactant series			
6	*Sc-ethanol*	*1*	*400*	*2:1*	
7	*Sc-ethanol*	*1*	*400*	*1:1*	
8	*Sc-ethanol*	*1*	*400*		*2:1*
9	*Sc-ethanol*	*1*	*350*	*2:1*	
10	*Sc-ethanol*	*1*	*350*	*1:1*	

The temperatures of 400, 350, 300 and 250°C were investigated to confirm the possibility to control the reaction kinetics at a constant pressure of 25 MPa. Unfortunately, 250°C was too low a temperature to initiate a reaction, therefore, data analysis is performed only from 300°C.

Also, while the supersaturation conditions were observed for 3 precursor concentrations of 1.0, 0.5 and 0.25 mol/L, for the latter the signal was too low to be properly interpreted during PDF analysis. Finally, nanoparticle growth quench through surface functionalization of the synthesized nanoparticles was performed with hexanoic acid as it is commonly used in functionalizing procedures during supercritical fluid syntheses [116, 320, 321, 322, 323], and trioctylphosphine (TOP), not only because its impact on nanoparticle synthesis in supercritical fluids is already known [324, 325], but also because its oxidized form has been used to produce uniform, extremely small and almost pure t-ZrO_2 nanoparticles in N.H.S.G reactions [63]. Precursor to surfactant molar ratios of 2:1 and 1:1 were investigated for both HA and TOP. However, in the case of TOP the reaction did not occur for a 1:1 molar ratio and will not be presented. Through these various experimental conditions, discussion will focus on the modification of ZrO_2 structural properties depending on the initial experimental parameters such as temperature, precursor concentration and use of additives. Table IV-4 lists all the refined parameters in the supercritical ethanol series to obtain PDF using PDFgui.

Table IV-4. Refined parameters for the last frame of each *in situ* measurement in the supercritical ethanol series. The parameter Delta 2 was chosen to remain constant throughout all refinements, with a value of 3.

Series	***Temperature***					***Concentration***	
Experiment N°	***1***		***2***		***3***	***4***	***5***
Temperature	***400°C***		***350°C***		***300°C***	***400°C***	***350°C***
[Zr^{4+}]	***1M***		***1M***		***1M***	***0.5M***	***0.5M***
Scale factor	***0.48***	***0.11***	***0.56***	***0.05***	***0.16***	***0.52***	***0.49***
a	***5.1427***	***3.5594***	***5.1081***	***3.5328***	***3.5485***	***3.577***	***3.5638***
b	***5.1336***	***3.5594***	***5.119***	***3.5328***	***3.5485***	***3.577***	***3.5638***
c	***5.2671***	***5.1392***	***5.2443***	***5.1353***	***5.0812***	***5.1393***	***5.1004***
Sp diameter	***19.8***	***20.5***	***20.1***	***21.5***	***17.5***	***18.8***	***19.2***
O_Z						***0.0591***	***0.058***
$U_{11\ (Zr)}$						***0.00678***	***0.00811***
$U_{22\ (Zr)}$						***0.00678***	***0.00811***
$U_{33\ (Zr)}$						***0.00567***	***0.0054***
$U_{11\ (O)}$						***0.013***	***0.0715***
$U_{22\ (O)}$						***0.0488***	***0.0197***
$U_{33\ (O)}$						***0.0024***	***0.0314***
Structure	***m-ZrO_2***	***t-ZrO_2***	***m-ZrO_2***	***t-ZrO_2***	***t-ZrO_2***	***t-ZrO_2***	***t-ZrO_2***
Phase %	***81***	***19***	***71***	***29***	***100***	***100***	***100***
Series	***Surfactant***						
Experiment N°	***6***		***7***		***8***	***9***	***10***
Temperature	***400°C***		***350°C***		***400°C***	***400°C***	***350°C***
[Zr^{4+}]	***1M***		***1M***		***1M***	***1M***	***1M***
Surfactant	***HA***		***HA***		***TOP***	***HA***	***HA***
[Zr^{4+}]:[Surfactant]	***2:1***		***2:1***		***2:1***	***1:1***	***1:1***
Scale factor	***0.19***	***0.28***	***0.33***	***0.26***	***0.23***	***0.39***	***0.44***
a	***5.1622***	***3.5678***	***5.1519***	***3.5434***	***3.5418***	***3.5815***	***3.5769***
b	***5.1185***	***3.5678***	***5.0849***	***3.5434***	***3.5418***	***3.5815***	***3.5769***
c	***5.2454***	***5.1421***	***5.2409***	***5.1164***	***5.0989***	***5.1582***	***5.1266***
Sp diameter	***19.3***	***20.3***	***15.1***	***19.4***	***19.6***	***17.9***	***18.9***
O_Z	***0.0535***		***0.0535***	***0.0741***		***0.0589***	***0.057***
$U_{11\ (Zr)}$							***0.0071***
$U_{22\ (Zr)}$							***0.0071***
$U_{33\ (Zr)}$							***0.0053***
$U_{11\ (O)}$							***0.053***
$U_{22\ (O)}$							***0.0051***
$U_{33\ (O)}$							***0.014***
Structure	***m-ZrO_2***	***t-ZrO_2***	***m-ZrO_2***	***t-ZrO_2***	***t-ZrO_2***	***t-ZrO_2***	***t-ZrO_2***
Phase %	***36***	***64***	***55***	***45***	***100***	***100***	***100***

IV.2.3.1 Temperature series

PDF refinements of ZrO_2 synthesized in supercritical ethanol as a function of temperature are displayed in Figure IV-2.

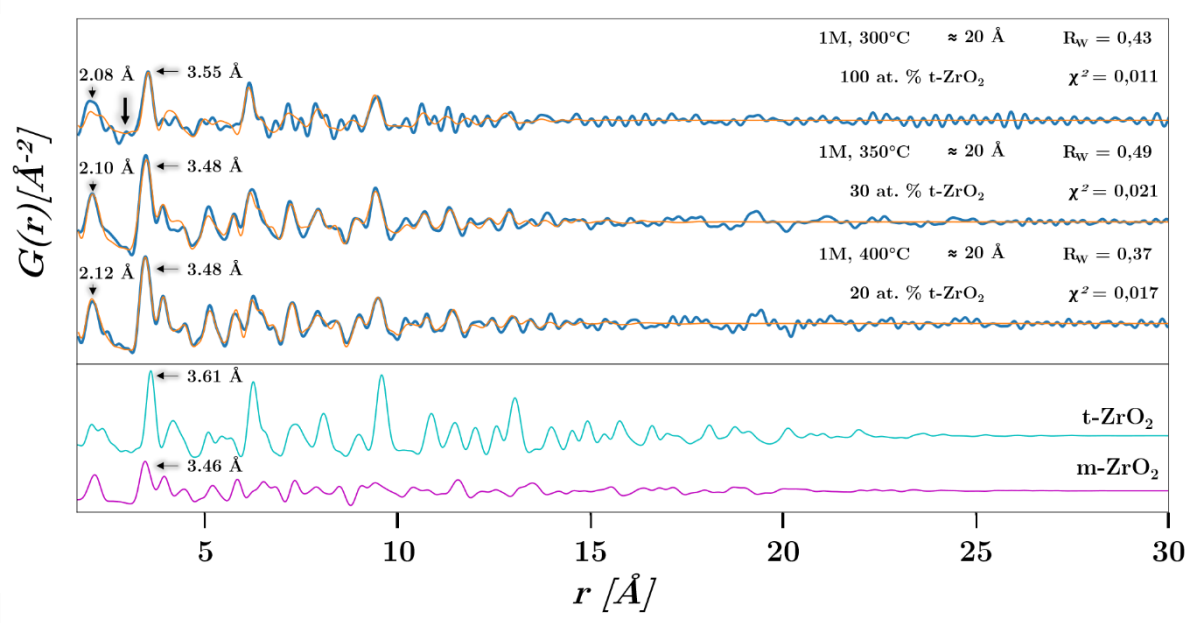

Figure IV-2. PDF refinements obtained for the last frames of ZrO_2 formation measured in supercritical ethanol at 25 MPa, 1 mol/L and at 400, 350 and 300°C from bottom to top, respectively, and where dark blue and orange curves represent the observed (G_{Obs}) and calculated (G_{Calc}) PDF, respectively. The respective temperature; t-ZrO_2 atomic fractions, expected R_W and χ^2 factors obtained from the refinements are displayed on each plot. Below are t- and m-ZrO_2 PDF simulated from the models in cyan and magenta, respectively. Black arrow represents signal from what may correspond to an amorphous fraction.

All PDF in Figure IV-2 correspond to a reaction time of 1400 s (23 min) corresponding to the moment when the reaction at 400°C was stopped though reactions at 350 and 300°C lasted 60 and 36 minutes, respectively. Coherent diffracting domains provided by PDF refinements revealed Spd values of more or less 20 Å for all three measurements. PDF from both measurements at 400 and 350°C could be refined combining t- and m-ZrO_2 models, however PDF from the measurement at 300°C could only be refined using a t-ZrO_2 model. We have seen in Chapter II-3.2.7.2 that at low interatomic distances both Zr-O and Zr-Zr atomic pairs could easily be differentiated in atomic PDF representations. In Figure IV-2, at 400 and 350°C Zr-Zr atomic correlations in the first coordination shell are located at ≈ 3.48 Å (≈ 3.46 Å in the m-

ZrO_2 model in Figure IV-2), while at 300°C the first Zr-Zr shell is distant of 3.55 Å thus close to the Zr-Zr first coordination shell of t-ZrO_2 (3.61 Å in the t-ZrO_2 model in Figure IV-2). PDF refinements revealed that after 23 min of reaction, ≈ 20 and 30 at. % t-ZrO_2 were still measured at 400°C and 350°C, respectively. However, after 60 min of measurement at 350°C, the PDF refinements revealed that only 7 at. % t-ZrO_2 remained in the sample. The synthesis at 300°C resulted in 100 at. % t-ZrO_2 for the whole time of the measurement.

IV.2.3.2 Concentration series

As it was possible to stabilize t-ZrO_2 at 300°C for a precursor concentration of 1 mol/L, it was decided to decrease the precursor concentration down to 0.5 mol/L and measurements were performed at 400 and 350°C as presented in Figure IV-3.

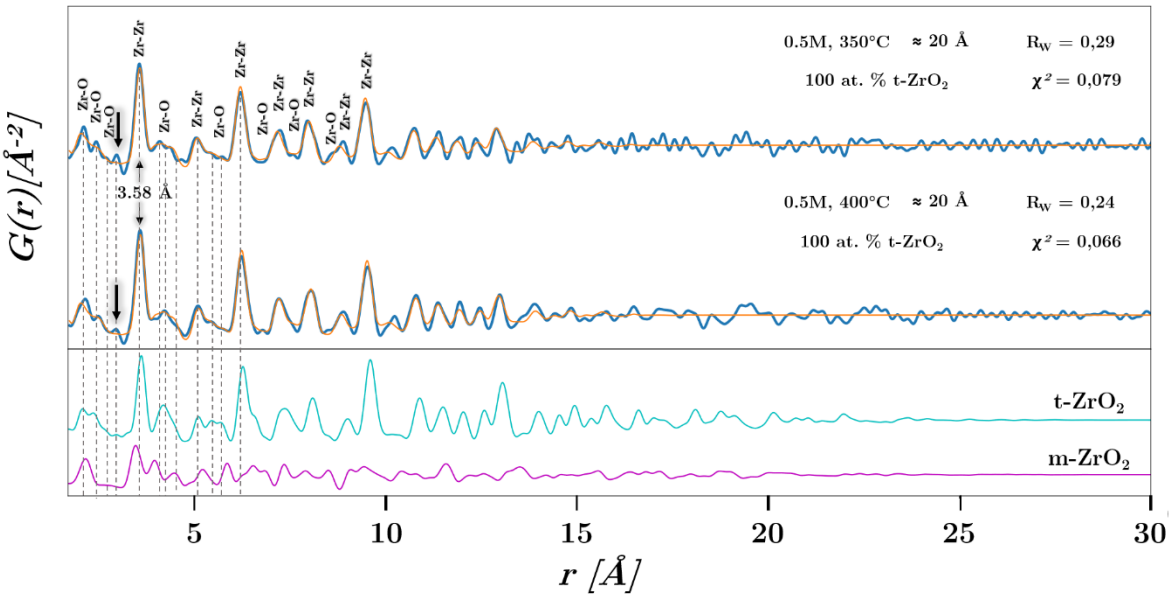

Figure IV-3. PDF refinements obtained for the last frames of ZrO_2 formation measured in supercritical ethanol at 25 MPa, 0.5 mol/L and at 400, 350°C from bottom to top, respectively. Dark blue and orange curves represent (G_{Obs}) and (G_{Calc}), respectively. The respective temperature; t-ZrO_2 atomic fractions, expected R_W and χ^2 factors obtained from the refinements are displayed on each plot. Below are the model independent simulated PDF. Black arrows represent signal from what may correspond to amorphous fractions inside the sample holder.

PDF refinements displayed in Figure IV-3 could only be performed with a t-ZrO_2 model and this is clearly comprehensible seeing the striking similitudes between the experimental PDF and the tetragonal model up to ≈ 15 Å though the first experimental metal-metal distance is

0.04 Å lower than in the models. Nevertheless, it is extremely interesting to see that a decrease in concentration led to stabilizing the t-ZrO_2 structure. However, though R_W factors are lower than those observed in Figure IV-2, χ^2 factors on the other hand are almost 4 times as large as those observed in Figure IV-2. They nevertheless remain quite low, thus allowing to confirm the quality of both refinements.

IV.2.3.3 Surfactant series

Hexanoic acid (HA) and trioctylphosphine (TOP) were used to produce ZrO_2 nanoparticles in supercritical ethanol and all details on the syntheses are listed in Table IV-I. Figure IV-4 shows the PDF after 20 min of measurement for each experiment.

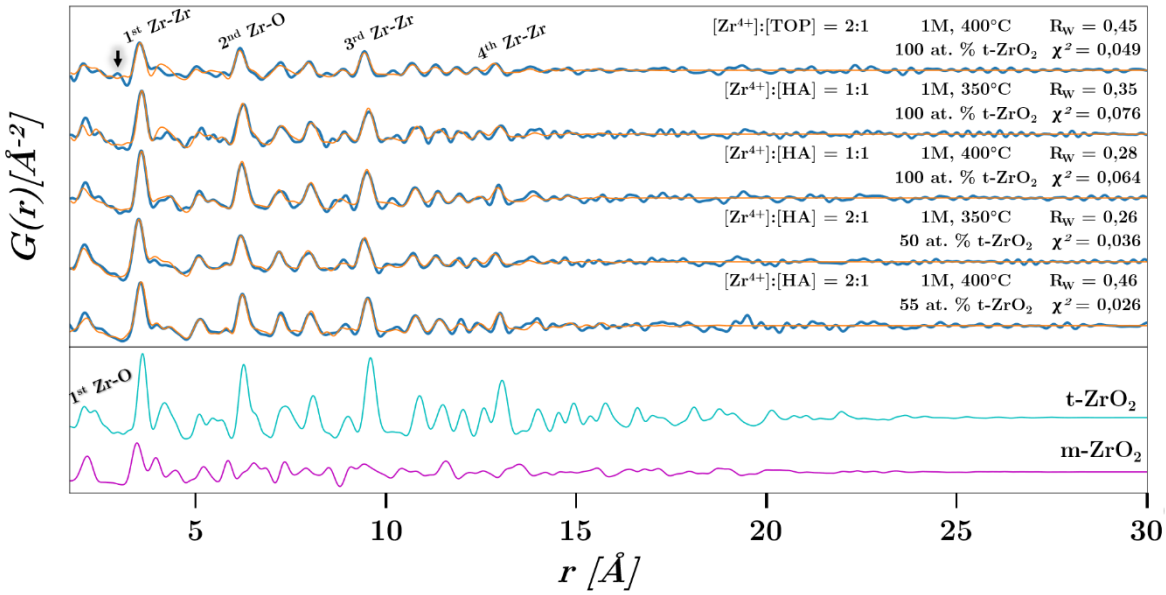

Figure IV-4. PDF refinements obtained for the last frames of surfactant assisted ZrO_2 formation measured in supercritical ethanol at 25 MPa, 1 mol/L and at 400 and 350°C. Dark blue and orange curves represent (G_{Obs}) and (G_{Calc}), respectively. The respective temperatures, surfactant molar ratios, t-ZrO_2 atomic fractions, expected R_W and χ^2 agreement factors obtained from the refinements are displayed for each plot. Below are the model independent simulated PDF. Are also displayed the major metal-metal and metal-oxygen coordination shells. When TOP is used, the black arrow represents signal from what may correspond to an amorphous fraction inside the sample holder.

All PDF in Figure IV-4 extend as far as the 4th Zr-Zr coordination shell, thus ≈ 20 Å, like those displayed previously. We have also seen previously that PDF for measurements at both 400 and 350°C and [Zr^{4+}] = 1 mol/L revealed mixtures of t- and m-ZrO_2 structures, therefore the same experimental parameters were chosen and HA and TOP were added to the precursor solutions

to reach 2:1 and 1:1 [Zr^{4+}]:[surfactant] molar ratios for both temperatures. While a 2:1 molar ratio was not sufficient to obtain 100 at. % t-ZrO_2 at both temperatures, a 1:1 molar ratio succeeded in stabilizing the t-ZrO_2 structure for both temperatures. Also, the synthesis with a 2:1 [Zr^{4+}]:[TOP] molar ratio succeeded in stabilizing t-ZrO_2, thus, the measurement was not performed at 350°C.

Adding surfactants to the precursor solution favored the stabilization of the t-ZrO_2 structure. However, one must keep in mind that the synthesis conditions may have drastically changed by adding surfactants, switching maybe between B.N.H.S.G. and N.H.S.G. reactions as the amounts of surfactants added to the precursor solutions are far from those generally admitted during functionalizing agents assisted syntheses.

However, it seems that the phase transformation was greatly impacted for a 2:1 precursor to HA molar ratio at both 400 and 350°C as the atomic % did not vary during the whole course of both reactions and were maintained at ≈ 50 at. %.

IV.2.4 ZrO_2 nanoparticle growth profiles in supercritical ethanol

IV.2.4.1 Temperature series

PDFgui allows the refinement of PDF in a sequential procedure starting form the last and most accurate PDF of a whole data set to the very first integrated PDF, enabling observation of the evolution of refined parameters in time. Growth profiles obtained from each sequential refinement reveal the evolution in the total particle size, and this for each structure present in the powder, but also the kinetics of formation of each structure in each synthesis, which are extremely valuable information to understand ZrO_2 formation mechanisms.

However, as the nanoparticle size is extremely small for all measurements in supercritical ethanol, only the nanoparticle size evolution will be discussed, allowing us more insight into crystal growth mechanisms in supercritical fluids. Figure IV-5 displays the sequential PDF refinements for ZrO_2 synthesized at 25 MPa and at 400, 350 and 300°C.

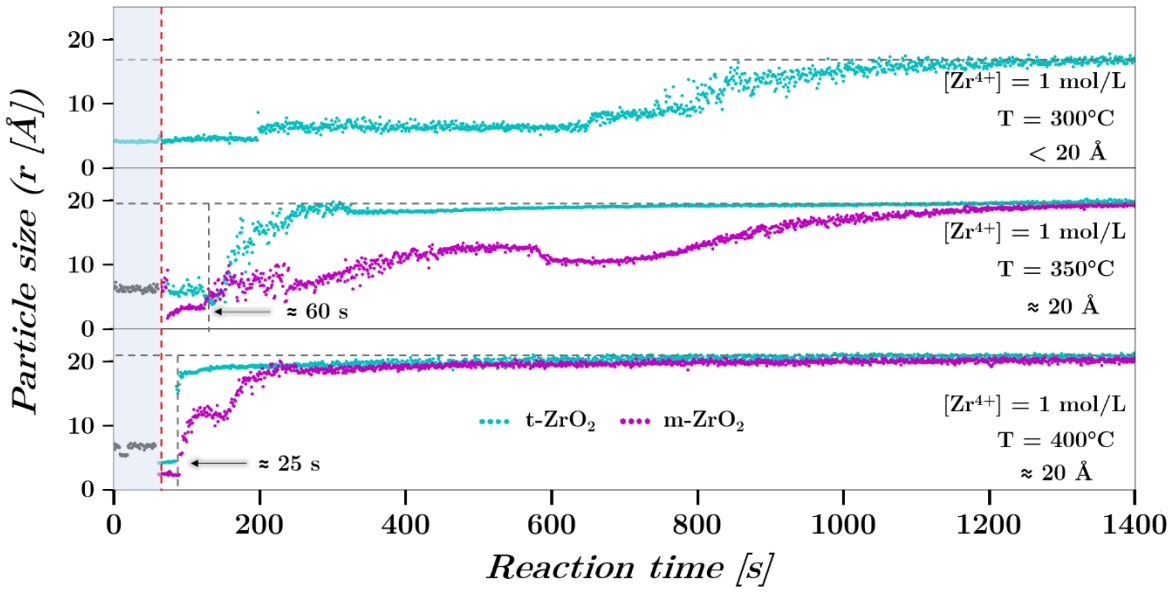

Figure IV-5. Growth profiles during the formation of ZrO_2 in supercritical ethanol at 25 MPa, 1 mol/L and at 400, 350 and 300°C from bottom to top, respectively obtained from the sequential refinements. Cyan and magenta dots represent the t- and m-ZrO_2 structures, respectively. The red dashed-line ending the blue zone on the far left represents the moment the heat was turned on, while the horizontal grey dashed-lines represent the final particle size at the end of each reaction.

Figure IV-5 displays the growth profiles for the first 23 min of ZrO_2 formation measured in supercritical ethanol at 400, 350 and 300°C. These profiles are plotted as the evolution of the extension of the measured PDF (Spd value) as a function of time. As seen previously, at 400 and 350°C both t- and m-ZrO_2 are present, and thus could be refined all along each reaction while at 300°C, only t-ZrO_2 could be used as a model for the refinements. Also, with decreasing temperature, the measured nanoparticle size (Spd) seemed to decrease slightly from just above 20 Å (400°C) to ≈ 17 Å (300°C). However, such small variation in Spd value should be cautiously considered.

A first observation considering difference in growth profiles shows that at 400 and 350°C nucleation of the tetragonal phase rapidly reaches a final plateau at ≈ 20 Å. Also, the simultaneous formation of m-ZrO_2 can be observed, which seems to occur via a two-step process. At first m-ZrO_2 size is stabilized at ≈ 13 Å, and then the second step sees a secondary growth regime where the size of m-ZrO_2 converges towards the size of t-ZrO_2 nanoparticles at ≈ 20 Å and stabilizes until the end of the reaction.

Also, when both t- and m-ZrO_2 are present (400 and 350°C), they are both refined as soon as the reactions take off: i.e., at 400°C burst nucleation of t-ZrO_2 nanoparticles occurs after to ≈

25 s within less than 10 s while nucleation of m-ZrO_2 nanoparticles is much slower. At 350°C, nucleation kinetics of both t- and m- ZrO_2 nanoparticles are slower though still concomitant. Considering the measurement at 300°C, an extremely slow and gradual growth of only t-ZrO_2 nanoparticles occurs.

Between 400 and 350°C, a delay of ≈ 40 s is observed in the ignition of the reaction, probably corresponding to the time necessary to produce enough water molecules *in situ* from supercritical ethanol decomposition but also for the scattering signal to be high enough to be observed on the 2D detector. However, at 300°C, production of water is so slow that the reaction occurs extremely slowly, which can be observed in Figure IV-5 where a step by step increase in particle size is observed for 13 min before a slow and steady increase in particle size is finally observed. This step by step increase in particle size should not be interpreted as such, but rather believed to be resulting from low scattering signal collected by the detector, thus introducing bias in the refinement procedure.

One very interesting feature present in the growth profiles at 400 and 350°C is the similar two-step mechanism by which m-ZrO_2 nanoparticles undergo to reach their final size. However, at 350°C, nucleation kinetic of the m-ZrO_2 structure occurs slowly compared to 400°C in the first growth stage. Subsequent growth of the m-ZrO_2 structure in the second stage also occurs very slowly at 350°C to reach a particle size of ≈ 20 Å like the t-ZrO_2 structure.

These different profiles tend to reveal that the precursor consumption depends on the synthesis temperature due to the number of water molecules released through solvent dehydration as discussed in Chapter I-6. We may thus confirm from these temperature dependent measurements that the synthesis temperature acts as a kinetic lever by releasing water molecules from solvent decomposition at different rates.

IV.2.5 Concentration series

Figure IV-6 displays total X-ray scattering measurements realized at 0.5 mol/L and at both 400 and 350°C for 1100 s (18 min).

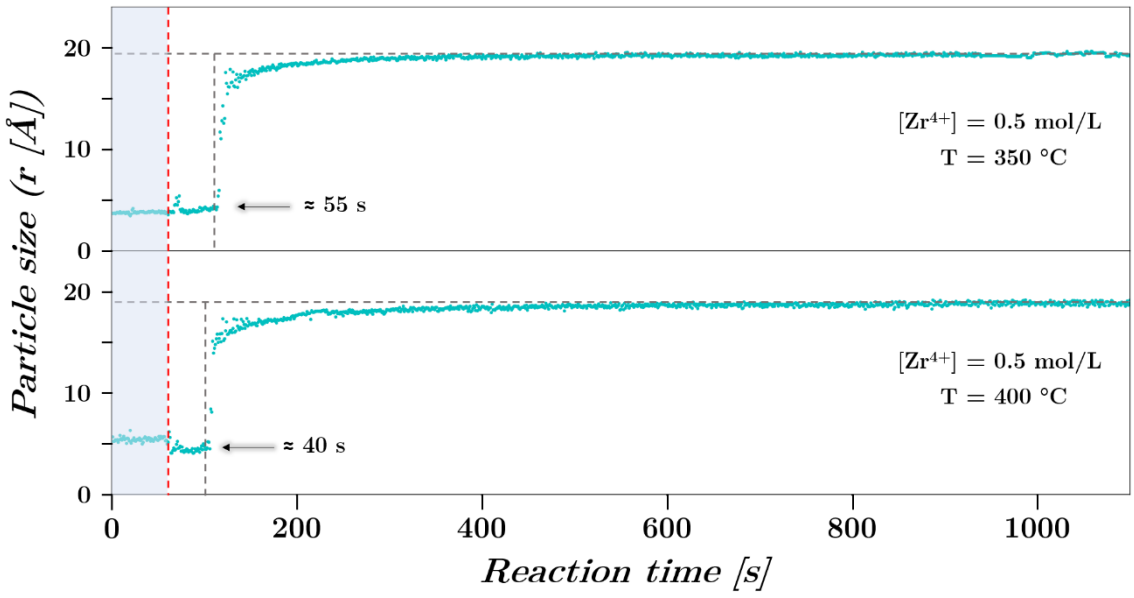

Figure IV-6. Growth profiles, obtained from the PDF sequential refinement, during the formation of ZrO_2 in supercritical ethanol at 25 MPa, 0.5 mol/L and at 400 and 350°C from bottom to top, respectively. The red dashed-line ending the blue zone on the far left represents the moment the heat was turned on, while the horizontal grey dashed-lines represent the final particle size at the end of each reaction, while vertical ones define the triggering of nucleation.

Decreasing the precursor concentration led to stabilizing the pure t-ZrO_2 structure relatively fast and with growth profiles similar to those of the t-ZrO_2 structure at 400°C and 1 mol/L. However, though it only took less than 10 s for t-ZrO_2 nanoparticles to reach 80% of their final size at 1 mol/L and 400°C, for a precursor concentration of 0.5 mol/L, 20 and 30 s were necessary at 400 and 350°C.

IV.2.5.1 Surfactant series

Growth profiles for the surfactant assisted i*n situ* measurements of ZrO_2 formation in supercritical ethanol with both HA and TOP are displayed in Figure IV-7.

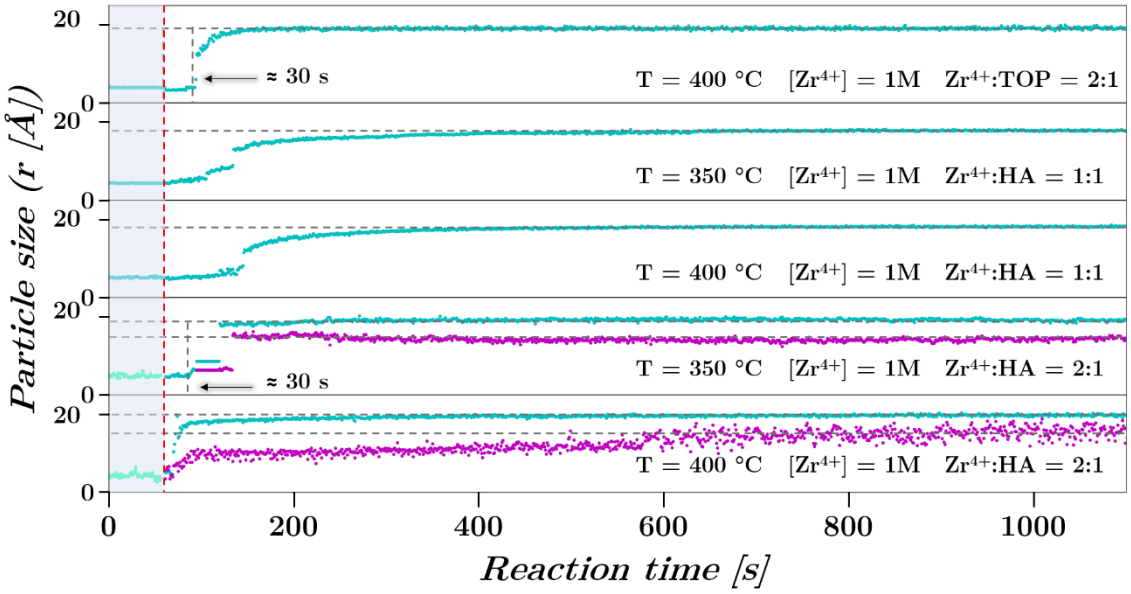

Figure IV-7. Growth profiles during the surfactant assisted formation of ZrO_2 in supercritical ethanol at 25 MPa, 1 mol/L and at 400 and 350°C obtained from the PDF sequential refinements of each data set. Cyan and magenta dots represent the t- and m-ZrO_2 structures, respectively. The red dashed-line ending the blue zone on the far left represents the moment the heat was turned on, while the horizontal grey dashed-lines represent the final particle size at the end of each reaction. All initial conditions and precursor solution contents are displayed for each growth profile.

Out of the 5 measurements displayed in Figure IV-7, 4 were performed with HA: $[Zr^{4+}]$:[HA] = 2:1 and 1:1, both at 400 and 350°C; while with TOP, only a $[Zr^{4+}]$:[TOP] = 2:1 molar ratio was measured at 400°C. The precursor concentration was 1 mol/L for all 5 measurements as in these conditions.

Growth profiles for the syntheses displayed in Figure IV-7 seem to reveal two different mechanisms, where those with a 2:1 molar ratio are similar to those previously presented in Figure IV-5, while the ones with a 1:1 molar ratio seem very different. However, the measurement realized with TOP looks as familiar as those observed in Figure IV-6.

While at 400°C, for a 2:1 $[Zr^{4+}]$:[HA] molar ratio, both structures are present as observed in the temperature series, the m-ZrO_2 structure seems to be stabilized longer at the intermediate size

observed previously (≈ 11 Å) before a slight increase to ≈ 17 Å occurs after 10 min. At 350°C and for 2:1 [Zr^{4+}]:[HA] molar ratio, this intermediate m-ZrO_2 nanoparticle size is stabilized during the 18 min of the measurement. Nevertheless, it is important to note that both structures appear at the same moment for both measurements and that a delay in the ignition of the reactions is observed again.

When a 1:1 [Zr^{4+}]:[HA] molar ratio is used, ignition of the reactions is a slow process at both 400 and 350°C leading to a slow and steady stabilization of t-ZrO_2 with the final size reached in ≈ 4 min for both syntheses.

When TOP is used with a 2:1 molar ratio, t-ZrO_2 nanoparticle nucleation starts with a slight delay after the heat is turned on and the final nanoparticle size is reached within 1 min once the signal from the first nuclei are collected by the detector, revealing also a relatively slow growth process.

These first observations tend to show that a critical size of 15 to 20 Å to stabilize metastable t-ZrO_2 would be plausible as all nanoparticles encompassed in that size range exhibited purely the t-ZrO_2 structure when considering PDF analysis. This metastable structure was stabilized in supercritical ethanol at 25 MPa and for all experimental temperatures chosen: 400, 350 and 300°C. However, initial experimental parameters needed to be adjusted to achieve the stabilization.

IV.2.6 Conclusion

As the starting point of this set of measurements was to confirm or infirm the role of the critical size the control of crystalline structure, or the role of lattice defects generated kinetically through control of water molecules released *in situ* from dehydration of ethanol, we may not at this point pronounce ourselves on the role of the critical size, as all nanoparticle sizes were encompassed between 17 and 20 Å though above 20 Å, measurements reveal structural mixtures while below 20 Å measurements reveal only the presence of t-ZrO_2. We have yet seen in Chapter I that the amount of water generated *in situ* from the decomposition of ethanol above its critical temperature at a constant pressure and for a constant residence time increased linearly with an increase in temperature [146]. Therefore, the role of reaction kinetics at this point seems more appropriate to explain the stabilization of t-ZrO_2. We have however with these measurements, shown that switching between either a thermodynamic regime or a kinetic regime leads to the presence of both structures or only to the tetragonal structure, respectively.

We have emphasized in Chapter I that the dehydration kinetics in relatively apolar alcohols strongly depended on the alkyl chain length. Therefore, to confirm that the difference in results obtained in the temperature series are not temperature dependent, but rather guided by dehydration kinetics, a series of experiments in supercritical alcohols was realized and will be the subject of the next sections, where results will be compared to observations made in supercritical ethanol.

IV.2.7 *In situ* investigation of ZrO_2 formation in supercritical alcohols

For this set of measurements, a fixed temperature of 400°C was chosen and was not varied, along with the constant pressure of 25 MPa and a precursor concentration of 1 mol/L. By doing so, the idea was to generate less and less water as the solvent alkyl chain increased in the same fashion as decreasing the temperature in supercritical ethanol led to reduce dehydration kinetics.

IV.2.8 Sample preparation

All sample preparations were identical to previously detailed for measurements in supercritical ethanol.

IV.2.8.1 Materials

Zirconium(IV) propoxide solution 70 wt. % in 1-propanol [$Zr(OCH_2CH_2CH_3)_4$], absolute propanol [C_3H_7OH], butanol [C_4H_9OH], pentanol [$C_5H_{11}OH$] and hexanol [$C_6H_{13}OH$] were used to synthesize ZrO_2 in supercritical alcohols. All chemicals were purchased from sigma-Aldrich and used as received.

IV.2.8.2 Procedure

Unfortunately, measurements on the formation of ZrO_2 in supercritical propanol were extremely hard to interpret and will therefore not be presented in this work. Therefore, only the measurements in supercritical butanol, pentanol and hexanol will be presented with the aim to investigate the role of the nanoparticle size and the influence of the solvent alkyl chain length on the final structure, but also corroborate with the idea that reaction kinetics should be adjustable depending on the alcohol used, as discussed in the literature survey in Chapter I.

IV.2.9 Measurements conducted in supercritical alcohols

Table IV-5. lists the different experiments conducted to study the formation of ZrO_2 nanoparticles in different supercritical alcohols. Table IV-5. List of all experiments performed in supercritical alcohols.

Experiment	*Solvent*	*$[Zr^{4+}]$ (M)*	*T (°C)*
1	*Sc-butanol*	*1*	*400*
2	*Sc-pentanol*	*1*	*400*
3	*Sc-hexanol*	*1*	*400*

The list of refined parameters and their final values is given in Table IV-6.

Table IV-6. List of all the refined parameters for the supercritical alcohol series.

Refined parameters	*Alcohol series, 400°C, 25 MPa*		
	Sc-butanol	*Sc-pentanol*	*Sc-hexanol*
		Tetragonal phase	
Scale factor	*0.15*	*0.27*	*0.14*
a (Å)	*3.6020*	*3.6104*	*3.6412*
b (Å)	*3.6020*	*3.6104*	*3.6412*
c (Å)	*5.1979*	*5.2070*	*5.259*
Sp diameter (Å)	*67.5*	*61.7*	*65*
O_Z	*0.0648*	*0.0535*	*0.0457*
$U_{11\ (Zr)}$ ($Å^2$)	*0.00817*	*0.00828*	*0.0084*
$U_{22\ (Zr)}$ ($Å^2$)	*0.00817*	*0.00828*	*0.0084*
$U_{33\ (Zr)}$ ($Å^2$)	*0.0101*	*0.0101*	*0.0117*
$U_{11\ (O)}$ ($Å^2$)	*0.015*	*0.017*	*0.0531*
$U_{22\ (O)}$ ($Å^2$)	*0.0535*	*0.042*	*0.0138*
$U_{33\ (O)}$ ($Å^2$)	*0.06026*	*0.1532*	*0.0672*
Phase percentage (at. %)	*63*	*100*	*100*
		Monoclinic phase	
Scale factor	*0.1*		
a (Å)	*5.1626*		
b (Å)	*5.1834*		
c (Å)	*5.3283*		
Sp diameter (Å)	*68.8*		
$U_{11\ (O\text{-}I)}$ ($Å^2$)	*0.0095*		
$U_{22\ (O\text{-}I)}$ ($Å^2$)	*0.017*		
$U_{33\ (O\text{-}I)}$ ($Å^2$)	*0.0466*		
$U_{11\ (O\text{-}II)}$ ($Å^2$)	*0.0001*		
$U_{22\ (O\text{-}II)}$ ($Å^2$)	*0.018*		
$U_{33\ (O\text{-}II)}$ ($Å^2$)	*0.0536*		
Phase percentage (at. %)	*37*		
Delta 2	*3*	*3*	*3*
R_W	*0.24*	*0.18*	*0.3*

The parameter Delta 2 was chosen to remain constant throughout all 3 refinements, with a value of 3.

IV.2.9.1 ZrO_2 formation in supercritical butanol

Figure IV-8 shows a characteristic reduced PDF after 20 min of ZrO_2 formation, thus at the end of the reaction measured in supercritical butanol at 25 MPa and 400°C.

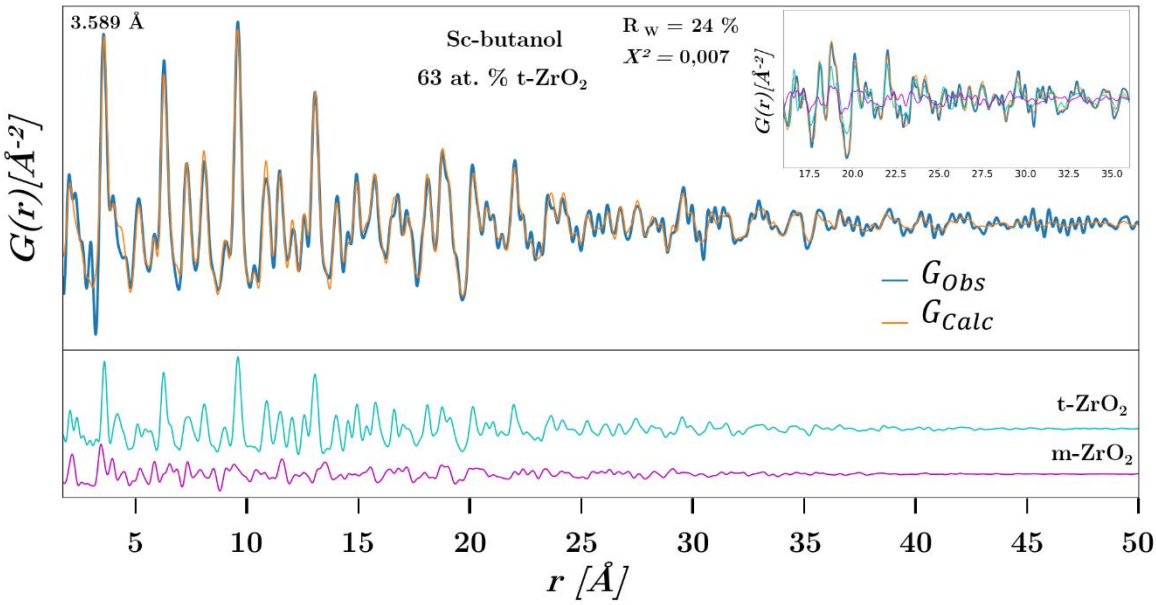

Figure IV-8. PDF refinement in the 1.72 to 50 Å range obtained for the last frame of ZrO_2 measured in supercritical butanol at 25 MPa, 1 mol/L and at 400°C. Dark blue and orange curves represent (G_{Obs}) and (G_{Calc}), respectively. t-ZrO_2 atomic fraction, expected R_W and χ^2 agreement factors obtained from the refinement are also displayed. Below are simulated PDF of t-and m-ZrO_2 60 Å nanoparticles in cyan and magenta, respectively. In the inset are represented the PDF and the models in the 17-35 Å range.

The PDF refinement represented in Figure IV-8 revealed ≈ 70 Å t- and m- ZrO_2 nanoparticles (Table IV-6), which is almost 3 times as large as ZrO_2 nanoparticles synthesized in supercritical ethanol (≈ 20 Å). Also, the powders consisted of a mixture of 63 at. % t-ZrO_2 and 37 at. % m-ZrO_2. The quality of the refinement is emphasized by the χ^2 factor = 0.007 and the extent of the refinement until ≈ 40 Å as shown in the inset of Figure IV-8 where both models (G_{Calc}) fit nicely the experimental data (G_{obs}) up to ≈ 35-40 Å. However, though atomic correlations are observed in the PDF further than 50 Å, PDFgui cannot perform refinements as the intensity of the signal is too low due to the dampening of the scattered intensity during X-ray measurements. The inset in Figure IV-8 also shows that the structure is relatively well refined with both models

where most PDF peaks fit nicely the t-ZrO_2 structure at distant bond correlations, supporting the determined atomic fractions.

IV.2.9.2 ZrO_2 formation in supercritical pentanol

A PDF characteristic of the last moments of the measurement of ZrO_2 formation in supercritical pentanol at 25 MPa, 1 mol/L and 400°C is presented in Figure IV-9.

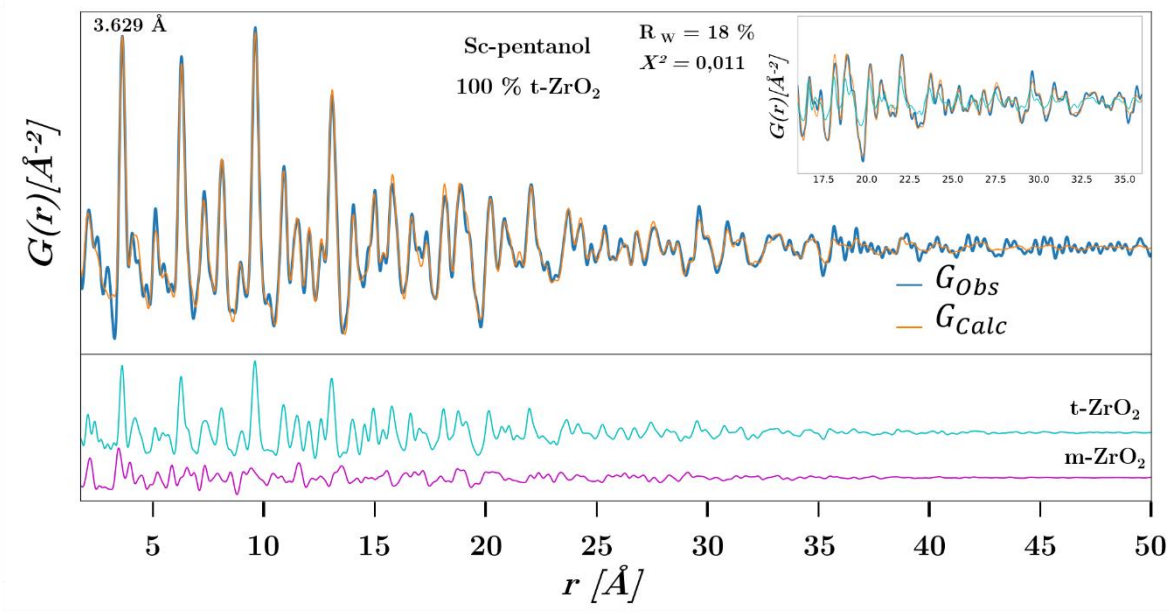

Figure IV-9. PDF refinement in the 1.72 to 50 Å range obtained for the last frame of ZrO_2 measured in supercritical pentanol at 25 MPa, 1 mol/L and at 400°C. Dark blue and orange curves represent (G_{Obs}) and (G_{Calc}), respectively. R_W and χ^2 agreement factors are also displayed. Below are simulated PDF of t-and m-ZrO_2 60 Å nanoparticles in cyan and magenta, respectively. In the inset are represented the PDF and the models in the 17-35 Å range.

PDF refinements of ZrO_2 formation in supercritical pentanol could not be performed with both t- and m-ZrO_2 structures without systematically diverging from the model at any point of the reaction, thus the experimental data were modeled only as t-ZrO_2 nanoparticles. The PDF in Figure IV-9 could accurately be refined up to 35-40 Å though the total size of the particles obtained after the refinement was 68 Å as listed in Table IV-6. However, a slight gradual shift between bond correlations expected from the model and those refined is observed as r increases as shown in the inset of Figure IV-9. The χ^2 parameter for this PDF refinement is 0.011, thus,

it is expected that the structure of the powders synthesized in supercritical pentanol is purely tetragonal.

IV.2.9.3 ZrO_2 in formation supercritical hexanol

As for observations made in supercritical pentanol, PDF refinements of ZrO_2 formation in supercritical hexanol could not be performed with both t- and m-ZrO_2 structures without systematically diverging from the model and were therefore also fitted using only a t-ZrO_2 model. Figure IV-10 shows a typical PDF of ZrO_2 crystallized in supercritical hexanol.

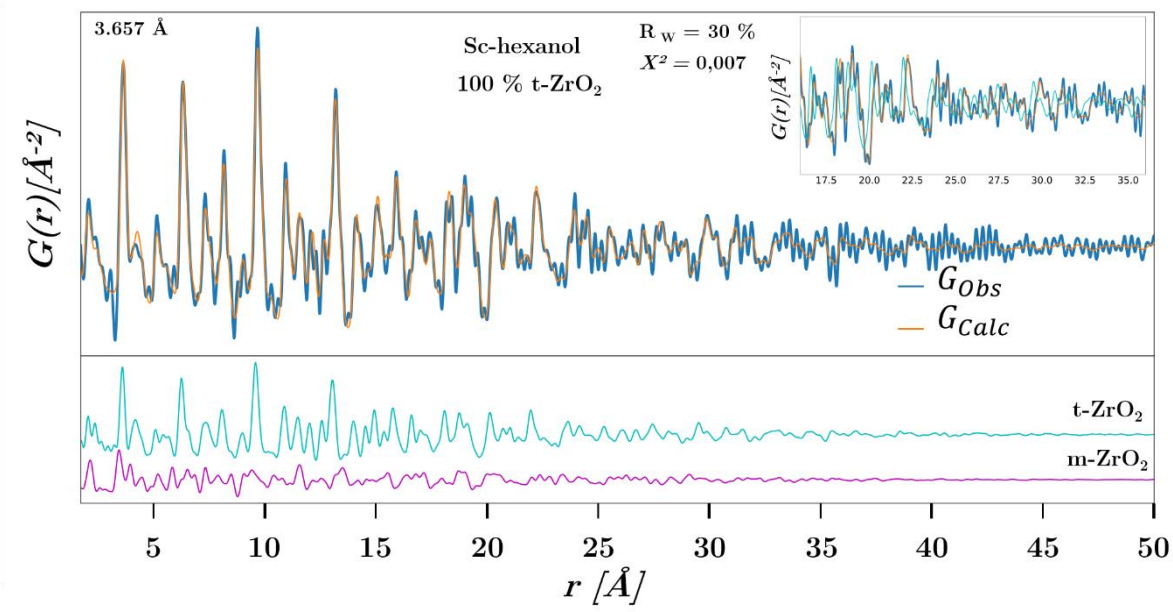

Figure IV-10. PDF refinement in the 1.72 to 50 Å range obtained for the last frame of ZrO_2 measured in supercritical hexanol at 25 MPa, 1 mol/L and at 400°C. Dark blue and orange curves represent (G_{Obs}) and (G_{Calc}), respectively. R_W and χ^2 agreement factors are also displayed. Below are simulated PDF of t-and m-ZrO_2 60 Å nanoparticles in cyan and magenta, respectively. In the inset are represented the PDF and the models in the 17-35 Å range.

In Figure IV-10 the accuracy of the PDF refinement extends up to 25 Å, and though still acceptable until 32 Å, the total size of the nanoparticles (Spd) obtained from the PDF refinements however is 62 Å as listed in Table IV-6. Also important to note is the increasing noise observed with an extent in bond correlations relatively to both Figures IV-8 and 9. Nevertheless, for this PDF χ^2 = 0.007, which is relatively as good as for the two previous refinements. However, in the inset of Figure IV-10, a large shift in bond correlations between

the model and the refined distances is observed as r increases, indicating that between butanol, pentanol and hexanol, structural disorder increases and spreads through the whole structure.

IV.2.10 ZrO_2 nanoparticle growth profiles in supercritical alcohols

As for the previous measurements in supercritical ethanol, sequential PDF refinements of ZrO_2 formation measured in supercritical alcohols were performed and are represented in Figure IV-11.

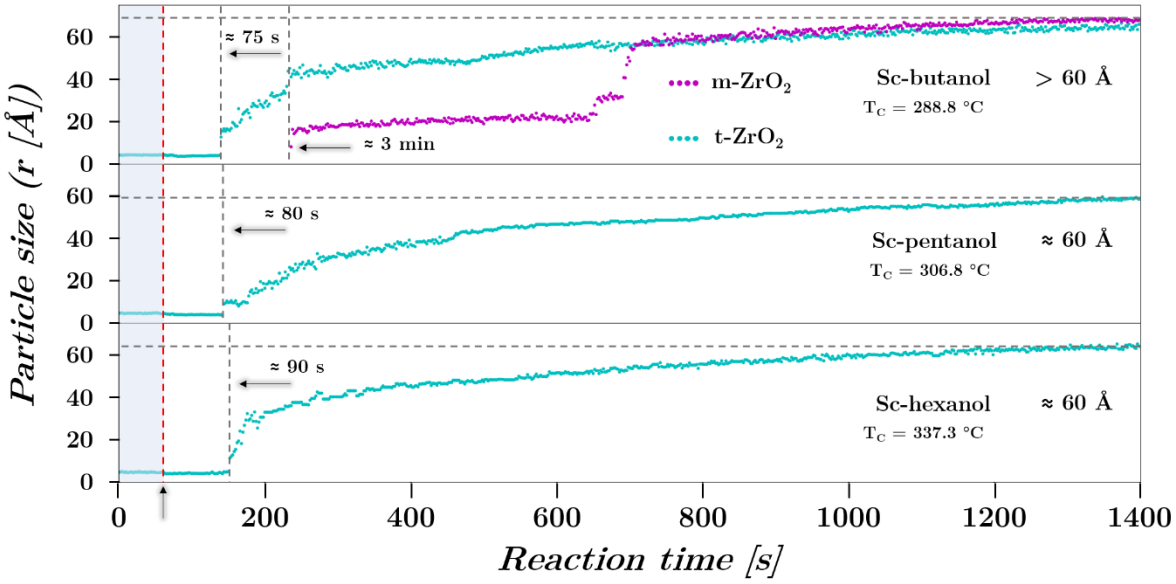

Figure IV-11. Growth profiles for ZrO_2 formation measured in supercritical alcohols at 25 MPa, 1 mol/L and at 400°C. with, in cyan and in magenta respectively t- and m-ZrO_2 structures. The red dashed-line ending the blue zone on the far left represents the moment the heat was turned on, while the horizontal grey dashed-lines represent the final particle size at the end of each reaction.

We can see in Figure IV-11 that, though a 3-step process is observed here in the formation of m-ZrO_2, the formation of t- and m-ZrO_2 structures measured in supercritical butanol at 400°C follow a similar trend as those observed during the formation of ZrO_2 in supercritical ethanol at 350°C (Figure IV-5). However, the sequential refinements do not reveal that nucleation of both t- and m-ZrO_2 structures occurs simultaneously with the first traces of m-ZrO_2 nucleation collected by the detector only after 3 min of synthesis and more than 1 min after t-ZrO_2 nucleation is detected. Also, the slow growth of t-ZrO_2 seems to occur in a multistep process with many plateaus reached at 20, 30 and 40 Å during many minutes. Scattering signal from m-

ZrO_2 becomes visible and reaches ≈ 17 to 23 Å for at least 10 min when the size of t-ZrO_2 is ≈ 40 Å. A sudden second stage in m-ZrO_2 growth process leads to a particle size of ≈ 33 Å for almost 30 s before bursting to its final size averaged at the converging limit of the t-ZrO_2 nanoparticles.

Growth profiles for the two other syntheses are somewhat easier to describe as they involve only the t-ZrO_2 structure and the average particle size converges to the same limit as when the synthesis is realized in butanol.

In the case of supercritical pentanol, burst nucleation results in a first plateau at ≈ 10 Å and subsequent slow homogeneous nucleation occurs all through the reaction. Finally, considering the measurement performed in supercritical hexanol, a continuous homogeneous nucleation profile is visible until the reaction is stopped after 23 min. The reaction kinetics of the two measurements performed in supercritical pentanol and hexanol are showing similitudes with those observed in supercritical ethanol at 300°C and those with a 1:1 [Zr^{4+}]:[HA] molar ratio in terms of reaction kinetics and thus particle growth.

IV.2.10.1 Conclusion

These observations show that pure t-ZrO_2 could be stabilized in both supercritical pentanol and hexanol at a nanoparticle size three times as large as all of those seen in the case of supercritical ethanol, but also at a temperature it couldn't possibly be done in supercritical ethanol. Indeed, when considering the increase in the solvent's respective critical temperatures (Figure IV-1) from ethanol to hexanol, the difference increases from 47.24°C between ethanol and butanol, 65.24°C between ethanol and pentanol and up to 95.74°C between ethanol and hexanol while the temperature was varied from 400, to 350 and finally 300°C in the supercritical ethanol series. Therefore, seeing such behaviors for the alcohol series does not seem absurd. When combining observations on all three temperature dependent measurements performed in supercritical ethanol to those performed in supercritical alcohols, we may believe that there exist great similarities between *in situ* measurements performed in supercritical ethanol and those performed in the other supercritical alcohols at 400°C. Indeed, while reaction kinetics were controlled by the synthesis temperature in the former, in the latter reaction kinetics were controlled by using supercritical alcohols displaying critical temperatures closer to 400°C as the alkyl chain length increased, thus were believed to generate less water molecules at 400°C as the alcohol chain length increased if our suppositions presented in chapter I were correct.

Finally, stabilization of t-ZrO_2 by size effect does not seem appropriate in view of these results as the A.C.S. obtained in supercritical alcohols are three times as large as those obtained in supercritical ethanol. However, as it has been clearly identified by these two sets of measurements that reaction kinetics are critical in stabilizing metastable t-ZrO_2, and that this parameter seems far more important than the size effect, we will therefore focus our attention on oxygen vacancy concentrations, responsible for the increasing local disorder and atomic correlation distances as observed in the insets of Figures IV- 8, 9 and 10, as well as the structural similarities between the precursor configurations and reactional pathway in the future sections of this work.

IV.3 Structural local order/disorder in ZrO_2 synthesized in supercritical alcohols

IV.3.1 ZrO_2 short-range local ordering in supercritical butanol

Figure IV-12 shows the PDF of ZrO_2 synthesized in supercritical butanol (Figure IV-8) in the 1.75-14 Å range, thus the short-range local structure of the nanoparticles.

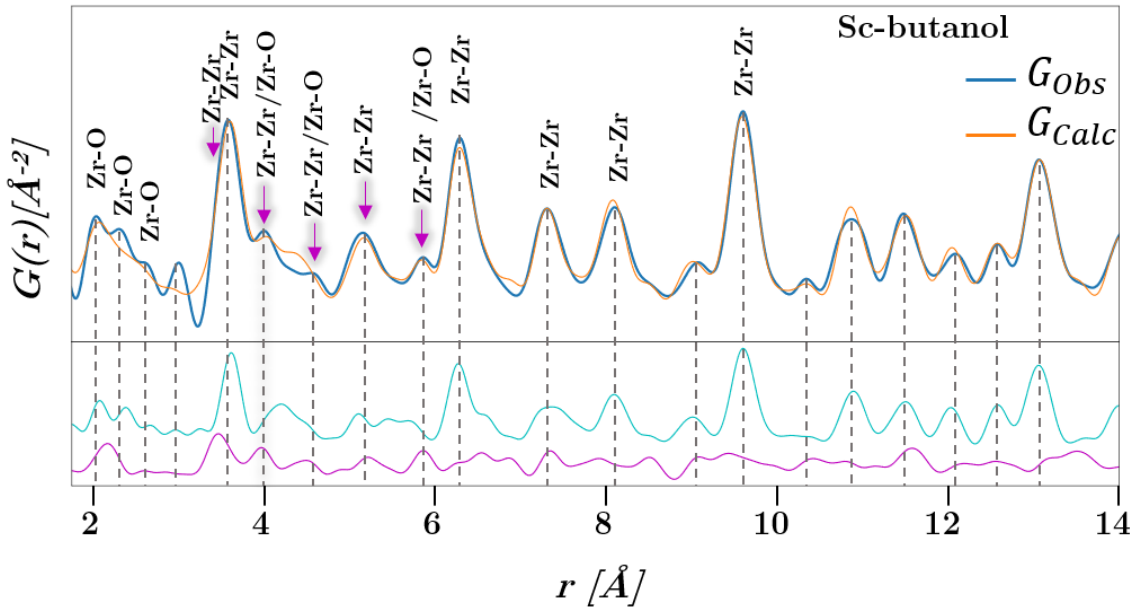

Figure IV-12. PDF refinement in the 1.72 to 14 Å range of ZrO_2 synthesized in supercritical butanol where major bond correlations are listed up to 10 Å (3rd t-Zr-Zr shell). Both t- and m-ZrO_2 models are displayed below for comparison in cyan and magenta, respectively. Magenta arrows attribute the major m-Zr-Zr and m-Zr-O bond correlations visible in the PDF.

In Figure IV-12, we see that the first Zr-O interatomic distances are located between 1.8 and 2.8 Å, versus 1.89 - 2.84 Å and 1.89 - 2.43 Å for the t-ZrO_2 and m-ZrO_2 models, respectively. The first Zr-Zr interatomic distances at 3.59, 4.01 and 5.21 Å also can be compared to both models where for m-ZrO_2, the first metal-metal distance in the model is located at 3.47 Å, while for t-ZrO_2, it is located at 3.62 Å, but also the second and third Zr-Zr distances correspond to those of the model for m-ZrO_2 (3.98 and 5.21 Å). The small peak at 5.86 Å, which is also at 5.86 Å in the m-ZrO_2 model, is the last m-ZrO_2 contribution clearly visible as its scattering signal is then too low compared to t-ZrO_2 in the whole r range. Mismatches in intensities in the Zr-O bond correlations are observed in the second coordination shell at 4.38 Å, probably due to the presence of oxygen vacancies, while all Zr-Zr correlation intensities are well fitted up to the 3rd shell.

IV.3.2 ZrO_2 short-range local ordering in supercritical pentanol

Figure IV-13 shows the PDF refinement presented in Figure IV-9 in the 1.72-14 Å range to observe the local structure of the nanoparticles.

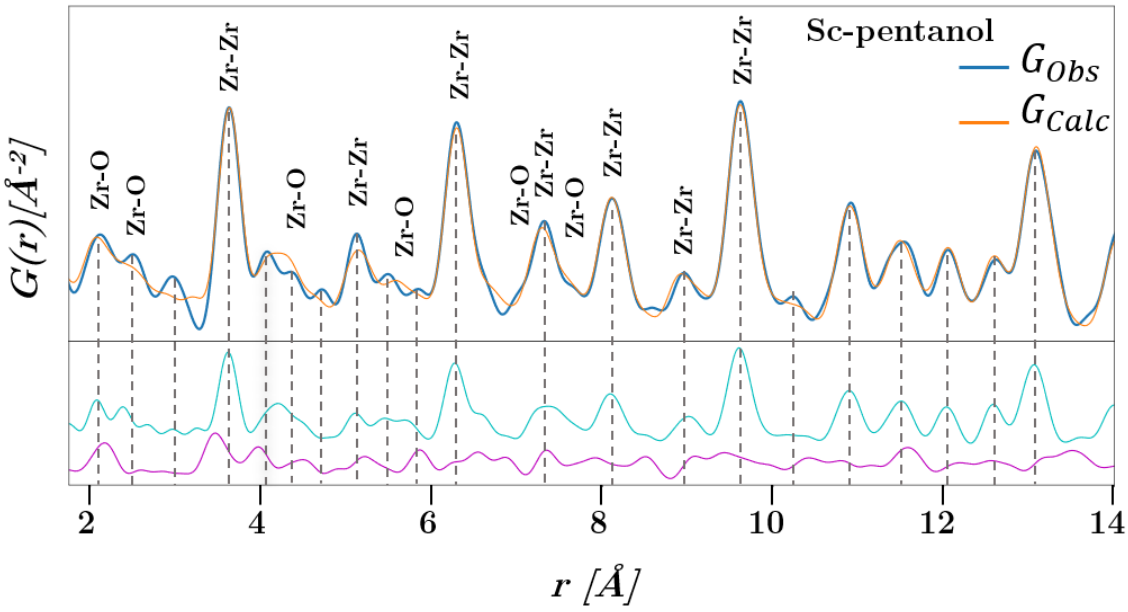

Figure IV-13. PDF refinement in the 1.72 to 14 Å range of ZrO_2 synthesized in supercritical pentanol where major bond correlations are listed up to 10 Å. Both t- and m-ZrO_2 models are displayed below for comparison in cyan and magenta, respectively.

PDF refinement representing the local ordering in the 1.72 to 14 Å range of ZrO_2 synthesized in supercritical pentanol. Both t- and m-ZrO_2 models are displayed below for comparison in cyan and magenta, respectively.

In Figure IV-13, both models are displayed for comparison though the one for m-ZrO_2 could not be refined. The first Zr-O and Zr-Zr shells in the PDF are located between 1.8 - 2.8 Å and ≈ 3.63 Å, corresponding clearly to those observed on the t-ZrO_2 model. Interesting also, no shouldering is visible on the left of the peak at 3.63 Å. The PDF in Figure IV-13 however reveals a slight deviation from the model right from the first Zr-O and Zr-Zr shells, probably due to increasing structural distortion involving both Zr and O atoms. Also, though a slight shift in bond correlations was observed between 18 and 35 Å in the inset of Figure IV-9, the phenomenon in the 1.72-14 Å range in Figure IV-13 is extremely small in comparison.

IV.3.3 ZrO_2 short-range local ordering in supercritical hexanol

Figure IV-14 shows the PDF refinement shown in Figure IV-10 in the 1.72-14 Å range.

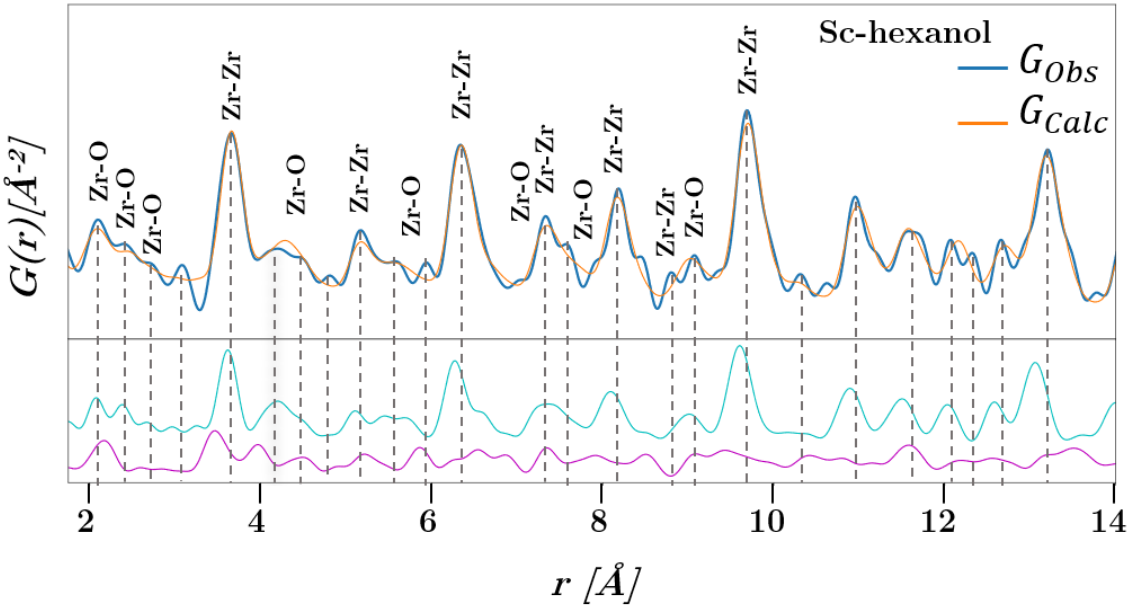

Figure IV-14. PDF refinement in the 1.72 to 14 Å range of ZrO_2 synthesized in supercritical hexanol. Both t- and m-ZrO_2 models are displayed below for comparison in cyan and magenta, respectively.

One can see in the PDF shown in Figure IV-14 that the first and second Zr-O correlations between 1.8 - 5 Å are clearly similar to those in the t-ZrO_2 model. Also, all coordination shells

are subject to a relatively large increase in bond correlations compared to the model. However, lower intensities in Zr-O correlations are observed, spreading through each of the Zr-O positions in the r range, and while Zr-Zr positions and intensities at 3.65 and 6.34 Å could be refined to the model, the intensities of the ones at 9.69 and 13.21 Å are lower than the model's, probably caused by the observed large structural distortions.

Local disorder in the structure is clearly visible from the shift in atomic correlation operating from as low as 2.08 Å (first Zr-O coordination shell), and spreads throughout the structure in a large elastic increase from peak to peak as observed in Figures IV-10 and 14. Another indicator of disorder is the enlargement of the Zr-Zr PDF peak at 6.34 Å, where structural distortion is observed on both sides of the peak. These results tend to show that the t-ZrO_2 structure is stabilized by large amounts of structural defects when synthesized in supercritical hexanol. Table IV-7 lists the variations in Zr-Zr correlations, and compared to those of the model used (ICSD # 66781), for the first 4 coordination shells ($r \approx 14$ Å), obtained from all measurements were only t-ZrO_2 could be refined during PDF analysis as displayed in Figures IV-2, 3, 4, 9 and 10. However PDF from the measurement in supercritical butanol (Figure IV-8) are also listed in Table IV-7 for the extreme closeness in lattice constants to the model is astonishing.

Table IV-7. Zr-Zr bond correlations obtained from PDF analysis for pure t-ZrO_2 nanoparticles, except for the measurement performed in supercritical butanol.

Supercritical ethanol series, interatomic distances (Å)						
Model	1M, 300°C	0.5M, 400°C	0.5M, 350°C	1M, 400°C, Zr:HA [1:1]	1M, 350°C, Zr:HA [1:1]	1M, 400°C, Zr:TOP [2:1]
3.61	3.55	3.58	3.57	3.58	3.59	3.54
6.27	6.18	6.24	6.21	6.22	6.25	6.18
9.6	9.47	9.52	9.49	9.51	9.56	9.45
13.06	nc	12.98	12.92	12.97	13.03	12.89

Supercritical alcohol series, interatomic distances (Å)			
Model	SC-butanol	SC-pentanol	SC-hexanol
3.61	3.58	3.62	3.65
6.27	6.28	6.29	6.34
9.6	9.6	9.62	9.69
13.06	13.06	13.08	13.21

From Table IV-7, one can see that stabilization of t-ZrO_2 nanocrystallites in supercritical ethanol occurs for particles displaying interatomic distances encompassed between those of m- and t-ZrO_2 reported interatomic distances, thus a regular t-ZrO_2 lattice compressive stress. These bond correlations display very slight discrepancies regardless of the reaction media used to synthesize ZrO_2 nanoparticles. Considering the measurement performed in supercritical

butanol, all 4 coordination shells display interatomic distances extremely close to those of a regular t-ZrO_2 lattice, though only 63 at. % t-ZrO_2 was determined from the PDF refinement. The interesting observation comes from both measurements performed in longer alkyl chain alcohols, where all bond correlations are larger than the t-ZrO_2 model used. Indeed, in both supercritical pentanol and hexanol, bond correlations increase for all 4 coordination shells, as already observed in Figures IV-13 and 14, thus tensile stress applied to the crystal lattice for ZrO_2 synthesized in these two solvents.

Though it is not possible to conclude yet, it is highly plausible that oxygen sublattices containing large amounts of defects generate structural disorder, induced by either compressive or tensile stress, allowing the stabilization of t-ZrO_2. But gaining deeper understanding necessitates to gain information on the local environment of Zr atoms.

IV.4 Lattice oxygen vacancies

The local average structure around Zr atoms was observed in detail in the first PDF peaks, corresponding to the first Zr-O and Zr-Zr coordination shells, and modelled using a Gaussian distribution as the atomic deviations from thermal and non-zero point motion from non-Gaussian distributions is negligible [263].

IV.4.1 Local ordering around zirconium atoms

Figure IV-15 is a representation of the first Zr-O and Zr-Zr coordination shells for the t-ZrO_2 structure where local order will be observed in this section.

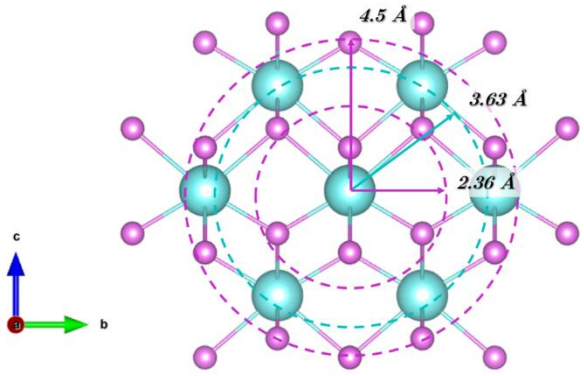

Figure IV-15. Representation of the first and second Zr-O and first Zr-Zr coordination shells. Zr and O atoms are represented in cyan and magenta, respectively, while coordination shells are represented in dashed lines of the corresponding colors.

For the measurements that allowed only pure t-ZrO_2, the low region of the final PDF was magnified around the first Zr-O and Zr-Zr shells to observe the relative variation in Zr coordination number and structural distortions. The aim was to obtain information on the impact of reaction kinetics on the local structure depending on the measurements, and their related structural defects. Figure IV-16 shows the PDF of the last scattered intensity frames for all measurements resulting in pure t-ZrO_2.

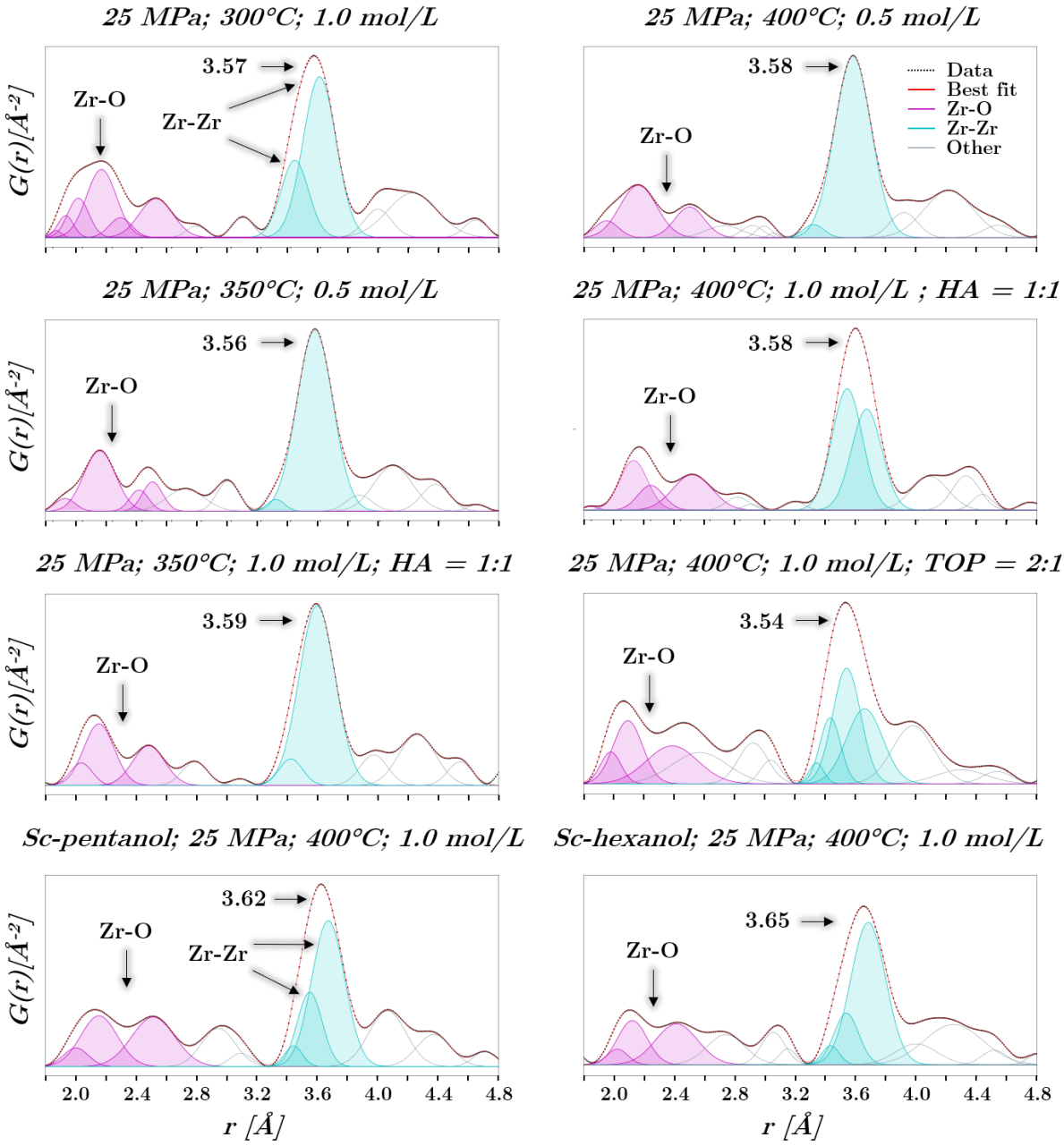

Figure IV-16. Low r region for all pure t-ZrO_2 measured PDF ($G(r)$).

The trend in oxygen coordination variation around Zr atoms was semi quantified by calculating the total integrated intensity underneath the PDF peaks of the first Zr-O and Zr-Zr coordination shells, as expressed in Equation (II − 18) in Chapter II-3.2.7 [263]. A reference of 12 for the pair correlation in the first Zr-Zr coordination shell was estimated for the crystallized ≈ 20 and ≈ 60 Å ZrO_2 nanoparticles as it is the number of Zr atoms coordinated to a central Zr atom in t-ZrO_2. The value of O atoms in the first Zr-O coordination shell, expected to be 8, was then determined from the ratio between integrated areas in both shells for each PDF.

The total areas for the first Zr-O and Zr-Zr coordination shells were integrated using Fityk software from the fits displayed in Figure IV-16. Areas for the Zr-O coordination shell were integrated between 1.8 and 2.8 Å, while those for the first Zr-Zr shell were integrated between 3.2 and 4.0 Å, corresponding to the extent of both Zr-O and Zr-Zr bond distributions in ZrO_2. In the t-ZrO_2 model, Zr-O interatomic distances in the first coordination shell are equally distributed at 2.09 and 2.36 Å, however, Zr-Zr bonds are unequally distributed, with 4 and 8 bonds are distant of 3.59 and 3.63 Å, respectively.

We can see that though PDF were all refined as pure t-ZrO_2, all Zr-O correlations are larger than expected by the model and most do not display, in the first coordination shell, equally distributed Zr-O bond correlations as would be expected appart of measurements performed in supercritical pentanol and hexanol. Also, the fact that the largest Zr-O bond distribution is observed in the measurement realized at 300°C and 1 mol/L is not surprizing as its formation was the less kinetically favored, as observed in Figure IV-5.

Also, the mean average Zr-Zr bond correlations are located between 3.54 and 3.59 Å, corresponding to the smallest bond correlations observed in the t-ZrO_2 models, but also to the intermediate Zr-Zr bond lengths in the m-ZrO_2 model. Interestingly, the PDF representing measurement with TOP has the Zr-O and Zr-Zr bond distributions the closest to the t-ZrO_2 model, though the largest Zr-Zr bond distribution.

From the PDF peak integration, the metal to oxygen atomic ratio obtained were all approximately 12 to 7, though 12 to 8 is expected for t-ZrO_2. As all possible m-, t- and c-ZrO_2 models were fitted to the experimental PDF, even those including oxygen substoichiometry, the most accurate model was selected and therefore all refinements are trusted to be representative of the best possible fits as the number of refined parameters was varied until the best fit was observed for each refinement. Therefore, it must be admitted that, due to the presence of defects, such small nanoparticles exhibit bond correlations of both m- and t-ZrO_2 structures.

Results, displayed in Figure IV-16 reveal that pure t-ZrO_2 could be stabilized by large oxygen vacancy concentration with zirconium coordination encompassed between 6.9 and 7.2 while this value should be slightly lower than 8. However, caution is required when estimating from radial distribution functions absolute values for zirconium coordination number on measurements performed during syntheses. Therefore, values for coordination numbers are only considered relatively to one another rather than absolute, and thus only as tendancies. Unfortunately it is difficult to observe any correlation between experimental conditions and oxygen vacancy concentrations at this point though regarding the coordination number values of ≈ 7 for all PDF, we may believe that the stabilization metastable t-ZrO_2 may highly be correlated to short-range structural distortions induced by large L.O.V. concentrations.

IV.4.2 Zirconium oxygen coordination evolution as a function of time

The evolution of oxygen coordination around Zr atoms was qualitatively estimated from Equation $(II-18)$ for the various initial experimental conditions leading to pure t-ZrO_2 and plotted as a function of time as represented in Figure IV-17. The reason coordination numbers were qualitatively estimated only for pure t-ZrO_2 samples is that in the case of mixture of t- and m-ZrO_2 structures, the number of O atoms coordinated to Zr atoms are different (7 and 8 O atoms m- and t-ZrO_2, respectively), thus difficult to estimate accurately.

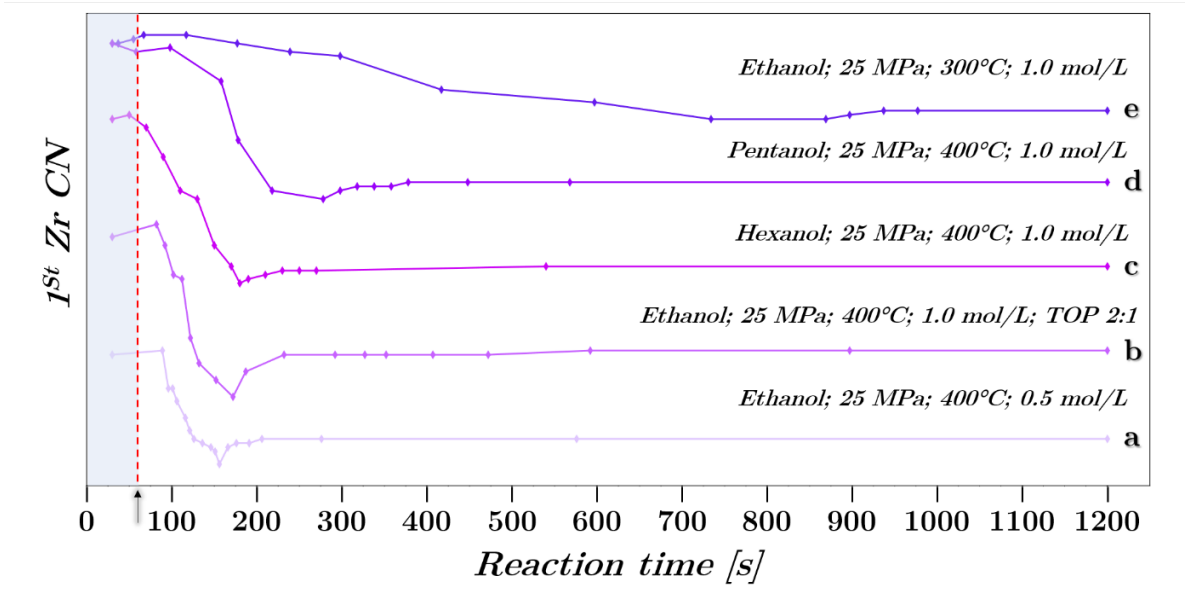

Figure IV-17. Variation of the relative number of O atoms coordinated to Zr atoms in the course of reactions with various initial conditions leading to pure t-ZrO_2. The blue zone ended with a red dashed line on the far-left end of the plots represents the lapse of time before heat was switched on (60 s in total).

In Figure IV-17, though the total number of O atoms around one Zr atom should be almost 8, values for all samples yield a value of ≈ 7 O atoms per Zr atom at the end of each reaction, as seen previously in Figure IV-16. What Figure IV-17 shows however is that for all measurements, the increase in temperature sees the relative number of O atoms around central Zr atoms decrease rapidly except in the case of Figure IV-17 e, where the relative number of O atoms decreases slowly relatively to all other measurements. Also, all profiles undergo a drop to a minimum at ≈ 5 to 6 O atoms around Zr atoms before an increase in coordination number occurs either rapidly in Figures IV-17 a and b, or relatively slowly for the other measurements. When comparing each profile in Figure IV-17 to its corresponding growth profile, the drop in O atoms seems highly correlated to the growth profiles, where the drop occurs as the scattering signal of t-ZrO_2 is collected on the detector as well as the slow oxygen uptake gradually increases as the particle size increases.

The behavior of O atoms seems to show that the stabilizing process may be correlated to the presence of oxygen substoichiometry generated abruptly, within newly formed clusters, by the reaction kinetics. And though the stoichiometry may increase as the cluster size increases, oxygen vacancies cannot be completely filled as the dehydration kinetics do not provide sufficient amounts of water, thus t-ZrO_2 may be stabilized. Variations in Zr coordination number therefore confirmed the key role of oxygen vacancies in stabilizing the metastable t-ZrO_2 structure, as had already been proposed [17].

IV.5 ZrO_2 formation mechanism in supercritical fluids

As Zr coordination allowed us to confirm the key role of oxygen vacancies in stabilizing the metastable t-ZrO_2 structure, analysis based on the total X-ray scattering intensities will allow us to determine, when both structures are present, if a phase transformation occurs or if both structures are formed and grow independently. Therefore, to understand the formation mechanism of ZrO_2 in supercritical alcohols and the reasons for the variations in structures, two different parameters were analyzed: the total scattered intensity variations in time, and the correlation in nanoparticle volume and total scattered intensity variations as a function of time.

IV.5.1 Variation of the total X-ray scattered intensities

We will describe in this section only the measurements where the fluctuations in structure scale factors, directly related to each structure's scattering intensity, and nanoparticle sizes were sufficiently small to enable comparison between nanoparticle volume scattering intensity variations. Fortunately, the following measurements allowed collection of both scale factors and Spd values with relatively little fluctuations to enable linking both variables together:

- Supercritical ethanol at 25 MPa, 400°C and 1 mol/L,
- Supercritical ethanol at 25 MPa, 350°C and 1 mol/L,
- Supercritical butanol at 25 MPa, 400°C and 1 mol/L,
- Supercritical pentanol at 25 MPa, 400°C and 1 mol/L,
- Supercritical hexanol at 25 MPa, 400°C and 1 mol/L.

For the other measurements, due to the very small size of the nanoparticles, the fluctuations in scale factors were too important for proper and precise interpretation of the results.

IV.5.2 Nucleation and growth behaviors

To understand how t- and m-ZrO_2 were formed in supercritical ethanol (Figure IV-5) and butanol (Figure IV-8), as well as through which mechanism pure t-ZrO_2 could be stabilized in supercritical pentanol (Figure IV-9) and hexanol (Figure IV-10) though in the same experimental conditions, but also why the structural transformation occurred under certain conditions, PDF analysis can be quite powerful. Differentiating condensation from coalescence growth processes for a given structure can be performed by comparing the evolution of the particle volume and scale intensity versus reaction time [254]. Therefore, the evolution of nanoparticle volumes (ΔV_{NPs}) along with the scale factors resulting from the above presented scattering intensities were plotted as a function of time. The nanoparticle volume was determined as expressed in Equation ($IV-1$),

$$V_{NPs} = \frac{\pi Spd^3}{6} \qquad (IV-1)$$

where V_{NPs} refers to the volume of coherent scattering nanodomains, and Spd is the single particle diameter obtained from the PDF refinements, in nanometer (nm). In the case of measurements in supercritical ethanol and butanol, Spd values for both m- and t-ZrO_2 were obtained, whereas in the case of those performed in supercritical pentanol and hexanol, Spd

values could only be obtained for t-ZrO_2 as m-ZrO_2 could not be refined due to its quasi or total absence in the scattering intensity.

IV.5.2.1 Cases where both structures are formed

Figure IV-18 shows the variation of normalized scale factors and particle volumes as a function of time for the measurements performed in supercritical ethanol at 400°C and 350°C and supercritical butanol at 400°C, all with a precursor concentration of 1 mol/L.

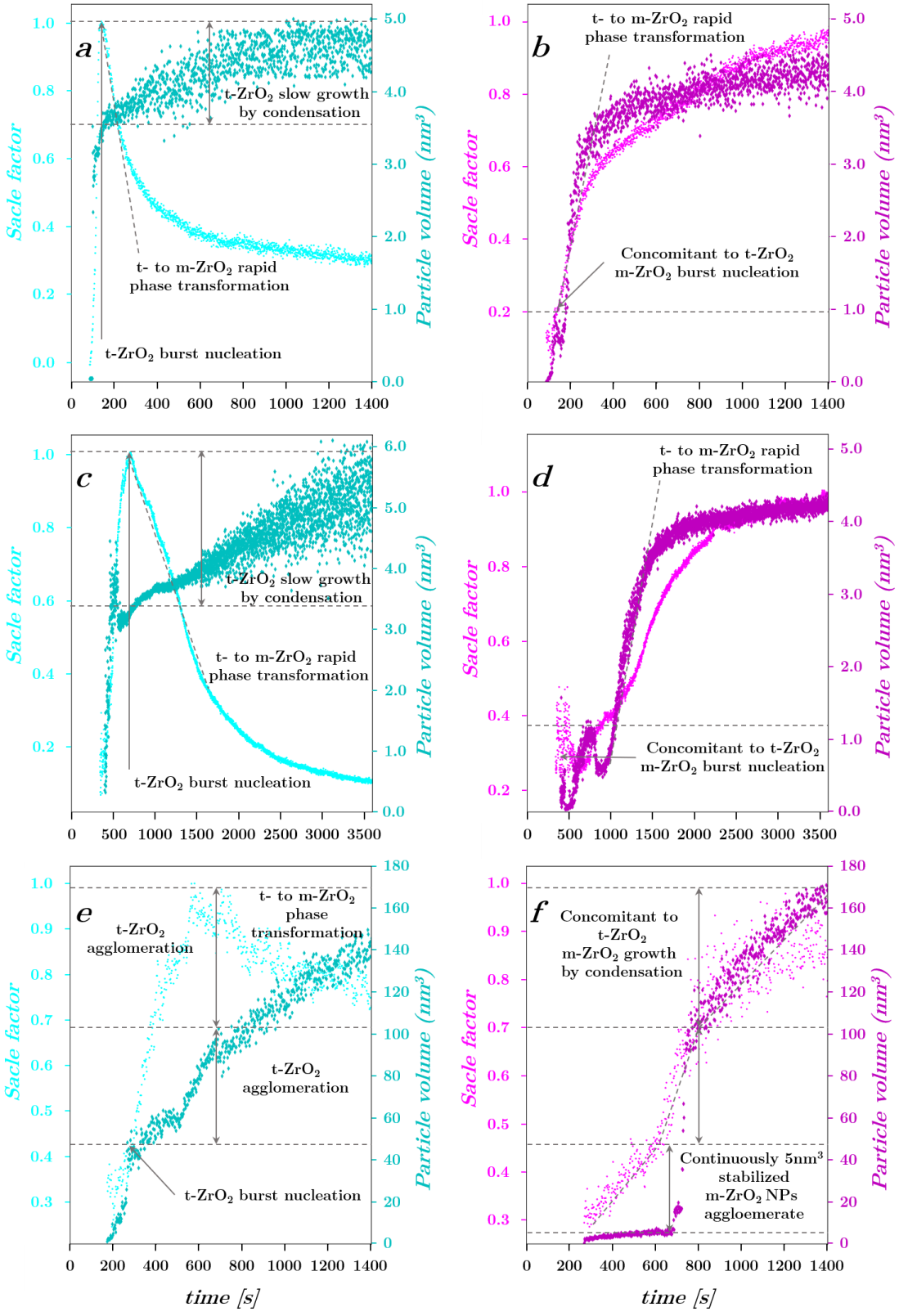

Figure IV-18. Correlation between normalized structure scale factors and nanoparticle volume variations (ΔV_{NPs}) for: a and b, t- and m-ZrO_2 measured in supercritical ethanol at 400°C, respectively; c and d, t- and m-ZrO_2 in supercritical ethanol at 350°C; e and f, t- and m-ZrO_2 in supercritical butanol at 400°C.

Considering first t-ZrO_2 in Figure IV-18 a, one can see burst nucleation occurring in the very first seconds up to V_{NPs} stabilized at ≈ 3.5 - 3.8 nm^3 (Spd ≈ 20 Å). The phase intensity then abruptly decreases though the nanoparticle volume still slightly increases until the end of the reaction to V_{NPs} ≈ 3.8 to 4.5 nm^3.

Analysis of m-ZrO_2 formation in Figure IV-18 b reveals rapid nucleation of m-ZrO_2 to V_{NPs} ≈ 1 nm^3 (Spd < 15 Å) in less than 30 s, then the average nanoparticle volume quickly decreases as the amount of m-ZrO_2 keeps increasing for another 30 s. V_{NPs} then abruptly increases up to ≈ 4 nm^3 within seconds, following the total scattering evolution curve.

The exact same observations can be made concerning the measurements in supercritical ethanol at 350°C (Figures IV-18 c and d), except that each of the moments described for the measurement performed at 400°C occur farther in time. Nevertheless, the coincident maxima in the t-ZrO_2 scale factor and increase in m-ZrO_2 also seem to reveal a structural transformation, though delayed in time, probably due to slower reaction kinetics.

In Figures IV-18 e and f, the profiles reveal slightly different behaviors for both structures, though the mechanisms seem very similar. Indeed, the scale factor of m-ZrO_2 increases smoothly while V_{NPs} remains almost constant at ≈ 4-5 nm^3 for almost 7 minutes before the average volume increases to ≈ 20 nm^3 and then bursts to ≈ 100 nm^3 within seconds. A final and constant increase in volume is then observed until the end of the reaction. The bursts in volume from 5 to 20 and finally 100 nm^3 in Figure IV-18 f corresponds, in Figure IV-18 e to the moment where the t-ZrO_2 scale factor and V_{NPs} slopes decouple at ≈ 300 s, and to when the maxima in t-ZrO_2 scale factor is reached at ≈ 600 s before slowly decreasing.

IV.5.2.2 Cases where only pure t-ZrO_2 is synthesized

Observations made on scale factor and V_{NPs} variations versus time for the measurements performed in supercritical pentanol and hexanol are quite different from the previous ones as only t-ZrO_2 was present in both supercritical alcohols at 400°C and 1 mol/L, as shown in Figures IV-19 a and b.

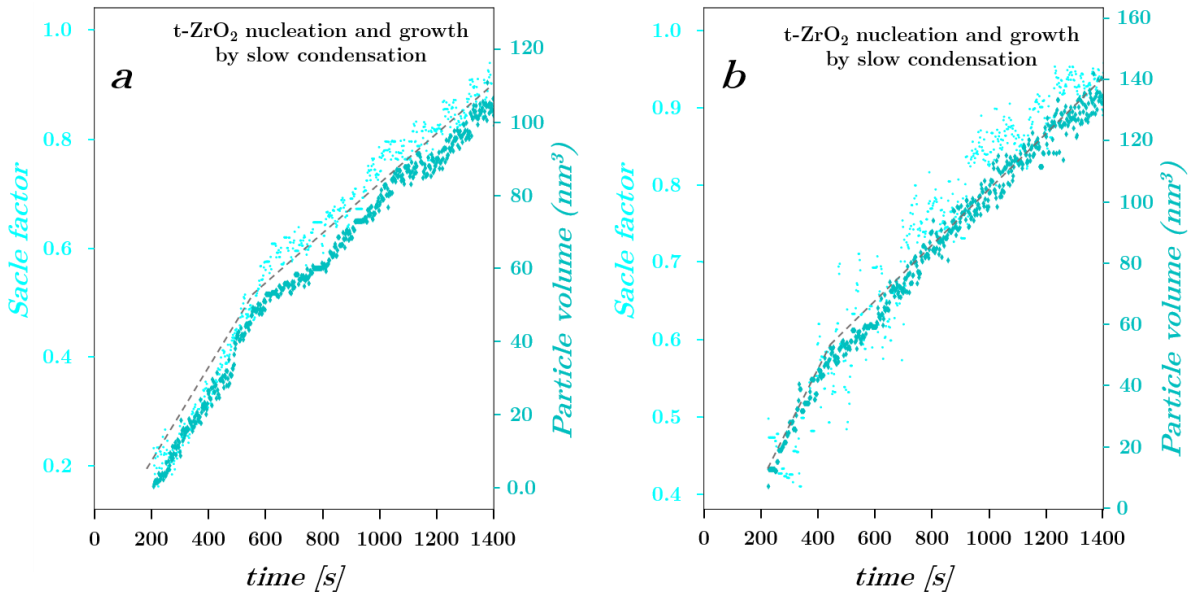

Figure IV-19. Correlation between normalized structure scale factors and nanoparticle volume variations (ΔV_{NPs}) for: a and b, t-ZrO_2 formation measured in supercritical pentanol and hexanol, respectively at 400°C and 1 mol/L.

In Figures IV-19 a and b, two striking differences are observed, for both alcohols, in the growth profiles of ZrO_2 synthesized relatively to Figures IV-18 a to f: the first one is the total absence of m-ZrO_2 as previously observed from PDF refinements shown in Figure IV-11; while the second is how the scale factors and V_{NPs} variations evolve quasi-monotonously. However, when we recall the growth profiles previously discussed, we must keep in mind that decoupling between t-ZrO_2 scale factors and V_{NPs} were observed as m-ZrO_2 V_{NPs} abruptly increased, whereas in the case of these two measurements, the presence of m-ZrO_2 was not detected during the PDF sequential refinements (Figure IV-11).

We have seen previously that the total scattering intensity remains stable throughout the reaction. Therefore, the forward transformation hypothesis undergoing is now strongly supported by these observations where the decrease in t-ZrO_2 scale factor, thus decreasing amounts of t-ZrO_2 nanoparticles concomitant to increasing amounts of m-ZrO_2, would be the result of a structural transformation. Visualization of m- and t-ZrO_2 scale factor and V_{NPs} variations curves combined to the observations made on the total scattering intensities gives valuable information as to when the forward transformation occurs.

Now the question is to know how they occur. A sketch of an answer will be given in the next section where growth profiles will be analyzed and compared to two main hypotheses: either

growth by coalescence of nanoparticles or growth by condensation of precursor molecules at the surface of ZrO_2 nanoparticles.

IV.5.3 Hypothesis on ZrO_2 formation mechanisms

In Figure IV-20 are represented expected observations for the growth of nanosized coherent scattering domains for both surface condensation of precursors (Figure IV-20 a) or coalescence of small nanoparticles (Figure IV-20 b).

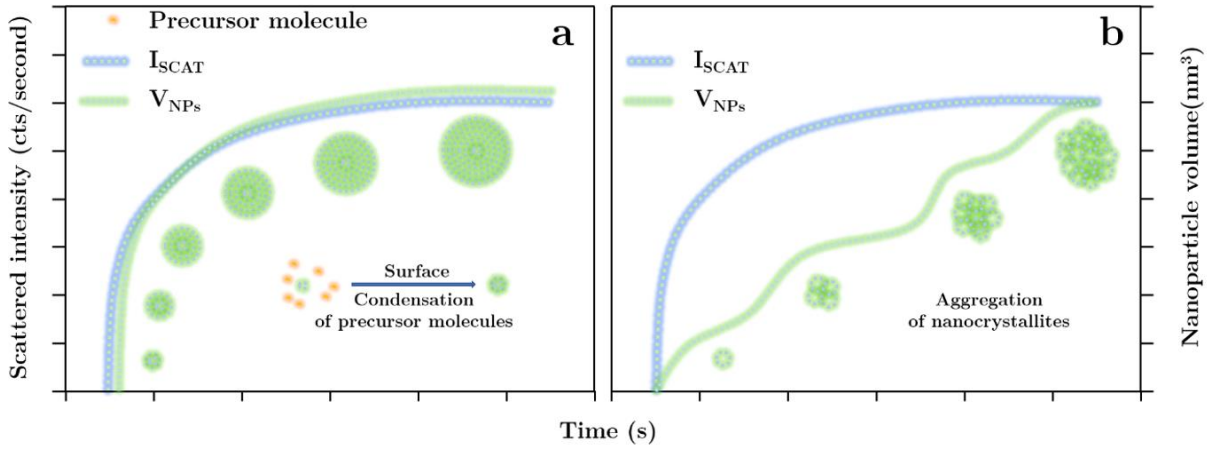

Figure IV-20. Representation for both plots and as a function of time, on the left axis the evolution of the total X-ray scattering intensity (I_{SCAT}) and on the right axis the evolution of the nanoparticle volume (ΔV_{NPs}). In light orange are represented individual precursor molecules, green dashed spheres represent coherent scattering domains, blue and green curves are the evolution versus time of scattered intensity and nanoparticle volume, respectively. Adapted from [254, 326].

When nanoparticle growth is driven by either slow or fast condensation of precursor molecules on the surface of continuously increasing coherent nanodomains (Figure IV-20 a), the nanoparticle volume (V_{NPs}) is expected to increase steadily as the scale factor increases [43]. On the other hand, if the scale factor and the V_{NPs} curves are decorrelated (Figure IV-20 b), or in other words, if the intensity increases while the coherent nanodomain volume remains more or less stable and jumps in V_{NPs} are observed in time, this situation may be regarded as the formation of nanoparticles by coalescence of individual smaller nanoparticles.

Therefore, from the five measurements previously discussed, the general trend in t-ZrO_2 volume increase may be attributed to a constant condensation of precursor molecules at the surface of nuclei after burst nucleation. This can be observed in the very first minutes of measurements

when both t- and m-ZrO_2 are present, but is clearly visible in the cases when measurements are performed in supercritical pentanol and hexanol when comparing Figures IV-18 and 19 to Figures IV-20 a and b.

However, the formation mechanism for m-ZrO_2 is slightly more complex to describe as measurements performed in supercritical ethanol and supercritical butanol led, at the end of the measurements, to $V_{NPs} \approx 4$ nm^3 (Spd =2 nm) and ≈ 170 nm^3 (Spd = 7 nm), respectively and these extremely larges differences in volumes may be the reason for slightly different mechanisms. In the supercritical ethanol measurements, the V_{NPs} fluctuations observed may be attributed to secondary growth of m-ZrO_2 nanoparticles where after reaching a first maxima, newly formed m-ZrO_2 nuclei are formed simultaneously to growth of m-ZrO_2 nanoparticles already formed for a small lapse of time. Thus the average volume of m-ZrO_2 nanoparticles is observed to decrease for ≈ 30 s after which V_{NPs} evolves extremely fast.

For the measurement performed in supercritical butanol, coalescence and probable transformation of ≈ 4 nm^3 t- to m-ZrO_2 nanoparticles agglomerating into ≈ 20 nm^3 and finally ≈ 100 nm^3 m-ZrO_2 nanoparticles is observed before surface condensation occurs until V_{NPs} ≈ 170 nm^3 when the reaction is stopped.

IV.5.3.1 Reactional pathways

The growth profiles by condensation (through diffusion) when only t-ZrO_2 is present or secondary growth profiles (for m-ZrO_2) when both structures are present appear clearly from our observations on total X-ray scattering measurements. Therefore, two main and simultaneous routes may be discussed whereas to by which t- and m-ZrO_2 nanoparticles may form as shown in Figure IV-21, namely T- and M-routes, leading to the formation of t- and m-ZrO_2 structures in the synthesized powders, respectively.

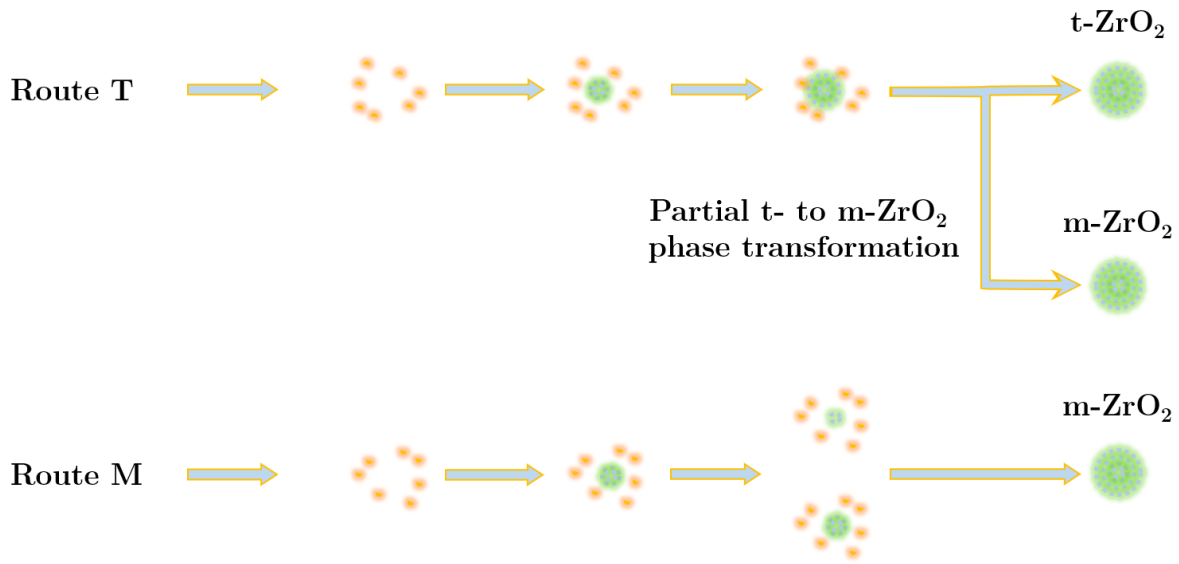

Figure IV-21. Representing the two simultaneous routes in supercritical ethanol during B.N.H.S.G. syntheses of ZrO_2, leading inevitably to a mixture of t- and m- ZrO_2.

In this hypothesis, an extremely fast and uncomplete hydrolysis of the metal alkoxide precursors stabilizes both phases as discussed in Chapters I and III will be used as the basis of our comprehension of the formation mechanisms.

IV.5.3.1.1 Nucleation and growth along the T-route

In the process of the T-route (Figure IV-21), a growth profile by condensation has been step by step successively developed where kinetics are controlled by the amount of water molecules released in B.N.H.S.G. reactions. In the process of B.N.H.S.G. reactions, hydroxyl groups (OH) may be trapped inside non-fully hydrolyzed nuclei gathered as relatively large clusters. During the reaction, the release of trapped structural OH generates oxygen vacancies and help maintaining the tetragonal-like structure as kinetics do not supply sufficient amounts of water molecules to fully hydrolyze other precursor molecules. Therefore, t-ZrO_2 distorted nanoparticles are formed and grow with many structural defects as observed in the PDF presented from section IV.3.1 to IV.4.2. The presence of distorted t-ZrO_2 structures was observed specifically in supercritical pentanol and hexanol (sections IV.3.2 and IV.3.3) by the expanding stretch in bond correlations and deviations in the Zr-O bond correlations may be attributed to the presence of trapped OH groups. This would explain also the relatively large discontinuities in the lattice planes observed through HRTEM analysis in Chapter III.4.6.1 for t-ZrO_2 nanoparticles synthesized *ex situ*. Also, we have seen for measurements in all series that

the overall oxygen vacancy concentration decreases slower than nanoparticles are formed to their final size, meaning oxygen diffusion to fill oxygen vacancies may occur as reactions are carried on.

IV.5.3.1.2 Nucleation and growth along the M-route

A secondary growth process however has been developed from our successive observations concerning the process of the M-route (Figure IV-21), where m-ZrO_2 nanoparticles initially form simultaneously to t-ZrO_2 by rapid condensation of precursor molecules. Suddenly, a drastic increase in m-ZrO_2 nanoparticle size results from forward transformation before subsequent slow growth occurs by surface condensation of precursor molecules on m-ZrO_2 nanoparticles. It may be possible that the phase transformation occurs at some point where burst nucleation is not possible anymore, as systematically surface condensation is observed after the structural transformation, or it may also be possible that the structural transformation is triggered when oxygen vacancies in t-ZrO_2 are fully filled as generally observed [88, 90].

This simultaneous apparition of both structures is only possible in experimental conditions where large amounts of water are generated *in situ* from the dehydration of alcohols. In these conditions, after nucleation of both structures the remaining precursor molecules enable, at first, majorly nucleation of smaller m-ZrO_2 nanoparticles simultaneously to surface condensation on t-ZrO_2 surface, which may be attributed to the fact that the higher concentration in acidic surface sites of m-ZrO_2 nanoparticles kinetically favor dehydration reactions. Indeed, we have seen in Chapter I-6.3.2 that surface dehydration on m-ZrO_2 nanoparticles is expected to be favored due to the higher concentration of stronger acidic surface sites [203, 208]. This antagonism between both processes is maintained through high nucleation kinetics versus surface condensation rates in high water conversion rate conditions.

Another explanation in t-ZrO_2 stabilization could arise from eventual structural similarities between the precursor structure and final structure of the synthesized nanoparticles. Fortunately, PDF analysis allows the observation of the precursor molecular configuration.

IV.5.4 Role of structural similarities

To understand whether or not stabilization of metastable t-ZrO_2 was the result, or partially resulted in the existence of structural similarities between the precursor molecular configuration and the final structure, total X-ray scattering intensity measurements of the precursors were collected at 25 MPa and room temperature and integrated into PDF to observe the existing bond correlations within the precursor molecules before nanoparticle crystallization occurred. Table IV-8 lists all the different initial conditions observed in this work.

Table IV-8. Initial conditions for all total scattering measurements

Initial conditions
1 mol/L, 25 MPa, RT, ethanol
0.5 mol/L, 25 MPa, RT, ethanol
1 mol/L, 25 MPa, RT, HA 2:1, ethanol
1 mol/L, 25 MPa, RT, HA 1:1, ethanol
1 mol/L, 25 MPa, RT, TOP 2:1, ethanol
1 mol/L, 25 MPa, RT, butanol
1 mol/L, 25 MPa, RT, pentanol
1 mol/L, 25 MPa, RT, hexanol

To do so, precursor PDF refinements were performed using Diffpy complex modelling infrastructure (CMI) which is a software toolbox for structural analysis where the refinements were configured and managed with the diffpy.srfit package. This package includes multiple configurable codes for solving atomic structures by providing frameworks allowing to build global optimizers, regression algorithms and structure models. Parameters for the different structural models used may either be restrained, constrained or refined in a unique refinement. The returned values for the "goodness of the fit" are R_W and χ^2, very similar to those obtained in Reitveld and PDF refinements.

The precursor PDF refinements were performed in the "small box" modelling approach, where small clusters were generated, using Vesta software, as a collection of fractional coordinates defining the different atomic positions from an absolute zero in a "3D box". From these different positions, a statistical collection of bond correlations was thus generated between atom pairs (G_{Calc}) and compared to the experimental precursor PDF data sets (G_{obs}). The scale of the structural model, their individual "boxes" structural scales, thermal parameters and Delta 2 parameter could then be refined to match the experimental data. Also, varying the bond lengths

was performed by expanding or contracting the "box" size of the models to fit the experimental PDF data. Therefore, it is in a certain way a rigid model used in the optimization process. Though different clusters were created from the various ZrO_2 existing CIF files from all ZrO_2 polymorphs, only t- and m-ZrO_2 CIF files could be used to match the experimental PDF.

IV.5.4.1 Precursor molecular configuration in ethanol

Figures IV-22 a, b and c display the precursor PDF refinement pattern measured at RT and 25 MPa, the models used for the refinement, and the evolution of nanoparticle crystallization in time at 25 MPa and 400°C, respectively for [Zr^{4+}] = 1mol/L in ethanol.

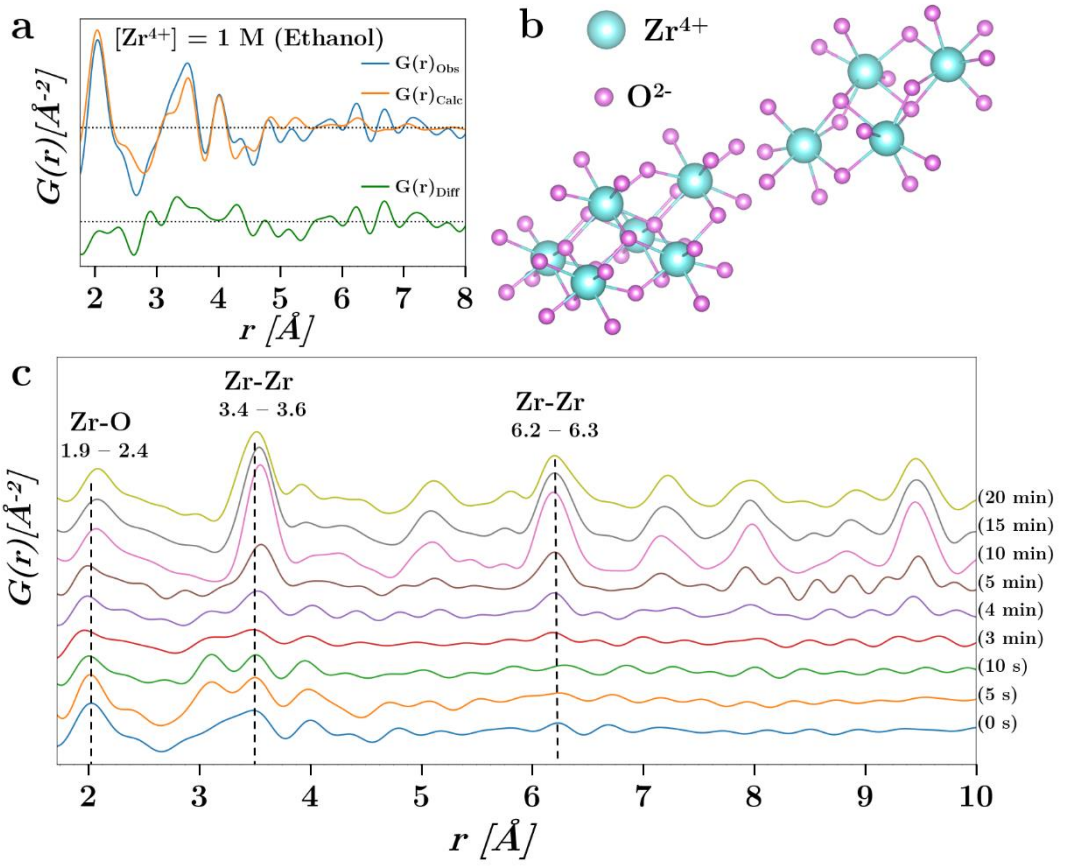

Figure IV-22. Representation of: a, experimental, calculated and difference PDF patterns of the precursor molecular configuration in ethanol at 25 MPa, 1 mol/L and RT; b, the structural models used in the PDF refinement; and c, evolution of the material inside the capillary in the 20 first min of the reaction at 400°C (crystallization).

The PDF refinement displayed in Figure IV-22 a was performed using both t- and m-ZrO_2 models with 70 % contribution of the t-ZrO_2 model. The t-ZrO_2 model consisted of 6 Zr atoms, each surrounded by 8 O atoms while the m-ZrO_2 model consisted of 4 Zr atoms coordinated to 7 O atoms (Figure IV-22 b). The first Zr-O shell is centered at r ≈ 2.04 Å for both experimental and fitted curves and clearly identifiable as 4 and 1 Zr-O distances in the t- and m-ZrO_2 models, respectively. The first Zr-Zr shell between ≈ 3 and 4 Å consists of 3 major bond correlations at ≈ 3.2, 3.5 and 4.0 Å. While those centered around 3.5 Å lack Zr atoms, the ones at ≈ 4 Å match perfectly in intensity. Also, the models used allow observation of bond correlations up to ≈ 6.1 Å. These observations tend to show that there are slightly too many O and too little Zr atoms in the models. However, varying their numbers by increasing or decreasing the number of polyhedral in the models generally lead to larger discrepancies between the observed and calculated PDF.

Figure IV-22 c shows that the variation in the first Zr-O coordination shell only undergoes slight variations during the first 20 min of the reaction. However, a separation of the first Zr-Zr shell is rapidly observed between 3.0 and 3.7 Å which after 3 min of reactions centers back around 3.5 Å until the end of the reaction.

Figure IV-23 depicts with more details the interpretation of the refinements obtained with the Diffpy-CMI package for the PDF when 0.5 mol/L of Zr^{4+} precursor was dissolved in absolute ethanol at 25 MPa.

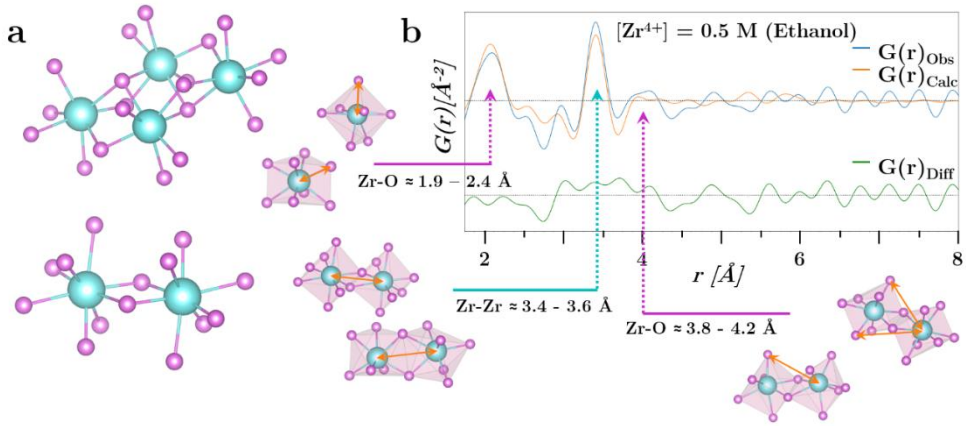

Figure IV-23. Representing: a, the t- and m-ZrO_2 structural models used for the PDF refinement; and b, the experimental, calculated and difference PDF patterns of the precursor molecular configuration in ethanol at 25 MPa, 0.5 mol/L and RT. Along with b are represented the various clusters cut into single or interconnected polyhedra and the bond correlations observed in both experimental data and the refinement. Magenta and cyan arrows and dotted lines correspond to Zr-O and Zr-Zr correlations, respectively, while the orange double arrows connecting atoms represent the respective observed bond correlations.

In Figure IV-23 a are displayed the t- and m-ZrO_2 clusters used as structural models for the PDF refinement consisting of 2 and 4 Zr atoms, respectively with Zr atoms coordinated to 8 and 7 O atoms for t- and m-ZrO_2, respectively. From the refinement, the t-ZrO_2 model contributed to only 30 % of the total signal in the precursor PDF pattern, meaning that Zr-Zr and Zr-O bond distributions are close to those of a tetragonal structure.

One may observe the relatively good match between observed and calculated PDF in Figure IV-23 b up to 4.5 Å with the same slight imbalance in Zr-O and Zr-Zr correlations as observed in Figure IV-22 a. Unlike for the PDF at 1 mol/L, bond correlations couldn't be described up to ≈ 6.1 Å, resulting in smaller clusters matching the experimental data.

Figure IV-24 shows the crystallization process observed for a concentration of 0.5 mol/L, 25 MPa and at 400°C.

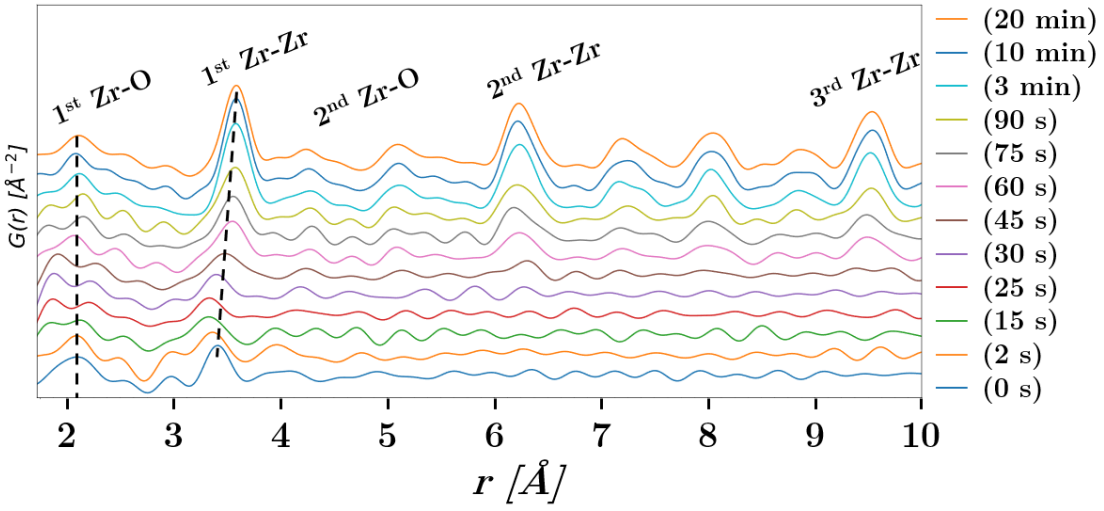

Fgure IV-24. PDF patterns for the reaction at 0.5 mol/L, 25 MPA and 400°C at different reaction times from 0 seconds to 20 minutes.

Unlike the crystallization process observed in Figure IV-22 c, in Figure IV-24 one can observe large structural variations in the first Zr-O shell, as well as a large increase in the bond correlations of the first Zr-Zr shell. Considering the first Zr-O shell, though the initial and final Zr-O correlations are very similar, they undergo a large separation in the first min of the reaction before centering around ≈ 2.1 Å at the end of the reaction while a large shift from 3.4 to 3.6 Å is observed for the first Zr-Zr shell, indicating larger differences between the precursor and crystallized ZrO_2 bond correlations when the concentration is decreased. The large variation in the first Zr-Zr shell between the precursor molecular organization and the final crystallized

ZrO_2 nanoparticles could be the result of lattice expansion resulting from the introduction of lattice oxygen vacancies [17].

IV.5.4.2 Precursor molecular configuration in ethanol and surfactants

The same type of measurements and observations were performed for the surfactant series where Figure IV-25 a, b and c show the PDF refinement patterns for the precursor solutions containing surfactants at 25 MPa and RT.

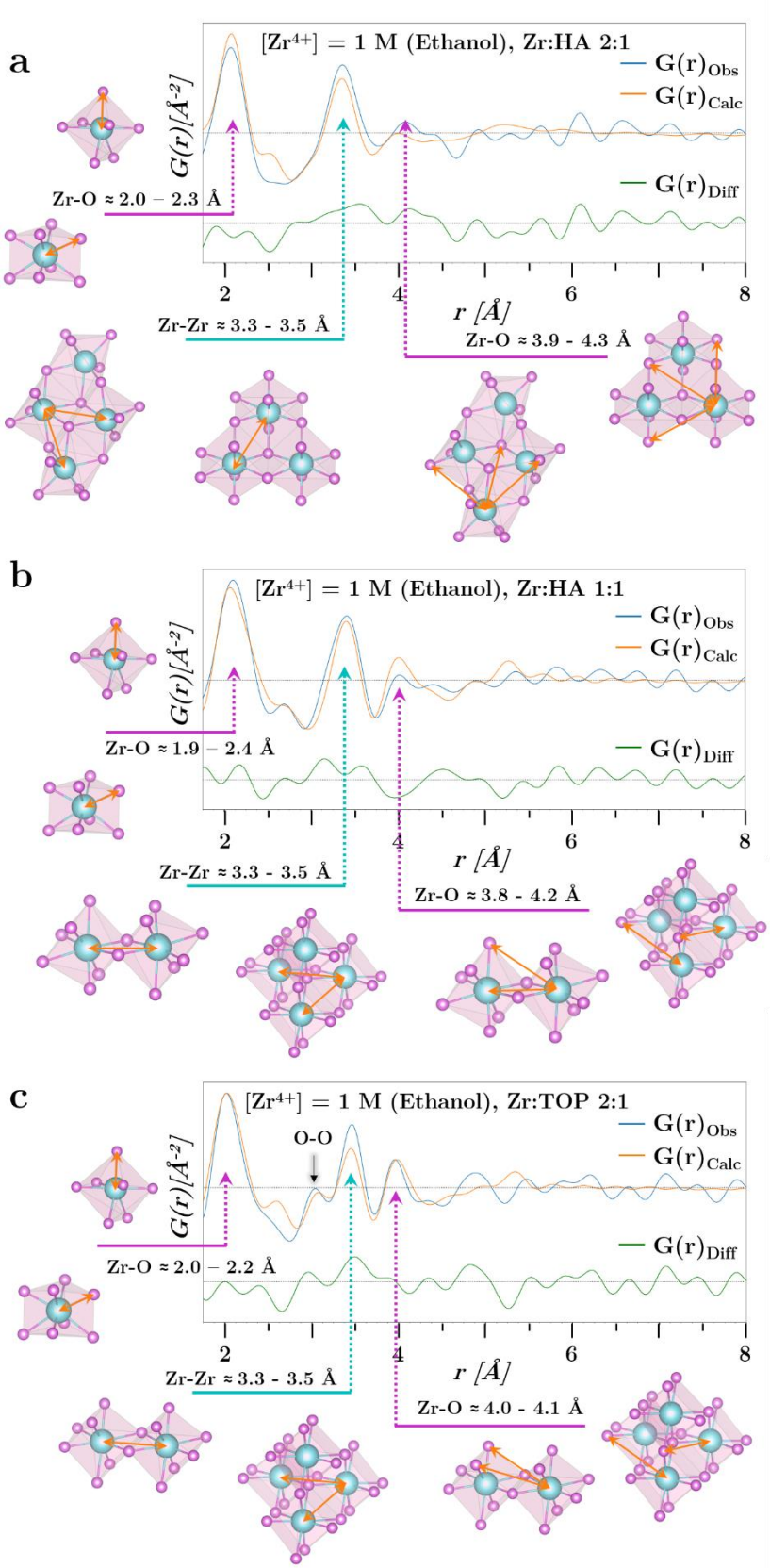

Figure IV-25. representing the refined PDF patterns for 1 mol/L Zr^{4+} precursor solutions in ethanol at 25 MPa and containing: in a and b 2:1 and 1:1 Zr/HA molar ratios, respectively; and c 2:1 Zr/TOP molar ratio. Alongside on the right side of each pattern are the structural models used during the refinements.

Local atomic ordering in the experimental PDF patterns is relatively well defined in Figures IV-25 a, b and c up to ≈ 4 Å. While in Figure IV-25 a both t- and m-ZrO_2 models were used with the major interatomic distances observed corresponding to the monoclinic cluster (60 %), refinements presented in Figures IV-25 b and c could however only be reliably performed using two t-ZrO_2 models with ≈ 50 and 78 % of bond correlations corresponding to the larger Zr tetrahedra, respectively. It is important to note that the two Zr_2O_{14} clusters are slightly different: in Figure IV-25 b the Zr-Zr distance is slightly smaller than in Figure IV-25 c, which is clearly visible in the shouldering on the left side of the first Zr-Zr shell at ≈ 3.4 Å.

Figure IV-26 shows the crystallization observed for the measurements performed in ethanol and with surfactants and compared to the precursor PDF in the 1.72-10 Å range.

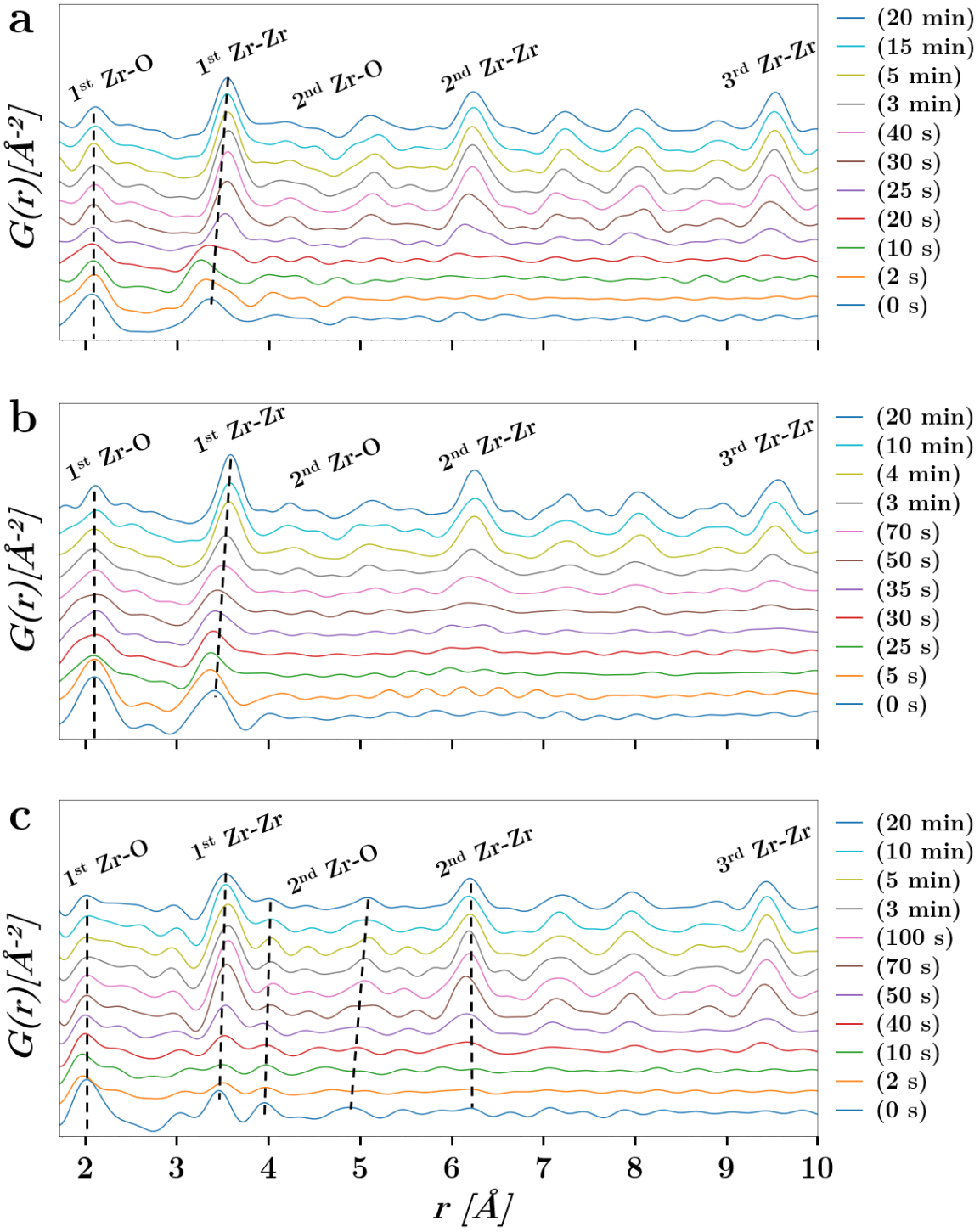

Figure IV-26. PDF patterns of ZrO_2 crystallization in ethanol and with: in a and b, HA added to the precursor solution with 2:1 and 1:1 molar ratios, respectively; and in c TOP with a 2:1 molar ratio. Black dashed lines reveal interatomic correlations expansion and contraction with reaction time.

In Figures IV-26 a, b and c the reaction time labelled on the right-hand side of each graph allows one to see the crystallization of ZrO_2 from the precursor atomic organization to the final

nanoparticles. Also, the Zr-O and Zr-Zr coordination shells labelled enable to see that though the Zr-O distances in the first shell remain relatively unchanged during the reaction in all 3 measurements, the behavior in the first Zr-Zr shell is different for each reaction. In Figure IV-26 a, the maximum in intensity fluctuates around the black dashed line which can be explained by the fact that in the precursor molecular configuration, most bond correlations are similar to monoclinic ones. However, in Figures IV-26 b and c, the Zr-Zr correlations slightly retract or expand along the black dashed lines, revealing relatively unchanged Zr-Zr correlations during the reaction. Also, important similitudes in interatomic configuration are observed in Figure IV-26 c until the second Zr-Zr coordination shell, though very slightly.

We clearly see in this set of measurements that when both structures can be refined using both t- and m-ZrO_2 CIF files as models, the Zr-Zr bond correlations split after heat is turned on before restructuring into an almost symmetric single peak (Figure IV-26 a), whereas when only t-ZrO_2 models can describe the observed precursor PDF a gradual shift in the first Zr-Zr distance is observed (Figures IV-26 b and c).

IV.5.4.3 Alcohol series

Figure IV-27 shows the PDF refinement patterns for the 1 mol/L Zr^{4+} precursor solutions larger alcohols at 25 MPa.

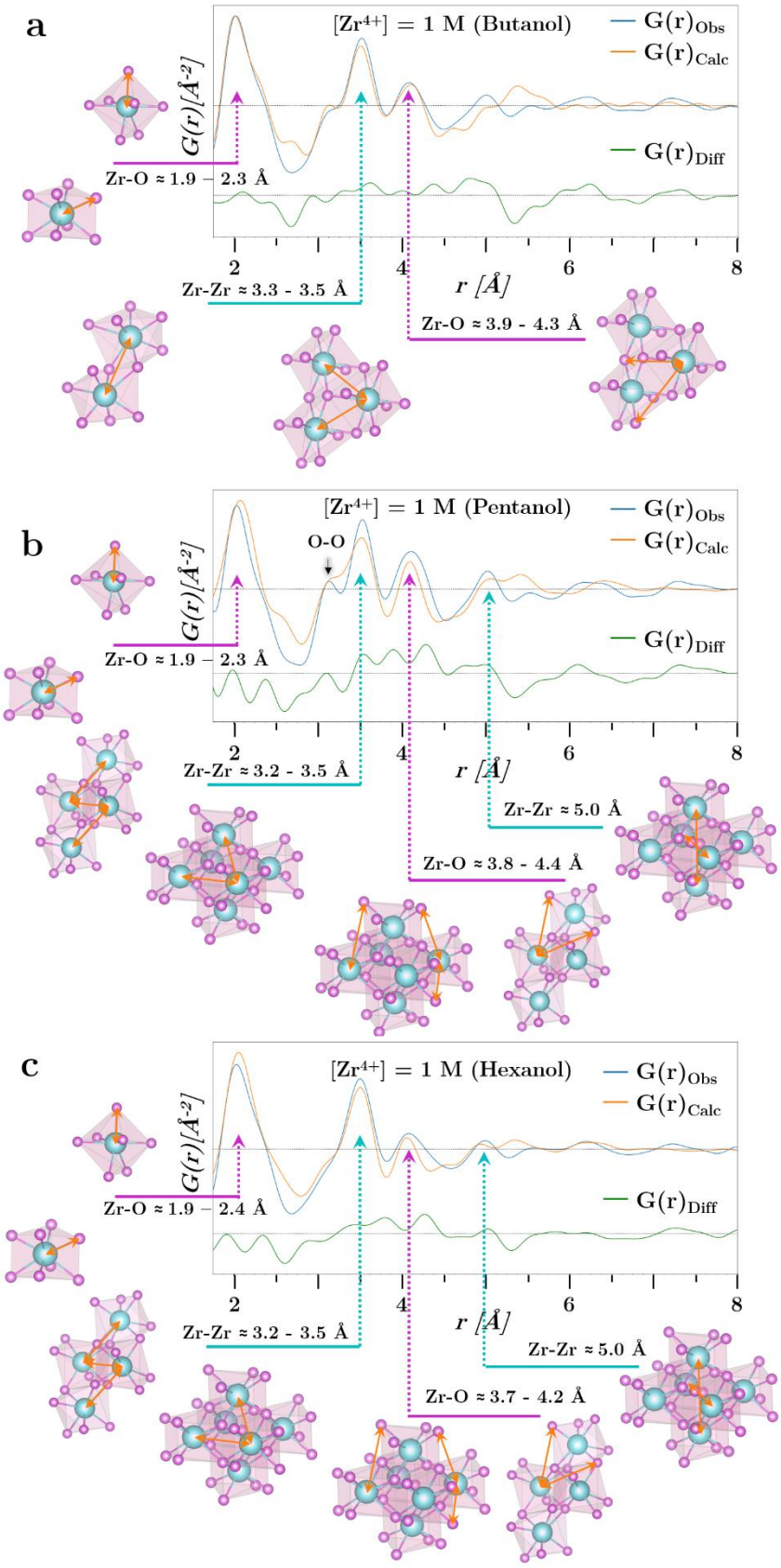

Figure IV-27. Refined PDF patterns for 1 mol/L Zr^{4+} precursor solutions at 25 MPa and RT in: a, butanol; b, pentanol; and c, hexanol. Alongside on the right-hand side of each pattern are the structural models used during the refinements.

Atomic ordering in the experimental PDF patterns is relatively well defined in Figures IV-27 a, b and c up to ≈ 4 Å though it seems that a general pattern, which could not be refined, may extend to 7 Å. All PDF in Figure IV-27 could be refined with both t- and m-ZrO_2 models and 40 %, 16 % and 58 % of the total intensity could be attributed to t-ZrO_2 for calculated PDF in Figures IV-27 a, b and c, respectively.

In Figure IV-27 a, the observed and calculated PDF display the greatest match of all 3 PDF until 4.5 Å in both peak position and intensity. Differences in observed and calculated PDF in Figures IV-27 b and c however lie in the relative numbers of Zr and O atoms. Indeed, the number of O atoms bonded to Zr atoms in the first shell are slightly larger in the calculated PDF while the number of Zr atoms in the first shell are slightly lower than observed, meaning the number of O atoms may be slightly overestimated in our model. However, their position in the calculated PDF is relatively well defined until 4 Å, meaning that in these precursor solutions, Zr and O atoms are interconnected in arrays whit statistically well distributed t- and m-ZrO_2 interatomic distances in Figures IV-27 a and c, while in Figure IV-27 b interatomic distances are rather closer to those of m-ZrO_2.

Figure IV-28 shows the crystallization observed for the measurements performed with in larger alcohols at 25 MPa, [Zr^{4+}] = 1mol/L and 400°C and are compared to the precursor PDF in the 1.72-10 Å range.

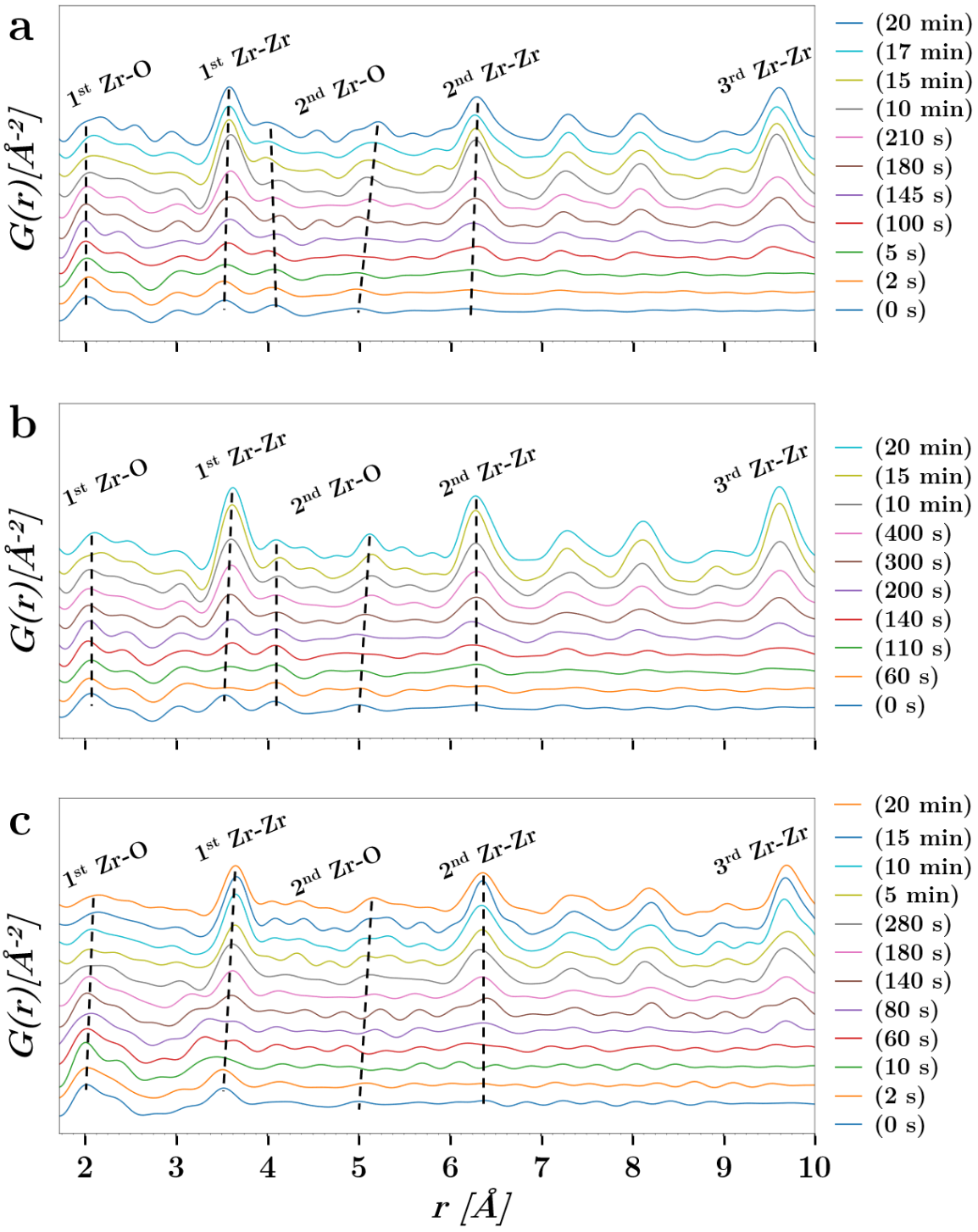

Figure IV-28. PDF patterns of ZrO_2 crystallization in supercritical: a, butanol; b, pentanol; and c, hexanol. Black dashed lines reveal how interatomic correlations vary in time by either contracting or expanding.

In Figures IV-28 a, b and c the evolution of the Zr-O and Zr-Zr coordination shells labelled with black dashed lines enable to clearly see similitudes between the precursor organization

and final crystalline ZrO_2 PDF up to ≈ 6.2 Å. Though very small variations in the position of the first Zr-O shell are observed in Figures IV-28 a, b and c, increasing expansion is observed for the first Zr-Zr shell from Figure IV-28 a to c. Similitudes are flagrant in Figures IV-28 a and b where similar peaks are observed at ≈ 2, 2.5, 3, 3.5 and 4 Å in both precursor and crystalized ZrO_2 PDF. The same similarities may also be observed in Figure IV-28 c, however, those observed in the precursor PDF are not sufficiently resolved to clearly confirm this observation.

Finally, fluctuations in bond correlations are very smooth in all 3 measurements, probably revealing a smooth and linear atomic arrangement in time as we have seen earlier, reaction kinetics are relatively slow in these larger alcohols.

Exposure time for the alcohol series was 2 seconds per frame, thus the PDF generally exhibit slightly higher resolution than the ethanol series, allowing to observe clearly similarities between the first and last PDF in all 3 measurements up to ≈ 6.2 Å corresponding to the distance of the second Zr-Zr coordination shell.

IV.5.5 Conclusions

PDF refinements of the precursor molecular organization for all the different initial conditions have clearly emphasized the existence, in most conditions, of an atomic organization where Zr-O and Zr-Zr interatomic distances are statistically distributed between distances similar to those observed either in t- or m-ZrO_2 crystalline material with however, different weights on contributions. Also, similarities in the precursor and crystalline PDF were clearly identified and unequivocal in the larger alcohol series where exposure time was doubled during total X-ray scattering measurements.

However, as the Diffpy CMI algorithm used in the precursor PDF refinements is a semi-rigid model, therefore, the question on whether only statistical bond size distributions in predefined clusters were varied or if observations on truly identified existing clusters were performed is delicate to answer. Nevertheless, structural similarities were clearly observed between Zr-O and Zr-Zr interatomic distances existing in both precursor molecular organization and specifically t-ZrO_2 nanoparticles.

IV.6 General conclusion on Chapter IV

We have seen in this chapter that B.N.H.S.G. reactions could be successfully performed in various supercritical primary alcohols including ethanol, propanol (though not presented herein), butanol, pentanol and hexanol. In supercritical ethanol, many temperatures and precursor concentrations were investigated to be compared to syntheses performed *ex situ* in continuous flow reactors and presented in Chapter III, while many syntheses were performed with additives in surfactant assisted B.N.H.S.G. A series of measurements was also performed in larger supercritical alcohols to validate the kinetic character in stabilizing metastable t-ZrO_2 nanoparticles.

The aim of these measurements was to gain deeper understanding in the stabilizing process by considering, at the root of all: the influence of the nanoparticle size; the role of lattice oxygen vacancies; the existence of structural similarities; or the influence of the reaction media. To do so, total X-ray scattering measurement were performed in different experimental conditions, and the resulting sample intensities were converted into pair distribution functions (PDF) to allow observation on the existing crystalline structures and their local atomic ordering.

Observations revealed that t- and m-ZrO_2 nucleation occurred simultaneously where t- and m-ZrO_2 nanoparticle formation followed either growth by condensation and secondary growth processes by coalescence, respectively. Also, the t- to m-ZrO_2 forward transformation was clearly identified.

It has also been demonstrated that the decreasing lattice oxygen vacancy concentrations during the condensation of metastable t-ZrO_2 were responsible for the stabilization process, favored by the existence of structural similarities between the precursor molecular organization and crystalline t-ZrO_2 atomic ordering.

However, the effect of the critical size was not evidenced as sizes observed in the alcohol series were ≈ 3 times larger than those measured in ethanol and in both types of measurements pure t-ZrO_2 nanoparticles could be stabilized. Therefore, we may believe that stabilization of metastable t-ZrO_2 cannot result from the critical size effect. Nevertheless, the size effect must be considered as indivisible of the stabilizing process, as small nanoparticles favor the stabilization of oxygen vacancies.

General conclusion

t-ZrO_2 stabilization process in nanoparticles has been a great and vast subject of investigations where many theories have emerged in order to interpret experimental observations. Over the past decades, attempts in achieving pure t-ZrO_2 nanocrystallites have opened the route to as many interpretations as there have been initial experimental conditions with 3 predominant and reliable explanations: the effect of the nanocrystallite size, though still not finding unequivocal consensus; the influence of lattice oxygen vacancies; and the role of structural similarities.

While, as we have seen in Chapter I, the non-hydrolytic sol-gel (N.H.S.G.) reactions offered the best possible route to achieve quasi pure t-ZrO_2 nanocrystallites, we first focused on reproducing the concept in supercritical fluids, with ethanol as the solvent leading to the lesser known "borderline" non-hydrolytic sol-gel (B.N.H.S.G.) reactions, where water molecules are available for hydrolysis and condensation of metal alkoxide zirconium precursors only while the solvent is in a supercritical state.

In our continuous flow synthesis conditions, t-ZrO_2 molar fractions encompassed between $85 < x < 95$ mol. % only could be achieved, where structural proportions characterized by both conventional X-ray diffraction and Raman spectroscopy agreed unequivocally. HRTEM analysis further led on us the path of considering a stabilization process influenced by lattice oxygen vacancies as observations of microscopy images revealed large discrepancies in the lattice plane distances in the very small t-ZrO_2 nanoparticles. However, HRTEM and Rietveld analyses showed that though the size of ZrO_2 nanoparticles could be significantly decreased during surfactant assisted syntheses, the molar fractions did not vary much with the decreasing size, revealing that t-ZrO_2 formation was favored in terms of the number of t-ZrO_2 nanoparticles produced versus m-ZrO_2 nanoparticles, but not in terms of molar fractions. These results obtained in Chapter III did not comfort the critical size theory and therefore, our investigations focused on the role of lattice oxygen vacancies and structural similarities where a possible formation mechanism was sketched in view of the obtained results.

The total X-ray scattering measurements presented in Chapter IV showed that t- and m-ZrO_2 nucleation occurred simultaneously when both structures were observed at the end of the reactions, though m-ZrO_2 nucleation could be greatly impacted by the alcohol dehydration reaction kinetics. To slow reaction kinetics, the temperature was either lowered in the case of measurements performed in supercritical ethanol, or alcoholic solvents displaying a higher critical temperature were used, thus ending *in fine* with similar nucleation behaviors.

After identifying this lever, the nucleation and growth mechanisms were investigated, and led us to the conclusion that after simultaneous nucleation of both structures, a forward transformation occurred after which m-ZrO_2 growth occurred *via* agglomeration of newly

formed m-ZrO_2 very small nanoparticles in a coalescence process. However, in the case of t-ZrO_2 nanoparticles, systematic growth by condensation was observed to occur and drive the formation of nanoparticles all through the reaction.

In the metastable t-ZrO_2 stabilization process favored by alcohol dehydration reaction kinetics, the role of lattice oxygen vacancies was highlighted and identified as the key parameter where a general decrease in their concentration was observed as the nanoparticle size increased during condensation of possibly none fully hydrolyzed precursor molecules at the surface of metastable t-ZrO_2.

The existence of structural similarities between precursor and crystalline t-ZrO_2 interatomic distances was also clearly evidenced for most of the initial conditions experienced in this Chapter.

However, the effect of the crystallite size was not evidenced as in ethanol all reported sizes were too similar (≈ 20 Å), while in larger alcohols sizes were reported ≈ 3 times larger than those measured in ethanol. Therefore, we may believe that though it is necessary to decrease the size of nanoparticles to obtain structural defects, it is rather more reaction kinetics when controlled, and in our case alcohol dehydration kinetics, that enable the formation of pure metastable t-ZrO_2 nanoparticles.

It is therefore believed, in regards of the *in situ* measurements performed in this work, that the structuration and stabilization of t-ZrO_2 is only driven by slow reaction kinetics from an initial precursor solution having the choice in two different pathways: either fast condensation and coalescence favored by fast kinetics, or slow condensation favored by slow kinetics. In our reaction media, the kinetics were controlled by the decomposition of alcohols releasing water molecules hydrolyzing metal alkoxide precursor molecules. We strongly believe that non-fully hydrolyzed precursor molecules inevitably end up in disordered clusters containing OH structural defects as observed in Chapter III.4.5, further combining to form lattice oxygen vacancies as generally observed and seen in Chapter I.3.3.

Though the presence of lattice oxygen vacancies in synthesized ZrO_2 nanoparticles was clearly visible in Chapter III, we could not rigorously confirm their presence using only a high-resolution electron microscope. Therefore, it would be interesting to observe these oxygen vacancies with the latest generation of HRTEM such as the TITAN.

Also, another information we lack to fully close the WAXS study is the intensity of the precursor molecular organization at both ambient temperature and pressure as in the PDF of precursor solutions presented in Chapter IV, the organization of zirconium alkoxide precursor molecules are already altered by the applied pressure.

It would also either be necessary to further optimize our continuous flow reactors to synthesize pure t-ZrO_2 nanoparticles in supercritical larger alcohols, either switch to batch reactor processes to achieve this goal. Designing continuous flow reactors for *in situ* measurements is mandatory in order to fully understand the formation mechanisms undergoing in our laboratory reactors.

Also, characterization of the thermal stability of the synthesized ZrO_2 nanoparticles presented in Chapter III should not be avoided in order to define eventual applications for these ultrafine t-ZrO_2 nanoparticles.

References

1. Bergson, H. *Creative Evolution*. (University Press of America, 1984).
2. Horne, P. de M. de. *Dictionnaire de chimie: Une approche étymologique et historique*. (De Boeck Superieur, 2013).
3. Shen, Z.-X. & Dessau, D. S. Electronic structure and photoemission studies of late transition-metal oxides — Mott insulators and high-temperature superconductors. *Physics Reports* **253**, 1–162 (1995).
4. Ahn, C. H., Rabe, K. M. & Triscone, J.-M. Ferroelectricity at the Nanoscale: Local Polarization in Oxide Thin Films and Heterostructures. *Science* **303**, 488–491 (2004).
5. Philippot, G. *et al.* Continuous BaTi1-yZryO3 ($0 \leq y \leq 1$) Nanocrystals Synthesis in Supercritical Fluids for Nanostructured Lead-Free Ferroelectric Ceramics. *Materials & design* **86**, 354 (2015).
6. Huang, W. & Gao, Y. Morphology-dependent surface chemistry and catalysis of CeO2 nanocrystals. *Catal. Sci. Technol.* **4**, 3772–3784 (2014).
7. Xu, T., Zhang, L., Cheng, H. & Zhu, Y. Significantly enhanced photocatalytic performance of ZnO via graphene hybridization and the mechanism study. *Applied Catalysis B: Environmental* **101**, 382–387 (2011).
8. Harriman, A., Pickering, I. J., Thomas, J. M. & Christensen, P. A. Metal oxides as heterogeneous catalysts for oxygen evolution under photochemical conditions. *J. Chem. Soc., Faraday Trans. 1* **84**, 2795–2806 (1988).
9. Giannakoudakis, D. A. *et al.* Barium titanate perovskite nanoparticles as a photoreactive medium for chemical warfare agent detoxification. *Journal of Colloid and Interface Science* **531**, 233–244 (2018).
10. Henrich, V. E. & Cox, P. A. *The surface science of metal oxides*. (Cambridge University Press, 1994).

11. Zecchina, A., Scarano, D., Bordiga, S., Spoto, G. & Lamberti, C. Surface structures of oxides and halides and their relationships to catalytic properties. in *Advances in Catalysis* vol. 46 265–397 (Academic Press, 2001).
12. Fierro, J. L. G. *Metal Oxides: Chemistry and Applications*. (CRC Press, 2005).
13. Kašpar, J., Fornasiero, P. & Graziani, M. Use of CeO2-based oxides in the three-way catalysis. *Catalysis Today* **50**, 285–298 (1999).
14. Balducci, G. *et al.* An unusual promotion of the redox behaviour of CeO2/ZrO2 solid solutions upon sintering at high temperatures. *Catal Lett* **33**, 193–200 (1995).
15. Becker, J. *et al.* Critical Size of Crystalline ZrO2 Nanoparticles Synthesized in Near- and Supercritical Water and Supercritical Isopropyl Alcohol. *ACS Nano* **2**, 1058–1068 (2008).
16. Denkewicz, R. P., TenHuisen, K. S. & Adair, J. H. Hydrothermal crystallization kinetics of m-ZrO2 and t-ZrO2. *Journal of Materials Research* **5**, 2698–2705 (1990).
17. Dippel, A.-C. *et al.* Towards atomistic understanding of polymorphism in the solvothermal synthesis of ZrO2 nanoparticles. *Acta Cryst A, Acta Cryst Sect A, Acta Crystallogr A, Acta Crystallogr Sect A, Acta Crystallogr A Cryst Phys Diffr Theor Gen Crystallogr, Acta Crystallogr Sect A Cryst Phys Diffr Theor Gen Crystallogr* **72**, 645–650 (2016).
18. Py, W., K, U., H, T. & K, K. Versatility of one-pot, single-step synthetic approach for spherical porous (metal) oxide nanoparticles using supercritical alcohols. *J. Supercrit. Fluids* **78**, 124–131 (2013).
19. Tyrsted, C. *et al.* Watching nanoparticles form: an in situ (small-/wide-angle X-ray scattering/total scattering) study of the growth of yttria-stabilised zirconia in supercritical fluids. *Chemistry* **18**, 5759–5766 (2012).

20. Srinivasan, R., Harris, M. B., Simpson, S. F., Angelis, R. J. D. & Davis, B. H. Zirconium oxide crystal phase: The role of the pH and time to attain the final pH for precipitation of the hydrous oxide. *Journal of Materials Research* **3**, 787–797 (1988).
21. Slostowski, C., Marre, S., Babot, O., Toupance, T. & Aymonier, C. CeO2 Nanocrystals from Supercritical Alcohols: New Opportunities for Versatile Functionalizations? *Langmuir* **30**, 5965–5972 (2014).
22. Giroire, B. *et al.* Tuning surface grafting density of CeO2 nanocrystals with near- and supercritical solvent characteristics. *Phys. Chem. Chem. Phys.* **18**, 1727–1734 (2016).
23. Slostowski, C., Marre, S., Babot, O., Toupance, T. & Aymonier, C. Near- and Supercritical Alcohols as Solvents and Surface Modifiers for the Continuous Synthesis of Cerium Oxide Nanoparticles. *Langmuir* **28**, 16656–16663 (2012).
24. Slostowski, C. *et al.* CeO2 nanopowders as solid sorbents for efficient CO2 capture/release processes. *Journal of CO2 Utilization* **20**, 52–58 (2017).
25. Aymonier, C., Philippot, G., Erriguible, A. & Marre, S. Playing with chemistry in supercritical solvents and the associated technologies for advanced materials by design. *The Journal of Supercritical Fluids* **134**, 184–196 (2018).
26. Shukla, S. & Seal, S. Mechanisms of room temperature metastable tetragonal phase stabilisation in zirconia. *International Materials Reviews* **50**, 45–64 (2005).
27. Agricola, G., Hoover, H. & Hoover, L. H. *De Re Metallica*. (Courier Corporation, 1950).
28. Lavoisier, A.-L. de. *Traité élémentaire de chimie*. (Deterville, 1801).
29. Bannister, M. *Science and Technology of Zirconia V*. (CRC Press, 1993).
30. Li, P., Chen, I.-W. & Penner-Hahn, J. E. X-ray-absorption studies of zirconia polymorphs. I. Characteristic local structures. *Phys. Rev. B* **48**, 10063–10073 (1993).
31. Wolten, G. M. Diffusionless Phase Transformations in Zirconia and Hafnia. *Journal of the American Ceramic Society* **46**, 418–422 (1963).

32. Hannink, R. H. J., Kelly, P. M. & Muddle, B. C. Transformation Toughening in Zirconia-Containing Ceramics. *Journal of the American Ceramic Society* **83**, 461–487 (2000).

33. Abriata, J. P., Garcés, J. & Versaci, R. The O−Zr (Oxygen-Zirconium) system. *Bulletin of Alloy Phase Diagrams* **7**, 116–124 (1986).

34. Kisi, E. H., Howard, C. J. & Hill, R. J. Crystal Structure of Orthorhombic Zirconia in Partially Stabilized Zirconia. *Journal of the American Ceramic Society* **72**, 1757–1760 (1989).

35. G. Tolliard, R. Benmechta, D. Mercurio,. Pure orthorhombic zirconia islands grown on single-crystal sapphire substrates. *Acta Materialia* **55**, 6011–6018 (2007).

36. Varez, A., Garcia-Gonzalez, E., Jolly, J. & Sanz, J. Structural characterization of Ce1−xZrxO2 (0≤x≤1) samples prepared at 1650°C by solid state reaction: A combined TEM and XRD study. *Journal of the European Ceramic Society* **27**, 3677–3682 (2007).

37. Bondars, B. *et al.* Powder diffraction investigations of plasma sprayed zirconia. *Journal of Materials Science* **30**, 1621–1625 (1995).

38. Patil, R. N. & Subbarao, E. C. Monoclinic–tetragonal phase transition in zirconia: mechanism, pretransformation and coexistence. *Acta Cryst A, Acta Cryst Sect A, Acta Crystallogr A, Acta Crystallogr Sect A, Acta Crystallogr A Cryst Phys Diffr Theor Gen Crystallogr, Acta Crystallogr Sect A Cryst Phys Diffr Theor Gen Crystallogr* **26**, 535–542 (1970).

39. Wang, D., Guo, Y., Liang, K. & Tao, K. Crystal structure of zirconia by Rietveld refinement. *Sci. China Ser. A-Math.* **42**, 80 (1999).

40. Dutta, P. *et al.* Concentration of Ce3+ and Oxygen Vacancies in Cerium Oxide Nanoparticles. *Chem. Mater.* **18**, 5144–5146 (2006).

41. Espinoza-González, R. & Mosquera, Edgar. Influence of micro- and nanoparticles of zirconium oxides on the dielectric properties of CaCu3Ti4O12. *Ceramics International* **43**, 14659–14665 (2017).

42. Vykhodets, V. B. *et al.* Inhomogeneous depletion of oxygen ions in metal oxide nanoparticles. *Surface Science* **644**, 141–147 (2016).

43. Gunnarsson, R., Helmersson, U. & Pilch, I. Synthesis of titanium-oxide nanoparticles with size and stoichiometry control. *Journal of Nanoparticle Research* **17**, (2015).

44. Chen, S. *et al.* Facile Strategy for Synthesizing Non-Stoichiometric Monoclinic Structured Tungsten Trioxide (WO3−x) with Plasma Resonance Absorption and Enhanced Photocatalytic Activity. *Nanomaterials* **8**, 553 (2018).

45. Zavodinsky, V. G. & Chibisov, A. N. Stability of cubic zirconia and of stoichiometric zirconia nanoparticles. *Phys. Solid State* **48**, 363–368 (2006).

46. Priya, N. S., Somayaji, C. & Kanagaraj, S. Optimization of Ceria-Zirconia Solid Solution based on OSC Measurement by Cyclic Heating Process. *Procedia Engineering* **64**, 1235–1241 (2013).

47. Gao, P., Meng, L. J., dos Santos, M. P., Teixeira, V. & Andritschky, M. Characterisation of ZrO2 films prepared by rf reactive sputtering at different O2 concentrations in the sputtering gases. *Vacuum* **56**, 143–148 (2000).

48. Li, P., Chen, I.-W. & Penner-Hahn, J. E. Effect of Dopants on Zirconia Stabilization-An X-ray Absorption Study: I, Trivalent Dopants. *Journal of the American Ceramic Society* **77**, 118–128 (1994).

49. Kim, D.-J. Effect of Ta2O5, Nb2O5, and HfO2 Alloying on the Transformability of Y2O3-Stabilized Tetragonal ZrO2. *Journal of the American Ceramic Society* **73**, 115–120 (1990).

50. Veal, B. W., McKale, A. G., Paulikas, A. P., Rothman, S. J. & Nowicki, L. J. EXAFS study of yttria stabilized cubic zirconia. *Physica B+C* **150**, 234–240 (1988).

51. Bokhimi, X. *et al.* Tetragonal Nanophase Stabilization in Nondoped Sol–Gel Zirconia Prepared with Different Hydrolysis Catalysts. *Journal of Solid State Chemistry* **135**, 28–35 (1998).

52. Philippot, G., Elissalde, C., Maglione, M. & Aymonier, C. Supercritical fluid technology: A reliable process for high quality BaTiO3 based nanomaterials. *Advanced Powder Technology* **25**, 1415–1429 (2014).

53. Sheldon, B. W. & Shenoy, V. B. Space Charge Induced Surface Stresses: Implications in Ceria and Other Ionic Solids. *Phys. Rev. Lett.* **106**, 216104 (2011).

54. Nawale, A. B., Kanhe, N. S., Bhoraskar, S. V., Mathe, V. L. & Das, A. K. Influence of crystalline phase and defects in the ZrO2 nanoparticles synthesized by thermal plasma route on its photocatalytic properties. *Materials Research Bulletin* **47**, 3432–3439 (2012).

55. Hernando, A., Crespo, P. & García, M. A. Metallic Magnetic Nanoparticles. *The Scientific World Journal* https://www.hindawi.com/journals/tswj/2005/353792/abs/ (2005) doi:10.1100/tsw.2005.121.

56. Perebeinos, V., Chan, S.-W. & Zhang, F. 'Madelung model' prediction for dependence of lattice parameter on nanocrystal size. *Solid State Communications* **123**, 295–297 (2002).

57. Deshpande, S., Patil, S., Kuchibhatla, S. V. & Seal, S. Size dependency variation in lattice parameter and valency states in nanocrystalline cerium oxide. *Appl. Phys. Lett.* **87**, 133113 (2005).

58. Marrocchelli, D., Bishop, S. R., Tuller, H. L. & Yildiz, B. Understanding Chemical Expansion in Non-Stoichiometric Oxides: Ceria and Zirconia Case Studies. *Advanced Functional Materials* **22**, 1958–1965 (2012).

59. Chatzichristodoulou, C., Norby, P., Hendriksen, P. V. & Mogensen, M. B. Size of oxide vacancies in fluorite and perovskite structured oxides. *J Electroceram* **34**, 100–107 (2015).

60. Aidhy, D. S., Liu, B., Zhang, Y. & Weber, W. J. Chemical expansion affected oxygen vacancy stability in different oxide structures from first principles calculations. *Computational Materials Science* **99**, 298–305 (2015).

61. Li, P., Chen, I.-W. & Penner-Hahn, J. E. X-ray-absorption studies of zirconia polymorphs. II. Effect of Y 2 O 3 dopant on ZrO 2 structure. *Physical Review B* **48**, 10074–10081 (1993).

62. Garvie, R. C. The Occurrence of Metastable Tetragonal Zirconia as a Crystallite Size Effect. *J. Phys. Chem.* **69**, 1238–1243 (1965).

63. Joo, J. *et al.* Multigram Scale Synthesis and Characterization of Monodisperse Tetragonal Zirconia Nanocrystals. *J. Am. Chem. Soc.* **125**, 6553–6557 (2003).

64. Chraska, T., King, A. H. & Berndt, C. C. On the size-dependent phase transformation in nanoparticulate zirconia. *Materials Science and Engineering: A* **286**, 169–178 (2000).

65. Valmalette, J. Ch. & Isa, M. Size Effects on the Stabilization of Ultrafine Zirconia Nanoparticles. *Chem. Mater.* **14**, 5098–5102 (2002).

66. Shukla, S. & Seal, S. Thermodynamic Tetragonal Phase Stability in Sol−Gel Derived Nanodomains of Pure Zirconia. *J. Phys. Chem. B* **108**, 3395–3399 (2004).

67. Zhan, Z. & Zeng, H. C. Metastability of tetragonal ZrO2 derived from Zr-n-propoxide-acetylacetone-water-isopropyl alcohol. *Journal of Materials Research* **13**, 2174–2183 (1998).

68. Garvie, R. C. & Goss, M. F. Intrinsic size dependence of the phase transformation temperature in zirconia microcrystals. *J Mater Sci* **21**, 1253–1257 (1986).

69. Garvie, R. C. Stabilization of the tetragonal structure in zirconia microcrystals. *The Journal of Physical Chemistry* **82**, 218–224 (1978).

70. Block, S., Jornada, J. a. H. D. & Piermarini, G. J. Pressure-Temperature Phase Diagram of Zirconia. *Journal of the American Ceramic Society* **68**, 497–499 (1985).

71. Jornada, J. a. H. D., Piermarini, G. J. & Block, S. Metastable Retention of a High-Pressure Phase of Zirconia. *Journal of the American Ceramic Society* **70**, 628–630 (1987).

72. Yashima, M., Ohtake, K., Kakihana, M. & Yoshimura, M. Synthesis of Metastable Tetragonal (t′) Zirconia–Ceria Solid Solutions by the Polymerized Complex Method. *Journal of the American Ceramic Society* **77**, 2773–2776 (1994).

73. Mitsuhashi, T., Ichihara, M. & Tatsuke, U. Characterization and Stabilization of Metastable Tetragonal ZrO2. *Journal of the American Ceramic Society* **57**, 97–101 (1974).

74. Djurado, E., Bouvier, P. & Lucazeau, G. Crystallite Size Effect on the Tetragonal-Monoclinic Transition of Undoped Nanocrystalline Zirconia Studied by XRD and Raman Spectrometry. *Journal of Solid State Chemistry* **149**, 399–407 (2000).

75. Malakooti, R., Mahmoudi, H., Hosseinabadi, R., Petrov, S. & Migliori, A. Facile synthesis of pure non-monoclinic zirconia nanoparticles and their catalytic activity investigations for Knoevenagel condensation. *RSC Adv.* **3**, 22353–22359 (2013).

76. Carvalho, J. *et al.* Structure–property relationship of luminescent zirconia nanomaterials obtained by sol–gel method. *Journal of Materials Science* **50**, (2015).

77. Adamski, A., Jakubus, P. & Sojka, Z. Structural and textural evolution of zirconia nanocrystals induced by thermal treatment. *Materials Science-Poland* **26**, 9 (2008).

78. Srinivasan, R., Angelis, R. D. & Davis, B. H. Factors influencing the stability of the tetragonal form of zirconia. *Journal of Materials Research* **1**, 583–588 (1986).

79. Adamski, A., Jakubus, P. & Sojka, Z. Synthesis of nanostructured tetragonal ZrO2 of enhanced thermal stability. *Nukleonika* **Vol. 51,suppl.1**, 27–33 (2006).

80. Ouyang, H., Li, C., Li, K., Li, H. & Zhang, Y. Effect of pH on crystallization of nanocrystalline zirconia in a microwave-hydrothermal process. *J. Wuhan Univ. Technol.-Mat. Sci. Edit.* **31**, 68–73 (2016).

81. Karapetrova, E. *et al.* Oxygen Vacancies in Pure Tetragonal Zirconia Powders: Dependence on the Presence of Chlorine during Processing. *Journal of the American Ceramic Society* **84**, 65–70 (2001).

82. Osendi, M. I., Moya, J. S., Serna, C. J. & Soria, J. Metastability of Tetragonal Zirconia Powders. *Journal of the American Ceramic Society* **68**, 135–139 (1985).

83. Igawa, N. *et al.* Crystal Structure of Metastable Tetragonal Zirconia by Neutron Powder Diffraction Study. *Journal of the American Ceramic Society* **76**, 2673–2676 (1993).

84. Gómez, R. *et al.* Dehydroxylation and the Crystalline Phases in Sol-Gel Zirconia. *Journal of Sol-Gel Science and Technology* **11**, 309–319 (1998).

85. Teufer, G. The crystal structure of tetragonal ZrO2. *Acta Crystallographica* **15**, 1187–1187 (1962).

86. Michel, D., Mazerolles, L. & Perez Y Jorba, M. Fracture of metastable tetragonal zirconia crystals. *J Mater Sci* **18**, 2618–2628 (1983).

87. Igawa, N. & Ishii, Y. Crystal Structure of Metastable Tetragonal Zirconia up to 1473 K. *Journal of the American Ceramic Society* **84**, 1169–1171 (2001).

88. Keramidas, V. G. & White, W. B. Raman Scattering Study of the Crystallization and Phase Transformations of ZrO2. *Journal of the American Ceramic Society* **57**, 22–24 (1974).

89. Vage, J. L., Doi, K. & Mazieres, C. Nature and Thermal Evolution of Amorphous Hvdrated Zirconium Oxide. *Journal of the American Ceramic Society* **51**, 349–353 (1968).

90. Mommer, N., Lee, T. & Gardner, J. A. Stability of monoclinic and tetragonal zirconia at low oxygen partial pressure. *Journal of Materials Research* **15**, 377–381 (2000).

91. Srinivasan, R., Davis, B. H., Cavin, O. B. & Hubbard, C. R. Crystallization and Phase Transformation Process in Zirconia: An in situ High-Temperature X-ray Diffraction Study. *Journal of the American Ceramic Society* **75**, 1217–1222 (1992).

92. Bansal, G. K. & Heuer, A. H. On a martensitic phase transformation in zirconia (ZrO2)—I. Metallographic evidence. *Acta Metallurgica* **20**, 1281–1289 (1972).

93. Bouvier, P., Djurado, E., Lucazeau, G. & Le Bihan, T. High-pressure structural evolution of undoped tetragonal nanocrystalline zirconia. *Phys. Rev. B* **62**, 8731–8737 (2000).

94. Jamali, H., Mozafarinia, R., Shoja Razavi, R. & Ahmadi-Pidani, R. Comparison of thermal shock resistances of plasma-sprayed nanostructured and conventional yttria stabilized zirconia thermal barrier coatings. *Ceramics International* **38**, 6705–6712 (2012).

95. Lee, E. Y., Sohn, Y., Jha, S. K., Holmes, J. W. & Sisson, R. D. Phase Transformations of Plasma-Sprayed Zirconia–Ceria Thermal Barrier Coatings. *Journal of the American Ceramic Society* **85**, 2065–2071 (2002).

96. Shim, J. H., Chao, C.-C., Huang, H. & Prinz, F. B. Atomic Layer Deposition of Yttria-Stabilized Zirconia for Solid Oxide Fuel Cells. *Chem. Mater.* **19**, 3850–3854 (2007).

97. Hampikian, J. M. & Carter, W. B. The combustion chemical vapor deposition of high temperature materials. *Materials Science and Engineering: A* **267**, 7–18 (1999).

98. Han, J., Zeng, Y., Xomeritakis, G. & Lin, Y. S. Electrochemical vapor deposition synthesis and oxygen permeation properties of dense zirconia–yttria–ceria membranes. *Solid State Ionics* **98**, 63–72 (1997).

99. Scott, H. G. Phase relationships in the zirconia-yttria system. *J Mater Sci* **10**, 1527–1535 (1975).

100. Yashima, M., Takashina, H., Kakihana, M. & Yoshimura, M. Low-Temperature Phase Equilibria by the Flux Method and the Metastable–Stable Phase Diagram in the ZrO2–CeO2 System. *Journal of the American Ceramic Society* **77**, 1869–1874 (1994).

101. Tani, E., Yoshimura, M. & Somiya, S. Revised Phase Diagram of the System ZrO2-CeO2 Below 1400°C. *Journal of the American Ceramic Society* **66**, 506–510 (1983).

102. Yashima, M., Morimoto, K., Ishizawa, N. & Yoshimura, M. Zirconia–Ceria Solid Solution Synthesis and the Temperature–Time–Transformation Diagram for the 1:1 Composition. *Journal of the American Ceramic Society* **76**, 1745–1750 (1993).

103. Okubo, T. & Nagamoto, H. Low-temperature preparation of nanostructured zirconia and YSZ by sol-gel processing. *JOURNAL OF MATERIALS SCIENCE* **30**, 749–757 (1995).

104. Pascual, R., Sayer, M., Kumar, C. V. R. V. & Zou, L. Rapid thermal processing of zirconia thin films produced by the sol-gel method. *Journal of Applied Physics* **70**, 2348–2352 (1991).

105. Skovgaard, M., Ahniyaz, A., Sørensen, B. F., Almdal, K. & van Lelieveld, A. Effect of microscale shear stresses on the martensitic phase transformation of nanocrystalline tetragonal zirconia powders. *Journal of the European Ceramic Society* **30**, 2749–2755 (2010).

106. Matsui, K., Suzuki, H., Ohgai, M. & Arashi, H. Raman Spectroscopic Studies on the Formation Mechanism of Hydrous-Zirconia Fine Particles. *Journal of the American Ceramic Society* **78**, 146–152 (1995).

107. Srinivasan, R., Angelis, R. J. D., Ice, G. & Davis, B. H. Identification of tetragonal and cubic structures of zirconia using synchrotron x-radiation source. *Journal of Materials Research* **6**, 1287–1292 (1991).

108. Eom, H.-J. *et al.* Zirconia catalysts (ZrO2 and Na-ZrO2) for the conversion of phenethyl phenyl ether (PPE) in supercritical water. *Applied Catalysis A: General* **493**, 149–157 (2015).

109. Li, P., Chen, I.-W. & Penner-Hahn, J. E. X-ray-absorption studies of zirconia polymorphs. III. Static distortion and thermal distortion. *Phys. Rev. B* **48**, 10082–10089 (1993).

110. Catlow, C. R. A., Chadwick, A. V., Greaves, G. N. & Moroney, L. M. EXAFS Study of Yttria-Stabilized Zirconia. *Journal of the American Ceramic Society* **69**, 272–277 (1986).

111. Li, P., Chen, I.-W. & Penner-Hahn, J. E. X-ray-absorption studies of zirconia polymorphs. I. Characteristic local structures. *Phys. Rev. B* **48**, 10063–10073 (1993).

112. Yao, M. H., Baird, R. J., Kunz, F. W. & Hoost, T. E. An XRD and TEM Investigation of the Structure of Alumina-Supported Ceria–Zirconia. *Journal of Catalysis* **166**, 67–74 (1997).

113. Lee, J., Hur, Y. G., Kim, M.-S. & Lee, K.-Y. Catalytic reduction of nitrite in water over ceria- and ceria–zirconia-supported Pd catalysts. *Journal of Molecular Catalysis A: Chemical* **399**, 48–52 (2015).

114. Taniguchi, T. *et al.* Nanoscale heterogeneities in CeO2 –ZrO2 nanocrystals highlighted by UV-resonant Raman spectroscopy. *Nanoscale* **2**, 1426–1428 (2010).

115. Kim, J.-R., Myeong, W.-J. & Ihm, S.-K. Characteristics in oxygen storage capacity of ceria–zirconia mixed oxides prepared by continuous hydrothermal synthesis in supercritical water. *Applied Catalysis B: Environmental* **71**, 57–63 (2007).

116. Taguchi, M. *et al.* Supercritical hydrothermal synthesis of hydrophilic polymer - modified water-dispersible CeO 2 nanoparticles. *CrystEngComm* **13**, 2841–2848 (2011).

117. Rodriguez, J. A. *et al.* Properties of CeO2 and Ce1-xZrxO2 Nanoparticles: X-ray Absorption Near-Edge Spectroscopy, Density Functional, and Time-Resolved X-ray Diffraction Studies. *J. Phys. Chem. B* **107**, 3535–3543 (2003).

118. Yamaguchi, T. Application of ZrO2 as a catalyst and a catalyst support. *Catalysis Today* **20**, 199–217 (1994).

119. Abriata, J. P., Garcés, J. & Versaci, R. The O−Zr (Oxygen-Zirconium) system. *Bulletin of Alloy Phase Diagrams* **7**, 116–124 (1986).

120. Amsel, G., Béranger, G., de Gélas, B. & Lacombe, P. Use of the Nuclear Reaction O16(d, p)O17 to Study Oxygen Diffusion in Solids and its Application to Zirconium. *Journal of Applied Physics* **39**, 2246–2255 (1968).

121. Chen, P.-L. & Chen, I.-W. Grain Growth in CeO2: Dopant Effects, Defect Mechanism, and Solute Drag. *Journal of the American Ceramic Society* **79**, 1793–1800 (1996).

122. Zhao, C., Roebben, G., Heyns, M. M. & Van der Biest, O. Crystallisation and Tetragonal-Monoclinic Transformation in ZrO2 and HfO2 Dielectric Thin Films. *KEM* **206–213**, 1285–1288 (2001).

123. Cameron, M. A. & George, S. M. ZrO2 film growth by chemical vapor deposition using zirconium tetra-tert-butoxide. *Thin Solid Films* **348**, 90–98 (1999).

124. Zhang, F. *et al.* Application of zirconia thermal barrier coating on the surface of pulling-straightening roller. *International Journal of Heat and Technology* **35**, 765–772 (2017).

125. Chadwick, A. V. *et al.* Solid-State NMR and X-ray Studies of the Structural Evolution of Nanocrystalline Zirconia. *Chem. Mater.* **13**, 1219–1229 (2001).

126. Wang, H.-C. & Lin, K.-L. Characterization and metastability of alkoxy-derived tetragonal zirconia powder. *J Mater Sci* **26**, 2501–2506 (1991).

127. De Keukeleere, K. *et al.* Fast and Tunable Synthesis of ZrO2 Nanocrystals: Mechanistic Insights into Precursor Dependence. *Inorg. Chem.* **54**, 3469–3476 (2015).

128. Mizuno, M., Sasaki, Y., Lee, S. & Katakura, H. High-Yield Sol−Gel Synthesis of Well-Dispersed, Colorless ZrO2 Nanocrystals. *Langmuir* **22**, 7137–7140 (2006).

129. Asim, N. *et al.* Research and Development Aspects on Chemical Preparation Techniques of Photoanodes for Dye Sensitized Solar Cells. *International Journal of Photoenergy* **Volume 2014**, 21 pages (2014).

130. Zirconium Oxide Structure Prepared by the Sol-Gel Route: I, The Role of the Alcoholic Solvent. *ResearchGate* https://www.researchgate.net/publication/249463498_Zirconium_Oxide_Structure_Prepared_by_the_Sol-Gel_Route_I_The_Role_of_the_Alcoholic_Solvent doi:http://dx.doi.org/10.1111/j.1151-2916.2000.tb01200.x.

131. Livage, J., Henry, M. & Sanchez, C. Sol-gel chemistry of transition metal oxides. *Progress in Solid State Chemistry* **18**, 259–341 (1988).

132. Shane, M. & Mecartney, M. L. Sol-gel synthesis of zirconia barrier coatings. *Journal of Materials Science* **25**, 1537–1544 (1990).

133. Santos, V., Zeni, M., Bergmann, C. P. & Hohemberger, J. M. Correlation Beween Thermal Treatment and Tetragonal/Monoclinic nanostructured Zirconia Powder Obtained by Sol-Gel Process. *Reviews On Advanced Materials Science* **17**, 62–70 (2008).

134. Lind, C., Gates, S. D., Pedoussaut, N. M. & Baiz, T. I. Novel Materials through Non-Hydrolytic Sol-Gel Processing: Negative Thermal Expansion Oxides and Beyond. *Materials (Basel)* **3**, 2567–2587 (2010).

135. Chang, S. & Doong, R. Characterization of Zr-Doped TiO2 Nanocrystals Prepared by a Nonhydrolytic Sol−Gel Method at High Temperatures. *J. Phys. Chem. B* **110**, 20808–20814 (2006).

136. Yu, T., Joo, J., Park, Y. I. & Hyeon, T. Large-Scale Nonhydrolytic Sol–Gel Synthesis of Uniform-Sized Ceria Nanocrystals with Spherical, Wire, and Tadpole Shapes. *Angewandte Chemie* **117**, 7577–7580 (2005).

137. Vioux, A. Nonhydrolytic Sol−Gel Routes to Oxides. https://pubs.acs.org/doi/abs/10.1021/cm970322a (1997) doi:10.1021/cm970322a.

138. Tana, F. *et al.* Synthesis and characterization of scratch-resistant hybrid coatings based on non-hydrolytic sol-gel ZrO2 nanoparticles. *Progress in Organic Coatings* **103**, 60–68 (2017).

139. Styskalik, A., Skoda, D., Barnes, C. E. & Pinkas, J. The Power of Non-Hydrolytic Sol-Gel Chemistry: A Review. *Catalysts* **7**, 168 (2017).

140. Niederberger, M. & Garnweitner, G. Organic Reaction Pathways in the Nonaqueous Synthesis of Metal Oxide Nanoparticles. *Chemistry – A European Journal* **12**, 7282–7302 (2006).

141. Non-Aqueous Synthesis of High-Purity Metal Oxide Nanopowders Using an Ether Elimination Process - Pinna - 2004 - Advanced Materials - Wiley Online Library.

142. Mutin, P. H. & Vioux, A. Nonhydrolytic Processing of Oxide-Based Materials: Simple Routes to Control Homogeneity, Morphology, and Nanostructure. https://pubs.acs.org/doi/abs/10.1021/cm802348c (2009) doi:10.1021/cm802348c.

143. Omata, T., Goto, Y. & Otsuka-Yao-Matsuo, S. Nanocrystals of zirconia- and ceria-based solid electrolytes: Syntheses and properties. *Science and Technology of Advanced Materials* **8**, 524–530 (2007).

144. Pinna, N., Karmaoui, M. & Willinger, M.-G. The “benzyl alcohol route”: An elegant approach towards doped and multimetal oxide nanocrystals. *J Sol-Gel Sci Technol* **57**, 323–329 (2011).

145. Pinna, N. The “benzyl alcohol route”: an elegant approach towards organic–inorganic hybrid nanomaterials. *J. Mater. Chem.* **17**, 2769–2774 (2007).

146. Bondesgaard, M. *et al.* Guide to by-products formed in organic solvents under solvothermal conditions. *The Journal of Supercritical Fluids* **113**, 166–197 (2016).

147. Tani, E., Yoshimura, M. & Sōmiya, S. Formation of Ultrafine Tetragonal ZrO2 Powder Under Hydrothermal Conditions. *Journal of the American Ceramic Society* **66**, 11–14 (1983).

148. Wang, H., Li, G., Xue, Y. & Li, L. Hydrated surface structure and its impacts on the stabilization of t-ZrO2. *Journal of Solid State Chemistry* **180**, 2790–2797 (2007).

149. Štefanić, G., Musić, S., Gržeta, B., Popović, S. & Sekulić, A. Influence of pH on the stability of low temperature t-ZrO2. *Journal of Physics and Chemistry of Solids* **59**, 879–885 (1998).

150. Masoodiyeh, F., Mozdianfard, M. R. & Karimi-Sabet, J. Modeling zirconia nanoparticles prepared by supercritical water hydrothermal synthesis using population balance equation. *Powder Technology* **317**, 264–274 (2017).

151. Dudnik, E. V. Modern methods for hydrothermal synthesis of ZrO2-based nanocrystalline powders. *Powder Metall Met Ceram* **48**, 238–248 (2009).

152. Aymonier, C., Beslin, P., Jolivalt, C. & Cansell, F. Hydrothermal oxidation of a nitrogen-containing compound: the fenuron. *The Journal of Supercritical Fluids* **17**, 45–54 (2000).

153. Masoodiyeh, F., Karimi-Sabet, J., Khanchi, A. R. & Mozdianfard, M. R. Zirconia nanoparticle synthesis in sub and supercritical water — particle morphology and chemical equilibria. *Powder Technology* **269**, 461–469 (2015).

154. Loppinet-Serani, A., Aymonier, C. & Cansell, F. Supercritical water for environmental technologies. *J. Chem. Technol. Biotechnol.* **85**, 583–589 (2010).

155. Voisin, T. *et al.* Solubility of inorganic salts in sub- and supercritical hydrothermal environment: Application to SCWO processes. *The Journal of Supercritical Fluids* **120**, 18–31 (2017).

156. Tassaing, T., Danten, Y. & Besnard, M. Infrared spectroscopic study of hydrogen-bonding in water at high temperature and pressure. *Journal of Molecular Liquids* **101**, 149–158 (2002).

157. Bondarenko, G. V. & Gorbaty, Y. E. An infrared study of water vapour in the temperature range 573–723 K. Dimerization enthalpy and absorption intensities for monomer and dimer. *Molecular Physics* **74**, 639–647 (1991).

158. P. Lalanne *et al.* Hydrogen Bonding in Supercritical Ethanol Assessed by Infrared and Raman Spectroscopies. https://pubs.acs.org/doi/abs/10.1021/jp0309466 (2004) doi:10.1021/jp0309466.

159. Savage, P. E., Gopalan, S., Mizan, T. I., Martino, C. J. & Brock, E. E. Reactions at supercritical conditions: Applications and fundamentals. *AIChE Journal* **41**, 1723–1778 (1995).

160. Hakuta, Y., Onai, S., Terayama, H., Adschiri, T. & Arai, K. Production of Ultra-fine Ceria Particles by Hydrothermal Synthesis Under Supercritical Conditions. *Journal of Materials Science Letters* **17**, 1211–1213 (1998).

161. Benedetti, A., Fagherazzi, G. & Pinna, F. Preparation and Structural Characterization of Ultrafine Zirconia Powders. *Journal of the American Ceramic Society* **72**, 467–469 (1989).

162. Slostowski, C., Marre, S., Bassat, J.-M. & Aymonier, C. Synthesis of cerium oxide-based nanostructures in near- and supercritical fluids. *The Journal of Supercritical Fluids* **84**, 89–97 (2013).

163. Aymonier, C., Philippot, G., Erriguible, A. & Marre, S. Playing with chemistry in supercritical solvents and the associated technologies for advanced materials by design. *The Journal of Supercritical Fluids* **134**, 184–196 (2018).

164. Giroire, B., Marre, S., Garcia, A., Cardinal, T. & Aymonier, C. Continuous supercritical route for quantum-confined GaN nanoparticles. *React. Chem. Eng.* **1**, 151–155 (2016).

165. Giroire, B. *et al.* Tuning surface grafting density of CeO2 nanocrystals with near- and supercritical solvent characteristics. *Phys Chem Chem Phys* **18**, 1727–1734 (2016).

166. Sarathy, S. M., Oßwald, P., Hansen, N. & Kohse-Höinghaus, K. Alcohol combustion chemistry. *Progress in Energy and Combustion Science* **44**, 40–102 (2014).

167. Kritzer, P. Corrosion in high-temperature and supercritical water and aqueous solutions: a review. *The Journal of Supercritical Fluids* **29**, 1–29 (2004).

168. Norton, T. S. & Dryer, F. L. The flow reactor oxidation of C1−C4 alcohols and MTBE. *Symposium (International) on Combustion* **23**, 179–185 (1991).

169. Esarte, C. *et al.* Pyrolysis of Ethanol: Gas and Soot Products Formed. *Ind. Eng. Chem. Res.* **50**, 4412–4419 (2011).

170. Akerlof, G. Dielectric Constants of Some Organic Solvent-Water Mixtures at Various Temperatures. *J. Am. Chem. Soc.* **54**, 4125–4139 (1932).

171. Dannhauser, W. & Bahe, L. W. Dielectric Constant of Hydrogen Bonded Liquids. III. Superheated Alcohols. *The Journal of Chemical Physics* **40**, 3058–3066 (1964).

172. Kusdiana, D. & Saka, S. Kinetics of transesterification in rapeseed oil to biodiesel fuel as treated in supercritical methanol. *Fuel* **80**, 693–698 (2001).

173. D'Aprano, A., Donato, D. I. & Caponetti, E. The static dielectric constant of solutions of water inn-alcohols at 15, 25, 35, and 45°C. *J Solution Chem* **8**, 135 (1979).

174. Carstensen, H.-H. & Dean, A. M. Development of Detailed Kinetic Models for the Thermal Conversion of Biomass via First Principle Methods and Rate Estimation Rules. in *Computational Modeling in Lignocellulosic Biofuel Production* vol. 1052 201–243 (American Chemical Society, 2010).

175. Zhao, L., Ye, L., Zhang, F. & Zhang, L. Thermal Decomposition of 1-Pentanol and Its Isomers: A Theoretical Study. *J. Phys. Chem. A* **116**, 9238–9244 (2012).

176. Park, J., Zhu, R. S. & Lin, M. C. Thermal decomposition of ethanol. I. Ab Initio molecular orbital/Rice–Ramsperger–Kassel–Marcus prediction of rate constant and product branching ratios. *J. Chem. Phys.* **117**, 3224–3231 (2002).

177. Li, J., Kazakov, A. & Dryer, F. L. Experimental and Numerical Studies of Ethanol Decomposition Reactions. *J. Phys. Chem. A* **108**, 7671–7680 (2004).

178. El-Nahas, A. M., Mangood, A. H., Takeuchi, H. & Taketsugu, T. Thermal Decomposition of 2-Butanol as a Potential Nonfossil Fuel: A Computational Study. *J. Phys. Chem. A* **115**, 2837–2846 (2011).

179. Oßwald, P. *et al.* Combustion of butanol isomers – A detailed molecular beam mass spectrometry investigation of their flame chemistry. *Combustion and Flame* **158**, 2–15 (2011).

180. An experimental and kinetic modeling study of n-propanol and i-propanol ignition at high temperatures | Request PDF. *ResearchGate* https://www.researchgate.net/publication/260024362_An_experimental_and_kinetic_mo

deling_study_of_n-propanol_and_i-propanol_ignition_at_high_temperatures doi:http://dx.doi.org/10.1016/j.combustflame.2013.08.003.

181. Harper, M. R., Van Geem, K. M., Pyl, S. P., Marin, G. B. & Green, W. H. Comprehensive reaction mechanism for n-butanol pyrolysis and combustion. *Combustion and Flame* **158**, 16–41 (2011).
182. Sarathy, S. M. *et al.* An experimental and kinetic modeling study of n-butanol combustion. *Combustion and Flame* **156**, 852–864 (2009).
183. Black, G., Curran, H. J., Pichon, S., Simmie, J. M. & Zhukov, V. Bio-butanol: Combustion properties and detailed chemical kinetic model. *Combustion and Flame* **157**, 363–373 (2010).
184. Wang, G., Yuan, W., Li, Y., Zhao, L. & Qi, F. Experimental and kinetic modeling study of n-pentanol pyrolysis and combustion. *Combustion and Flame* **162**, 3277–3287 (2015).
185. Cai, J. *et al.* Experimental and Kinetic Modeling Study of n-Butanol Pyrolysis and Combustion. *Energy Fuels* **26**, 5550–5568 (2012).
186. Noorani, K. E., Akih-Kumgeh, B. & Bergthorson, J. M. Comparative High Temperature Shock Tube Ignition of C1−C4 Primary Alcohols. *Energy Fuels* **24**, 5834–5843 (2010).
187. Kasper, T. S., Oßwald, P., Kamphus, M. & Kohse-Höinghaus, K. Ethanol flame structure investigated by molecular beam mass spectrometry. *Combustion and Flame* **150**, 220–231 (2007).
188. Xu, Z. F., Xu, K. & Lin, M. C. Thermal decomposition of ethanol. 4. Ab initio chemical kinetics for reactions of H atoms with CH3CH2O and CH3CHOH radicals. *J Phys Chem A* **115**, 3509–3522 (2011).
189. Frassoldati, A. *et al.* An experimental and kinetic modeling study of n-propanol and isopropanol combustion. in (2009).

190. Tsang, W. Thermal stability of alcohols. *International Journal of Chemical Kinetics* **8**, 173–192 (1976).

191. Cai, J. *et al.* Experimental and kinetic modeling study of i-butanol pyrolysis and combustion. *Combustion and Flame* **161**, 1955–1971 (2014).

192. Shi, B., Dabbagh, H. A. & Davis, B. H. Alcohol dehydration. Isotope studies of the conversion of 3-pentanol. *Journal of Molecular Catalysis A: Chemical* **141**, 257–262 (1999).

193. Catalytic activity of ZrO2 and ThO2 for HD exchange reaction between methyl group of adsorbed isopropyl alcohol-d8 and surface OH group. *ResearchGate* https://www.researchgate.net/publication/244718935_CATALYTIC_ACTIVITY_OF_ZrO2_AND_ThO2_FOR_HD_EXCHANGE_REACTION_BETWEEN_METHYL_GROUP_OF_ADSORBED_ISOPROPYL_ALCOHOL-d8_AND_SURFACE_OH_GROUP doi:http://dx.doi.org/10.1246/cl.1976.677.

194. Carrizosa, I. & Munuera, G. Study of the interaction of aliphatic alcohols with TiO2: I. Decomposition of ethanol, 2-propanol, and tert-butanol on anatase. *Journal of Catalysis* **49**, 174–188 (1977).

195. Carrizosa, I. & Munuera, G. Study of the interaction of aliphatic alcohols with TiO2: II. On the mechanism of alcohol dehydration on anatase. *Journal of Catalysis* **49**, 189–200 (1977).

196. Carrizosa, I., Munuera, G. & Castañar, S. Study of the interaction of aliphatic alcohols with TiO2: III. Formation of alkyl-titanium species during methanol decomposition. *Journal of Catalysis* **49**, 265–277 (1977).

197. Davis, B. H. Catalytic conversion of alcohols: VI. Selectivity of indium oxide. *Journal of Catalysis* **52**, 435–444 (1978).

198. Siddhan, S. & Narayanan, K. Dehydration of alcohols over oxide catalysts γ-eliminations-stereospecificity and selectivity. *Journal of Catalysis* **59**, 405–422 (1979).

199. Larsen, G., Lotero, E., Petkovic, L. M. & Shobe, D. S. Alcohol Dehydration Reactions over Tungstated Zirconia Catalysts. *Journal of Catalysis* **169**, 67–75 (1997).

200. Nel, R. J. J. & de Klerk, A. Dehydration of C5−C12 Linear 1-Alcohols over η-Alumina to Fuel Ethers. *Ind. Eng. Chem. Res.* **48**, 5230–5238 (2009).

201. Halász, I., Vinek, H., Thomke, K. & Noller, H. Rate Determining Step in Alcohol Dehydration on La2O3, ThO2 and MoO3, and Relations to Double Bond Shift in Olefins. *Zeitschrift für Physikalische Chemie* **144**, 157–163 (2011).

202. Nguyen, T. T. N. *et al.* Synthesis, characterization and study of lanthanum phosphates as light alcohols dehydration catalysts. *Applied Catalysis B: Environmental* **166–167**, 432–444 (2015).

203. Albuquerque, E. M., Borges, L. E. P., Fraga, M. A. & Sievers, C. Relationship between Acid–Base Properties and the Activity of ZrO2-Based Catalysts for the Cannizzaro Reaction of Pyruvaldehyde to Lactic Acid. *ChemCatChem* **9**, 2675–2683 (2017).

204. Tyrsted, C. *et al.* Watching nanoparticles form: an in situ (small-/wide-angle X-ray scattering/total scattering) study of the growth of yttria-stabilised zirconia in supercritical fluids. *Chemistry* **18**, 5759–5766 (2012).

205. Guglielmi, M. & Carturan, G. Precursors for sol-gel preparations. *Journal of Non-Crystalline Solids* **100**, 16–30 (1988).

206. Sanchez, C., Livage, J., Henry, M. & Babonneau, F. Chemical modification of alkoxide precursors. *Journal of Non-Crystalline Solids* **100**, 65–76 (1988).

207. Shinohara, Y., Nakajima, T. & Suzuki, S. A theoretical study of the dehydration and the dehydrogenation processes of alcohols on metal oxides using MOPAC. *Journal of Molecular Structure: THEOCHEM* **460**, 231–244 (1999).

208. Kostestkyy, P., Yu, J., Gorte, R. J. & Mpourmpakis, G. Structure–activity relationships on metal-oxides: alcohol dehydration. *Catal. Sci. Technol.* **4**, 3861–3869 (2014).

209. Phung, T. K., Proietti Hernández, L. & Busca, G. Conversion of ethanol over transition metal oxide catalysts: Effect of tungsta addition on catalytic behaviour of titania and zirconia. *Applied Catalysis A: General* **489**, 180–187 (2015).

210. Bringué, R., Ramírez, E., Iborra, M., Tejero, J. & Cunill, F. Kinetics of 1-hexanol etherification on Amberlyst 70. *Chemical Engineering Journal* **246**, 71–78 (2014).

211. Dallali Isfahani, T., Javadpour, J., Khavandi, A., Goodarzi, M. & Rezaie, H. R. Nanocrystalline Growth Activation Energy of Zirconia Polymorphs Synthesized by Mechanochemical Technique. *Journal of Materials Science & Technology* **30**, 387–393 (2014).

212. Wu, D. *et al.* Hydrogen generation properties and the hydrolysis mechanism of Zr(BH4)4·8NH3. *J. Mater. Chem. A* **5**, 16630–16635 (2017).

213. Shukla, S., Seal, S., Vij, R. & Bandyopadhyay, S. Reduced Activation Energy for Grain Growth in Nanocrystalline Yttria-Stabilized Zirconia. *Nano Lett.* **3**, 397–401 (2003).

214. Bartlett, J. R., Woolfrey, J. L., Percy, M., Spiccia, L. & West, B. O. Kinetics of colloid formation during the preparation of sol-gel zirconia. *J Sol-Gel Sci Technol* **2**, 215–220 (1994).

215. Adschiri, T., Hakuta, Y. & Arai, K. Hydrothermal Synthesis of Metal Oxide Fine Particles at Supercritical Conditions. *Ind. Eng. Chem. Res.* **39**, 4901–4907 (2000).

216. Tyrsted, C. *et al.* In-Situ Synchrotron Radiation Study of Formation and Growth of Crystalline CexZr1−xO2 Nanoparticles Synthesized in Supercritical Water. *Chem. Mater.* **22**, 1814–1820 (2010).

217. Demoisson, F., Ariane, M., Piolet, R. & Bernard, F. Original Supercritical Water Device for Continuous Production of Nanopowders. *Advanced Engineering Materials* **13**, 487–493 (2011).

218. Tyrsted, C. *et al.* Watching nanoparticles form: an in situ (small-/wide-angle X-ray scattering/total scattering) study of the growth of yttria-stabilised zirconia in supercritical fluids. *Chemistry* **18**, 5759–5766 (2012).

219. Adschiri, T., Kanazawa, K. & Arai, K. Rapid and Continuous Hydrothermal Crystallization of Metal Oxide Particles in Supercritical Water. *Journal of the American Ceramic Society* **75**, 1019–1022 (1992).

220. Hakuta, Y., Ohashi, T., Hayashi, H. & Arai, K. Hydrothermal synthesis of zirconia nanocrystals in supercritical water. *Journal of Materials Research* **19**, 2230–2234 (2004).

221. Sue, K. *et al.* Size-controlled synthesis of metal oxide nanoparticles with a flow-through supercritical water method. *Green Chem.* **8**, 634–638 (2006).

222. Becker, J. *et al.* Experimental setup for in situ X-ray SAXS/WAXS/PDF studies of the formation and growth of nanoparticles in near- and supercritical fluids. *J Appl Cryst, J Appl Crystallogr* **43**, 729–736 (2010).

223. ADAMSKI, A., JAKUBUS, P. & SOJKA, Z. Structural and textural evolution of zirconia nanocrystals induced by thermal treatment. 8.

224. Chraska, T., King, A. H. & Berndt, C. C. On the size-dependent phase transformation in nanoparticulate zirconia. *Materials Science and Engineering: A* **286**, 169–178 (2000).

225. Valmalette, J. Ch. & Isa, M. Size Effects on the Stabilization of Ultrafine Zirconia Nanoparticles. *Chem. Mater.* **14**, 5098–5102 (2002).

226. Joo, J. *et al.* Multigram Scale Synthesis and Characterization of Monodisperse Tetragonal Zirconia Nanocrystals. *J. Am. Chem. Soc.* **125**, 6553–6557 (2003).

227. Becker, J. *et al.* Critical Size of Crystalline ZrO2 Nanoparticles Synthesized in Near- and Supercritical Water and Supercritical Isopropyl Alcohol. *ACS Nano* **2**, 1058–1068 (2008).

228. Adschiri, T., Hakuta, Y. & Arai, K. Hydrothermal Synthesis of Metal Oxide Fine Particles at Supercritical Conditions. *Industrial & Engineering Chemistry Research* **39**, 4901–4907 (2000).

229. MATSON, D. W., LINEHAN, J. C. & GEUSIC, M. E. Ultrafine Oxide Powders Produced by Rapid Thermal Decomposition of Precursors in Solution. *Particulate Science and Technology* **10**, 143–154 (1992).

230. Tsunekawa, S., Ito, S., Kawazoe, Y. & Wang, J.-T. Critical Size of the Phase Transition from Cubic to Tetragonal in Pure Zirconia Nanoparticles. *Nano Lett.* **3**, 871–875 (2003).

231. Marre, S. *et al.* Kinetically Controlled Formation of Supported Nanoparticles in Low Temperature Supercritical Media for the Development of Advanced Nanostructured Materials. https://pubs.acs.org/doi/abs/10.1021/jp809533n (2009) doi:10.1021/jp809533n.

232. Aymonier, C. *et al.* Hybrids of silver nanoparticles with amphiphilic hyperbranched macromolecules exhibiting antimicrobial properties. *Chemical Communications* **0**, 3018–3019 (2002).

233. Cansell, F. & Aymonier, C. Design of functional nanostructured materials using supercritical fluids. *The Journal of Supercritical Fluids* **47**, 508–516 (2009).

234. Aymonier, C., Loppinet-Serani, A., Reverón, H., Garrabos, Y. & Cansell, F. Review of supercritical fluids in inorganic materials science. *The Journal of Supercritical Fluids* **38**, 242–251 (2006).

235. Philippot, G. *et al.* Coupling in situ synchrotron radiation with ex situ spectroscopy characterizations to study the formation of Ba1−xSrxTiO3 nanoparticles in supercritical fluids. *The Journal of Supercritical Fluids* **87**, 111–117 (2014).

236. Newton, P., Copeland, C. S. & Benson, S. W. Dielectric Constant of Ethanol in the Neighborhood of the Critical Temperature. *The Journal of Chemical Physics* **37**, 339–346 (1962).

237. Voisin, T. *et al.* Investigation of the precipitation of Na2SO4 in supercritical water. *Chemical Engineering Science* **174**, 268–276 (2017).

238. Slostowski, C., Marre, S., Babot, O., Toupance, T. & Aymonier, C. Near- and Supercritical Alcohols as Solvents and Surface Modifiers for the Continuous Synthesis of Cerium Oxide Nanoparticles. *Langmuir* **28**, 16656–16663 (2012).

239. Fateley, W. G., McDevitt, N. T. & Bentley, F. F. Infrared and Raman Selection Rules for Lattice Vibrations: The Correlation Method. *Appl Spectrosc* **25**, 155–173 (1971).

240. Phillippi, C. M. & Mazdiyasni, K. S. Infrared and Raman Spectra of Zirconia Polymorphs. *Journal of the American Ceramic Society* **54**, 254–258 (1971).

241. Keramidas, V. G. & White, W. B. Raman Scattering Study of the Crystallization and Phase Transformations of ZrO2. *Journal of the American Ceramic Society* **57**, 22–24 (1974).

242. Perry, C. H., Liu, D.-W. & Ingel, R. P. Phase Characterization of Partially Stabilized Zirconia by Raman Spectroscopy. *Journal of the American Ceramic Society* **68**, C-184-C–187 (1985).

243. Hirata, T., Asari, E. & Kitajima, M. Infrared and Raman Spectroscopic Studies of ZrO2 Polymorphs Doped with Y2O3 or CeO2. *Journal of Solid State Chemistry* **110**, 201–207 (1994).

244. López, E. F., Escribano, V. S., Panizza, M., Carnasciali, M. M. & Busca, G. Vibrational and electronic spectroscopic properties of zirconia powders. *J. Mater. Chem.* **11**, 1891–1897 (2001).

245. Petkov, V. *et al.* Solving the nanostructure problem: exemplified on metallic alloy nanoparticles. *Nanoscale* **6**, 10048–10061 (2014).

246. Billinge, S. J. L. & Levin, I. The Problem with Determining Atomic Structure at the Nanoscale. *Science* **316**, 561–565 (2007).

247. Billinge, S. J. L. Nanoscale structural order from the atomic pair distribution function (PDF): There's plenty of room in the middle. *Journal of Solid State Chemistry* **181**, 1695–1700 (2008).

248. Nayak, N. B. & Nayak, B. B. Temperature-mediated phase transformation, pore geometry and pore hysteresis transformation of borohydride derived in-born porous zirconium hydroxide nanopowders. *Sci Rep* **6**, 26404 (2016).

249. Golubev, I. F., Vasil'kovskaya, T. N. & Zolin, V. S. Experimental study of the density of aliphatic alcohols at various temperatures and pressures. *Journal of Engineering Physics* **38**, 399–401 (1980).

250. Akerlof, G. Dielectric Constants of Some Organic Solvent-Water Mixtures at Various Temperatures. *J. Am. Chem. Soc.* **54**, 4125–4139 (1932).

251. Bremholm, M., Becker-Christensen, J. & Iversen, B. B. High-Pressure, High-Temperature Formation of Phase-Pure Monoclinic Zirconia Nanocrystals Studied by Time-Resolved in situ Synchrotron X-Ray Diffraction. *Advanced Materials* **21**, 3572–3575 (2009).

252. Bremholm, M., Birkedal, H., Iversen, B. B. & Pedersen, J. S. Structural Evolution of Aqueous Zirconium Acetate by Time-Resolved Small-Angle X-ray Scattering and Rheology. *J. Phys. Chem. C* **119**, 12660–12667 (2015).

253. Tyrsted, C. *et al.* Understanding the Formation and Evolution of Ceria Nanoparticles Under Hydrothermal Conditions. *Angewandte Chemie International Edition* **51**, 9030–9033 (2012).

254. Jensen, K. M. Ø. *et al.* Revealing the Mechanisms behind SnO2 Nanoparticle Formation and Growth during Hydrothermal Synthesis: An In Situ Total Scattering Study. *J. Am. Chem. Soc.* **134**, 6785–6792 (2012).

255. Mi, J.-L. *et al.* Rapid Hydrothermal Preparation of Rutile TiO2 Nanoparticles by Simultaneous Transformation of Primary Brookite and Anatase: An in Situ Synchrotron PXRD Study. *Crystal Growth & Design* **12**, 6092–6097 (2012).

256. Grangeon, S. *et al.* Quantitative X-ray pair distribution function analysis of nanocrystalline calcium silicate hydrates: a contribution to the understanding of cement chemistry. *J Appl Cryst, J Appl Crystallogr* **50**, 14–21 (2017).

257. Gamez-Mendoza, L., Terban, M. W., Billinge, S. J. L. & Martinez-Inesta, M. Modelling and validation of particle size distributions of supported nanoparticles using the pair distribution function technique. *J Appl Cryst, J Appl Crystallogr* **50**, 741–748 (2017).

258. Usher, T.-M., Olds, D., Liu, J. & Page, K. A numerical method for deriving shape functions of nanoparticles for pair distribution function refinements. *Acta Cryst A, Acta Cryst Sect A, Acta Crystallogr A, Acta Crystallogr Sect A, Acta Crystallogr A Cryst Phys Diffr Theor Gen Crystallogr, Acta Crystallogr Sect A Cryst Phys Diffr Theor Gen Crystallogr* **74**, 322–331 (2018).

259. Prill, D., Juhás, P., Billinge, S. J. L. & Schmidt, M. U. Towards solution and refinement of organic crystal structures by fitting to the atomic pair distribution function. *Acta Cryst A, Acta Cryst Sect A, Acta Crystallogr A, Acta Crystallogr Sect A, Acta Crystallogr A Cryst Phys Diffr Theor Gen Crystallogr, Acta Crystallogr Sect A Cryst Phys Diffr Theor Gen Crystallogr* **72**, 62–72 (2016).

260. Prill, D., Juhás, P., Schmidt, M. U. & Billinge, S. J. L. Modelling pair distribution functions (PDFs) of organic compounds: describing both intra- and intermolecular correlation functions in calculated PDFs. *J Appl Cryst, J Appl Crystallogr* **48**, 171–178 (2015).

261. Terban, M. W., Cheung, E. Y., Krolikowski, P. & Billinge, S. J. L. Recrystallization, Phase Composition, and Local Structure of Amorphous Lactose from the Total Scattering Pair Distribution Function. *Crystal Growth & Design* **16**, 210–220 (2016).

262. Chapman, K. W. Emerging operando and x-ray pair distribution function methods for energy materials development. *MRS Bulletin* **41**, 231–240 (2016).

263. Egami, T. & Billinge, S. J. L. *Underneath the Bragg Peaks: Structural Analysis of Complex Materials*. (Elsevier, 2003).

264. Palosz, B. *et al.* High pressure x-ray diffraction studies on nanocrystalline materials. *J. Phys.: Condens. Matter* **16**, S353 (2004).

265. Dinnebier, R. Rietveld Refinement from Powder Diffraction Data. *Commission on powder diffraction* 47 (2001).

266. Proffen, T. & Billinge, S. J. L. PDFFIT, a program for full profile structural refinement of the atomic pair distribution function. *J Appl Cryst* **32**, 572–575 (1999).

267. Farrow, C. L. *et al.* PDFfit2 and PDFgui: computer programs for studying nanostructure in crystals. *J. Phys.: Condens. Matter* **19**, 335219 (2007).

268. L. Farrow, C., Shi, C., Juhás, P., Peng, X. & Billinge, S. Robust structure and morphology parameters for CdS nanoparticles by combining small-angle X-ray scattering and atomic pair distribution function data in a complex modeling framework. *Journal of Applied Crystallography* **47**, (2014).

269. Gilbert, B. Finite size effects on the real-space pair distribution function of nanoparticles. *J Appl Cryst* **41**, 554–562 (2008).

270. Farrow, C. L. & Billinge, S. J. L. Relationship between the atomic pair distribution function and small-angle scattering: implications for modeling of nanoparticles. *Acta Crystallographica Section A* **65**, 232–239 (2009).

271. Masadeh, A. S. *et al.* Quantitative size-dependent structure and strain determination of CdSe nanoparticles using atomic pair distribution function analysis. *Phys. Rev. B* **76**, 115413 (2007).

272. Shi, C. *et al.* Evidence for Anomalous Bond Softening and Disorder Below 2 nm Diameter in Carbon-Supported Platinum Nanoparticles from the Temperature-Dependent Peak Width of the Atomic Pair Distribution Function. *J. Phys. Chem. C* **117**, 7226–7230 (2013).

273. Gamez-Mendoza, L., Terban, M. W., Billinge, S. J. L. & Martinez-Inesta, M. Modelling and validation of particle size distributions of supported nanoparticles using the pair distribution function technique. *J Appl Cryst* **50**, 741–748 (2017).

274. Cervellino, A., Giannini, C. & Guagliardi, A. DEBUSSY: a Debye user system for nanocrystalline materials. *J Appl Cryst* **43**, 1543–1547 (2010).

275. Farrow, C. L., Bediako, D. K., Surendranath, Y., Nocera, D. G. & Billinge, S. J. L. Intermediate-Range Structure of Self-Assembled Cobalt-Based Oxygen-Evolving Catalyst. *J. Am. Chem. Soc.* **135**, 6403–6406 (2013).

276. Zhu, M. *et al.* Structure of Sulfate Adsorption Complexes on Ferrihydrite. *Environ. Sci. Technol. Lett.* **1**, 97–101 (2014).

277. Scardi, P., Billinge, S. J. L., Neder, R. & Cervellino, A. Celebrating 100 years of the Debye scattering equation. *Acta Cryst A* **72**, 589–590 (2016).

278. Usher, T.-M., Olds, D., Liu, J. & Page, K. A numerical method for deriving shape functions of nanoparticles for pair distribution function refinements. *Acta Cryst A* **74**, 322–331 (2018).

279. Cernuto, G., Masciocchi, N., Cervellino, A., Colonna, G. M. & Guagliardi, A. Size and Shape Dependence of the Photocatalytic Activity of TiO2 Nanocrystals: A Total Scattering Debye Function Study. *J. Am. Chem. Soc.* **133**, 3114–3119 (2011).

280. Raghavan, S. *et al.* Ta2O5/Nb2O5 and Y2O3 Co-doped Zirconias for Thermal Barrier Coatings. *Journal of the American Ceramic Society* **87**, 431–437 (2008).

281. Yashima, M., Morimoto, K., Ishizawa, N. & Yoshimura, M. Zirconia-Ceria Solid Solution Synthesis and the Temperature-Time-Transformation Diagram for the 1:1 Composition. *Journal of the American Ceramic Society* **76**, 1745–1750 (1993).

282. Priya, N. S., Somayaji, C. & Kanagaraj, S. Optimization of Ceria-Zirconia Solid Solution based on OSC Measurement by Cyclic Heating Process. *Procedia Engineering* **64**, 1235–1241 (2013).

283. Kim, J.-R., Myeong, W.-J. & Ihm, S.-K. Characteristics in oxygen storage capacity of ceria–zirconia mixed oxides prepared by continuous hydrothermal synthesis in supercritical water. *Applied Catalysis B: Environmental* **71**, 57–63 (2007).

284. Catlow, C. R. A., Chadwick, A. V., Greaves, G. N. & Moroney, L. M. EXAFS Study of Yttria-Stabilized Zirconia. *Journal of the American Ceramic Society* **69**, 272–277 (1986).

285. Garvie, R. C. The Occurrence of Metastable Tetragonal Zirconia as a Crystallite Size Effect. *The Journal of Physical Chemistry* **69**, 1238–1243 (1965).

286. Joo, J. *et al.* Multigram Scale Synthesis and Characterization of Monodisperse Tetragonal Zirconia Nanocrystals. *Journal of the American Chemical Society* **125**, 6553–6557 (2003).

287. Bokhimi, X. *et al.* Tetragonal Nanophase Stabilization in Nondoped Sol–Gel Zirconia Prepared with Different Hydrolysis Catalysts. *Journal of Solid State Chemistry* **135**, 28–35 (1998).

288. Chraska, T., King, A. H. & Berndt, C. C. On the size-dependent phase transformation in nanoparticulate zirconia. *Materials Science and Engineering: A* **286**, 169–178 (2000).

289. Shukla, S. & Seal, S. Thermodynamic Tetragonal Phase Stability in Sol−Gel Derived Nanodomains of Pure Zirconia. *J. Phys. Chem. B* **108**, 3395–3399 (2004).

290. Becker, J. *et al.* Critical Size of Crystalline ZrO $_2$ Nanoparticles Synthesized in Near- and Supercritical Water and Supercritical Isopropyl Alcohol. *ACS Nano* **2**, 1058–1068 (2008).

291. Igawa, N. *et al.* Crystal Structure of Metastable Tetragonal Zirconia by Neutron Powder Diffraction Study. *Journal of the American Ceramic Society* **76**, 2673–2676 (1993).

292. Galkin, A. A. & Lunin, V. V. Subcritical and supercritical water: a universal medium for chemical reactions. *Russ. Chem. Rev.* **74**, 21 (2005).

293. Guinebretière, R., Dauger, A., Lecomte, A. & Vesteghem, H. Tetragonal zirconia powders from the zirconium n-propoxide-acetylacetone-water-isopropanol system. *Journal of Non-Crystalline Solids* **147–148**, 542–547 (1992).

294. Philippot, G. *et al.* Coupling in situ synchrotron radiation with ex situ spectroscopy characterizations to study the formation of Ba1−xSrxTiO3 nanoparticles in supercritical fluids. *The Journal of Supercritical Fluids* **87**, 111–117 (2014).

295. Sadykov, V. A. *et al.* Nanoscale Structural Features of Ultra-fine Zirconia Powders Obtained Via Precipitation-hydrothermal Treatment Route. *MRS Online Proceedings Library Archive* **878**, (2005).

296. Wu, L. *et al.* Oxidation state and lattice expansion of CeO2−x nanoparticles as a function of particle size. *Phys. Rev. B* **69**, 125415 (2004).

297. Hirata, T., Asari, E. & Kitajima, M. Infrared and Raman Spectroscopic Studies of ZrO2 Polymorphs Doped with Y2O3 or CeO2. *Journal of Solid State Chemistry* **110**, 201–207 (1994).

298. Keramidas, V. G. & White, W. B. Raman Scattering Study of the Crystallization and Phase Transformations of ZrO2. *Journal of the American Ceramic Society* **57**, 22–24 (1974).

299. Matsui, K., Suzuki, H., Ohgai, M. & Arashi, H. Raman Spectroscopic Studies on the Formation Mechanism of Hydrous-Zirconia Fine Particles. *Journal of the American Ceramic Society* **78**, 146–152 (1995).

300. Bouvier, P., Djurado, E., Ritter, C., Dianoux, A. J. & Lucazeau, G. Low temperature phase transformation of nanocrystalline tetragonal ZrO2 by neutron and Raman scattering studies. *International Journal of Inorganic Materials* **3**, 647–654 (2001).

301. Alzyab, B., Perry, C. H. & Ingel, R. P. High-Pressure Phase Transitions in Zirconia and Yttria-Doped Zirconia. *Journal of the American Ceramic Society* **70**, 760–765 (1987).

302. Santos, V., Zeni, M., Bergmann, C. P. & Hohemberger, J. M. CORRELATION BETWEEN THERMAL TREATMENT AND TETRAGONAL/MONOCLINIC NANOSTRUCTURED ZIRCONIA POWDER OBTAINED BY SOL–GEL PROCESS. 9.

303. Wang, Q., Li, C., Guo, M., Hu, C. & Xie, Y. Controllable synthesis of zirconia nano-powders using vapor-phase hydrolysis and theoretical analysis. *J. Mater. Chem. A* **2**, 1346–1352 (2014).

304. Taguchi, M., Takami, S., Naka, T. & Adschiri, T. Growth Mechanism and Surface Chemical Characteristics of Dicarboxylic Acid-Modified CeO2 Nanocrystals Produced in Supercritical Water: Tailor-Made Water-Soluble CeO2 Nanocrystals. *Crystal Growth & Design* **9**, 5297–5303 (2009).

305. McAfee, L. Infrared and Raman Spectra of Inorganic and Coordination Compounds. Part A: Theory and Applications in Inorganic Chemistry; Part B: Application in

Coordination, Organometallic, and Bioinorganic Chemistry, 5th Edition (Nakamoto, Kazuo). *J. Chem. Educ.* **77**, 1122 (2000).

306. Wu, J. C.-S. & Cheng, L.-C. An improved synthesis of ultrafiltration zirconia membranes via the sol–gel route using alkoxide precursor. *Journal of Membrane Science* **167**, 253–261 (2000).
307. Collins, D. E. & Bowman, K. J. Influence of atmosphere on crystallization of zirconia from a zirconium alkoxide. *Journal of Materials Research* **13**, 1230–1237 (1998).
308. Wolf, C. & Rüssel, C. Sol-gel formation of zirconia: preparation, structure and rheology of sols. *J Mater Sci* **27**, 3749–3755 (1992).
309. Klenov, D. O., Donner, W., Foran, B. & Stemmer, S. Impact of stress on oxygen vacancy ordering in epitaxial (La0.5Sr0.5)CoO3−∂ thin films. *Appl. Phys. Lett.* **82**, 3427–3429 (2003).
310. Li, N. *et al.* Effects of oxygen vacancies on the electrochemical performance of tin oxide. *J. Mater. Chem. A* **1**, 1536–1539 (2013).
311. Jia, C. L. & Urban, K. Atomic-Resolution Measurement of Oxygen Concentration in Oxide Materials. *Science* **303**, 2001–2004 (2004).
312. Leger, J. M., Tomaszewski, P. E., Atouf, A. & Pereira, A. S. Pressure-induced structural phase transitions in zirconia under high pressure. *Phys. Rev. B* **47**, 14075–14083 (1993).
313. Kusunoki, M., Yonemitsu, K., Sasaki, Y. & Kubo, Y. In Situ Observation of Zirconia Particles at 1200°C by High-Resolution Electron Microscopy. *Journal of the American Ceramic Society* **76**, 763–765 (1993).
314. Rodriguez, J. A. *et al.* Properties of CeO2 and Ce1-xZrxO2 Nanoparticles: X-ray Absorption Near-Edge Spectroscopy, Density Functional, and Time-Resolved X-ray Diffraction Studies. *J. Phys. Chem. B* **107**, 3535–3543 (2003).

315. Zhang, F. *et al.* In situ Study of the Crystallization from Amorphous to Cubic Zirconium Oxide: Rietveld and Reverse Monte Carlo Analyses. *Chem. Mater.* **19**, 3118–3126 (2007).

316. High-Pressure, High-Temperature Formation of Phase-Pure Monoclinic Zirconia Nanocrystals Studied by Time-Resolved in situ Synchrotron X-Ray Diffraction - Research - Aarhus University. http://pure.au.dk/portal/en/persons/martin-bremholm(3f49d1f0-1e6f-40a1-bbff-d660220561c0)/publications/highpressure-hightemperature-formation-of-phasepure-monoclinic-zirconia-nanocrystals-studied-by-timeresolved-in-situ-synchrotron-xray-diffraction(fb2d9360-e586-11de-9c17-000ea68e967b).html.

317. Tyrsted, C. *et al.* In-Situ Synchrotron Radiation Study of Formation and Growth of Crystalline CexZr1−xO2 Nanoparticles Synthesized in Supercritical Water. *Chem. Mater.* **22**, 1814–1820 (2010).

318. Dippel, A. C. *et al.* Towards atomistic understanding of polymorphism in the solvothermal synthesis of ZrO2 nanoparticles. *Acta Crystallogr A Found Adv* **72**, 645–650 (2016).

319. Billinge, S. J. L. & Kanatzidis, M. G. Beyond crystallography: the study of disorder, nanocrystallinity and crystallographically challenged materials with pair distribution functions. *Chem. Commun. (Camb.)* 749–760 (2004) doi:10.1039/b309577k.

320. Sui, R., Rizkalla, A. S. & Charpentier, P. A. Direct Synthesis of Zirconia Aerogel Nanoarchitecture in Supercritical CO2. *Langmuir* **22**, 4390–4396 (2006).

321. Takami, S., Ohara, S., Adschiri, T., Wakayama, Y. & Chikyow, T. Continuous synthesis of organic–inorganic hybridized cubic nanoassemblies of octahedral cerium oxide nanocrystals and hexanedioic acid. *Dalton Trans.* **0**, 5442–5446 (2008).

322. Pradeep, E. K. C., Habu, T., Tooriyama, H., Ohtani, M. & Kobiro, K. Ultra-simple synthetic approach to the fabrication of CeO2–ZrO2 mixed nanoparticles into homogeneous, domain, and core–shell structures in mesoporous spherical morphologies using supercritical alcohols. *The Journal of Supercritical Fluids* **97**, 217–223 (2015).

323. Kim, J., Park, Y.-S., Veriansyah, B., Kim, J.-D. & Lee, Y.-W. Continuous Synthesis of Surface-Modified Metal Oxide Nanoparticles Using Supercritical Methanol for Highly Stabilized Nanofluids. *Chem. Mater.* **20**, 6301–6303 (2008).

324. Roig, Y., Marre, S., Cardinal, T. & Aymonier, C. Synthesis of Exciton Luminescent ZnO Nanocrystals Using Continuous Supercritical Microfluidics. *Angewandte Chemie International Edition* **50**, 12071–12074 (2011).

325. Ilin, E. S., Marre, S., Jubera, V. & Aymonier, C. Continuous supercritical synthesis of high quality UV-emitting ZnO nanocrystals for optochemical applications. *J. Mater. Chem. C* **1**, 5058–5063 (2013).

326. Bøjesen, E. D. & Iversen, B. B. The chemistry of nucleation. *CrystEngComm* **18**, 8332–8353 (2016).

Titre : Étude des mécanismes de stabilisation de nanoparticules de ZrO_2 quadratique en milieux fluides supercritiques

Résumé : Afin d'expliquer la stabilisation de nanoparticules de ZrO_2 de structure quadratique dans des conditions où seule la structure monoclinique est attendue, l'effet de taille est mis en avant depuis plusieurs décennies. A ce jour, aucun consensus ne préfigure au sein de la communauté scientifique. Nous proposons dans ce travail une nouvelle méthode de synthèse, basée sur le principe du sol-gel non-hydrolytique (N.H.S.G.) dans l'éthanol supercritique, permettant de stabiliser des nanoparticules de ZrO_2 dont la taille se situe sous la limite de la « taille critique » généralement admise (< 3 nm). Les qualités des nanoparticules obtenues en synthèse continue supercritique ont été mises en avant à l'aide de techniques de caractérisation *ex situ* conventionnelles telles que la diffraction des rayons X, les spectroscopies Raman et Infrarouge, ainsi que la microscopie électronique en transmission. Des mesures de diffusion des rayons X aux grands angles ont ensuite été réalisées in situ au synchrotron lors de la formation de nanoparticules de ZrO_2 dans l'éthanol, le butanol, le pentanol et l'hexanol supercritiques. L'analyse des fonctions de distributions de paires ont ainsi pu nous éclairer sur les mécanismes prépondérants pour la stabilisation de nanoparticules de ZrO_2 quadratiques : les similitudes structurelles et les lacunes en oxygène, dont la présence est liée à l'effet de taille.

Mots clés : ZrO_2, nanoparticules, fluides supercritiques, mesures *in situ*, fonction de distribution de paires

---

Title : Study of the stabilization mechanisms of tetragonal ZrO_2 nanocrystals in supercritical fluids

Abstract: To gain deeper understanding concerning the stabilization of tetragonal ZrO_2 nanoparticles when only monoclinic ZrO_2 is expected, the critical size theory has been established many decades ago. However, the theory has not yet found a consensus in the scientific community. We herein propose a new synthesis method, based on non-hydrolytic sol-gel (N.H.S.G.) reactions performed in supercritical alcohols, to stabilize ZrO_2 nanoparticles below the critical size limit generally admitted (< 3 nm). Conventional ex situ analysis techniques such as X-ray diffraction, Raman and Infrared spectroscopies and transmission electron microscopy were combined to investigate the crystal structure of ultrafine ZrO_2 nanoparticles formed in supercritical continuous flow reactors. Wide angle X-ray scattering measurements were then performed in similar conditions under a high energy X-ray source at a synchrotron to unravel in situ the formation mechanism of ZrO_2 nanoparticles in supercritical ethanol, butanol, pentanol and hexanol. Pair distribution function analysis performed on these measurements enabled us to understand the stabilization mechanisms of the tetragonal structure: structural similarities and formation of oxygen vacancies linked to the ZrO_2 nanoparticle size.

Keywords: ZrO_2, nanoparticles, supercritical fluids, *in situ* measurements, pair distribution functions

---

Unité de recherche

ICMCB-CNRS, UPR9048, 87 Av. du Dr Albert Schweitzer, 33608 Pessac (France)